RIO

PUC

Tese de Doutorado

Development and evaluation of *N*-acylhydrazonic ligands as chelators of aluminum(III): Potential implications on parkinsonism syndrome treatment

Dayanne Martins da Silva

Pontifícia Universidade Católica do Rio de Janeiro
Centro Técnico Científico
Departamento de Química

Rio de Janeiro, 01 de setembro de 2025

Pontifícia
Universidade
Católica do
Rio de Janeiro

Tese de Doutorado

Development and evaluation of *N*-acylhydrazonic ligands as chelators of aluminum(III): Potential implications on parkinsonism syndrome treatment

Dayanne Martins da Silva

Orientação: Professor Dr. Nicolás Adrián Rey
Coorientação: Professora Dra. Daphne Schneider Cukierman

Tese apresentada como requisito parcial para a obtenção do grau de Doutora em Química pelo programa de Pós-Graduação em Química, no Departamento de Química.

Rio de Janeiro, 01 de setembro de 2025

Pontifícia
Universidade
Católica do
Rio de Janeiro

Development and evaluation of *N*-acylhydrazonic ligands as chelators of aluminum(III): Potential implications on parkinsonism syndrome treatment

Dayanne Martins da Silva

Tese apresentada como requisito parcial para a obtenção do grau de Doutora em Química. Aprovada pela Comissão examinadora abaixo:

Professor Dr. Nicolás Adrián Rey
Orientador
Departamento de Química – PUC-Rio

Professora Dra.Daphne Schneider Cukierman
Co-orientadora
Instituto de Química – UERJ

Dr. Claudio Oscar Fernández
Laboratório Max Planck de Rosario – UNR

Professor Dr. Victor Marcelo Deflon
Departamento de Química e Física Molecular – USP

Professor Dr. Thomas Eichenberg Krahe
Departmento de Psicologia – PUC-Rio

Professor Dr. Julio Cesar da Rocha
Departmento de Fármacia – UERJ

Professor Dr.Renan Lira de Farias
Departamento de Química – PUC-Rio

Dra. Anna De Falco
Rensselaer Polytechnic Institute

Rio de janeiro, 01 de setembro de 2025

Pontifícia
Universidade
Católica do
Rio de Janeiro

Dayanne Martins da Silva
Formada em Química pela Universidade Estadual do Pará em 2019. Mestre em Química pela Pontifícia Universidade Católica do Rio de Janeiro (PUC-Rio) em 2021. Possui experiência em métodos analíticos e síntese orgânica aplicada à produção de fármacos.

Ficha Catalográfica

Silva, Dayanne Martins da

Development and evaluation of *N*-acylhydrazonic ligands as chelators of aluminum(III): Potential implications on parkinsonism syndrome treatment/ Dayanne Martins da Silva; co-orientador: Daphne Schneider Cukierman; orientador: Nicolás Adrián Rey. – Rio de Janeiro: PUC-Rio, Departamento de Química, 2025.

315 f.: il. (color.); 30 cm

1. Tese (Doutorado) – Pontifícia Católica do Rio de Janeiro, Departamento de Química, 2025

Inclui bibliografia.

2. Química – Teses. 3. Aluminum. 4. Parkinsonism. 5. *N*-acylhydrazone. 6. Toxicity. 7. Neuroprotetion I. Rey, Nicolás Adrián. II. Cukierman, Daphne Schneider. III. Pontifícia Católica do Rio de Janeiro. Departamento de Química. IV. Título.

CDD: 540

Acknowledgements

I would like to thank PUC-Rio and the Department of Chemistry, for making a home out of a university. To all the professors who taught and helped me throughout the semesters, thank you for your support throughout this journey.

The *Coordenação de Aperfeiçoamento de Pessoal de Nível Superior - Brasil* (CAPES) - Funding Code 001. I would also like to thank the CNPq and FAPERJ funding agencies for their support for research and funding for science.

To the members of this thesis committee. Thank you for accepting the invitation to read and collaborate with this work.

I would like to thank my advisor, Prof. Nicolás A. Rey, for accompanying me for 4 years on this academic journey in general and for the "Tio Nico, do you have 5 minutes?" that were key to the development of this work and to my maturing as a scientist. I'm very grateful for the introduction to the world of bioinorganics and I'll take all the teachings about "aluminum" with me.

I would like to deeply thank my co-advisor, Prof. Dr. Daphne S. Cukierman. Mamacita, you were so much more than a co-advisor, you were a guide, an endless source of inspiration, and, above all, a true friend. Your constant support, your passion for science, and your generosity in sharing your knowledge and time meant more than words can express. Thank you for welcoming me with such kindness and strength, especially during my most vulnerable moments. This work would not have been possible without you. Thank you so, so much!

To all collaborators (professors, student, postdocs and technicians) of this work: Dr. Claudio Fernández, Dr. Phelippe do Carmo Gonçalves and Dr. Francisco Hita for the α-synuclein NMR studies;
Prof. Dr. J. Landeira-Fernandez, Prof. Dr. Thomas Eichenberg Krahe and Dr. Silvia Maisonnette from the Department of Psychology of PUC-Rio, for the availability of space, animals and ideas.
Dr. Carolina Bastos Pereira Ligiero, from the Chemistry Institute of the Federal Fluminense University, Brazil, for the crystallographic measurements and all the support in data analysis.
Prof. Dr. Adriana Gioda, and Dr. Carlos Leonny Fragoso from the Department of Chemistry of PUC-Rio, and Dr. Anna De Falco CBIS (United States of America), for the tests involving yeast cell culture.
Prof. Dr. Tatiana Dillenburg Saint'Pierre from the Department of Chemistry of PUC-Rio, for the Inductively Coupled Plasma Optical Emission Spectrometry analyses.
Prof. Dr. Carlos German Massone from the Department of Chemistry of PUC-Rio, for the High-Performance Liquid Chromatography analyses.

My thanks also go to the Analytical Center “Fr. Leopoldo Hainberger” of the Chemistry Department at PUC-Rio for access to the various pieces of equipment used to carry out this work. I would especially like to thank the technicians, Rodrigo, Mauricio, Diogo, Matheus, Álvaro, Sulamita and Leticia for all their support.

To Dr. Rachel Ann Hauser-Davis, Dr. Renan Lira de Farias, and Dr. Carlos Leonny Fragoso, my sincerest gratitude for the valuable advice and invaluable support throughout this journey. You were there whenever I felt lost, and your help was fundamental. Thank you!

To Dr. Anna De Falcon, who so often welcomed me, calmed me, and reached out when everything seemed unbearable. For the 10-minute meetings (which always saved me), for the guidance during the experiments, and above all, for the life lessons. Anna, you were a safe haven, a true example of generosity and strength, you were genuinely a scientific mother to me. Thank you!

To my lab colleagues and IC students at LABSO-Bio, especially Hellora Eloise, for their willingness to help and for the conviviality that made it possible to give lightness and joy even on days with more failures than successes.

To the 103 rats that were sacrificed during this work: may your sacrifice not be in vain.

To my grandparents, Raimundo and Maria, to my brothers Frank and Arthur and to my family, for the support, affection and encouragement they have always given me.

To my dear friends, my family in Rio de Janeiro: Franccesca, Jessica, Annielle, and Luis Fhernando. No words can express the depth of my gratitude. You weren't just friends; you were my foundation and my home. I thank you for every laugh and every hug, but above all, for having saved me in countless ways. You kept me standing when I needed it most. This achievement belongs to you as much as it does to me.

To Marcelo Folhadella. This is the hardest part to write, because no words seem sufficient to thank you. Thank you for being my peace, for listening to my vents, for reminding me to rest, and for taking care of me. More than just support, you were the reason every effort was worthwhile. None of this would make sense or have the same joy without you by my side. Thank you for building this life and this dream with me. With all my love.

A very special thank you to David Zeitune, for our conversations at the padoca and for always being there when I needed it. My “Prefeitinho do Horto”, you made the difficult days bearable. I mean it, thank you so much!

To Alessandra Carvalho and Guilherme Lessa for their tips, advice, and partnership. You were the calm in the midst of the storms. Thank you for everything.

And if I forgot anyone, well... I would like to express my gratitude to everyone who helped me in any way.

Muito thank you!

Abstract

Silva, Dayanne Martins da; Cukierman, Daphne Schneider (co-advisor); Rey, Nicolás Adrián (Advisor). Development and evaluation of *N*-acylhydrazonic ligands as chelators of aluminum(III): Potential implications on parkinsonism syndrome treatment**.** Rio de Janeiro, 2025. 315p. Tese de Doutorado - Departamento de Química, Pontifícia Universidade Católica do Rio de Janeiro.

Parkinson's disease (PD) is a neurodegenerative condition associated with the aggregation of the protein α-Synuclein (α-Syn) and neuronal death. Biometals like copper and iron, and the non-physiological metal aluminum may be implicated in this pathology due to their involvement in protein aggregation and oxidative stress. This study aimed to develop and evaluate a set of *N*-acylhydrazone ligands as a promising strategy to mitigate the pathological effects caused by aluminum. Of the 15 compounds initially considered, 10 were selected by *in silico* analysis for synthesis and characterization. Among the synthesized compounds, **3a** (2-hydroxy-3-methylbenzaldehyde isonicotinoyl hidrazone) proved to be the most promising candidate. *In vitro* assays showed that **3a** has low toxicity to yeast cells. In human neuroblastoma cells, on the other hand, it demonstrated a dose-dependent cytotoxic effect, with a 40% reduction in cell viability at 90 μM. Investigation into its metal-binding properties revealed a good affinity for aluminum, with an apparent affinity constant of log K_{app} = 4.60 ± 0.08 for the ML stoichiometry in acidic media. Furthermore, solution studies using UV-vis and ^{1}H NMR suggested an unexpected M_2L stoichiometry possibly related to chloride-bridged aluminum salt dimerization. Regarding its interaction with α-Syn, the compound did not bind directly to the protein in solution, but, in the presence of Al^{3+}, it formed a novel ternary complex involving the protein and the metal ion. *In vivo* assays demonstrated that **3a** is capable of crossing the blood-brain barrier after oral administration and is well-tolerated at low concentrations, without affecting the homeostasis of endogenous metals like zinc and copper. However, at higher doses, the compound interfered with iron homeostasis in the liver, leading to a reduction in both the metal's levels and the organ's weight. Despite these dose-dependent effects that require further investigation, **3a** represents a promising candidate for additional preclinical studies.

Keywords: Aluminum; Parkinsonism; *N*-acylhydrazone; Toxicity; Neuroprotetion.

Resumo

Silva, Dayanne Martins da; Cukierman, Daphne Schneider (co-orientadora); Rey, Nicolás Adrián (orientador). Desenvolvimento e avaliação de ligantes *N*-acil-hidrazônicos como quelantes de alumínio(III): Implicações potenciais no tratamento da síndrome do parkinsonismo. Rio de Janeiro, 2025. 315p. Tese de Doutorado - Departamento de Química, Pontifícia Universidade Católica do Rio de Janeiro.

A doença de Parkinson (DP) é uma doença neurodegenerativa caracterizada pela presença de inclusões citoplasmáticas compostas da proteína α-sinucleína (α-Syn) agregada, e morte neuronal na região da *substantia nigra pars compacta*. Metais fisiológicos como cobre e ferro, e outros advindos de exposição ambiental como, por exemplo, o alumínio, tem sido associado a esta neuropatologia por sua atuação em processos de agregação proteica e no estresse oxidativo. O alumínio(III), em particular, constitui um agente neurotóxico de efeito conhecido sobre o sistema nervoso. Além de elevar a produção de espécies reativas de oxigênio e nitrogênio, a exposição a Al^{3+} também causa a desomeostase de ferro através do aumento na atividade de oxirredução de Fe^{3+}/Fe^{2+}. O desenvolvimento de novos medicamentos que evitem o acúmulo de íons metálicos que induzem a agregação de proteínas e, no caso do Al^{3+}, contribuem para o estresse oxidativo, parece ser uma via alternativa para retardar a progressão da DP.

Neste estudo, são relatadas 15 estruturas de *N*-acil-hidrazonas bioinspiradas em ativos farmacológicos e/ou substâncias bioativas relatadas na literatura. Após uma análise inicial *in silico*, foram selecionadas 10 moléculas com maior potencial farmacológico, que foram então sintetizadas e completamente caracterizadas em solução e no estado sólido. Nesta etapa, estruturas cristalinas inéditas foram elucidadas por difração de raios X e a solubilidade dos compostos foi avaliada em sistemas contendo no máximo 10% de solvente orgânico. Nessas condições, apenas 9 compostos apresentaram solubilidade adequada e foram submetidos a estudos de estabilidade em meio aquoso ácido e neutro. Observou-se forte influência dos substituintes na integridade das moléculas em solução, sendo um fator decisivo na estabilidade observada. Parte dos resultados obtidos na etapa de síntese e caracterização foram publicados no *Beilstein Journal of Organic Chemistry*, como primeiro artigo obtido a partir desta tese (DOI: 10.3762/bjoc.19.125).

Ao final desta etapa, apenas quatro estruturas foram consideradas para

estudos *in vitro:* 2-hidroxi-3-metilbenzaldeído isonicotinoyl hidrazona (**3a**); 3-cloro-2-hidroxibenzaldeído isonicotinoyl hidrazona (**5a**); 2-hidroxi-3-metilbenzaldeído-3,4,5-trimetoxibenzoyl hidrazona (**3b**) e 3-cloro-2-hidroxibenzaldeído-2-furoil hidrazona (**5c**). Sequencialmente, avaliou-se a tolerância ao veículo DMSO em linhagem de *Saccharomyces cerevisiae*, que demonstrou tolerância máxima de 7% ao solvente. Considerando esses limites, apenas um composto (**3a**) pôde ser testado quanto à toxicidade *in vitro* nas leveduras, demonstrando baixa toxicidade para esse tipo celular até 900 μmol L^{-1}.

O composto **3a** também foi testado em células de neuroblastoma humano, nas quais foi observada a redução da viabilidade celular em 40% na concentração de 90 μmol L^{-1}. O resultado sugere que o composto **3a** tem um efeito citotóxico dependente da dose nessas células.

Em uma próxima etapa, investigamos a capacidade de complexação do composto **3a** com íons Al^{3+}, no qual uma estequiometria M_2L inesperada em solução foi explorada por meio de experimentos de ^1H RMN. Os resultados sugerem que a estequiometria M_2L está relacionada a dimerização do sal por pontes de cloreto. Além disso, para determinação de uma constante de afinidade aparente, nitrato de alumínio foi utilizado como sal de partida. Um valor de log K_{app} = 4.60 ± 0.08 para a estequiometria ML foi obtido, indicando uma boa afinidade do ligante pelo metal mesmo em meio ácido. O complexo também foi investigado no estado sólido, no qual a hidrazona **3a** coordena o metal completamente desprotonada como um ligante tridentado doador de O_2N.

Neste trabalho também foram investigadas as interações entre a proteína α-Syn e o íon Al^{3+}, bem como o efeito do composto **3a** nesse sistema. Os resultados mostraram que embora o composto **3a** não interaja diretamente com a proteína em solução, a presença de alumínio levou à formação de um complexo ternário inédito, envolvendo α-Syn, Al^{3+} e o ligante.

In vivo, verificamos a capacidade de **3a** em atravessar a barreira hematoencefálica após ser administrado oralmente. O composto foi eficientemente identificado em extrato de cérebro de rato por HPLC. A respeito dos ensaios de toxicidade crônica, o composto foi bem tolerado em baixas concentrações, e não alterou os níveis de zinco e cobre nos órgãos de ratos sadios. No entanto, em altas doses, o composto **3a** interferiu na homeostase do ferro no fígado, resultando em

uma redução nos níveis desse metal e no peso do órgão. Apesar desses efeitos, que exigem mais investigação em doses terapêuticas, o composto pode ser considerado um candidato promissor para estudos pré-clínicos adicionais.

Palavras-chave: Alumínio; Parkinsonismo; *N*-acilhidrazona; Toxicidade; Neuroproteção

Summary

Alles, was Sie wollen, ist auf der anderen Seite de Angst…

List of Acronyms and Abbreviations

1a, 2-hydroxybenzaldehyde isonicotinoyl hydrazone

1b, 2-hydroxybenzaldehyde-3,4,5-trimethoxybenzoyl hydrazone

1c, 2-hydroxybenzaldehyde-2-furoyl hydrazone

2a, 2-hydroxy-3-methoxybenzaldehyde isonicotinoyl hydrazone

2c, 2-hydroxy-3-methoxybenzaldehyde-2-furoyl hydrazine

2-HBA, 2-hydroxy-benzaldehyde

3a, 2-hydroxy-3-methylbenzaldehyde isonicotinoyl hydrazone

3b, 2-hydroxy-3-methylbenzaldehyde-3,4,5-trimethoxybenzoyl hydrazone

3c, 2-hydroxy-3-methylbenzaldehyde-2-furoyl hydrazone

5a, 3-chloro-2-hydroxybenzaldehyde isonicotinoyl hydrazone

5c, 3-chloro-2-hydroxybenzaldehyde-2-furoyl hydrazone

Aβ, Beta amyloid

AD, Alzheimer's disease

ANOVA, Analysis of variance

α-Syn, a-synuclein

ATR, Attenuated Total Reflection

BAL, 2,3-dimercaptopropanol

BBB, Blood-brain barrier

CBA, 2-hydroxy-3-chlorobenzaldehyde

cLogP, Calculated partition coefficient

cLogS, Calculated aqueous solubility

CNS, Central nervous system

CO_2, Carbon dioxide

COSY, Correlated Spectroscopy

CRM, Certified reference materials

D_2O, Deuterium Oxide

DMEM, Dulbecco's modified Eagle's medium

DMSA, Meso-2,3- dimercaptosuccinic acid

DMSO, Dimethylsulfoxide

DMSO-d_6, Dimethylsulfoxide-d_6

DPA, D- penicillamine

EDG, Electron-donating groups

EDTA, Ethylenediaminetetraacetic acid

EWD, Electron-withdrawing groups

FBS, Fetal bovine serum

FDA, Food and Drug Administration

FUR, Furan-2-carboxyhydrazide

GC-MS, Gas Chromatography Coupled with Mass Spectrometry

H_2O_2, Hydrogen peroxide

HBA, Acceptors

HBD, Hydrogen bond donors

HCl, Hydrochloric acid

HED, Human equivalent dose

HEPES, N-(2-hidroxietil)piperazina-N′-(2-etanossulfônico)

HMBC, Heteronuclear Multiple Bond Correlation

HNO_3, Nitric acid

HPCIH, Isonicotinoyl 2-pyridine-carbaldehyde hydrazone

HPLC, High-performance liquid chromatography

HS, Hirshfeld surface analysis

HSAB, Hard and Soft Acids and Bases

HSQC, Heteronuclear Single Quantum Coherence

ICP-OES, Inductively Coupled Plasma Optical Emission Spectrometry

IDP, Intrinsically Disordered Protein

INH, Isonicotinic acid hydrazide

INHHQ, 8- hydroxyquinoline-2-carboxaldehyde isonicotinoyl hydrazone

IR, Infrared Vibrational Spectroscopy

Ka10, 2-pyridinecarboxaldehyde (N-adamantan-1-yl)benzoyl-4-amidohydrazone

KBr, Potassium Bromide

LB's, Lewy bodies

LD, Limits of Detection

LogP, Octanol-water partition coefficient

LogS, Solubility

LQ, Limits of Quantification

MBA, 2-hydroxy-3-methylbenzaldehyde

MES, Ácido 2-(N -morfolino)etanossulfônico

MP, Melting Point

MPACs, Metal-Protein Attenuating Compounds

MTT, 3-(4–dimethylthiazol-2-yl)-2,5-diphenyltetrazolium bromide

MW, Molecular weight

NAC, Non-amyloid-b hydrophobic component

NaCl, Sodium chloride

NaOH, Sodium hydroxide

NMR, Nuclear Magnetic Resonance

OBA, 2-hydroxy-3-methoxybenzaldehyde

PD, Parkinson's disease

PIH, Pyridoxal isonicotinoyl hydrazone

PLD2, Phospholipase D2

PSA, Polar surface area

REM, Rapid Eye Movement

RNS, Reactive nitrogen species

ROS, Reactive oxygen species

SDS-PAGE, Dodecil Sulfato de Sódio-Poliacrilamida Gel Electrophoresis

SNH6, 6-methoxysalicylaldehyde nicotinoyl hydrazone

SNpc, Substantia nigra pars compacta

SUG, Sugar paste

TCLM, Charge transfer process from the ligand to the metal

TGA, Thermogravimetry

ThT, Thioflavin T

TMP, 3,4,5-trimethoxybenzohydrazide

Uv, Ultraviolet

XRD, X-ray diffraction

YPD, Semi-solid medium of yeast extract-peptone-dextrose

YPG, Liquid medium yeast extract-peptone-glucose

List of Figures

List of Tables

List of Appendix Figures

List of Appendix Table

1. Introduction

1.1. Parkinson’s disease: definition and epidemiology

Parkinson's disease (PD) is a progressive multisystem disorder primarily related to the degeneration and subsequent loss of dopaminergic neurons in the *substantia nigra pars compacta* (SNpc) region, which consequently leads to a reduction in dopamine production in the presynaptic and inter synaptic space of the nigrostriatal pathway (Drui *et al*., 2014; Guatteo *et al*., 2022; Martins *et al*., 2013; Masato *et al*., 2019). The decrease in dopamine results in thecharacteristic motor symptoms of this neurodegenerative disease, such as slowness of movement (bradykinesia), resting tremor, stiffness and postural instability (De Rijk *et al*., 1997; Goedert, 2001; Silva; Carvalho, 2019; Verbaan *et al*., 2007). In addition to the deficit in the dopaminergic system, alterations have been more recently observed in the cholinergic, serotonergic and noradrenergic systems (multiple monoaminergic dysfunctions) as well, which have been linked to the observed non-motor symptoms in Parkinson's patients, such as Rapid Eye Movement (REM) sleep behavior disorder and olfactory loss (Chen *et al*., 2021), which precede the onset ofthe motor impairment, as well as anxiety, depression, and cognitive dysfunction that appear with advancing pathology (Aarsland; Zaccai; Brayne, 2005; Tibar *et al*., 2018; Williams; Litvan, 2013).

PD was first described by the English physician James Parkinson who, in 1817, published an article entitled *An Essay on The Shaking Palsy* in which he described the characteristics of six patients who presented with constant shaking (Parkinson, 2002). With thisbaseline study, it was possible to set a relationship between PD and advanced age, directing the disease mainly to individuals close to 60 years old. Besides idiopathic cases, there are the familial, or hereditary cases, called "early onset", which occur before the age of 50 and make up a small fraction (5–10 %) of the total cases (Bonato *et al*., 2025; Cristina *et al*., 2020; Post *et al*., 2020; Tenchov; Sasso; Zhou, 2025).

According to the World Health Organization, around 1 % of the world's population over the age of 65 has the disease and, currently, regions such as Europe and North America tend to record higher rates of the disease compared to other areas of the world (Li *et al*., 2025; Lim *et al*., 2019; Song *et al*., 2022). In the United States alone, approximately 90,000 new cases are diagnosed each year, a

50 % increase on previous estimates, which indicated around 60,000 new cases annually (Parkinson's Foundation, 2022). Currently, around 1.1 million people live with PD in the country, and projections suggest that this figure could exceed 1.2 million by 2030 (Michael J. Fox Foundation for Parkinson's research, 2025; Wisconsin Hospital Association, 2025). In addition, projections on a global scale indicate that this number could reach 25.2 million by 2050, representing an increase of 112 % compared to 2021 data (Su *et al*., 2025), which reflects the problems related to the increase in life expectancy.

The monogenic form of PD involves very well characterized genes, including PRKN, PINK1, DJ1, observed in young patients with autosomal recessive inheritance (Pitz *et al*., 2024). Autosomal dominant PD involves the Leucine-rich repeat kinase 2 (LRRK2) and SNCA genes (Ciampelli *et al*., 2025; Karimi-Moghadam *et al*., 2018; Rocha; De Miranda; Sanders, 2018; Somayaji *et al*., 2021). The latter is related to mutations and the overproduction of the α-synuclein protein (α-Syn) through multiplications of the gene responsible for coding this protein in humans (Kouli; Torsney; Kuan, 2018). More recently, alterations in the GBA1 gene, responsible for encoding the lysosomal enzyme glucocerebrosidase, have been identified as the main genetic risk factor for this disease (Huh *et al*., 2023; Skrahin *et al*., 2024; Vieira; Schapira, 2022).

On the other hand, exposure to toxic metals, pesticides, and fungicides constitute the main environmental factors involved in the aggravation of the disease, since they can trigger biochemical changes directly, through genotoxicity in neural cells, and indirectly through oxidative stress by increasing metal accumulation and free radical formation (Cupertino *et al*., 2017; Sule; Umbsaar; Prenner, 2020).

Regardless of the etiology linked to the disease, the main histological hallmark in PD patients is the presence of intracellular inclusions, known as Lewy bodies (LB's), which are composed mainly of aggregates of α-Syn (Figure 1A) (Binolfi *et al*., 2006; González-Baró *et al*., 2012; Lee *et al*., 2014; Spillantini *et al*., 1997a). This is an intrinsically disordered protein (IDP), with 140 amino acid residues and, in healthy individuals, it is abundant in the central nervous system. It is a protein characterized by low overall hydrophobicity, opposite charges at its ends, and can be divided into three regions (Figure 1B): the positively charged N-

terminal (residues 1-60, overall charge +4), the non-amyloid-β hydrophobic component (NAC, residues 61-95, overall charge -1), and the negatively charged C-terminal (residues 96-140, overall charge). This protein is expressed in the neuronal cytosol and in presynaptic terminals in the vicinity of synaptic vesicles, where it has been proposed that it participates in vesicle packaging, release and traffic (Bellucci *et al*., 2012; Breydo; Wu; Uversky, 2012; Flores-León; Outeiro, 2025; Geibl *et al*., 2024).

α-Syn is also involved in the processes of inhibiting the oxidation of membrane lipids, through interaction especially with those rich in acidic phospholipids such as phosphatidylserine (Barbuti, 2024; Sanluca *et al*., 2024; Schepers; Löser; Behl, 2024), as well as being involved in the regulation of various cellular enzymes such as phospholipase D2 (PLD2), responsible for phospholipid metabolism (Barbuti *et al*., 2025; Breuker; McLafferty, 2008; Vasquez *et al*., 2017). Under pathological conditions, however, α-Syn may adopt non-native conformations that lead to its aggregation and precipitation in LB's.

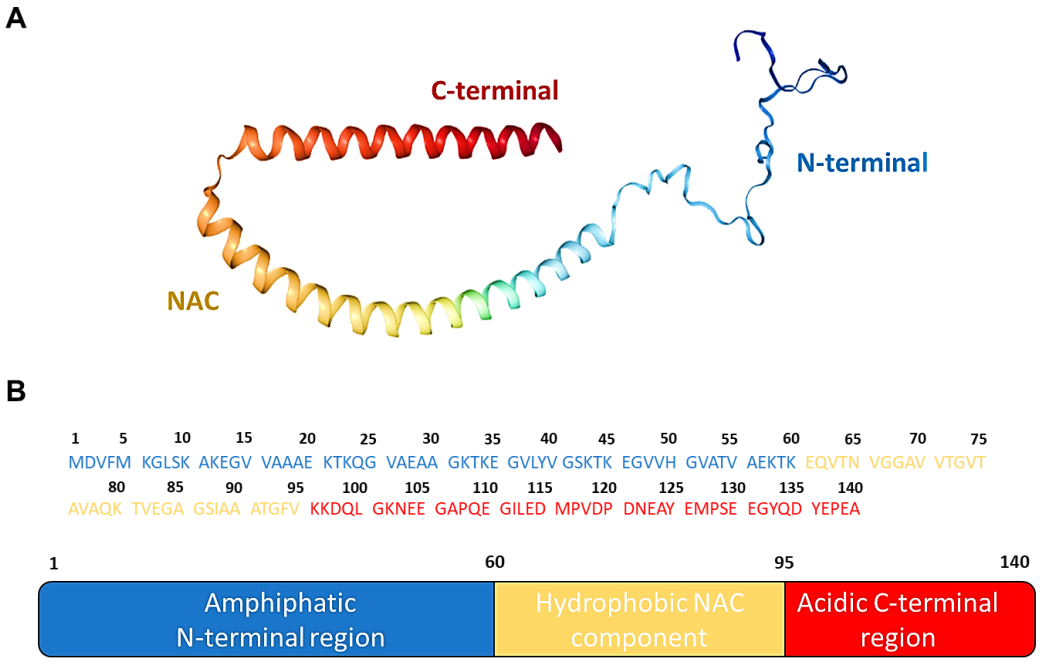

Figure 1. (**A**) Structure of human α-Syn, obtained from PDB (**B**) Primary sequence of α-Syn and N-terminal, NAC, and C-terminal regions. Adapted from (Ulmer *et al*., 2005).

In recent decades, the study of α-Syn aggregation mechanisms has contributed to understanding the etiology of a group of neurodegenerative diseases

known as synucleinopathies, including PD and diseases whose symptoms are similar to this primary condition, known as Parkinsonism. In any case, it is now accepted that the formation of protein aggregates leads to degeneration of the neocortical, limbic and nigrostriatal pathways and, as already mentioned, to dopaminergic degeneration in the SNpc in the case of PD (Nagatsu *et al*., 2022). In the latter case, the affected neurons show signs of Lewy body pathology (Figure 2) and an increase in local neuromelanin.

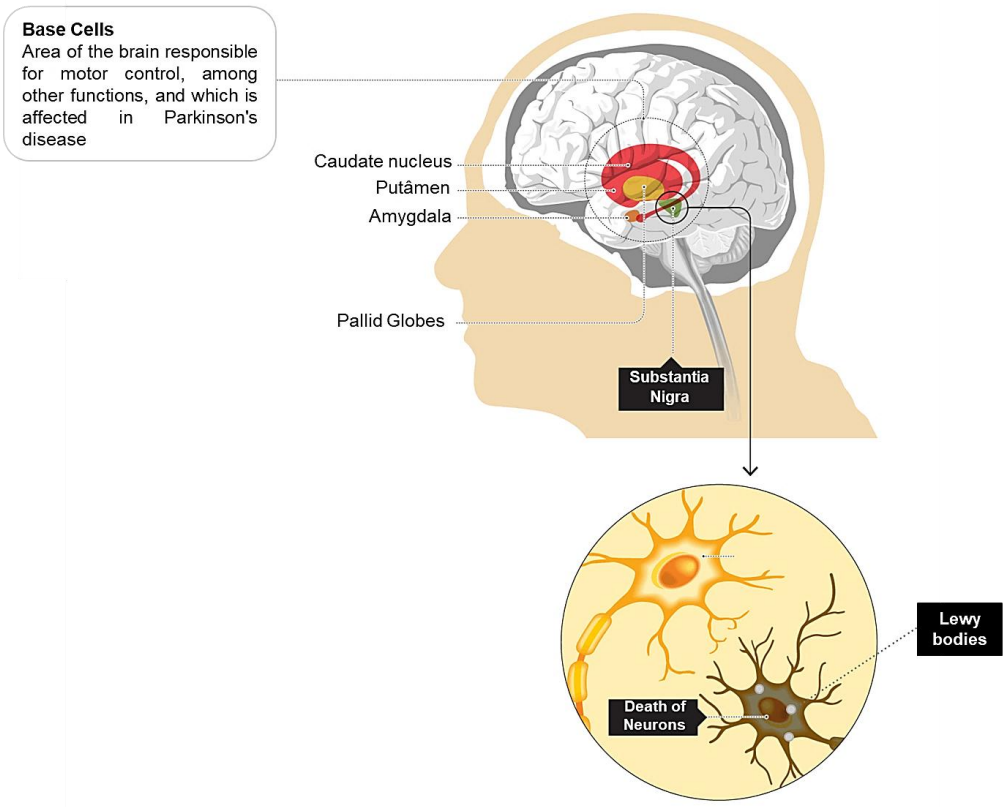

Figure 2. Representation of PD pathology. SN region of neuronal cells mainly affected in PD. Inset: Neuronal cell containing LBs. Adapted from (O GLOBO, 2017).

Because it is an IDP, α-Syn does not show a conformational preference, which facilitatesundesirable structural changes and favors the dynamic imbalance between unfolded monomericspecies and helical oligomers (α-tetramers) of this protein (Figure 3) (Gómez-Benito *et al*., 2020; Mehra; Sahay; Maji, 2019; Vidović; Rikalovic, 2022). The prevalence of unfolded monomericα-Syn favors homo-interactions due to the formation of β-sheet-rich conformers with a high propensity to aggregate into oligomeric species, currently accepted as the most toxic form of the protein (Villar-Piqué *et al*., 2018). These highly unstable species

are able to associate withmore monomers and form high molecular weight species, such as protofibrils and fibrils, that grow in a nucleation-dependent manner and precipitate in LB's.

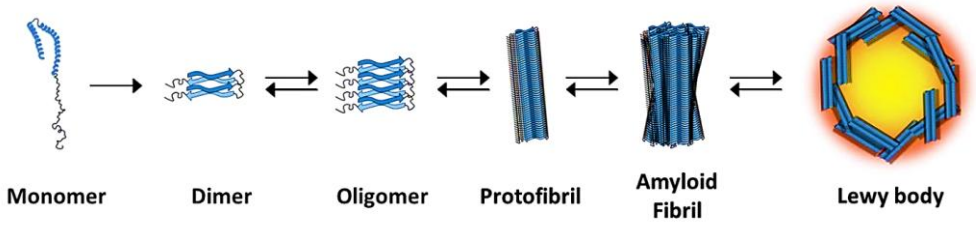

Figure 3. Schematic model of α-Syn aggregation. Adapted from (Lázaro; Pavlou; Outeiro, 2017).

1.2. Aluminum: Sources, distribution in the environment, chemical properties and solution chemistry

Aluminum is a grayish, ductile and malleable metal and is naturally present in the Earth's crust (Bonfiglio; Scimeca; Mauriello, 2023; Bryliński *et al*., 2023; Sánchez-Iglesias *et al*., 2009). Only the ^{27}Al isotope is present in nature and is mainly obtained from bauxite ores, rich in hydrated aluminum oxides such as gibbsite [$Al(OH)_3$], boehmite [γ-AlO(OH)] and diaspore [α-AlO(OH)] (Pickles; Lu, 2022).

In the natural environment, aluminum is widely distributed in the form of silicates present in igneous minerals such as clay and mica, as well as occurring as hydroxides in rocks and soils, in addition to being found in the form of oxides in precious minerals such as ruby and sapphire (Farmer, 2007; Jeršek *et al*., 2021). The action of atmospheric agents on rocks and minerals becomes a route for this metal to enter aquatic environments. Acidic rainfall, in particular, enhances the solubilization and transport of aluminum from mountainous terrains into surface waters (Bigham; Nordstrom, 2000; Blowes *et al*., 2003; Zarroca *et al*., 2021), since the reduction in pH facilitates the breakdown of aluminosilicate structures. As these minerals erode, aluminum is released into surface runoff and transported into rivers, lakes and reservoirs. The extent of this mobilization depends on factors such as the buffering capacity of the soil, vegetation cover and the mineralogical composition of the bedrock (Barabasz, 2002). Comparatively, groundwater tends to have lower concentrations of aluminum than shallow waters (Burrows; Hem, 1977). In unpolluted marine waters, on the other hand, metal levels vary according

to the clay sediments present on the seabed or suspended in the water column (Hızlı *et al*., 2023; Menzel Barraqueta *et al*., 2018).

Atmospheric agents also significantly influence aluminum dynamics in terrestrial systems. In soils, aluminum primarily in its trivalent ionic form (Al^{3+}), constitutes approximately 8 % of the total elemental composition (Aide, 2022; Drabek *et al*., 2003; Gupta; Gaurav; Kumar, 2013; Parsons; Berben, 2024). This high abundance results from the weathering of aluminosilicate minerals and is exacerbated under acidic conditions, which increase the solubility and mobility of Al^{3+} (Aide, 2022; Szczepanik *et al*., 2015; Zhang *et al*., 2022). Such processes not only affect soil chemistry but may also lead to the leaching of aluminum into groundwater (Mohammad; Zubaidy; Bassioni, 2014).

The natural presence of aluminum in the air is due to processes such as erosion and the resuspension of soil particles, especially in arid regions or those subject to strong winds (Exley, 2003; Jackson, 2024). Volcanic activity is also an important natural source, as particles containing aluminum are released in the form of ash (Alasfar; Isaifan, 2021; Al-Thani; Koç; Isaifan, 2018; Mold *et al*., 2019). In addition, rock abrasion, as well as physical and chemical weathering promote the release of mineral particles rich in aluminum, which can be carried by the wind and remain suspended in the air for long periods, depending on the size of the particles and the weather conditions (Exley, 2003).

The presence of aluminum in water, soil and air is not restricted to natural processes. Human activities also contribute greatly to the bioavailability of this metal, mainly through industrial use and the burning of fossil fuels (Alasfar & Isaifan, 2021). Processes such as the mining and processing of bauxite, the production of metallic aluminum, the incineration of urban waste, the use of food additives, cosmetics and medicines containing aluminum salts, as well as the application of phosphate fertilizers, represent relevant sources of anthropogenic emissions and dispersion of the metal in the environment (Berlana *et al*., 2024; Ganhör *et al*., 2024; Mold *et al*., 2019; Sabir *et al*., 2024). These activities increase the mobility and concentration of aluminum in different environmental compartments.

Regarding its chemical properties, aluminum in the elemental state (Al^0) has an electronic configuration of [Ne] $3s^2\ 3p^1$ with a crystalline radius of 0.675 Å. In its most common ionic form (Al^{3+}), aluminum loses its three valence electrons,

resulting in a significantly smaller ionic radius and a high positive charge density, which makes it an extremely hard Lewis acid, according to Pearson's acid-base classification (HSAB - Hard and Soft Acids and Bases) (Pearson, 1966). This implies a strong affinity for equally hard Lewis bases, especially O-donors owning negative charge such as carboxylates, phenolates, catecholates and phosphates (Alharbi *et al*., 2023).

With regard to its complexes, Al^{3+} tends to adopt an octahedral geometry, allowing the coordination of up to six donor atoms, often forming five- or six-membered chelate structures (Figure 4) which increase the thermodynamic stability of the formed complex. For this reason, multidentate ligands are preferably used in studies involving this metal (Douglas *et al*., 2023; Gallo *et al*., 2024; Parsons; Berben, 2024; Vegas *et al*., 2006).

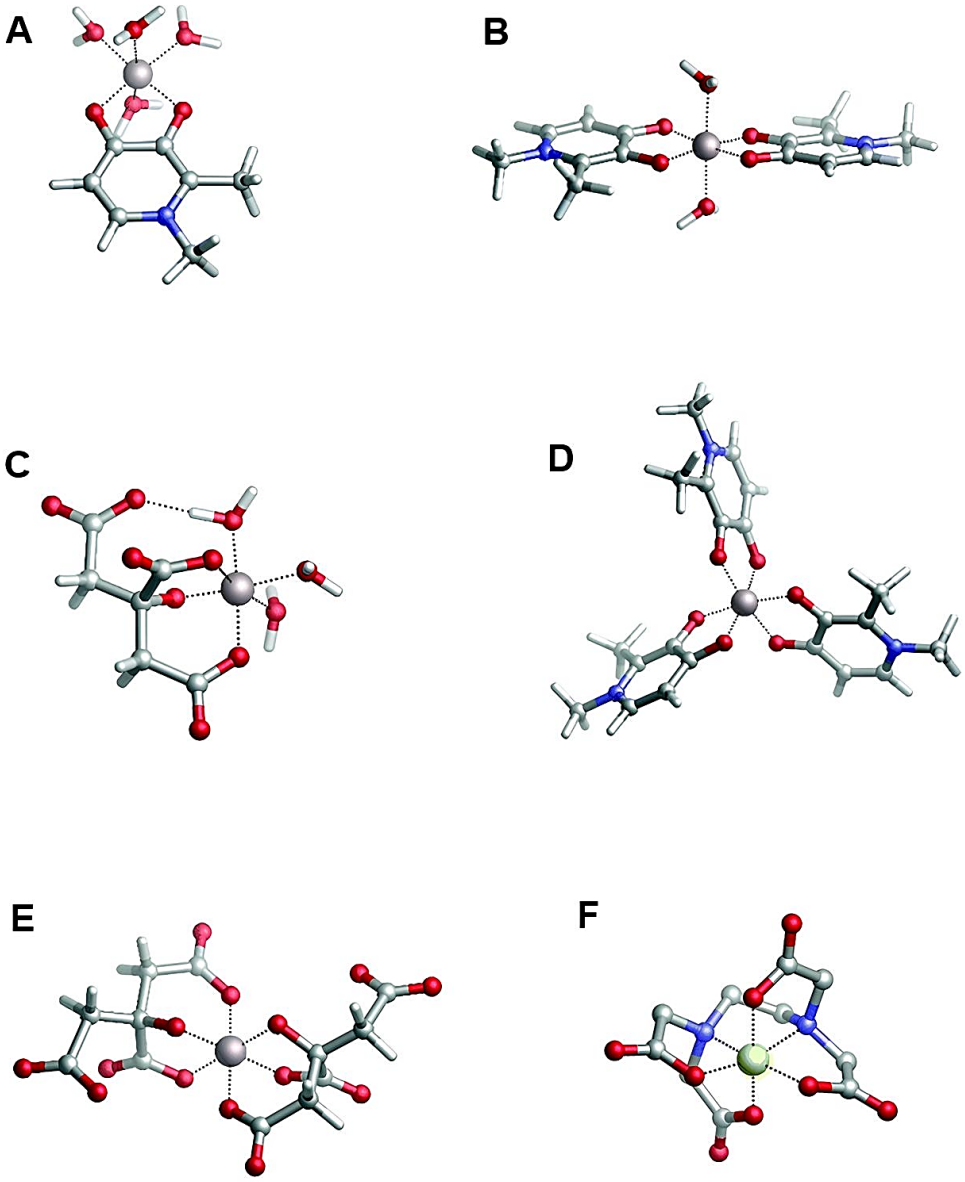

Figure 4. Proposed geometries for aluminum complexes and different ligands: (**A**) deferiprone:Al^{3+} (1:1), (**B**) deferiprone:Al^{3+} (2:1), (**C**) deferiprone:Al^{3+} (3:1), (**D**) citrate:Al^{3+} (1:1), (**E**) citrate:Al^{3+} (2:1) and (**F**) ethylenediaminetetraacetic acid:Al^{3+} (1:1). Note that deferiprone, citrate and ethylenediaminetetraacetic acid are, respectively, bidentate, tridentate and hexadentate aluminum chelators. Adapted from (Dalla Torre *et al*., 2019)

The solubility and bioavailability of aluminum in natural and biological systems are intrinsically related to its chemical speciation, which is directly dependent on the pH of the medium (Botté *et al*., 2022; Rodriguez *et al*., 2019). At a pH of less than 4, under conditions of room temperature and moderate ionic strength, aluminum remains predominantly in the form of the hexahydrate cation $[Al(H_2O)_6]^{3+}$. When the pH is changed to higher values, the progressive deprotonation of the coordinated water molecules is initiated, resulting in the

formation of hydroxylated mononuclear species, such as $[Al(OH)]^{2+}$, $[Al(OH)_2]^{+}$ and $Al(OH)_3$ (Figure 5).

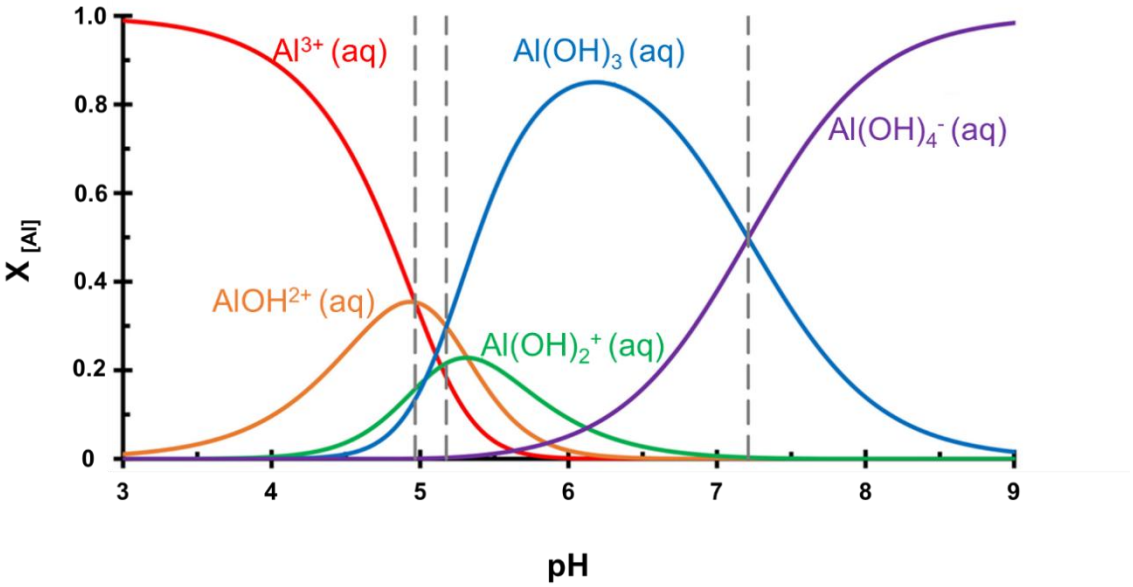

Figure 5. The calculated speciation diagram for monomeric aluminum aqueous species at 25 °C and 1 bar. Adapted from *Nikolaychuk & Kozeschnik, (2024).*

Neutral hydroxide $[Al(OH)_3]$ tends to form a precipitate around pH ≈ 4.5, representing a point of minimum solubility for aluminum in aqueous systems. However, at extremely low concentrations of aluminum (≤ 0.5 μmol L^{-1}), this precipitate can redissolve as the pH increases to approximately 6.3, promoting the formation of the tetrahedral aluminate anion $Al(OH)^{4-}$, one of the most soluble forms of aluminum in slightly basic environments (Savenko; Savenko, 2011). In addition to monomeric species, the presence of higher concentrations of aluminum (≥ 10 μmol L^{-1}) favors polymerization and the appearance of polynuclear species, such as $[Al_2(OH)_2]^{4+}$, $[Al_3(OH)_4]^{5+}$ and the Keggin-type cation $[Al_{13}(OH)_{32}]^{7+}$ (Chen *et al*., 2005; Giacobello *et al*., 2022). This transition in speciation is directly reflected in the mobility and reactivity of aluminum in environmental and biological systems, affecting its availability for absorption processes and potential toxicity.

1.3. Sources of exposure and metabolism in humans

Unlike metals such as iron and copper, which actively participate in various enzymatic reactions and essential metabolic processes, aluminum plays no known metabolic role, which makes it a non-essential metal for living beings (Jomova *et al*., 2025; Puentes-Díaz *et al*., 2023). For this reason, there are also no specific biological mechanisms for its regulation, which facilitates the progressive accumulation of this metal in tissues throughout life (Exley, 2016; Exley; Mold, 2015). The total body burden of aluminum (in healthy individuals) is estimated to be 30 to 50 mg (Malabadi *et al*., 2024).

In non-occupational conditions and in the absence of continuous use of drugs containing the metal, diet is the main source of exposure to aluminum in humans. The daily intake of aluminum through food is variable, between 3 and 10 mg (Yokel, 2025), however, its gastrointestinal absorption is relatively low, and it is estimated that approximately 0.3 % of the aluminum present in drinking water and around 0.1 % of the aluminum from food is effectively absorbed (Bryliński *et al*., 2023).

Through food, a large part of the aluminum species ingested is probably dissolved in the stomach due to the low pH; however, when it reaches the intestine, aluminum can precipitate in the form of hydroxide or hydroxyphosphate, which hinders its absorption (Yokel, 2000). On the other hand, the moderately acidic environment of the digestive system can still make a considerable percentage of this metal available in its free form, which has a transition from the intestinal barrier to the blood facilitated mainly by citric acid (Figure 6) (Cunat *et al*., 2000; Igbokwe; Igwenagu; Igbokwe, 2019).

The inhalation route represents another important way, particularly in occupational contexts that include exposure to aluminum dust in industrial environments, such as in welding, refining and bauxite extraction activities, which can increase absorption of the metal through the respiratory epithelium (Exley, 2016; Li *et al*., 2023; Rahimzadeh *et al*., 2022). The inhalation of vapors from the recreational use of psychoactive substances heated in aluminum foil, is also a relevant source of systemic exposure (Exley *et al*., 2006; Tietz *et al*., 2019).

Transdermal absorption, although less significant, can occur through the

topical and prolonged use of cosmetic products containing aluminum salts, such as antiperspirants, and is potentially relevant in contexts of chronic exposure (Rochman *et al*., 2021). The parenteral route also represents a direct way of introducing the metal into the body through the administration of medicines and immunobiologicals containing aluminum-based adjuvants, such as antacids (Bahar Akin, 2025; Romanowska *et al*., 2023; Schönenberger *et al*., 2023).

Regardless of the route of entry into the body, once in the blood and other tissue fluids, aluminum can complex with various carrier biomolecules, such as transferrin, allowing its systemic transport and possible access to the central nervous system, where it exerts its neurotoxic effect.

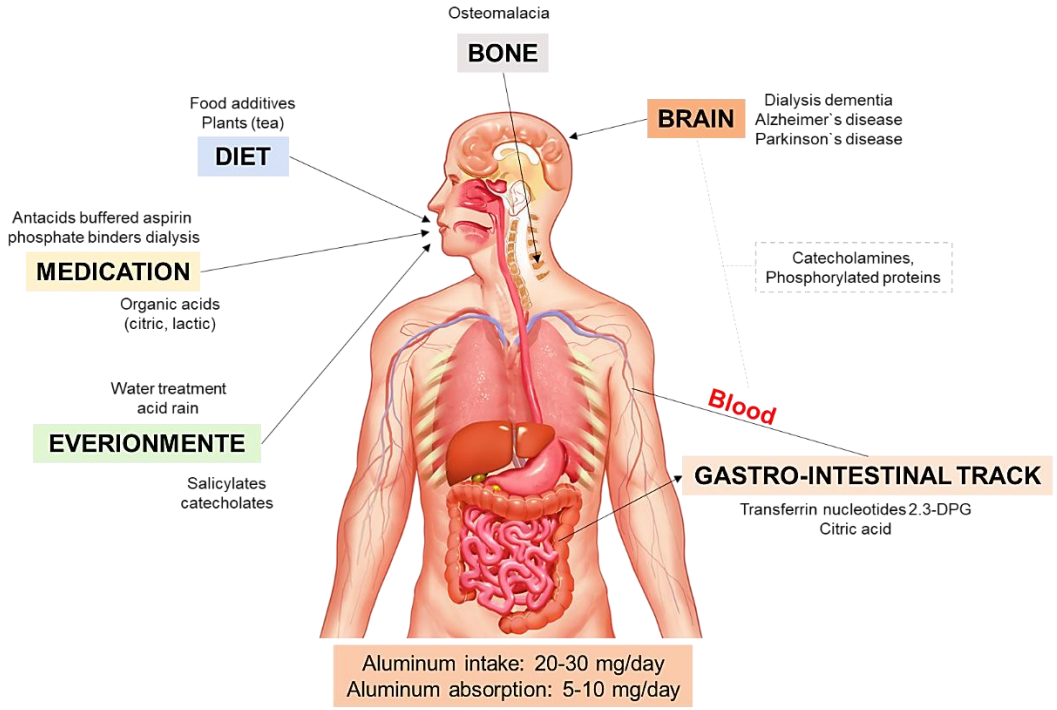

Figure 6. Different patways of aluminum entering in human body. Adapted from Rubini et al., (2002).

1.4. The role of aluminum(III) in Parkinson' disease

Although the relevance of protein aggregates for nerve cell loss is still debatable, several studies have inferred metal-protein interaction as one of the crucial factors for protein aggregation (Gentile *et al*., 2018; González *et al*., 2019; Poulson *et al*., 2020). Protein interaction with metal ions such as iron(II), aluminum(III), zinc(II), copper(I), copper(II),magnesium(II) and calcium(II) has

been shown to trigger the formation of amyloidogenic formsof β-amyloid (Aβ) and α-Syn, which are involved in the pathology of Alzheimer's disease (AD) and PD, respectively (Exley; Vickers, 2014; Shaw; Marler, 2013; Tomljenovic, 2011). α-Syn is able to coordinate metal ions through some of its side chains and also the backbone amides (Moriarty *et al*., 2014; Tian *et al*., 2019). Miotto *et al*., (2015) showed the ability of α-Syn to coordinate copper(I) through the N-terminal Methionine1-Methionine5 region, and a high-affinity site for copper(II) around Histidine50. Furthermore, studies by Abeyawardhane *et al*., (2018) demonstrated that both oxidation states of iron can interact with α-Syn *via* residues Aspartic acid119 to Glutamic acid124 in the C-terminal part of the protein (Figure 7). In both works, metal-protein interactions result in conformational changes that directly and dramatically accelerate the rate of α-Syn fibrillation.

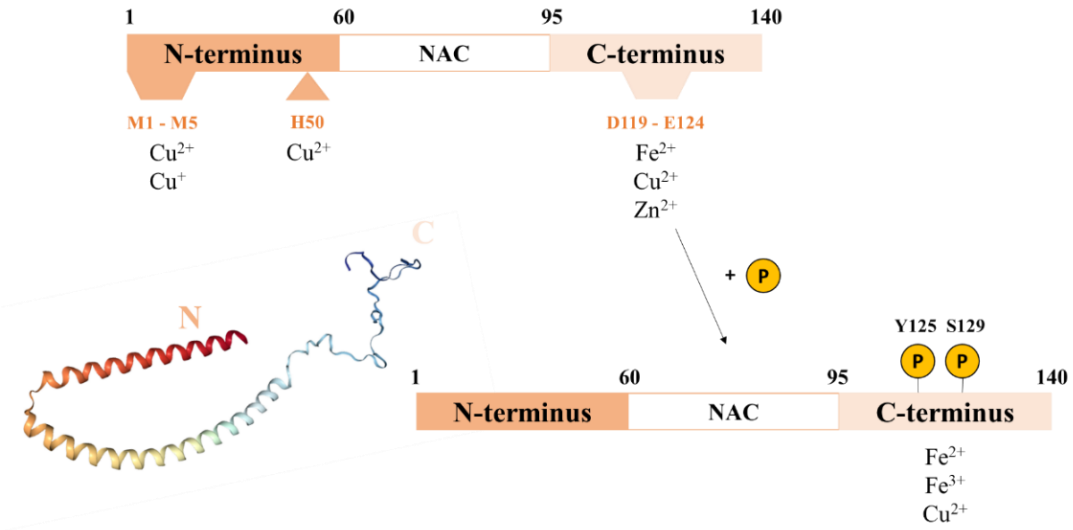

Figure 7. Metal anchoring sites in α-Syn. Adapted from González *et al*., (2019).

The exogenous metal ion Al^{3+} has also been reported to be an effective promoter of α-Syn fibrillation, and, therefore, has been suggested as one possible cause of the increased oxidative stress and cytotoxicity seen in synucleinopathies (Exley; Mold, 2019; Inan-Eroglu; Ayaz, 2018). In PD specifically, the toxicity induced by Al^{3+} ions seems to be mainly related to events leading to oxidative stress caused by increased metal accumulation and free radical formation.

Cell culture assays have shown that exposure to Al^{3+} can elevate the production of reactive oxygen and nitrogen species capable of interfering with

mitochondrial dynamics (Kumar; Bal; Gill, 2008), as well as causing iron depletion through an increase in iron(III)/iron(II) oxireduction activity (Figure 8) (Good; Olanow; Perl, 1992; Wu *et al*., 2012). In addition, aluminum also appears to act on the metabolism of iron-associated proteins. By binding to ferritin, the protein responsible for storing iron, the Al^{3+} ion can compete for the binding of the transferrin transporter, and is also carried to the brain where it can accumulate (El-Sayed *et al*., 2011).

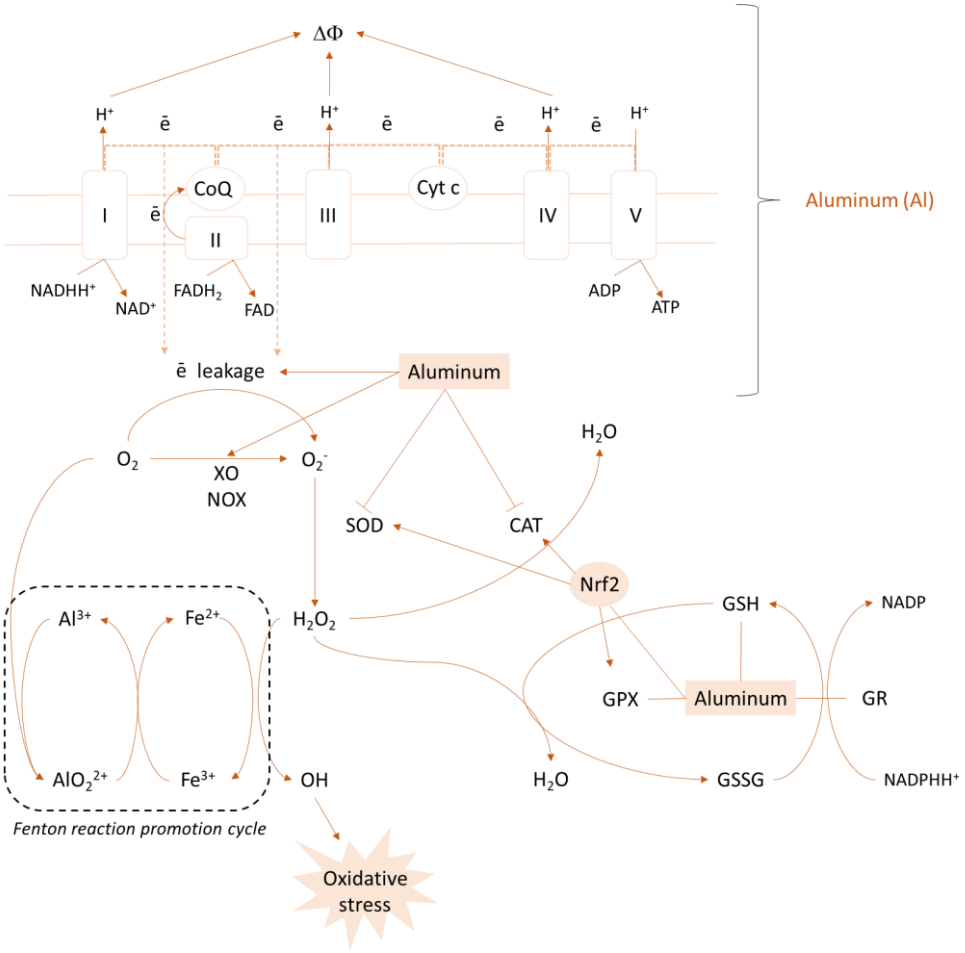

Figure 8. Mechanisms underlying the pro-oxidant effect of aluminum: Superoxide anion (O_2^-) radical formation and promotion of Fe^{2+} pro-oxidant activity in the Fenton reaction with hydroxyl radical (HO^-) generation. Adapted from Skalny *et al*., (2021).

Experimental animal models involving aluminum aimed at neurodegeneration studies usually include rats (Aitman *et al*., 2008; Fattorettif *et al*., 2004; Iannaccone; Jacob, 2009; Jayanthi M, 2013; Kumar, 2002; Majumdar; Nirwane; Kamble, 2014; Stevanović *et al*., 2009; Sumathi *et al*., 2015), mice (Sanghera; Trulson; German, 1984; Shati; Elsaid; Hafez, 2011; Singh; Goel, 2015;

Sivakumar; Sivasubramanian; Raja, 2012), the fly *Drosophila melanogaster* (Deleers; Servais; Wülfert, 1986; Kijak *et al*., 2014; Lenz *et al*., 2013; McGuire; Deshazer; Davis, 2005; Prüßing; Voigt; Schulz, 2013; Siegel; Haug, 1983; Wu *et al*., 2012) and the nematode *Caenorhabditis elegans* (Brockie *et al*., 2001; Chen *et al*., 2013; Horvitz *et al*., 1982; Mellem *et al*., 2002; Rogers *et al*., 2001; Sawin; Ranganathan; Horvitz, 2000; Ségalat; Elkes; Kaplan, 1995; Toth *et al*., 2012; Weinshenker; Garriga; Thomas, 1995), all of which show a direct effect on the inhibition of mitochondrial complexes that lead to oxidative stress, with the production of reactive oxygen species (ROS) and reactive nitrogen species (RNS) that can interfere with α-Syn protein proteostasis and consequently cause neuronal death.

In studies of brains of PD patients, high amounts of aluminum were observed both in neurons containing neuromelanin and in LB's of the SNpc (Irwin; Lee; Trojanowski, 2013). Furthermore, ithas been shown that aluminum can interact with phosphorylated α-Syn neurofilaments and thereby accumulate in the intracellular medium (Crapper; Dalton, 1973; Terry; Peña, 1965; Wiśniewski; Narkiewicz; Wiśniewska, 1967). *In vitro* and *in vivo* studies have shown that aluminum potentiates the development of neurofibrillary tangles, causes accumulation and accelerates theprocess of α-Syn oligomerization (Uversky; Li; Fink, 2001a). Other studies have shown that this metal affects the dopaminergic system by impairing the action of tyrosine hydroxylase, the enzyme that catalyzes the conversion of levodopa into dopamine (Exley; Mold, 2019; VanDuyn *et al*., 2013; Wu *et al*., 2012). Although there are already several studies on the role of the metal in PD, few in the literature are devoted to the development of viable compounds to ameliorate the impact of this metal on the body, especially in the neurological system.

1.5. *N*-acylhydrazones in the treatment of metal overload diseases

Over the years, several strategies have been researched in order to mitigate the deleterious effects attributed to metal overload in the attempt to attain a more complete treatment of some diseases. Chelation therapy was one of the first methods studied for the intervention of metal overload acquired, for example, by

copper accumulation due to Wilson's disease or neuropathologies associated with iron accumulation in the brain (Hayflick; Kurian; Hogarth, 2018; Popławska-Domaszewicz; Florczak-Wyspiańska; Kozubski, 2014), such as AD (Bulk *et al*., 2018; Lane; Ayton; Bush, 2018), PD and other parkinsonisms like Lewy body dementia, progressive supranuclear palsy, corticobasal degeneration (Connor *et al*., 1990; Devos *et al*., 2014; Lee *et al*., 2017; Martin-Bastida *et al*., 2017), the western variant of Huntington's disease (Bartzokis *et al*., 1999; Muller; Leavitt, 2014) and Friedreich's ataxia (Chiang *et al*., 2016; Richardson, 2003).

There is currently a range of chelating molecules available for clinical application, among which it is worth citing 2,3-dimercaptopropanol (BAL), ethylenediaminetetraacetic acid (EDTA), D- penicillamine (DPA) and meso-2,3-dimercaptosuccinic acid (DMSA) (Figure 9),which are used mostly to remove toxic metals such as cadmium, arsenic and mercury from thebody. However, reports in the literature highlight limitations of these compounds, such as the lack of selectivity in removing metals with important biological functions like iron, copper and zinc (Flora; Pachauri, 2010).

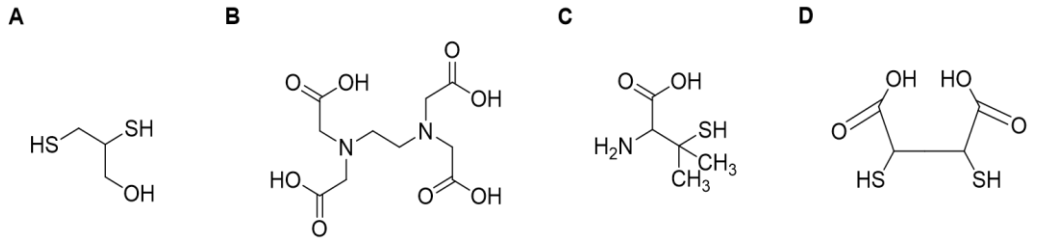

Figure 9. Structural representation of chelating agents. (**A**) 2,3-dimercaptopropanol; (**B**) ethylenediaminetetraacetic acid; (**C**) D-penicillamine; (**D**) meso-2,3- dimercaptosuccinic acid.

Because of the side effects observed in *in vivo* tests with these compounds, a search for analogues or new structures with better biocompatibility is of interest. In this broader scientific context, the investigation of bioactive *N*-Acylhydrazonic compounds becomes particularly significant, as it integrates into ongoing efforts to identify and develop novel molecules with potential pharmacological applications.

N-Acylhydrazones are a class of compounds that contain the hydrazonic functional group (–NH–N=C–) attached to an acyl group, which can be modified to generate a range of different structures with varying properties. Structurally, they have multiple reactive sites (Figure 10) and structural flexibility conferred by

the N–N rotatable bond in the hydrazine portion, while the carbonyl group introduces planarity to the molecule (Kadyan *et al*., 2025; Kostova; Saso, 2013).

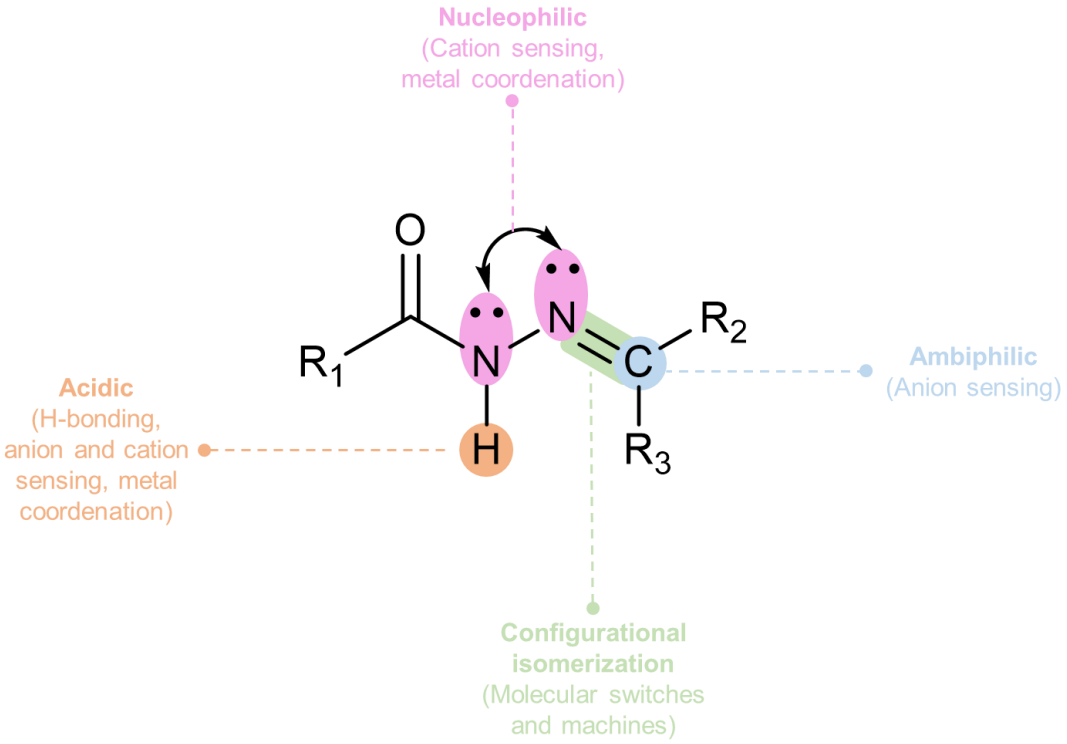

Figure 10. Multiple reactive sites in the framework of the *N*-acylhydrazone group.

The versatility of this class of compounds is also related to the ability of *N*-acylhydrazones to exist as different isomers and/or tautomers (Figure 11). They can exist as geometric isomers (*E/Z*), which differ in the orientation of the groups around the carbon–nitrogen double bond (Morjan *et al*., 2014a; Ţînţaş *et al*., 2014), as well as amido and iminol tautomers (Wegermann et al., 2022). The ability to undergo *E/Z* isomerization in a stimuli-responsive imine bond is what makes this class useful for applications in the field of molecu lar electronics, as switchers (Su; Aprahamian, 2014; Tatum; Su; Aprahamian, 2014). In addition, these compounds can also adopt *syn*- or *antiperiplanar* conformations, due to thamidoe constriction of the rotation around the conjugated amide single bond (N–C=O).

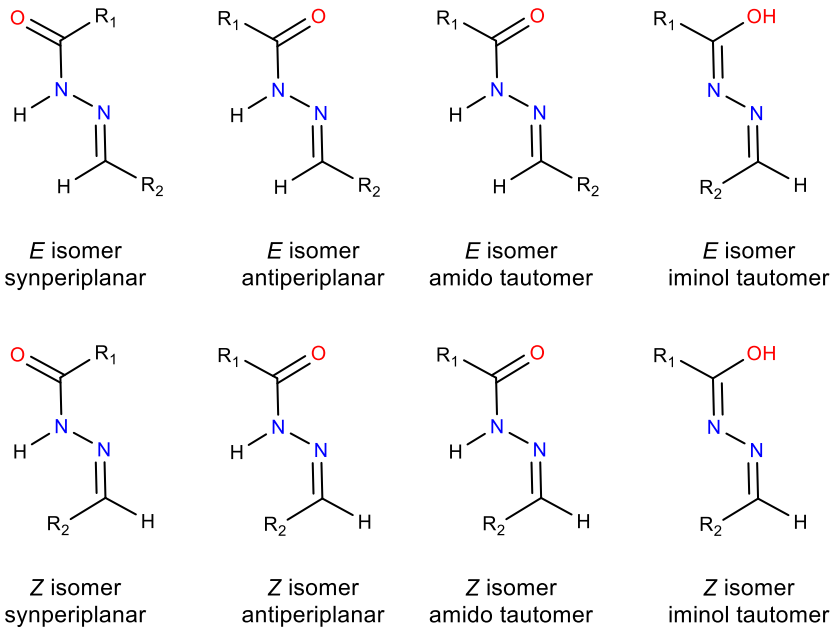

Figure 11. Isomeric sites in *N*-aroylhydrazone derivatives.

N-Acylhydrazones have also gained attention in literature due to other applications, ranging from medicine to supramolecular chemistry (Abulkhair *et al*., 2020; Abumelha, 2018). Among their applicability is the area of opto electronic devices, in which they are used for the manufacture of organic light-emitting diodes (OLEDs) (Bieliauskas *et al*., 2013; Chai *et al*., 2018; Moraes *et al*., 2016). Moreover, studies involving *N*-acylhydrazonic derivatives have high lighted their suitability for the treatment of pathologies associat ed with infection and/or inflammation (Da Costa Salomé *et al*., 2022; Dascalu *et al*., 2020; De Queiroz *et al*., 2022; Li *et al*., 2020; Singh *et al*., 2013; Thota *et al*., 2018). Antimicrobial activity is one of the most frequently studied and reported bio logical properties of this class (Morjan *et al*., 2014b; Rezki *et al*., 2019; Rohane *et al*., 2020; Xia *et al*., 2015a). Angelova and co-workers, for example, reported the ability of sulfonyl hydrazones and 4-methyl-1,2,3-thiadiazole-based hydrazone de rivatives to inhibit the growth of several bacterial strains by interfering with their metabolism or cell membrane integrity (Angelova *et al*., 2022).

In the context of cancer therapy development, metal complexes of *N*-acylhydrazones stand out. For example, Firmino *et al*. demonstrated that gallium(III) complexes of isoniazid-derived hydrazones exhibit strong cytotoxicity against HL-60 and HCT 116 cancer cell lines (Firmino *et al*., 2019). The study also found that those coor dination compounds were selective towards

abnormal cells, ex hibiting lower toxicity for healthy human hepatocytes. On the other hand, an important development in cancer research is the use of physiological metal ion complexes, which afford more biocompatibility and thus less side-effects in therapy (Wehbe *et al*., 2017). In this sense, we have reported dicopper(II) complexes from different *N*-acylhydrazonic binucleating ligands with potent antiproliferative activity against a panel of cancer cell lines (Rada *et al*., 2019, 2020, 2021).

In the bioinorganic field, the pharmacological application of *N*-acylhydrazone has been the focus of studies to generate new polydentateligands capable of coordinating physiological and non-physiological metals under neuropathological conditions (Cukierman & Rey, 2022).

In the context of physiological metal ions under dyshomeostasis observed in some aggregopathies, our research group was the first to propose the use of *N*-acylhydrazones as Metal-Protein Attenuating Compounds (MPACs) capable of competing with the target peptide or protein for the binding of the metal (Cukierman *et al*., 2018; Cukierman; Rey, 2022; De Freitas *et al*., 2013). These compounds are able to lessen and/or prevent protein aggregation, as well as to reduce the widespread oxidative stress present under such conditions (Carvalho *et al*., 2023a; Cukierman *et al*., 2019a, 2020a, 2022a; Hauser-Davis *et al*., 2015). Our first lead compound, 8- hydroxyquinoline-2-carboxaldehyde isonicotinoyl hydrazone (INHHQ) (Figure 12A), prevents both short- and long- term memory impairments induced by the intracerebroventricular infusion of Aβ oligomers in a sporadic mice model of AD (De Falco *et al*., 2020). More recently, a new family of pharmacologically-improved *N*-acylhydrazones was developed and presented optimized affinities for copper(I), being described as a promising group of non-toxic compounds capable of reducing oxidative stress and affecting α-Syn aggregation in a synucleinopathy cell model (Cukierman *et al*., 2020).

Regarding metal overload, nicotinic acid-derived *N*-acylhydrazones have been proposed as potential agents for the treatment of iron-related systemic diseases and for neurological pathologies, including PD,due to their low molecular weight and ability to cross the blood-brain barrier (BBB). In 1979, Poňka and co-workers reported a new hydrazonic ligand, pyridoxal isonicotinoyl hydrazone (PIH) (Figure 12B), containing a tridentate coordination site with high affinity for Fe^{3+}. Subsequent studies by Richardson *et al*., (1989), Becker & Richardson,

(1999), and Galić *et al*., (2008) demonstrated the ability of this ligand to chelate not only iron, but also copper, reducing their free radical catalytic activity. Furthermore, Richardson *et al*., (1999) designed and patented a new class of ligands based on pyridine-2-carboxaldehyde isonicotinoyl hydrazone (HPCIH) (Figure 12C), which showed promise in *in vitro* assays, indicating a high chelation efficiency of iron and other physiological and non- physiological metal ions. Years later, our group also investigated the HPCIH ligand in a study that showed the importance of the hydrazone fraction for the chelating activity of metal ions such as Zn^{2+}, accounting for a large part of the ligand's affinity for the target ion. In this study it was also observed that the chelating activity of hydrazones do not depend exclusively on the presence of aromatic nuclei such as 8-hydroxyquinoline, but rather on the structure and reactivity of the hydrazone unit itself (Cukierman *et al*., 2018).

In 2018, Palanimuthu and co-workers developed a new hydrazone ligand derived from adamantane, namely 2-pyridinecarboxaldehyde (N-adamantan-1-yl)benzoyl-4-amidohydrazone (Ka10) (Figure 12D). Ka10 showed significant efficacy in iron binding, reduction of copper(II)-induced β-amyloid clustering and advantageous characteristics for efficient crossing of the BBB. This same group developed another chelator, 6-methoxysalicylaldehyde nicotinoyl hydrazone (SNH6) (Figure 12E), with similar results against these metals (Wu *et al*., 2020). More recently, *N*-acylhydrazone derivatives of vitamin B6 and pyridine-4-carbaldehyde have been evaluated for their biological potential against multiple characteristics of AD, such as their chelating capacity against biometals (Zn^{2+}, Fe^{2+}, Cu^{2+}) and their antioxidant activity (Bartolić *et al*., 2024).

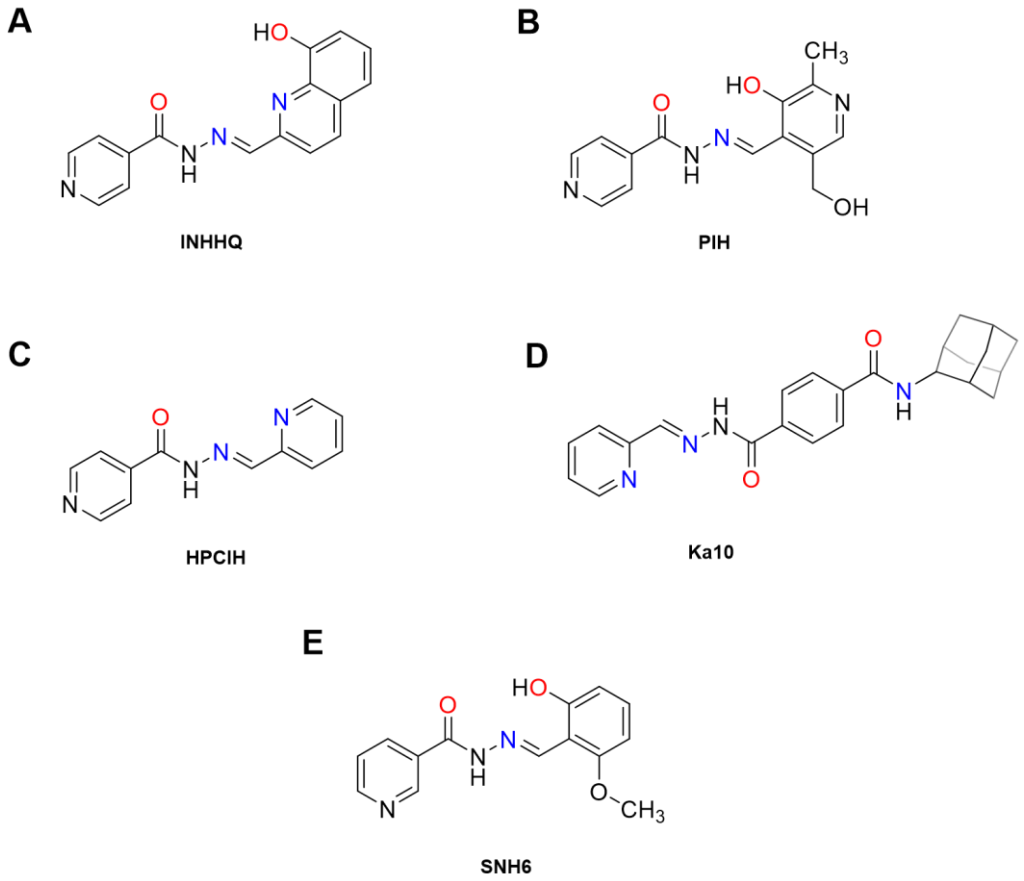

Figure 12. Chemical structures of (**A**) INHHQ: 8-hydroxyquinoline-2-carboxaldehyde isonicotinoyl hydrazone; (**B**) PIH: pyridoxal isonicotinoyl hydrazine; (**C**) HPCIH: pyridine-2-carboxaldehyde isonicotinoyl hydrazone; 3-pyridinecarbohydrazide; (**D**) Ka10: 2-pyridinecarboxaldehyde (N-adamantan-1-yl)benzoyl-4-amidohydrazone; (**E**) SNH6: 6-methoxysalicylaldehyde nicotinoyl hydrazone.

1.6. *N*-acylhydrazones: Optimized chelators for aluminum(III)

As discussed above, *N*-acylhydrazones have been widely investigated as chelating ligands in the context of metal dehomeostasis in neurodegenerations. In the specific case of aluminum(III), on the other hand, the *N*-acylhydrazone ligands designed until a few years ago were limited to applications as luminescent probes for the selective detection of Al^{3+} in solution, and involved more elaborate synthetic routes. Fan *et al*., (2014), for example, reported the development of a luminescent probe for this metal. The 7-methoxychromone-3-carbaldehyde-(pyridylformyl) hydrazone was synthesized after two synthetic steps to obtain the precursor aldehyde, with a final yield of 58.3 % (Figure 13A).

In 2017, Tang and co-workers reported the synthesis of a new acylhydrazone derived from 2-(2′-hydroxyphenyl)quinazolin-4(3H)-one for the

fluorescent recognition of Al^{3+}, obtained by a three-step synthesis and a yield of 65 % (Figure 13B). The 6-ethoxycomone-3-carbaldehyde-(3-hydroxy-2-naphthalene acyl) hydrazone sensor reported by Liu & Yang, (2018) showed good selectivity and high sensitivity towards Al^{3+} in the presence of other metal ions, such as Cu^{2+} and Fe^{2+}. However, the synthesis of this compound consists of five steps, including a Friedel-Crafts reaction to prepare the intermediate (Figure 13C).

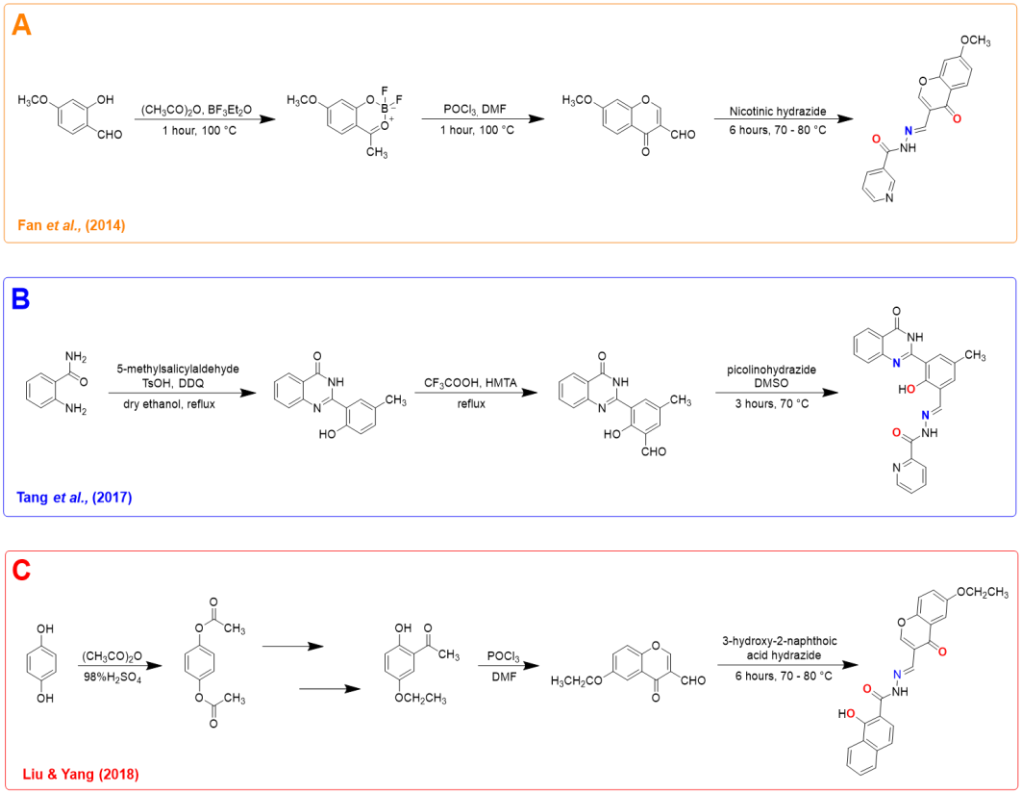

Figure 13. Synthetic route of (**A**) 7-methoxychromone-3-carbaldehyde-(pyridylformyl) hydrazine, (**B**) 2-(2′-hydroxyphenyl)quinazolin-4(3H)-one derived acylhydrazone and (**C**) 6-ethoxycomone-3-carbaldehyde-(3-hydroxy-2-naphthalene acyl) hydrazone.

Over the years, modifications and simplifications have been made to the methods used to synthesize these molecules, as well as the addition of structural elements to increase selectivity for the metal (Mathivanan *et al.*, 2021; Peng *et al.*, 2020; Wang *et al.*, 2019, 2020). Galić *et al.*, (2011) developed and tested a new series of *N*-acylhydrazones derived from salicylaldehyde that have been shown to have good affinity for Al^{3+}, which lead us to propose that this class of compounds, together with optimizations to increase the biocompatibility of these molecules, could be promising against the motor damage caused by exposure to this metal ion.

2. Work proposal

As outlined earlier, our research group pioneered this line of investigation, in the field of neurodegeneration, the applicability of *N*-acylhydrazones as new MPACs able to attenuate protein aggregation and/or oxidation, which is enhanced by the anomalous biometal-protein interactions related to Alzheimer's and Parkinson's, as well as to prion diseases.

The lead compound INHHQ (Patent codes: US 10.189.811 B2 and US 10.316.019 B2) has shown efficacy in preventing memory deficits in mice with sporadic Alzheimer's disease, as well as in reducing copper-mediated production of reactive oxygen species, which has been linked to its protective effects in the brain (De Falco *et al.*, 2020). However, INHHQ has some pharmacological limitations, such as low solubility and certain susceptibility to hydrolysis in a water-rich medium. On the other hand, the protective and metallophoric nature of this compound has served as a basis for the creation of new optimized generations of hydrazones, both in terms of pharmacological parameters and in terms of interaction or chelation with certain metal ions (Cukierman, 2021; Cukierman *et al.*, 2018, 2019a, 2020a, 2022a; Martins *et al.*, 2023). Figure 14 shows the *N*-acylhydrazones with the greatest pharmacological potential published by our group to date.

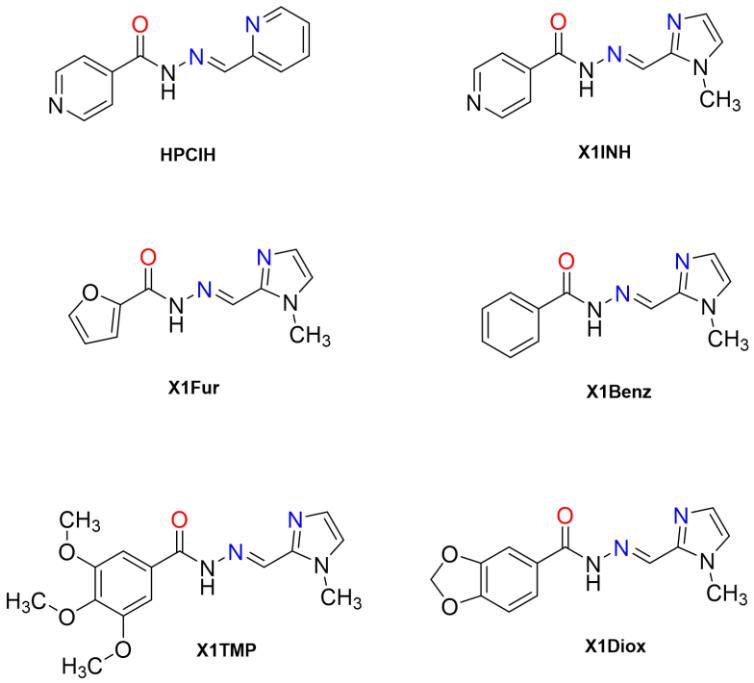

Figure 14. Structures of some *N*-acylhydrazones with the greatest pharmacological potential published by our group. The potential coordination atoms are highlighted in color.

In all these studies, precursor hydrazides were chosen based on their structural similarity to substances recognized by brain receptors, as well as to pharmacological agents applied in the treatment of other diseases. The goal was to increase the BBB permeability of the compounds and thus their bioavailability in the brain. Based on these data, in this work we initially proposed new *N*-acylhydrazones derived from 4-pyridinecarboxylic acid hydrazide (Figure 15A), 3,4,5-trimethoxybenzoic acid hydrazide (Figure 15B) and 2-furoic acid hydrazide (Figure 15C), modulated to increase affinity and specificity for Al^{3+}.

For this modulation, we worked with 2-hydroxybenzaldehyde derivatives, with substitution patterns of electron-donating groups (EDG) or electron-withdrawing groups (EWD) (Figure 15D) proposed on the basis of studies by Dalla Torre *et al*., (2018), in which the *ortho*-phenol function was used to increase the hardness of the tridentate ligand system present in the compounds (Pearson, 1963), which consequently optimizes their specificity for hard acids such as the Al^{3+} ion.

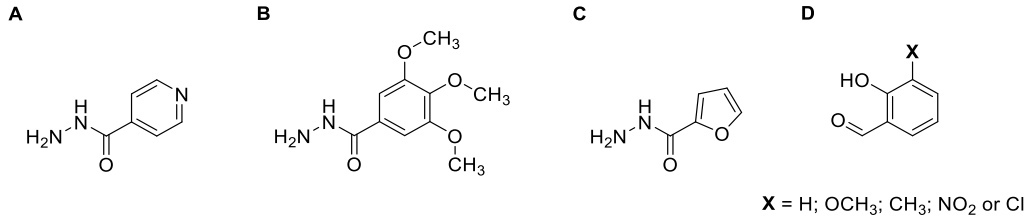

Figure 15. Structure (**A**) 4-pyridinecarboxylic acid hydrazide; (**B**) 3,4,5-trimethoxybenzoic acid hydrazide; (**C**) 2- furoic hydrazide; (**D**) Starting aldehyde substituted.

The synthesis of the new ligands was carried out based on the one-step Schiff base condensation reaction (Martins *et al*., 2023). The scheme below illustrates the general synthesis of *N*-acylhydrazones (Figure 16).

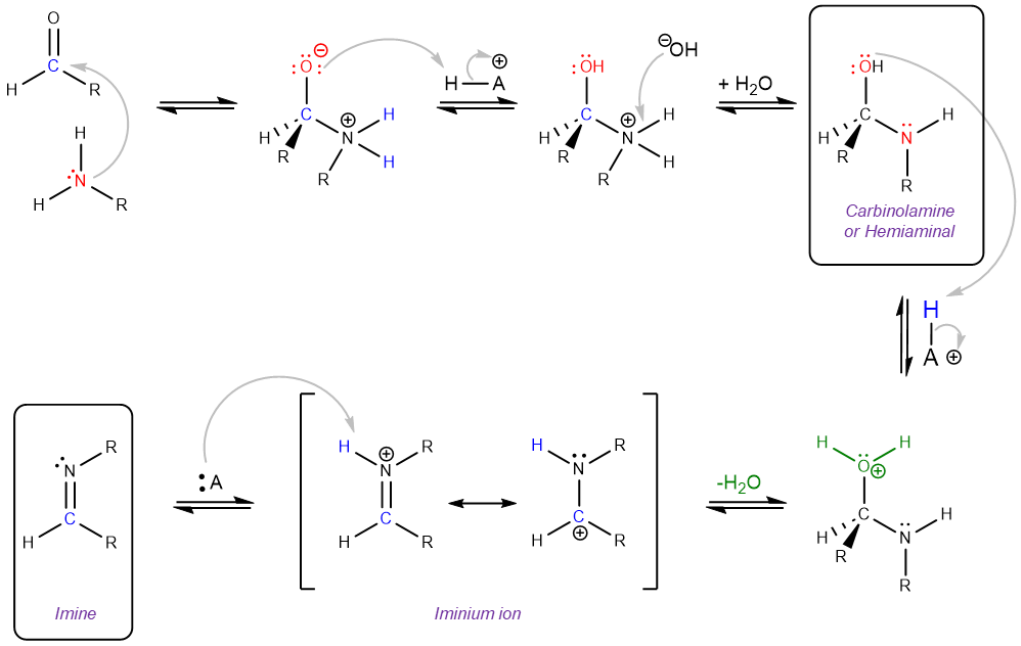

Figure 16. General mecanism representation of the synthesis.

In this work, structural rationalization resulted in 15 *N*-acylhydrazonic compounds, containing electron-donating and electron-withdrawing substituents (Figure 17). These different moieties are expected to affect the chemistry (*e.g.* acidity and susceptibility to hydrolysis) as well as structural features critical for the development of new therapeutic agents targeting aluminum(III)-related parkinsonism.

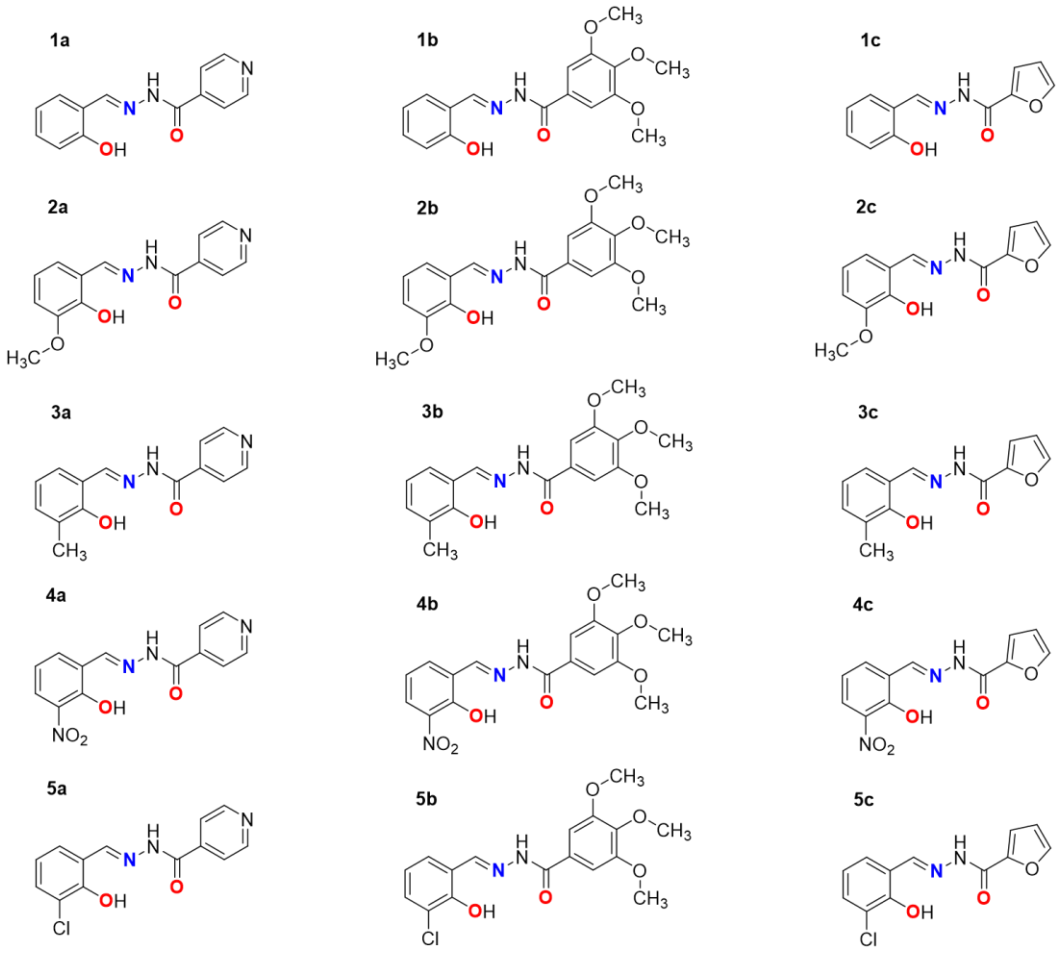

Figure 17. Structures of the 15 proposed *N*-acylhydrazones. The potential coordination atoms are highlighted in color.

3. Objectives

3.1. General objective

The general objective of this project is the synthesis and characterization of new *N*-acylhydrazones with optimized affinity for the Al^{3+} ion, with a view to investigating their potential as drugs for the treatment of parkinsonism syndrome.

3.2. Specific objectives

- To rationally propose molecules with related structure to that of the lead compound;
- To carry out a preliminary *in silico* study of the fundamental pharmacological parameters of the proposed compounds;
- To synthesize and purify the proposed *N*-acylhydrazones;
- To characterize the obtained compounds through one and two-dimensional Nuclear Magnetic Resonance, vibrational infrared and Ultraviolet-Visible molecular absorption spectroscopies, thermogravimetry, melting point, among other classical characterization techniques;
- To evaluate the solubility and stability of the hydrazones in aqueous solutions;
- To evaluate the cytotoxicity of selected hydrazones in eukaryotic cell models;
- To elucidate the coordination modes and structural features of Al^{3+} complexes with a selected hydrazone in solution and in the solid state;
- To study the interactions of α-Syn and Al^{3+} through 1D ^{1}H Nuclear Magnetic Resonance and 2D $^{1}H–^{15}N$ Heteronuclear Single Quantum Correlation using isotopically labelled protein;
- To evaluate the effect of a selected hydrazone ligand on the above-mentioned system;
- To perform short-term chronic toxicity assays on healthy male *Wistar* rats by oral administration of different concentrations of the most promising *N*-acylhydrazone;
- To determine the concentrations of metals in the organs of interest (brain,

kidneys and liver) by Inductively Coupled Plasma Optical Emission Spectrometry;

– To correlate and evaluate the effect of the most promising *N*-acylhydrazones as possible drugs for metal overload diseases.

4. Methodology

All the procedures described below were performed using analytical grade reagentsand solvents without prior purification, purchased from Sigma Aldrich, Tedia or Isofar, and the aqueous solutions for the analyses were prepared using high purity water obtained from an ELGA Purelab Ultra water purification system (resistivity 18.2 MΩ cm) at 25 °C.

4.1. *In silico* pharmacological analyses

The physicochemical parameters, potential for oral bioavailability and similarities to other published compounds were predicted using Osiris Property Explorer software: DataWarrior™, freely available for download at https://www.organic-chemistry.org/prog/peo/ (accessed on December 22, 2022).

4.2. Synthesis of the chelating agents

4.2.1. Ligand 1a

The ligand 2-hydroxybenzaldehyde isonicotinoyl hydrazone (**1a**) was prepared by dropwise adding an ethanolic solution (5 mL) containing 2-hydroxybenzaldehyde (2-HBA) (1.0 mmol, 0.122 g) to a solution of isonicotinic acid hydrazide (INH) (1.0 mmol, 0.137 g) dissolved in 15 mL of ethanol, under continuous stirring and slight heating. Two drops of concentrated hydrochloric acid were added to reach a pH value of 5. The starting pale-yellow solution immediately turned bright yellow and a precipitated was formed after 1 minute of acid addition. The system was left to stir at 50 °C for 4 hours and, at the end, the obtained solid was filtered and dried at room temperature. Yield: 42%. M.p. = 246 ± 2 ºC.

4.2.2. Ligand 2a

The ligand 2-hydroxy-3-methoxybenzaldehyde isonicotinoyl hydrazone (**2a**) was synthesized by dropwise adding an ethanolic solution (10 mL) containing

2-hydroxy-3-methoxybenzaldehyde (OBA) (1.0 mmol, 0.152 g) to a solution of INH (1.0 mmol, 0.137 g) dissolved in 15 mL of ethanol, under continuous stirring and slight heating. Two drops of concentrated hydrochloric acid were added to reach a pH value of 5. The starting pale-yellow solution immediately turned bright yellow and a precipitated was formed after 2 minutes of acid addition. The system was left to stir at 50 °C for 4 hours and, at the end, the obtained solid was filtered and dried at room temperature. Yield: 56%. M.p. = 229 ± 1 ºC.

4.2.3. Ligand 3a

The ligand 2-hydroxy-3-methylbenzaldehyde isonicotinoyl hydrazone (**3a**) was prepared by dropwise adding an ethanolic solution (5 mL) containing 2-hydroxy-3-methylbenzaldehyde (MBA) (1.0 mmol, 0.136 g) to a solution of INH (1.0 mmol, 0.137 g) dissolved in 15 mL of ethanol, under continuous stirring and slight heating. Three drops of concentrated hydrochloric acid were added to reach a pH value of 5. The starting pale orange solution immediately turned bright orange and a precipitated was formed after 2 minutes of acid addition. The system was left to stir at 50 °C for 4 hours and, at the end, the obtained solid was filtered and dried at room temperature. Yield: 63%. M.p. = 240 ± 1 ºC.

4.2.4. Ligand 5a

The ligand 3-chloro-2-hydroxybenzaldehyde isonicotinoyl hydrazone (**5a**) was synthesized by dropwise adding an ethanolic solution (10 mL) containing 2-hydroxy-3-chlorobenzaldehyde (CBA) (1.0 mmol, 0.156 g) to a solution of INH (1.0 mmol, 0.137 g) dissolved in 15 mL of ethanol, under continuous stirring and slight heating. Three drops of concentrated hydrochloric acid were added to reach a pH value of 5. The starting pale-yellow solution immediately turned bright yellow and a precipitated was formed after 2 minute of acid addition. The system was left to stir at 50 °C for 4 hours and, at the end, the obtained solid was filtered and dried at room temperature. Yield: 51%. M.p. = 266 ± 1 ºC.

4.2.5. Ligand 1b

The ligand 2-hydroxybenzaldehyde-3,4,5-trimethoxybenzoyl hydrazone (**1b**) was prepared by dropwise adding an ethanolic solution (5 mL) containing 2-HBA (1.0 mmol, 0.122 g) to a solution of 3,4,5-trimethoxybenzohydrazide (TMP) (1.0 mmol, 0.226 g) dissolved in 10 mL of ethanol, under continuous stirring and slight heating. Two drops of concentrated hydrochloric acid were added to reach a pH value of 5. The system was left to stir at 50 °C for 4 hours and the mixture was cooled to room temperature and set for slow evaporation of the solvent. After 5 days, very fine needle-shaped yellowish crystals were obtained, filtered and dried at room temperature. Yield: 51%. M.p. = 171 ± 1 ºC.

4.2.6. Ligand 3b

The ligand 2-hydroxy-3-methylbenzaldehyde-3,4,5-trimethoxybenzoyl hydrazone (**3b**) was synthesized by dropwise adding an ethanolic solution (5 mL) containing MBA (1.0 mmol, 0.136 g) to a solution of TMP (1.0 mmol, 0.226 g) dissolved in 10 mL of ethanol, under continuous stirring and slight heating. Two drops of concentrated hydrochloric acid were added to reach a pH value of 5. A beige precipitate formed from the initially translucent solution after 2 minutes of acid addition. The system was left to stir at 50 °C for 4 hours and, at the end, the obtained solid was filtered and dried at room temperature. Yield: 78%. M.p. = 180 ± 1 ºC.

4.2.7. Ligand 1c

Th ligand 2-hydroxybenzaldehyde-2-furoyl hydrazone (**1c**) was prepared by dropwise adding an ethanolic solution (5 mL) containing 2-HBA (1.0 mmol, 0.122 g) to a solution of furan-2-carboxyhydrazide (FUR) (1.0 mmol, 0.126 g) dissolved in 10 mL of ethanol, under continuous stirring and slight heating. Two drops of concentrated hydrochloric acid were added to reach a pH value of 5. The system was left to stir at 50 °C for 4 hours and, the mixture was cooled to room temperature and set for slow evaporation of the solvent. After 7 days, rectangular

yellow crystals were obtained, filtered and dried at room temperature. Yield: 38%. M.p. = 169 ± 1 ºC.

4.2.8. Ligand 2c

The ligand 2-hydroxy-3-methoxybenzaldehyde-2-furoyl hydrazone (**2c**) was synthesized by dropwise adding an ethanolic solution (10 mL) containing OBA (1.0 mmol, 0.152 g) to a solution of FUR (1.0 mmol, 0.126 g) dissolved in 10 mL of ethanol, under continuous stirring and slight heating. Three drops of concentrated hydrochloric acid were added to reach a pH value of 5. A white precipitate formed from the initially translucent solution after 2 minutes of acid addition. The system was left to stir at 50 °C for 4 hours and, at the end, the obtained solid was filtered and dried at room temperature. Yield: 35%. M.p. = 148 ± 2 ºC.

4.2.9. Ligand 3c

The ligand 2-hydroxy-3-methylbenzaldehyde-2-furoyl hydrazone (**3c**) was prepared by dropwise adding an ethanolic solution (5 mL) containing MBA (1.0 mmol, 0.136 g) to a solution of FUR (1.0 mmol, 0.126 g) dissolved in 10 mL of ethanol, under continuous stirring and slight heating. Two drops of concentrated hydrochloric acid were added to reach a pH value of 5. The system was left to stir at 50 °C for 4 hours and the mixture was cooled to room temperature and set for slow evaporation of the solvent. After 7 days, very fine needle-shaped yellow crystals were obtained, filtered and dried at room temperature. Yield: 77%. M.p. = 161 ± 1 ºC.

4.2.10. Ligand 5c

The ligand 3-chloro-2-hydroxybenzaldehyde-2-furoyl hydrazone (**5c**) was synthesized by dropwise adding an ethanolic solution (10 mL) containing CBA (1.0 mmol, 0.156 g) to a solution of FUR (1.0 mmol, 0.126 g) dissolved in 10 mL of ethanol, under continuous stirring and slight heating. Two drops of concentrated

hydrochloric acid were added to reach a pH value of 5. The system was left to stir at 50 °C for 4 hours and the mixture was cooled to room temperature and set for slow evaporation of the solvent. After 5 days, very fine needle-shaped pale-yellow crystals were obtained, filtered and dried at room temperature. Yield: 50%. M.p. = 180 ± 1 ºC.

4.3. Complex 1

Complex **1** was synthesized by the dropwise addition of 1.0 mmol of **3a** (0.255 g) to a solution of 1.0 mmol of aluminum nitrate nonahydrate [$Al(NO_3)_3 \cdot 9\ H_2O$] (0.375 g) in ethanol, resulting in a final volume of 20 mL. The mixture was stirred at room temperature for 6 hours, leading to the formation of a reddish-orange solution. The reaction mixture was then left undisturbed to allow slow evaporation of the solvent. After 7 days, red crystals were obtained, which were carefully collected and properly characterized.

4.4. Chemical Characterization

4.4.1. Nuclear Magnetic Resonance (NMR)

Hydrogen and carbon nuclear magnetic resonance spectra (NMR), homonuclear ^1H x ^1H COSY (Correlated Spectroscopy) and heteronuclear ^1H x ^{13}C HSQC (Heteronuclear Single Quantum Coherence) and HMBC (Heteronuclear Multiple Bond Correlation) experiments were recorded on a 400 MHz Avance III (Bruker™) at room temperature. Samples were dissolved in 0.5 mL deuterated dimethylsulfoxide (DMSO-d_6) and spectra were referenced based on the residual solvent signal (quintet at 2.50 ppm for ^1H and septet at 39.52 for ^{13}C). For experiments involving a mixture of deuterated solvents DMSO- d_6/D_2O (v/v), the spectra were calibrated on the basis of the residual DMSO-d_6 signal (quintet at 2.50 ppm for ^1H). These analyses were performed at the Analytical Facilities “Pe. Leopoldo Hainberger”, from the Department of Chemistry at PUC-Rio.

4.4.2. Mass Spectrometry

Gas Chromatography coupled with Mass Spectrometry (GC-MS) analyses were performed on a Trace 1300 gas chromatograph equipped with DB5-MS 20 m × 0,18 mm × 0,18 μm column coupled to an ISQ model mass spectrometry (Thermo Scientific™). Samples were prepared in methanol at 1 mg mL^{-1} concentration. These analyses were performed at the Analytical Facilities "Pe. Leopoldo Hainberger", from the Department of Chemistry at PUC-Rio.

4.4.3. Infrared Vibrational Spectroscopy (IR)

Absorption spectra in the mid-infrared region were obtained using either the attenuated total reflection (ATR) technique on a Bruker ALPHA II FTIR instrument equipped with an Eco-ATR QuickSnap™ sampling attached with a diamond/ZnSe crystal plate or as potassium bromide (KBr) pellets on a Perkin-Elmer 100 series Fourier transform spectrophotometer (Perkin-Elmer™) in the spectral range from 4000 to 400 cm^{-1} with a resolution of 4 cm^{-1}.

4.4.4. Thermogravimetry (TGA)

Thermogravimetric analyses were performed using a Pyris 1 TGA analyzer, Perkin-Elmer™. Samples were placed in platinum pans, heated under nitrogen flow (20 mL min^{-1}), with scans from 25 to 350 °C at a heating rate of 10 °C min^{-1}.

4.4.5. Melting Point (MP)

Melting point determinations of the ligands were performed in triplicate using a Fisatom™ model 431 apparatus.

4.4.6. X-ray Diffraction (XRD)

Crystallographic measurements were carried out in collaboration with Dr. Carolina Bastos Pereira Ligiero, from the Chemistry Institute of the Federal Fluminense University, Brazil.

X-ray diffraction analyses of the single crystals were obtained using a D8-Venture Bruker diffractometer equipped with Mo Kα X-ray source at 293 K. Diffraction images were collected with a Photon III area detector and the frames were integrated with the Bruker SAINT software using a narrow-frame algorithm (APEX3, 2012). Absorption correction was conducted with the multi-scan method in SADABS software (APEX3 system) (Krause *et al*., 2015). The structures were solved with directed methods in ShelxS and refined with full-matrix least-square in ShelxL (Sheldrick, 2015), implemented in WinGX (Farrugia, 2012) and ShelxLE (Hübschle; Sheldrick; Dittrich, 2011) platforms. Figures were prepared with Mercury (Macrae *et al*., 2006), Fourier maps, data and tables were prepared with Platon (Spek, 2009), and the Hirshfeld surfaces and fingerprint plots were calculated from the CIF files using Crystal Explorer (Spackman *et al*., 2021). Potential electrostatic maps and electron density surfaces were calculated with DFT method from the CIF files using TONTO, also implemented in Crystal Explorer (Spackman *et al*., 2021).

4.4.7. Aluminum Determination by Emission Spectroscopy

A sample containing 1 mg of the complex was digested with 1 mL of nitric acid (HNO_3, 67% v/v) and diluted to 50 mL with distilled water. This solution was then analyzed in triplicate by Inductively Coupled Plasma Optical Emission Spectrometry (ICP-OES), in an Optima 7300DV model (Perkin-Elmer™) equipment, previously calibrated for aluminum. The external calibration of the equipment was done from the appropriate dilutions of the multi-element standard (Merck IV). This assay was performed at the Analytical Facilities “Pe. Leopoldo Hainberger”, from the Department of Chemistry at PUC-Rio.

4.4.8. Molecular Absorption Spectroscopy

All spectrophotometric studies were performed in an Agilent™ Cary 100 conc UV-visible spectrophotometer, between 200 and 600 nm, using quartz cuvettes with a 1.0 cm opticalpath. All the tests were carried out at the Analytical Facilities “Pe. Leopoldo Hainberger”, from the Department of Chemistry at PUC-Rio.

4.4.8.1. Molar Absorptivity

To determine the molar absorptivity and, consequently, the experimental working range, stock solutions containing the respective compounds were prepared in pure DMSO (5.0×10^{-3} mol L^{-1}). From this solution, dilutions were made in the range of 6.0×10^{-5} to 5.0×10^{-6} mol L^{-1} to obtain solutions containing 1 or 10% DMSO in acetate buffer pH 4.5 or HEPES buffer [N-(2-hidroxietil)piperazina-N′-(2-etanossulfônico)] pH 7.4 (2.0×10^{-1} mol L^{-1}). These solutions were analyzed by spectrophotometry in the region between 200 and 600 nm and the linear relationship between the concentration of the ligand and its absorbance was determined using the Lambert-Beer law ($A = \varepsilon_x b_x c$).

4.4.8.2. Stability Against Hydrolysis

The compounds were prepared at low concentrations (5.0×10^{-5} mol L^{-1}) in acetate buffer pH 4.5 or HEPES buffer pH 7.4 (2.0×10^{-1} mol L^{-1}) containing 1 or 10% DMSO, from stock solutions (5.0×10^{-3} mol L^{-1}) in pure DMSO. The solutions were kept at room temperature throughout the experiment. Monitoring of the changes in the electronic spectrum of the compounds in the region between 200 and 600 nm were done at regular intervals for 12 hours, and a final measurementwas made after 2 days. The change in absorbance intensity was used to calculate the percentage decrease in concentration of the compound with respect to the first reading. A comparison with the spectra of the precursors under the same solvent and concentration conditions was done. A Gaussian fitting was performed on the first (t_0) and last spectrum(t_{12}) using OriginPro™ 21 software.

4.4.8.3. pKa Determination

The compounds were prepared in low concentrations (5.0×10^{-5} mol L^{-1}) in solutions containing 1 or 10% DMSO/buffer (acetate, phosphate, HEPES or carbonate-bicarbonate buffer in concentration 2.0×10^{-1} mol L^{-1}) with different pH values, ranging from 3.8 to 9.0. Solutions of hydrochloric acid (HCl) and sodium hydroxide (NaOH) at 10^{-1} mol L^{-1} were used for pH adjustment. The compounds solutions were analyzed by spectrophotometry in the region between 200 and 600 nm. The apparent pKa was obtained by fitting the curve with a sigmoidal function using OriginPro™ 21 software.

4.4.8.4. Complexation Kinetics

For the complexation kinetics, solutions of complexes with different Al^{3+}:hydrazone molar ratios (1:2, 1:1 and 2:1) were prepared in 1% DMSO/acetate buffer (2.0×10^{-1} mol L^{-1}, pH 4.5). The hydrazone concentration was kept constant (5.0×10^{-5} mol L^{-1}) while the Al^{3+} concentration was varied to obtain the desired Al^{3+}:hydrazone molar ratio. The solutions were kept at 25 ± 0.1 °C throughout the experiment using a ThermoShaker, KASVI™. The changes in the electronic spectra of the complexes were monitored in the region between 200 and 600 nm until the reaction stabilized. In each experiment, the ionic strength was kept constant at 10^{-1} mol L^{-1} by adding solid sodium chloride (NaCl).

4.4.8.5. Complexation Study

The hydrazones were prepared at low concentrations (5.0×10^{-5} mol L^{-1}) in acetate buffer (2.0×10^{-1} mol L^{-1}, pH 4.5) containing 1 or 10% solvent (DMSO), from pure solvent stock solutions (5.0×10^{-3} mol L^{-1}). The metal salt solution (10^{-2} mol L^{-1}) was prepared in a buffer solution using anhydrous aluminum chloride ($AlCl_3$). Different amounts of metal salt solution were added to the ligand solution and homogenized. The solutions were kept at 25 ± 0.1 °C under stirring at 500 rpm throughout the experiment using a ThermoShaker, KASVI™. Monitoring of the changes in the electronic spectra of the complexes in the region between 200 and

600 nm was done 6 hours after the addition of metal solution to the ligand. In each experiment, the ionic strength was kept constant at 10^{-1} mol L^{-1} by adding solid NaCl.

4.4.8.6. Method of Continuous Variations (Job Plot)

For the method of continuous variations, the molar absorptivities of the ligands were initially determined using 1% DMSO/acetate buffer (2.0 x 10^{-1} mol L^{-1}, pH 4.5) as the solvent. To determine the stoichiometry and apparent affinity constant, mixtures with different molar fractions of the ligand and metal salt [$Al(NO_3)_3 \cdot 9\ H_2O$] were prepared at low concentration (5.0 x 10^{-5} mol L^{-1}) in acetate buffer, containing 1% solvent (DMSO) from stock solutions in pure DMSO (5.0 x 10^{-3} mol L^{-1}). The solutions were kept at 25 ± 0.1 ºC and 500 rpm throughout the experiment using a ThermoShaker, KASVI™. Eletronic spectra of the mixtures in the region between 200 and 600 nm were aquired 6 hours after the preparation. From the molar absorptivity (ε) values of the ligands and the Lambert-Beer law, theoretical molar absorptivity of the complex was estimated from the intersection point of the linear regions of the Job plot. Using this ε value and the experimentally observed maximum absorbance, the equilibrium concentration of the complex was calculated. The concentration of the free ligand was determined from the residual absorbance of the hydrazone band at the molar fraction corresponding to the observed stoichiometry. With the equilibrium concentrations of the complex, free ligand, and metal ion established according to the reaction stoichiometry, the apparent affinity constant was calculated using the equilibrium expression K_{app} = [ML] / [L][M], valid for a 1:1 complex.

4.5. Cell Toxicity analyses

The tests involving yeast cell culture were carried out in collaboration with Prof. Dr. Adriana Gioda, from the Department of Chemistry of the Pontifical Catholic University of Rio de Janeiro, Brazil.

4.5.1. Yeast

The yeast *Saccharomyces cerevisiae* was isolated from fresh baker's yeast, as mentioned in De Falco *et al*., (2022). Briefly, a small sample of yeast was taken and homogenized in ultrapure water, forming a solution that was diluted sequentially until no turbidity was observed. For cultivation and isolation, an aliquot containing the yeast sown by exhaustion was transferred to a Petri dish containing a semi-solid medium of yeast extract-peptone-dextrose (YPD) (0.1% yeast extract, 1% peptone, 2% glucose and 3% agar) initially prepared in ultrapure water and pH (6.0 ± 0.1) adjusted with a solution of HCl (10^{-1} mol L^{-1}). The plate was then incubated for 24 hours in a cell growth incubator, without stirring, at a constant temperature of 30 °C. Finally, to prepare the pre-inoculum, a visibly isolated colony was transferred to the liquid medium yeast extract-peptone-glucose (YPG) [0.5% yeast extract, 1% peptone and 2% glucose in ultrapure water, pH (6.0 ± 0.1)], and kept in a growth incubator (Qualxtron™) for 12 h at 30 °C with shaking at 140 rpm. The resulting contents were stored and used to prepare the inoculums.

4.5.2. Assessment of growth inhibition in *Saccharomyces cerevisiae* by hydrazone exposure

For the toxicity studies, the cells were incubated with increasing concentrations (100, 200, 500, 900 and 1000 µmol L^{-1}) of the compound diluted in the culture medium. The procedure was carried out in 96-well microplates sealed with plastic film (Parafilm™ M) to minimize evaporation during the experiments, in YPG at 30 ± 1 °C for 24 h, resting without mechanical disturbance. Dimethylsulfoxide (Sigma-Aldrich™) was used as a vehicle and tested in an untreated condition to confirm its non-toxicity. For the positive control, the cells were exposed to hydrogen peroxide (H_2O_2) (10% v/v). Each condition was applied to five wells, and the same condition was repeated in three wells without added cells to detect the possible presence of microbiological contaminants and use the absorbance of these wells as blanks for the colorimetric evaluation of cell growth. The impact on cell growth was measured by turbidity at 570 nm using a

SPECTRAmax 190 Microplate Spectrophotometer (Molecular Devices™) in triplicate experiments.

4.6. Evaluation of cytotoxicity using reduction method

The tests involving SH-SY5Y human neuroblastoma cells were carried out in collaboration with Dr. Annielle Mendes, from the Fundação Oswaldo Cruz (Fiocruz).

4.6.1. Human Cell Culture

SH-SY5Y human neuroblastoma cells, purchased from the SK-N-SH line (ATCC HTB-11), were cultured in Dulbecco's modified Eagle's medium (DMEM) with 10% fetal bovine serum (FBS), 1% penicilin and streptomicin, and 2 mmol L^{-1} glutamine. The cells were then grown in a Series II Water-Jacketed CO_2 Incubator (Thermo Fisher Scientific™) with 5% carbon dioxide (CO_2) atmosphere at 37 ºC.

4.6.2. Cell Viability Assay

Cell viability was performed *via* the 3-(4–dimethylthiazol-2-yl)-2,5-diphenyltetrazolium bromide (MTT) assay. Briefly, SH-SY5Y cells (1×10^4 cells per well) were seeded in 96-well plates and treated with compound (10, 20, 50, 60, 90 and 100 µmol L^{-1}) for 24 h. The cells were then incubated in culture medium with 500 µg mL^{-1} MTT reagent for 3 h at 37 ◦C. For the positive control, the cells were exposed to Triton X-100 (0.01%). Each experimental condition was tested in five wells, while three additional wells containing only the medium, without the addition of cells, were used as controls to identify any microbiological contamination and serve as a blank in the colorimetric analysis of cell growth. The reduced MTT crystals were resolubilized with DMSO and the absorbance was measured at 570 nm using a Varioskan LUX microplate reader (Thermo Scientific™) in triplicate experiments. The value obtained from the untreated control cells was considered as 100% cell viability.

4.7. Studies of Ternary Metal-Protein-Hydrazone Systems

All the studies involving the α-Syn protein, Al^{3+} ions and *N*-acylhydrazone were carried out in collaboration with the research group of Dr. Claudio O. Fernández, at the Max Planck Laboratory for Structural Biology, Chemistry and Molecular Biophysics of Rosario (MPLbioR, UNR-MPINAT). Partner Laboratory of the Max Planck Institute for Multidisciplinary Sciences (MPINAT, MPG). Centro de Estudios Interdisciplinarios, Universidad Nacional de Rosario in Rosario, Argentina.

4.7.1. Protein and reagents

^{15}N isotopically enriched N-terminally acetylated α-Syn was obtained by co-transfecting *E. coli* BL21 cells with the plasmid harboring the protein gene and a second one that encodes for the components of yeast NatB acetylase complex (Miotto *et al*., 2014). Both plasmids carried different antibiotic resistance, namely ampicillin and chloramphenicol to select the doubly transformed *E. coli* colonies. Purification was carried out as previously reported (Hoyer *et al*., 2004), with the exception that, when required, both antibiotics were included in the growth flasks to avoid plasmid purge during growth and expression. The final purity of the protein samples was determined by SDS-PAGE (Sodium Dodecyl Sulfate PolyAcrylamide Gel Electrophoresis). ^{15}N NH_4Cl was purchased from Cambridge Isotope Laboratories. Purified protein samples were dissolved in 20 mmol L^{-1} MES buffer (2-morpholinoethanesulfonic acid) supplemented with 0.10 mol L^{-1} NaCl at pH 6.5. Protein concentrations were determined spectrophotometrically by measuring absorption at 274 nm and using a molar absorptivity value of 5600 L mol^{-1} cm^{-1}.

4.7.2. ^{1}H and ^{1}H x ^{15}N HSQC NMR

NMR spectra were recorded on a Bruker™ 600 MHz HD Avance III spectrometer, equipped with a cryogenically cooled triple resonance ^{1}H ($^{13}C/^{15}N$) TCI probe. Two-dimensional 2D ^{1}H–^{15}N Heteronuclear Single Quantum

Correlation (HSQC) experiments were recorded at 15 °C using standard pulse sequences form the Topspin suite (Bruker™) library. Acquisition and processing of NMR spectra were performed using TOPSPIN 7.0 (Bruker™ Biospin). 2D spectra analysis and visualization were performed with CCPN™ software.

4.7.3. Protein-aluminum(III) Complex Interactions

The characteristic features of aluminum(III) binding to the protein were determined from 2D ^{1}H-^{15}N HSQC experiment using protein samples recorded with increasing concentrations of the metal ion. Specifically, a concentration of 100 μmol L^{-1} of recombinant monomeric α-Syn was exposed to different concentrations of $AlCl_3$: 10, 15 and 20 mmol L^{-1}. The experiments were conducted in 20 mmol L^{-1} MES buffer, pH 6.5, supplemented with 100 mmol L^{-1} NaCl and 3% (v/v) DMSO, at 15 °C. A 2D ^{1}H-^{15}N HSQC NMR spectrum of 100 μmol L^{-1} of recombinant monomeric α-Syn was acquired under the same buffer conditions and temperature, and used as a reference to analyze the changes induced by the presence of the metal ion. The specific interactions of α-Syn residues were determined by comparing their intensities in the presence (I) and absence of $AlCl_3$ (I_0). The I/I_0 ratios of non-overlapping cross-peaks were plotted as a function of the protein sequence to obtain the protein-metal interaction profiles.

4.7.4. Protein-hydrazone Interactions

Protein-hydrazone interactions were performed by 2D ^{1}H-^{15}N HSQC experiments using protein samples recorded with increasing concentrations of the compound (i.e. 10, 15 and 20 mmol L^{-1}). The experiments were conducted in 20 mmol L^{-1} MES buffer, pH 6.5, supplemented with 100 mmol L^{-1} NaCl and 3% (v/v) DMSO, at 15 °C. The specific interactions of α-Syn residues with the compound were assessed by comparing signal intensities in its presence (I) and absence (I_0). The I/I_0 ratios of well-resolved, non-overlapping cross-peaks were mapped along the protein sequence to generate residue-level interaction profiles.

4.7.5. Protein-aluminum(III)-hydrazone Interactions

Protein-aluminum-hydrazone interactions were investigated using 2D ^{1}H-^{15}N HSQC experiments. Spectra were acquired for α-Syn samples in the presence of the $AlCl_3$ and compound (15 mmol L^{-1}). All experiments were conducted in 20 mmol L^{-1} MES buffer (pH 6.5) containing 100 mmol L^{-1} NaCl and 3% (v/v) DMSO, at 15 °C. Residue-specific interactions were assessed by comparing the signal intensities in the presence (I) and absence (I_0) of the compound. The resulting I/I_0 ratios for well-resolved, non-overlapping cross-peaks were plotted along the protein sequence to construct residue-level interaction profiles.

4.7.6. Aggregation assay

Aggregation kinetics were monitored using Thioflavin T (ThT) fluorescence assays. Protein samples (50 μM) were prepared in 20 mM MES buffer (pH 6.5) containing 100 mM NaCl, in the absence and presence of $AlCl_3$, hydrazone or hydrazone+$AlCl_3$, added in a molar ratio of 15:1 in relation to the protein. Aggregations were performed in a POLARstar® Omega plate reader (BMG Labtech) at 37 °C with 5 min intermittent orbital agitation at 300 r.p.m /pause cycle, until plateau was reached. The fluorescence of ThT was excited at 440 nm, and fluorescence emission was monitored at 480 nm. The standard deviations were calculated for repeated measurements. This analysis was performed with a minimum of three replicate experiments. The elongation rates (Ve) and aggregation half-times (Tm) were calculated by fitting (GraphPad™ Prism) the averaged fluorescence intensity (f_t) for each sample as function of time (t) with the aggregation equation: $f_t = (1-e^{-(t).Ve}) /(1+e^{-(t-Tm).Ve})$.

4.7.7. SDS-polyacrylamide gel electrophoresis

SDS-PAGE analysis was performed using monomeric α-Syn obtained at the end point of the aggregation process monitored by ThT fluorescence, as described in the previous section. Once the aggregation curve reached the plateau phase, ThT triplicates were pooled, and the resulting sample was centrifuged at 21.000 for 1

hour at 4 °C. The supernatant was carefully collected, while the pellet was resuspended in an equivalent volume of MES buffer. Subsequently, 20 μl of the supernatant and pellet were combined with 5 μl of Lämmli buffer (250 mM Tris pH 6.8, 10% SDS, 1.25% bromophenol blue, 5% β-mercaptoethanol, 50% glycerol). These samples were then boiled for 10 min at 98 °C and centrifuged for 3 min at maximum speed. Protein separation was carried out using 15% SDS-polyacrylamide resolving gels. Electrophoresis was performed at 90 V in a Mini-PROTEAN Tetra Vertical Electrophoresis Cell (Bio-Rad) with a running buffer containing 1.9 mM glycine, 0.25 mM Tris, and 0.035 mM SDS. After electrophoresis, proteins were visualized by Coomassie staining. Gels were first boiled in Solution A (0.5 g/L Coomassie-R, 10% acetic acid, 25% isopropanol) under agitation for 10 minutes. They were then sequentially transferred to Solution B (0.05 g/L Coomassie-R, 10% acetic acid, 10% isopropanol), Solution C (0.02 g/L Coomassie-R, 10% acetic acid), and finally Solution D (10% acetic acid), with brief boiling at each step. To enhance destaining, gels were incubated overnight in Solution D with gentle agitation, and the samples were then documented.

4.8. *In vivo* Toxicity Studies

The toxicity study of the most promising ligand was carried out in collaboration with Prof. Dr. Jesus Landeira-Fernandez and Prof. Dr. Thomas Eichenberg Krahe, from the Department of Psychology of the Pontifical Catholic University of Rio de Janeiro, Brazil.

The metals analysis was carried out in partnership with Prof. Dr. Tatiana Dillenburg Saint'Pierre from the Department of Chemistry at PUC-Rio, and the High-Performance Liquid Chromatography analysis with Prof. Dr. Carlos German Massone, also from the Department of Chemistry at PUC-Rio.

4.8.1. Animal Care and Handling

Certified pathogen-free male *Wistar* rats were used in all experiments. All animals were handled following the norms established by the Ethics Committee of PUC-Rio for animal handling (protocol in CEUA/036/2013), and are in accordance

with the Ethical Principles on Animal Experimentation adopted by the Brazilian Society of Science in Laboratory Animals / Brazilian College of Animal Experimentation in conformance with the Guide of the North American Society of Neurosciences and Behavior for Care and Use of Laboratory Animals.

The *Wistar* rats (10 weeks old), weighing 200-300 g, were housed in polycarbonate cages measuring 18 × 31 × 38 cm, with water and Nuvital CR-1 rat chow *ad libitum*, in a controlled environment maintained at a temperature of approximately 25 ± 1 °C, humidity of 50% and a 12-hour light/dark cycle.

4.8.2. Preparation of the Sugar Paste (SUG)

All administrations of the compound were carried out orally *via* a sugar paste used as the experimental vehicle. The ingredients of sugar paste (SUG) include sugar, whole milk and lactose. The caloric content of SUG is 328 kcal; the protein content is 0.72%; fats 0.82% and carbohydrates 5.6%. The paste was prepared over medium heat until it thickened using condensed milk (Nestlé S.A., Vevey, Vaud, Switzerland). After reaching the desired cooking point, the SUG was kept at 4 ºC until it was used as a vehicle.

4.8.3. Blood−Brain Barrier Crossing Experiment

The ability of the compound to cross the blood-brain barrier was evaluated after administration of a single 50 mg kg^{-1} dose of the compound via SUG. In this experiment, three 10-week-old male *Wistar* rats were acclimatized to the SUG for 2 days. The administration of the compound was monitored, and the observation period (1 hour) was counted when all the SUG containing the compound had been completely consumed. After this period, the rats were sacrificed by decapitation and the brains removed as described by Aboghazleh et al., (2024). The brains were washed with ice-cold ultra-pure water, weighed and an extraction was carried out by reflux in 10 mL acetonitrile (HPLC grade, Tedia™) for 30 minutes. The liquid portion of each sample was separated by centrifugation at room temperature (5000 rpm for 5 min). Filter supernatants through a 0.45-μm-pore-size filter into 15 ml plastic centrifuge tubes. The extract was analyzed by High Performance Liquid

Chromatography (HPLC) a Nexera series LC-40 chromatograph with an automatic injector, a column oven, a quaternary flow pump (Shimadzu™). A Luna C18(2) HPLC column (250 × 4.6 mm, id 5 μm) was used with a binary polarity elution gradient of 1 mL/min water (A) and acetonitrile HPLC grade (B), in a temperate column (30 °C). The matrix blanks, samples of the matrix extract fortified with the compound and its precursors, and blanks containing only the same solvent used in the matrix extraction were analyzed.

4.8.4. Short timescale chronic toxicity

The animals (50 male *Wistar* rats, 10 weeks old) were randomly divided into 5 groups (n = 10 rats each): untreated control group, animals treated with the vehicle (SUG) and those treated with 5, 25 and 50 mg kg^{-1} of *N*-acylhydrazone.

All groups receiving SUG were acclimatized for 2 days, during which they were fed approximately 1 g of the respective vehicle once a day to minimize neophobia and avoid incidents of incomplete ingestion. From the 3rd to the 7th day of treatment, a daily dose of compound-SUG was administered according to the weight of each rat, respecting the concentrations defined by treatment group. The final dose for all animals was administered between 6 and 8 am. Throughout the treatment, the weight of the animals was measured daily, as well as any relevant observations about their behavior, eating habits and state of excretion. Finally, on the 8th day, the rats were euthanized and the organs removed for analysis.

4.8.4.1. Necropsy

The rats were weighed and euthanized by administering a lethal dose of ketamine (100 mg kg^{-1}) and xylazine (10 mg kg^{-1}) intraperitoneally. At approximately three-minute intervals, sedation was checked by assessing the absence of the toe-pinch reflex in the animal. Organs of interest, namely, brain, liver and kidneys, were collected, washed with ultra-pure water, weighed, identified and individually frozen at –20 °C for 24 hours. Any changes in the gross anatomy of the animals were noted and taken into account when processing the data. The frozen organs were transferred to sterile petri dishes and freeze-dried using a Liobrás™

L101 freeze-dryer coupled to a Dosivac DVR140 vacuum pump. The freeze-dried samples were macerated, and the dry weight was recorded.

4.8.4.2. Metal Content Quantification

To determine the concentration of metals (^{66}Zn, ^{65}Cu, ^{57}Fe and ^{27}Al), 150 mg of the freeze-dried organs (brain, liver and kidney) were subjected to acid digestion with 1 mL of sub-boiled HNO_3 (67% v/v) and 1 mL of hydrochloric acid (HCl, 37% v/v) in plastic test tubes (50 mL PE test tubes), and laid overnight. The samples were then heated in a thermostatic bath to around 100 ºC for 4 h. After digestion, the samples were then allowed to cool to room temperature and diluted with deionized water to 10 mL (resistivity > 18 MΩ cm). Three blank analyses were prepared in the same way. The samples were analyzed on an Inductively Coupled Plasma Optical Emission Spectrometry, in an Optima 7300DV model (Perkin-Elmer™). Calibration was performed by external calibration in the quantitative mode for all assessed elements, obtained by appropriate dilutions of the ICP multi-element standard solution Merck IV. Method accuracy was confirmed by analyzing certified reference materials (CRM), BB184 and BB422 (European Commission, Joint Research Center, mussel tissue).

4.8.5. Statistical analyses

All experimental data were compiled and processed using Microsoft™ Excel. The assumption of data normality was preliminarily assessed using the Shapiro-Wilk test. Based on the normality results, the identification and treatment of *outliers* were performed specifically: the Grubb test was applied to parametric data, while the ROUT test was used for non-parametric data. The results were presented in a visual format consistent with their statistical distribution. Bar graphs were employed for parametric data, where values are expressed as the mean ± standard error of the mean. Conversely, non-parametric data were presented using Box Plots. A p-value < 0.05 was considered statistically significant. All statistical analyses were carried out using GraphPad™ Prism.

5. Results and Discussion: Design, Pharmacological Parameters, Synthesis and Characterization

5.1. *In silico* pharmacological descriptors

The rules formulated by Christopher A. Lipinski *et al*., (1997), also known as the "Lipinski's Rule of Five", are a set of guidelines used in pharmaceutical research and drug discovery to assess the suitability of a molecule as a possible oral drug. In this sense, after rationalizing the optimized molecules for aluminum chelation, we performed a computational screening using updated pharmacokinetic parameters described in recent literature (Gu *et al*., 2024; Kralj; Jukič; Bren, 2023; Zhu *et al*., 2023). Therefore, in this initial investigation, we considered, in addition to the classic Lipinski's rules, complementary criteria such as those proposed by Egan; Merz; Baldwin, (2000); Ghose; Viswanadhan; Wendoloski, (1999); and Veber *et al*., (2002a), to assess whether the proposed structures present, at least from a theoretical point of view, promising pharmacological viability.

Specifically, five phsicochemical properties evaluated were: solubility (cLogS), octanol-water partition coefficient (cLogP), hydrogen bond donors (HBD) and acceptors (HBA), and polar surface area (PSA) (Gleeson, 2008; Guimarães *et al*., 2012; Lipinski *et al*., 1997; Meanwell, 2011; Palm *et al*., 1997; Yang *et al*., 2012).

The first two parameters are associated with the solubility in aqueous solution and the hydrophilic-lipophilic balance of the prospective drug, respectively. Regarding the HBD and HBA parameters, they are used to determine the number of hydrogen bond donor and acceptor atoms that are ideal for a good drug. According to these guidelines, compounds with an excessive number of atoms capable of having such interactions may face problems related to permeability and oral bioavailability (Benet *et al*., 2016; Pollastri, 2010; Veber *et al*., 2002b). Finally, with the PSA, it is possible to make inferences about the transport properties of drugs, especially gastrointestinal absorption and penetration of the blood-brain barrier. In addition to these, *Druglikeness* and *DrugScore* are two other metrics that can be used in drug research and development to assess the viability of a molecule as a drug candidate.

Drug-likeness is a qualitative concept that describes how closely a compound's physicochemical and structural properties align with those of known drugs (Bickerton *et al*., 2012; Li *et al*., 2024). This includes important parameters such as molecular weight, lipophilicity, hydrogen bond donors and acceptors, solubility, and the absence of toxic or reactive substructures. Molecules that meet these criteria are considered more likely to have favorable pharmacokinetics and bioavailability profiles, making them promising drug candidates. In addition, the *Drugscore* is a composite metric that integrates all the calculated parameters according to predefined weights, estimating the likelihood of a compound becoming a drug based on data from approved pharmaceutical products (Dittrich *et al*., 2019; Velec; Gohlke; Klebe, 2005).

An ideal drug candidate should have an appropriate balance between hydrophilicity and lipophilicity. A high cLogP value can increase membrane penetration, but if the compound is too lipophilic, it can lead to poor solubility and distribution problems. On the other hand, if a molecule is too hydrophilic (low cLogP), it may dissolve well in water but not penetrate cell membranes effectively. For drugs targeting the central nervous system (CNS), a cLogP value of 2-3 is preferable (Hansch; Björkroth; Leo, 1987). The reference values for the descriptors relating to BBB crossing and cell permeability are summarized in Table 1.

Table 1. Reference values for the pharmacological descriptors.

	Cell permeability	**BBB-crossing**
MW	≤ 500	≤ 400
cLogP	≤ 5	0 - 3
cLogS	≥ -4	≥ -4
HBA	≤ 10	≤ 7
HBD	≤ 5	≤ 3
PSA	≤ 140	≤ 90
Druglikeness	> 0	> 0

Table 2 shows the theoretical value of each pharmacological descriptor obtained for the 15 *N*-acylhydrazones proposed. This preliminary pharmacological analysis showed that all the proposed compounds exhibit adequate MW for orally administered drugs (MW in the range of 200-450 g mol^{-1}), suggesting that these

compounds may have good cell membrane absorption properties (Leeson; Young, 2015).

Table 2. Pharmacological parameters calculated for the 15 *N*-acylhydrazones studied using OSIRIS Property Explorer: DataWarrior™ software. MW: molar weight, cLogP: cal culated partition coefficient, cLog S: calculated aqueous solubility, HBA and HBD parameters (H-bond acceptors and donors) PSA: polar surface area. Pharmacological descriptors that exceed the reference limits are highlighted in red.

Compound	MW	cLogP	cLogS	HBA	HBD	PSA	Druglikeness
1a	241	1.86	-2.63	2	5	74.58	5.8
2a	271	1.79	-2.65	2	6	83.81	4.64
3a	255	2.2	-2.97	2	5	74.58	4.61
4a	286	0.96	-3.09	2	7	**120**	**-2.68**
5a	275	2.46	-3.34	2	6	74.58	4.67
1b	330	2.65	-3.48	2	7	89.38	11.01
2b	360	2.58	-3.50	2	**8**	**98.6**	9.86
3b	344	2.99	-3.82	2	7	89.38	9.78
4b	375	1.72	-3.94	2	**9**	**135**	2.58
5b	364	3.05	**-4.21**	2	**8**	89.38	9.83
1c	230	2.04	-3.11	2	5	74.83	4.44
2c	260	1.97	-3.13	2	6	84.06	3.34
3c	244	3.09	-3.45	2	5	74.83	3.23
4c	275	1.12	-3.57	2	7	**121**	**-4.02**
5c	264	2.65	-3.84	2	6	74.83	3.28

With respect to the molecules in this study, the theoretical LogP values ranged from 0.96 to 3.09, which suggests that these compounds are suitable for penetrating biomembranes and, specifically, the BBB. From a structural point of view, the nitro-substituted compounds (i.e. **4a**, **4b** and **4c**) showed lower lipophilicity, while the chloro-substituted compounds were slightly more lipophilic. On the other hand, the methyl- and methoxyl-substituted compounds showed cLogP values closest to the ideal for CNS-targeted drugs.

Most of the compounds showed moderate solubility, with the exception of compound **5b**, which showed sub-optimal theoretical solubility (cLogS = -4.71). Compounds **2b**, **3b** and **4b** had much higher amounts of donor atoms (HBD) than is appropriate for drugs and the **4a**, **3b**, **4b** and **4c** compounds showed PSA values

well above the ideal, which may make it difficult for them to be absorbed by cell membranes. Finally, as described above, *Druglikeness* and *DrugScore* are important metrics for assessing the appropriateness of substances and may be relevant for determining their suitability for use in pharmaceutical, chemical or industrial applications. The values obtained for these parameters are within the range considered ideal for medicines only for the **1a**, **2a**, **3a**, **5a**, **1b**, **3b**, **1c**, **2c**, **3c** and **5c** compounds.

After this initial *in silico* pharmacological analysis, we concluded that only 10 compounds (Figure 18) showed relevant features for the development of a new drug, which is why only these compounds were considered for the next stages of this study.

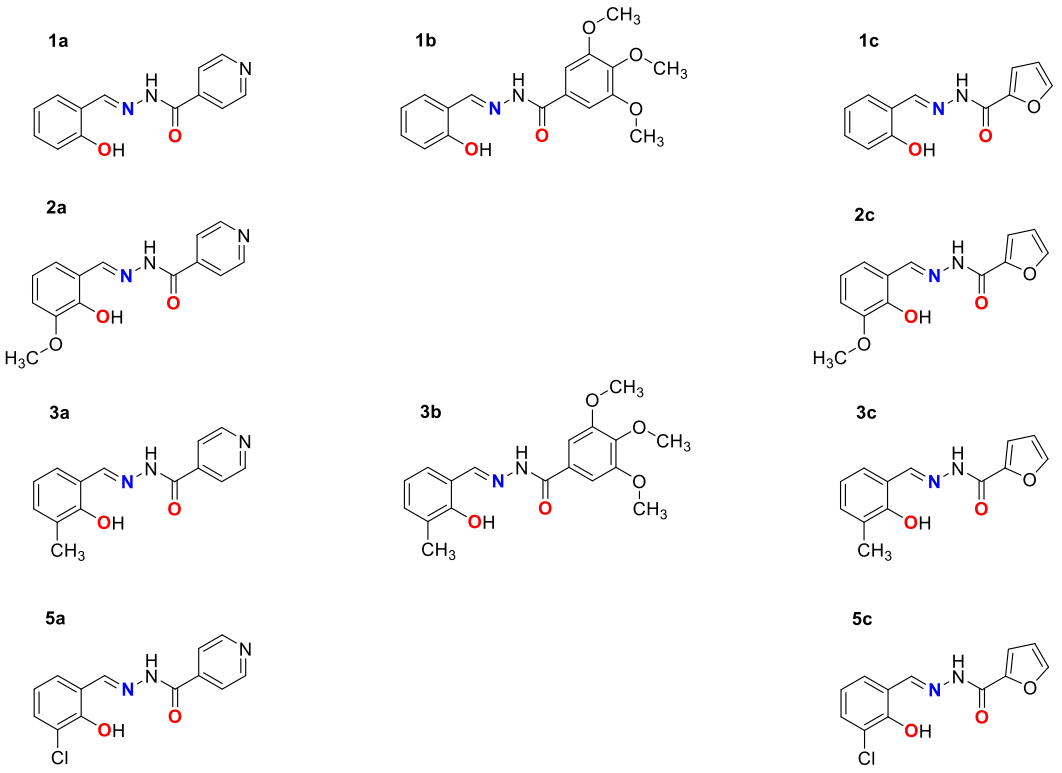

Figure 18. Structures of the 10 proposed *N*-acylhydrazones. The potential coordination atoms are highlighted in color.

5.2. Syntheses and chemical characterization

5.2.1. Compounds 1a, 2a, 3a and 5a: Isonicotinic acid hydrazide-derived *N*-acylhydrazones

The series of hydrazones derived from the hydrazide of the isonicotinic acid differ from each other in having an aromatic portion derived from the salicylaldehyde containing the *meta*-substitution with respect to the hydrazonic bond. For this reason, the synthesis and characterization of these compounds are discussed together comparatively here.

The isonicotinic acid hydrazide-derived *N*-acylhydrazones were obtained in good yields (between 41 and 63%) as yellow solids, except for **3a** which was obtained as an orange precipitate. Single crystals suitable for XRD characterization were obtained for all compounds of this series. The crystal of **3a** was isolated after recrystallization in a mixture of H_2O/acetone (50% v/v), while for **5a** yellow crystals were obtained from the synthesis' mother liquor. On the other hand, compounds **1a** and **2a** already have their XRD structures described in the literature (Charkoudian *et al*., 2007; Xu, 2013; Xu *et al*., 2007; Yang, 2007; Yin *et al*., 2005; Yu *et al*., 2005) and, for this reason, their structures were not determined again in this work. Also, the solid state and solution characterizations of these latter compounds have been extensively detailed in (Shan *et al*., 2015; Xia *et al*., 2015b) and our research group (De Falco, 2017; González-Baró *et al*., 2012), respectively. The experimental data of **1a** and **2a** obtained in this study can be found in Appendix Figures A1-A8 and Table A1, but their characterizations will not be discussed again here.

The ligands **3a** and **5a** were both obtained in the monoclinic crystalline system with space group $P2_1/n$' and C_2/c, respectively, both with two molecules in the asymmetric unit. The ORTEP representations of the crystal structures of **3a** and **5a** are shown in Figure 19. Crystal, data collection and refinement parameters are summarized in Table 3.

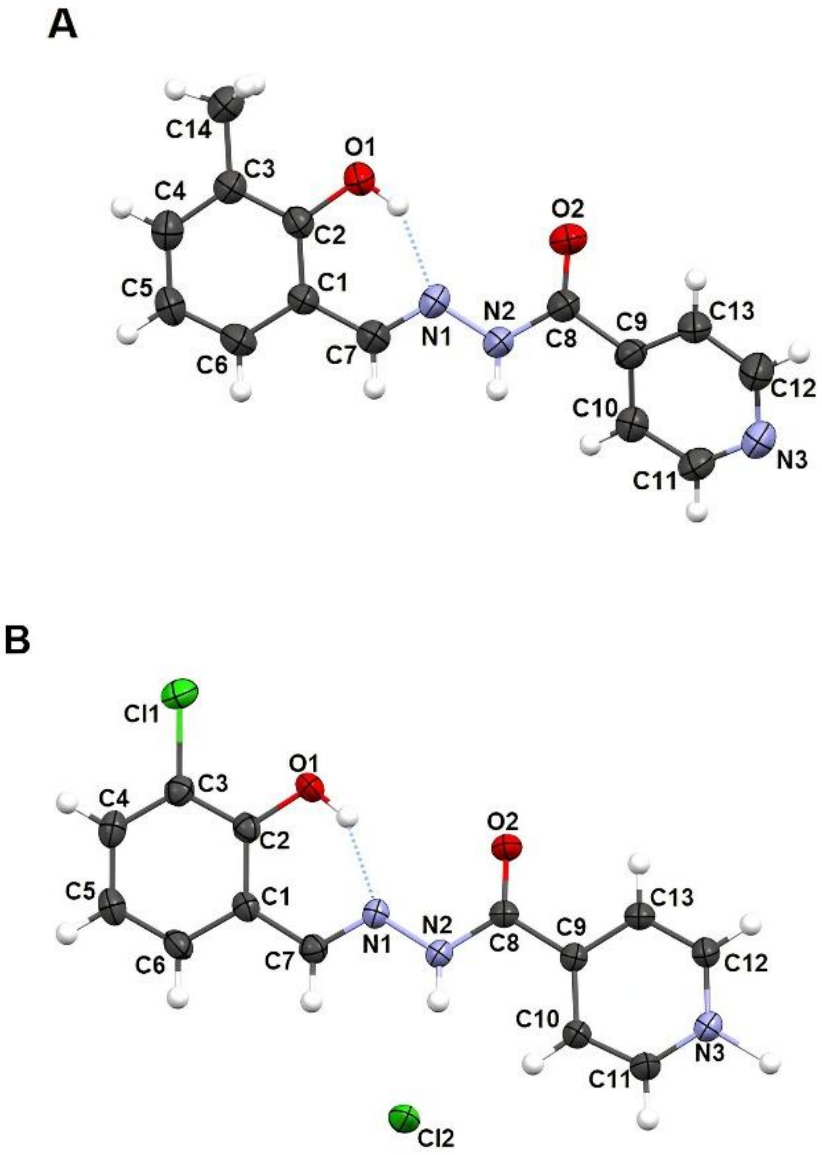

Figure 19. ORTEP representations of the crystal structures of compounds (**A**) **3a** and (**B**) **5a**. The ellipsoids were drawn with 50% probability level.

Table 3. Crystal, data collection and refinement parameters for compounds **3a** and **5a**.

Compound	**3a**	**5a**
Crystal size (mm)	0.32 x 0.18 x 0.06	0.10 x 0.25 x 0.72
Empirical formula	$C_{14}H_{13}N_3O_2$	$2(C_{13}H_{10.5}ClN_3O_2)Cl$
Formula weight (g mol^{-1})	255.27	587.84
F(000)	1072	1208
Temperature (K)	293	200
Absorption coefficient μ (mm^{-1})	0.094	3.627
Calculated density ($g.cm^{-3}$)	1.364	1.518
Crystal System	Monoclinic	Monoclinic
Space group	$P2_1/n$, (No. 14)	C_2/c, (No. 15)
a, b, c (Å)	10.8021(18)	9.9986(6)
	16.228(3)	12.8829(7)
	14.572(3)	20.0734(11)
α, β, γ (°)	90	90
	103.194(6)	95.863(2)
	90	90
Cell volume ($Å^3$)	2487.0(8)	2572.2(3)
Z, Z'	8, 2	4, 0.5
Reflections collected, R_{int}	36180, 0.246	18664, 0.078
Independent reflections	3490	2472
Index Ranges	$-11 < h < 12$	$-12 < h < 12$
	$-18 < k < 18$	$-15 < k < 15$
	$-16 < l < 16$	$-24 < l < 24$
Data/parameters	1883/350	2138/185
Final residual factor [I>2σ(I)]	R_1: 0.0738	R_1: 0.0576
	wR_2: 0.1263	wR_2: 0.1596
Goodness-of-fit on F^2	0.98	1.06
T_{min}, T_{max}	1.9, 23.3	4.4, 72.1
Largest diff. peak and hole ($e.Å^{-3}$)	-0.17, 0.20	-0.41, 0.41

a, *b*, *c*, *α*, *β*, *γ*: unit cell parameters; *Z*: formula unit per unit cell; *Z'*: number of formula units in the crystallographic unit cell divided by the number of independent general positions; F(000): structure factor in the zeroth-order case; F: structure factor; F^2: squared structure factor; T: transmission factor.

Compound **3a** was obtained as an isomer (*E*) with respect to the C7=N1 double bond, with a C1–C7–N1–N2 torsion angle equal to 174.5(2)º. Table 4 contains selected bond distances, bond angles and torsion angles, complete data in Table A2-A6 in the Appendix. The molecule is not completely planar: there is a considerable twisting of the pyridine ring in relation to the benzene ring (the dihedral angle between the two rings is 24.51°). The N1–N2–C8–O2 torsion angle is -6.4(4)º, indicating that the atom O2 is in an *anti*-conformation with respect to the N2 in the compound (Cukierman *et al*., 2020a; Martins *et al*., 2023). Finally, the crystal structure of **3a** proved that the compound presents amide tautomerism as evidenced by the bond distances between C8–O2 and C8–N2 [1.218(3) Å and 1.357(3) Å, respectively].

In the case of compound **5a**, the structure also adopts an *E* isomerism around the C7=N1 bond, which reflected in the C1–C7–N1–N2 torsion angle [178.53(19)°]. The dihedral angle of 3.47° between the mid-planes of the six-member rings confirms that the structure is, once again, not completely planar. The N1–N2–C8–O2 torsion angle of -1.1(4)° also indicates that the molecule assumes a *antiperiplanar* configuration with respect to the amide bond. In addition, the C8–O2 [1.218(3) Å] and C8–N2 [1.359(3) Å] bond distances are consistent with existing structures reported as amide tautomers (Meng *et al*., 2018; Sliter; Morgan; Greenberg, 2011). The complete data for compound **5a**, bond distances, bond angles and torsion angles are shown in Table A7-A11 in the Appendix.

Table 4. Select bond distances and angles for compounds **3a** and **5a**.

	3a	**5a**
Bond distance (Å)		
C1–C7	1.442(4)	1.457(4)
C7–N1	1.283(3)	1.284(3)
N1–N2	1.376(3)	1.375(3)
N2–C8	1.357(3)	1.359(3)
C8–O2	1.218(3)	1.218(3)
C8–C9	1.491(4)	1.502(4)
Bond angle (°)		
C1–C7–N1	120.9(3)	118.8(2)
C7–N1–N2	117.6(2)	118.5(2)
N1–N2–C8	117.8(2)	115.8(2)
N2–C8–O2	123.5(3)	122.7(2)
N2–C8–C9	114.8(3)	116.4(2)
C9–C8–O2	121.6(3)	120.8(2)
Torsion angle (°)		
C1–C7–N1–N2	174.5(2)	178.53(19)
C7–N1–N2–C8	172.7(3)	177.0(2)
N1–N2–C8–C9	172.8(2)	-179.5(2)
N1–N2–C8–O2	-6.4(4)	-1.1(4)
C10–C9–C8–O2	136.4(3)	4.9(4)

Regarding **3a**, an intramolecular hydrogen bond was observed, i.e. O1–H1···N1, with a distance of 2.602(3) Å. Intermolecular interactions, on the other hand, form the asymmetric unit of the compound: each molecule can form two intermolecular hydrogen bonds, involving the hydrogen bound to N2 and the pyridinic nitrogen N3 of a neighboring molecule as a hydrogen acceptor (symmetry code 3/2-x,1/2+y,1/2-z), resulting in a zigzag chain parallel to the *a* crystallographic axis (illustrated in Figure 20). Finally, no π-π stacking interactions were observed. The hydrogen bond distances are shown in Table 5.

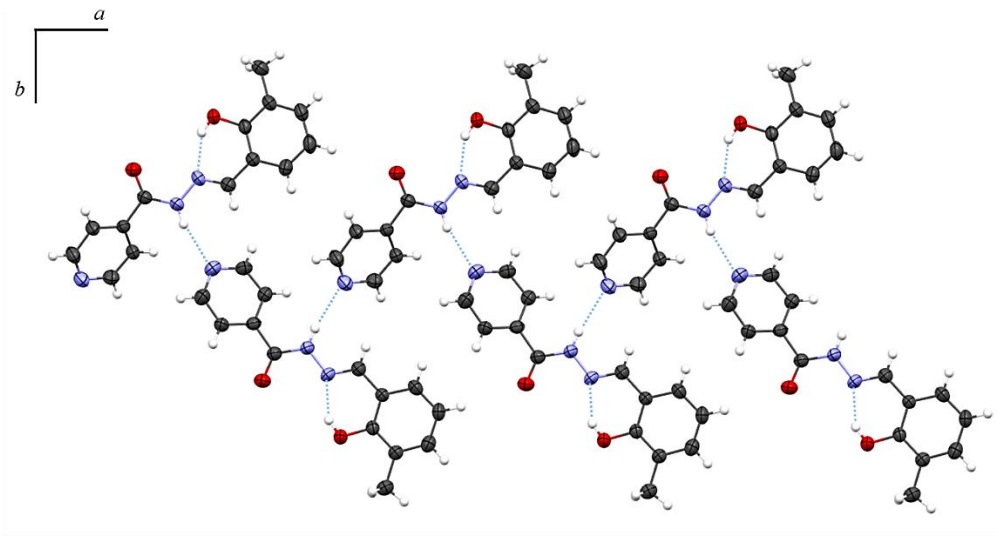

Figure 20. Hydrogen bond interactions in the crystal networks of compound **3a** ao longo do eixo cristalográfico *a*.

Table 5. Hydrogen bond geometric parameters for compound **3a**.

D-H···A	D-H (Å)	H···A (Å)	D···A (Å)	D-H···A (°)
O1A–H1A···N1A	0.81(2)	1.89(3)	2.602(3)	145(2)
N2B–H2B···N3A^{i}	0.8600	2.2300	3.075(3)	167.00

Symmetry code: *i* (1/2-x,-1/2+y,1/2-z).

The asymmetric unit of **5a** shows a disordered HCl (50%). The two positions with partial occupancy are Cl2 and H3A. The organic cation has unitary occupancy. Although theoretically this could indicate the presence of 50% neutral X molecules and 50% cationic $(X+H)^{+}$ species, what was observed experimentally was the presence of an $(X+X+H)^{+}$ dimer (Figure 21) which shares a proton through a symmetrical hydrogen bridge (pyridinium-pyridine dimer). The two partially cationic units are related by a binary rotation axis (2-fold).

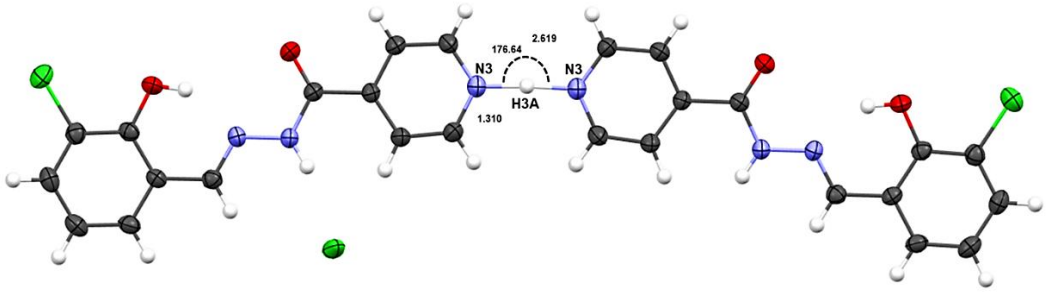

Figure 21. Dimers (X+X+H)+ (thermal ellipsoids at 50% probability).

The hydrogen bridge is almost linear (the N···H···N), with an angle of 176.64°, and the distance between the hydrogen and each nitrogen is much smaller than the sum of the van der Waals radii: the distance between the refined position for H3A and each nitrogen is 1.3 Å and the N3···N3 distance is 2.619 Å. These parameters are similar to those observed in other symmetrical bridges and is slightly shorter than that of the pyridinium-pyridine dimer described by Brammer & Zhao, (1995). The overlap of the van der Waals radii can be seen in Appendix Figure A9.

With the structural refinement without the inclusion of H3A, it is possible to observe the position and shape of the remaining experimental electronic density in the region using a Fourier difference map (F_o-F_{Calc}). This map makes it possible to compare the electronic density of the atomic model used and the experimental electronic density. The map was observed in the plane of the dimer, and the residual electronic density was drawn as a contour map (Figure 22). The position of H3A can be visualized with a full green line; it can be seen that the electronic density corresponding to H3A is located approximately in the middle of the distance between the two nitrogens. The distribution of the electronic density takes place over an extended region, which indicates that there may be a dynamic disorder of the proton's position in two distinct regions. In this case, the practical effect would be that a proton could occupy two different positions, with an energy barrier low enough for the two positions to be equally occupied. The energy profile of this hydrogen bond can be described as “single-well” and the hydrogen bond can be classified as a *charge-assisted hydrogen bond* [(+)CAHB].

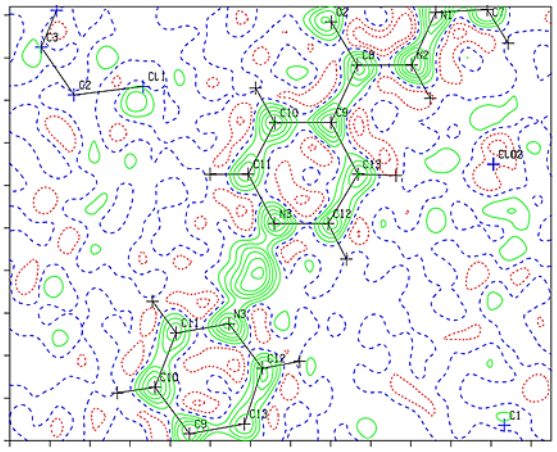

Figure 22. Fourier difference map (without H3A refinement).

In addition to the O1–H1···N1 and N3–H3A···N3 interactions, the crystalline packing of **5a** (Figure 23) is formed by other unconventional intermolecular hydrogen bond which stabilize the crystal structure, such as O2···H5, in which H5 is bound to the phenolic carbon C5, with a distance of 2,480 Å; O1···H6, in which H6 is bound to C6, with a distance of 2.580 Å and between H13···Cl2, in which H13 is bound to the pyridinic carbon C13, with a distance of 2,570 Å (Table 6). It is also possible to observe the existence of a weak interaction between the aromatic rings of structure **5a**, with a centroid-centroid distance of 4,006 Å.

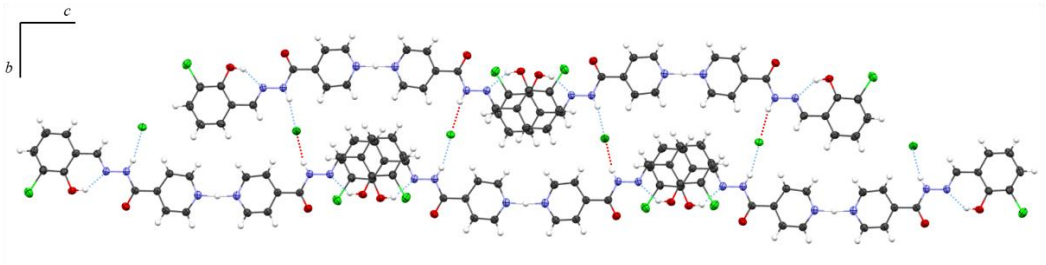

Figure 23. Hydrogen bond interactions in the crystal lattices of compound **5a** along the crystallographic axis *c*.

Table 6. Hydrogen bond geometric parameters for compound **5a**.

D-H···A	D-H (Å)	H···A (Å)	D···A (Å)	D-H···A (°)
O1–H1···N1	0.87(4)	1.82(3)	2.581(3)	145.0(12)
N2–H1BB···C12	0.88(4)	2.32(4)	3.180(2)	165(3)
N3–H3A···N3^{i}	1.310(2)	1.310(2)	2.619(3)	177(6)
C5–H5···O2^{ii}	0.9500	2.4800	3.208(3)	134.00
C6–H6···O1^{ii}	0.9500	2.5800	3.215(3)	124.00
C13–H13···Cl2	0.9500	2.5700	3.477(3)	161.00

Symmetry code: *i* (1-x,y,3/2-z); *ii* (x,-y,-1/2+z).

Bulk analyses showed that compounds **3a** and **5a** had melting points of 240.0 ± 1 °C and 266.0 ± 1 °C, respectively, indicating considerable purity in the solids obtained. The peaks at *m/z* 255.14 (**3a**) (calcd. 255.10) and 275.14 (**5a**) (calcd. 275.05) reinforce the purity of the compounds (Chromatrogram in Appendix Figures A10 and A11). The thermogravimetric curve of **3a** (Appendix Figure A12) shows two stages of decomposition. In the first stage, a loss of 9.6% between 150

and 225 ºC was observed, attributed to the presence of hydration water molecules in the compound's structure. The second stage was attributed to the decomposition of the organic ligand. The proposed chemical formula for **3a** is $C_{14}H_{13}O_2N_3 \cdot 1.5\ H_2O$ (Calcd.: 9.7% for MW = 277.10 g mol^{-1}). For compound **5a**, the TG curve (Appendix Figure A13) shows the loss of 6.25% between 170 and 250 ºC, consistent with the presence of ½ molecule of HCl (Calcd.: 6.2%), confirming that the solid obtained in the synthesis is also in the form of a hydrochloride, in agreement with the crystal structure described above ($C_{13}H_{10}ClO_2N_3 \cdot$ ½ HCl, MW = 293.92 g mol^{-1}).

Regarding their vibrational characterization, infrared spectra of compounds **3a** and **5a** showed stretching bands attributed to N–H at 3189 and 3128 cm^{-1}, respectively. Additionally, the vibrational mode of ν(C–OH) was assigned to the mid-intensity infrared band at 1276 cm^{-1} for compound **3a** and at 1283 cm^{-1} for compound **5a**, in line with what has been reported in the literature for hydrazones derived from salicylaldehyde (Benković *et al*., 2018; Demir *et al*., 2023; Galić *et al*., 2001; Sumrra *et al*., 2014). A band observed at 1637 cm^{-1} in **3a** and at 1626 cm^{-1} in compound **5a** was attributed to the characteristic C=N stretching mode, which appears due to the formation of the hydrazone, as previously observed for other compounds of this class (Aslanhan *et al*., 2023; Galić *et al*., 2012; Wang *et al*., 2014). In addition, some symmetric and antisymmetric stretchings of the C–H bonds were observed between 3005-2900 cm^{-1} for the methyl-containing compound (**3a**) and between 3032-2817 cm^{-1} for the choro compound (**5a**). More bands in the 1495 cm^{-1} region were identified in the spectrum of **3a** in comparison to that of its choro analogue, due to the presence of the CH_3 group in the first. The characteristic stretching vibration of the C–Cl halogen bond (651 cm^{-1}) were observed exclusively in **5a**.

The skeletal C=C stretching bands were observed around 1550 cm^{-1} in the spectra of the synthesized compounds which represents the presence of aromatic groups. Other vibrational modes characteristic of *N*-acylhydrazones, such as the ν(N–H), ν(C=O) and ν(N–N) stretches, as well as the characteristic band of in-plane deformation of the pyridine ring (δpy) can also be observed. The most explicit IR bands recorded for the synthesized compounds with their probable assignment are given in Table 7 and the spectra can be observed in Appendix Figures A14 and A15.

Table 7. Selected infrared frequencies of compounds **3a** and **5a**, along with their assignments. Samples were prepared as KBr pellets.

Assignment	3a	5a
	IR (cm^{-1})	
$\nu(O–H)_{water}$	3430	3439
$\nu(N–H)_{hydrazone}$	3189	3128
$\nu(C–H)_{azomethine}$	2917	2925
$\nu(C=O)_{carbonyl}$	1684	1680
$\nu(C=N)_{azomethine}$	1637	1626
$\nu(C=N)_{pyridine}$	1604	1604
$\nu(C–C)_{aromatic}$	1540	1554
$\nu(C–O)_{hydroxyl}$	1276	1283
ν(N–N)	1150	1145
δpy*	742	739

*characteristic band of the in-plane deformation of the pyridine ring (δpy).

N-acylhydrazones are usually prone to undergo speciation in DMSO-d_6 solution (Munir *et al*., 2021a). Our experience indicates that *N*-acylhydrazones derived from salicylaldehyde do not show interconversion between *E/Z* isomers in solution due to the stabilization of the *E* isomer through an intramolecular hydrogen bond (N–H···O), also observed by crystallographic analysis (Martins *et al*., 2023). On the other hand, the presence of two sets of signals can be seen in the ^{1}H NMR spectrum of **3a** (Figure 24A). The literature associates this behavior with the presence of *syn* and *anti* conformers for each compound (Fernández-Palacios *et al*., 2023; Franco *et al*., 2025. The literature highlights the greater stability of the *anti* conformation for these structures. Consistent with these findings, the relative integration of the signals, it was possible to conclude that approximately 95% of the *anti*- and only 5% of the *syn-periplanar* conformer for **3a**, due to the rotational restriction around the simple bond of the conjugated amide (N–C=O). Conformations around the amide bond (*anti/syn*) were also observed in the spectrum of **5a** (Figure 24B). Accordingly, the major set of signals was attributed to the *anti* conformer, which accounts for approximately 96% of the population in solution.

The signal at 12.79 ppm in the spectrum of **3a** was attributed to the NH

proton, which is slightly deshielded in the chloro-derivative (compound **5a**), resonating at 12.84 ppm. In addition, due to the presence of the EWD –Cl substituent in the aldehyde-derived portion of **5a**, strong deshielding of the hydroxyl group was observed (assigned at 12.17 ppm) as a result of the removal of electronic density on the carbon adjacent to –OH. On the other hand, in **3a**, the presence of the methyl substituent moderately shields this proton (11.73 ppm). The azomethine hydrogen H7 appears as a singlet at 8.70 ppm for both **3a** and **5a**. In addition, the equivalent hydrogens of the pyridine ring were identified as a pair of duplets at 8.13 and 8.94 ppm in compound **3a**, while these same protons appear at 8.01 and 8.88 ppm for compound **5a**, in accordance with studies previously carried out by Cukierman *et al*. (2018, 2019, 2020a) and González-Baró *et al*. (2012). The other aromatic ring protons were observed in a range of 6.87–7.53 ppm for these compounds. Full assignments, with the chemical shifts and coupling constants, can be found in Appendix Table A12.

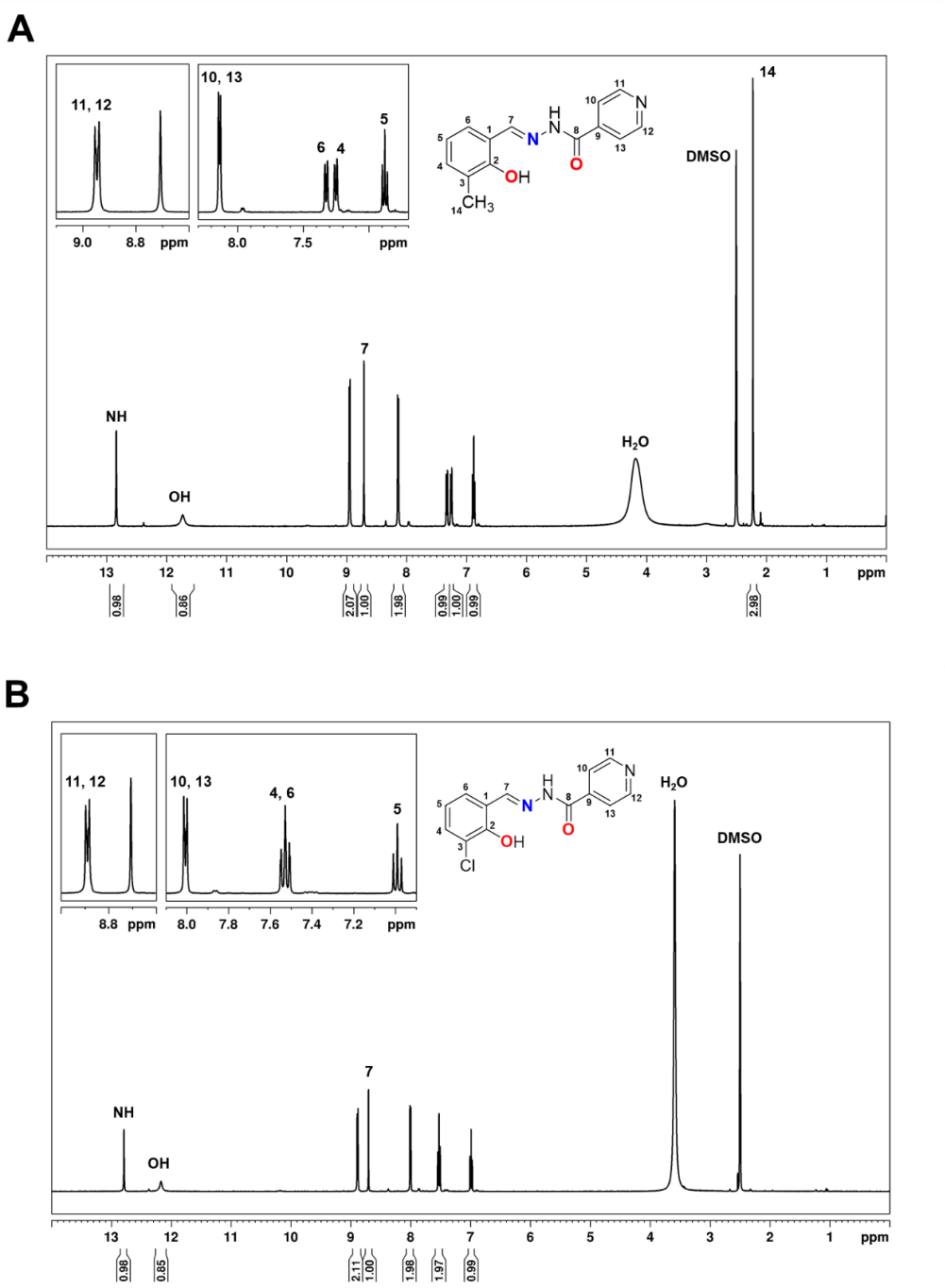

Figure 24. ^{1}H NMR (400 MHz) spectrum of (**A**) **3a** and (**B**) **5a** in DMSO-d_6 at 25 ºC.

5.2.2. Compounds 1b and 3b: 3,4,5-trimethoxybenzoic acid hydrazide-derived *N*-acylhydrazones

Compound **1b** was isolated as a white crystalline solid and **3b** as a beige solid in good yields (56% and 78%, respectively) under the synthesis conditions employed. The crystal structure of **1b** was reported previously by Charkoudian *et al.* (2007), so we report here only the XRD results obtained for **3b**.

Single crystals of **3b** were isolated from the mother-liquor as elongated needle-like crystals in the monoclinic system, space group C_2/c, and a water molecule attached by a hydrogen bond to the respective N2A. Crystal data, summary of experimental details, and refinement parameters of the measurement are shown in Table 8. The ORTEP representation of compound **3b** is shown in Figure 25.

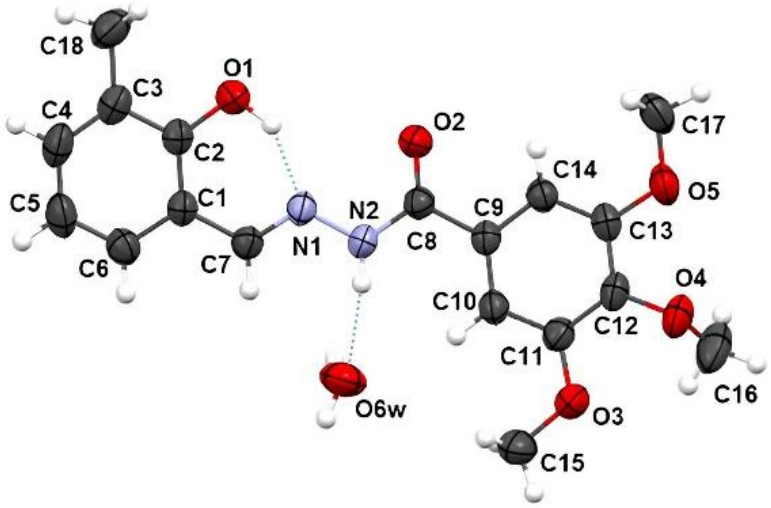

Figure 25. ORTEP representation of the crystal structure of **3b**. The ellipsoids were drawn with 30% probability level.

Table 8. Crystal, data collection and refinement parameters of the compound **3b**.

Compound	**3b**
Crystal size (mm)	0.99 x 0.14 x 0.14
Empirical formula	$C_{18}H_{22}N_2O_6$
Formula weight (g mol^{-1})	362.37
F(000)	1536
Temperature (K)	293
Absorption coefficient μ (mm^{-1})	0.101
Calculated density ($g.cm^{-3}$)	1.337
Crystal System	Monoclinic
Space group	C_2/c (n° 15)
a, b, c (Å)	32.1401(15) 8.4828(4) 14.3708(6)
α, β, γ (°)	90.000 113.2650(10) 90.000
Cell volume ($Å^3$)	3599.4(3)
Z, Z'	8, 1
Reflections collected, R_{int}	48639, 0.0363
Independent reflections	3651
Index Ranges	-40 < *h* <40 -10< *k* <10 -17 < *l* <17
Data/parameters	3651/250
Final residual factor [I>2σ(I)]	R_1: 0.0486 wR_2: 0.1450
Goodness-of-fit on F^2	1.11
T_{min}, T_{max}	0.906, 0.986
Largest diff. peak and hole ($e.Å^{-3}$)	0.17, -0.19

a, *b*, *c*, *α*, *β*, *γ*: unit cell parameters; *Z*: formula unit per unit cell; *Z'*: number of formula units in the crystallographic unit cell divided by the number of independent general positions; F(000): structure factor in the zeroth-order case; F: structure factor; F^2: squared structure factor; T: transmission factor.

The C7=N1 bond distance of 1.273(2) Å for the compound is in line with the value for a double bond as in similar Schiff base compounds (Arunagiri *et al*., 2024; Datta *et al*., 2014). The torsion angle around the C7=N1 bond (C1–C7–N1–N2 equal to 177.05º) suggests (*E*) isomerism around this bond. The dihedral angle between the phenyl rings (10.70º) shows that the structure is not completely planar. Furthermore, based on the distance of the C8–O2 bond (1.273(2) Å), the tautomeric form of the compound is the amide form in which the tautomeric proton (H2) is located on the nitrogen atom (N2) (Purandara; Foro; Gowda, 2017). The N1–N2–C8–O2 torsion angle of -3.01° indicates an *anti*- configuration around the N–C amide bond. Selected bond distances and angles for compound **3b** are shown in Table 9. All data can be found in Appendix Table A13-A17.

Table 9. Select bond distances and angles for compound **3b**.

Bond distance (Å)	
C1–C7	1.453(2)
C7–N1	1.273(2)
N1–N2	1.3728(19)
N2–C8	1.353(2)
C8–O2	1.221(2)
C8–C9	1.496(2)
Bond angle (°)	
C1–C7–N1	119.92(16)
C7–N1–N2	119.26(14)
N1–N2–C8	117.18(14)
N2–C8–O2	121.16(15)
N2–C8–C9	117.58(15)
C9–C8–O2	121.24(15)
Torsion angle (°)	
C1–C7–N1–N2	177.05
C7–N1–N2–C8	-179.40
N1–N2–C8–C9	175.37
N1–N2–C8–O2	-3.01
C10–C9–C8–O2	-178.30

Important hydrogen interactions contribute to the crystalline packing of **3b**. Figure 26A highlights hydrogen bond interactions in the crystal network of compound **3b** along the crystallographic plane *b*. All the interactions are summarized in Table 10. Structural analysis reveals two intramolecular interactions the first occurs between the hydroxyl and the nitrogen atom (O1–H1···N1) with an H1–N1 bond distance of 1.772 Å and bond angle of 144°; The second interaction occurs between C14–H14···O2 and has a distance of 2.400 Å. There is also a third interaction, categorized as intermolecular, between N2–H2a···O6w (the symmetry operator being 1-x,1-y,1-z), with a bond distance of N2···O6w = 2.910 Å and a bond angle of 148°. Finally, the stacked planes were organized by C–H···O non-classic hydrogen bonds comprising the methoxyl groups. In the columns, there are anti-parallel dimers that are sandwiched between two non-parallel molecules (Figure 26B).

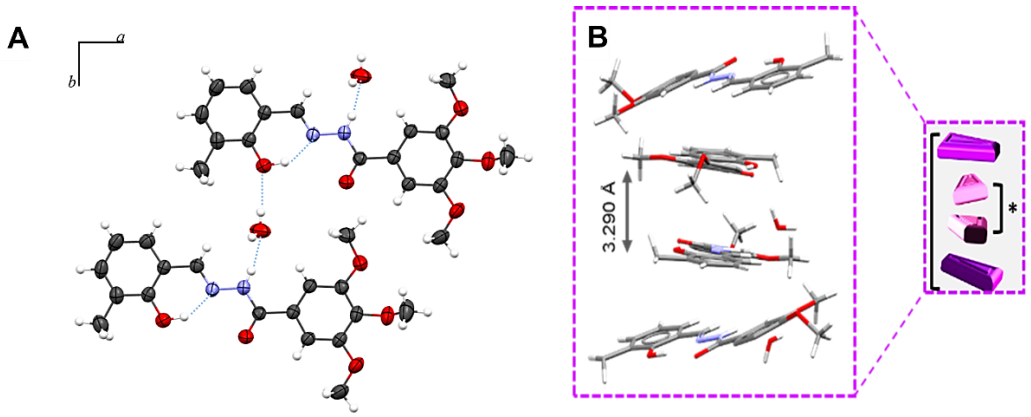

Figure 26. (**A**) Hydrogen bond interactions in the crystal lattices of compound **3b** along the crystallographic plane *b* and (**B**) Stacked motifs of compound **3b**.

Table 10. Hydrogen bond geometric parameters for compound **3b**.

D–H···A	D–H (Å)	H···A (Å)	D···A (Å)	D–H···A (°)
O1–H1···N1	0.93(2)	1.772(18)	2.581(2)	144(2)
O6w–Hw1···O2	0.84(3)	2.00(3)	2.816(2)	166(3)
N2–H2a···O6w^{i}	0.840(17)	2.164(18)	2.910(2)	148(2)
C14–H14···O2	0.9300	2.400	2.734(2)	101.00

Symmetry code: *i* (1-x,1-y,1-z).

Solid-state characterization of the bulk showed that compounds **1b** and **3b** had melting points of 172 ± 1 ºC and 180 ± 1 ºC, respectively. The low variation in

triplicate analyses indicate the purity of the solids obtained from the syntheses. Obtention of the compounds was also confirmed through CG-MS, with a peak at *m/z* 330.10 (calcd. 330.12) for **1b** and at *m/z* 344.14 (calcd. 344.14) for **3b** (Chromatrogram in Appendix Figures A16 and A17).

Thermal degradation of compound **1b** was observed in a single step starting from 250 °C, which is probably related to the beginning of organic decomposition and indicates the absence of solvent molecules in the structure of the compound in the solid state ($C_{17}H_{18}O_5N_2$, MW = 330.34 g mol^{-1}). On the other hand, compound **3b** showed a loss of 9.78% from around 80 to 190 °C, suggesting the presence of crystallization water molecules in its structural network (Calcd.: 9.78% for $C_{18}H_{20}O_5N_2 \cdot 2\ H_2O$, MW = 380.39 g mol^{-1}). TG curves can be found in Appendix Figure A18 and A19.

Still in the solid state, the IR spectra of compounds **1b** and **3b** showed bands in the region of 3000-3450 cm^{-1} due to the stretching of ν(NH) and ν(OH), previously observed in *N*-acylhydrazones (Dongare; Aswar, 2023; Sharma *et al*., 2023). Moreover, an absorption band was observed for both compounds around 2830 cm^{-1}, attributed to the ν(C–H) mode of the azomethine moiety, in addition to a strong absorption band in the region of 1650 cm^{-1}, related to the C=O stretching of the carbonyl portion present in these structures.

The stretching of the C=N bond formed in the condensation reaction for both **1b** and **3b** can be seen at 1606 and 1605 cm^{-1}, respectively, which confirms the success of the syntheses and the integrity of the hydrazones in the solid state (Munir *et al*., 2021b; Raczuk *et al*., 2022). Additionally, specific absorptions rising from the aromatic substituent in the aldehyde moieties are also present, such as the C–O stretching of the hydroxyl group around 1200 cm^{-1}, and other vibrational modes characteristic of the presence of aromatic rings [ν(C=C)], and bands arising from precursor bonds that remain present in the **1b** and **3b** spectra, such as ν(N–N) and $\nu(C–H)_{methoxyl}$. The most explicit IR bands recorded for the synthesized compounds with their probable assignment are given in Table 11 and the spectra can be observed in Appendix Figures A20 and A21.

Table 11. Selected infrared frequencies of compounds **1b** and **3b**, along with their assignments. Samples were prepared as KBr pellets.

Assignment	**1b**	**3b**
	IR (cm^{-1})	
$\nu(C–H)_{methoxyl}$	2836 and 2999	2836 and 2983
$\nu(O–H)_{water}$	3435	3370
$\nu(N–H)_{hydrazone}$	3171	3177
$\nu(C–H)_{aromatic}$	3072	3063
$\nu(C–H)_{azomethine}$	2828	2835
$\nu(C=O)_{carbonyl}$	1648	1652
$\nu(C=N)_{azomethine}$	1607	1605
$\nu(C–C)_{aromatic}$	1504	1506
$\nu(C–O)_{hydroxyl}$	1230	1240
$\nu(N–N)$	1123	1129
$\delta(C–C–H)_{methyl}$	-	845

In solution, ^{1}H NMR experiment showed only one set of signals in the spectra of **1b** and **3b**. Characteristic hydrazonic NH singlet, which appears around 12 ppm, was observed for both compounds, in agreement with previously published benzoyl hydrazones (Carvalho *et al*., 2023a), indicating the formation exclusively of the (*E*)–isomer. The compounds probably exhibit *antiperiplanar* conformations in solution due to the steric hindrance to the formation of the *syn* conformer.

The singlet at 11.24 ppm in the spectrum of **1b** (11.89 ppm for **3b**) corresponds to the phenolic proton present in both compounds. Typical azomethine hydrogen (H7) was observed at 8.65 ppm for **1b** and 8.58 ppm for **3b** (Figure 27A and 27B). In **1b**, the protons of the methoxyl group attached to the aromatic ring appear as a singlet at δ 3.87 ppm and δ 3.73 ppm, as also observed by Charkoudian *et al*., (2007).

In the **3b**, methoxy hydrogens occur as a pair of singlets: H15 and H17 at 3.88 ppm, and H16 at 3.74 ppm. Methyl H18 appears as a more shielded singlet at 2.22 ppm. Regarding the aromatic region of this com pound, the doublet related to H6 (7.28 ppm) is partially over lapped with the singlet appointed to H10 and H14 (7.27 ppm). These signals were unequivocally assigned using the 2D COSY and HMBC experiments Appendix Figures A22 and A23. The most shielded doublet at

7.22 ppm corresponds to H4, and H5 occurs as a triplet at 6.86 ppm. The inductive effect upon C4, caused by the presence of the methyl group, is another indication of the shielding of H4, while H6 was observed at δ 7.28, due to the minor effect of this substituent on C6. Aromatic protons appeared in the range of 6.93–7.55 ppm for **1b**. 2D homonuclear (COSY) was also used to unambiguously assign the H6, H10 and H14 proton nuclei of this compound (Appendix Figure A24). The signals and attributions made for the ^{1}H spectra of both compounds are summarized in Appendix Table A18.

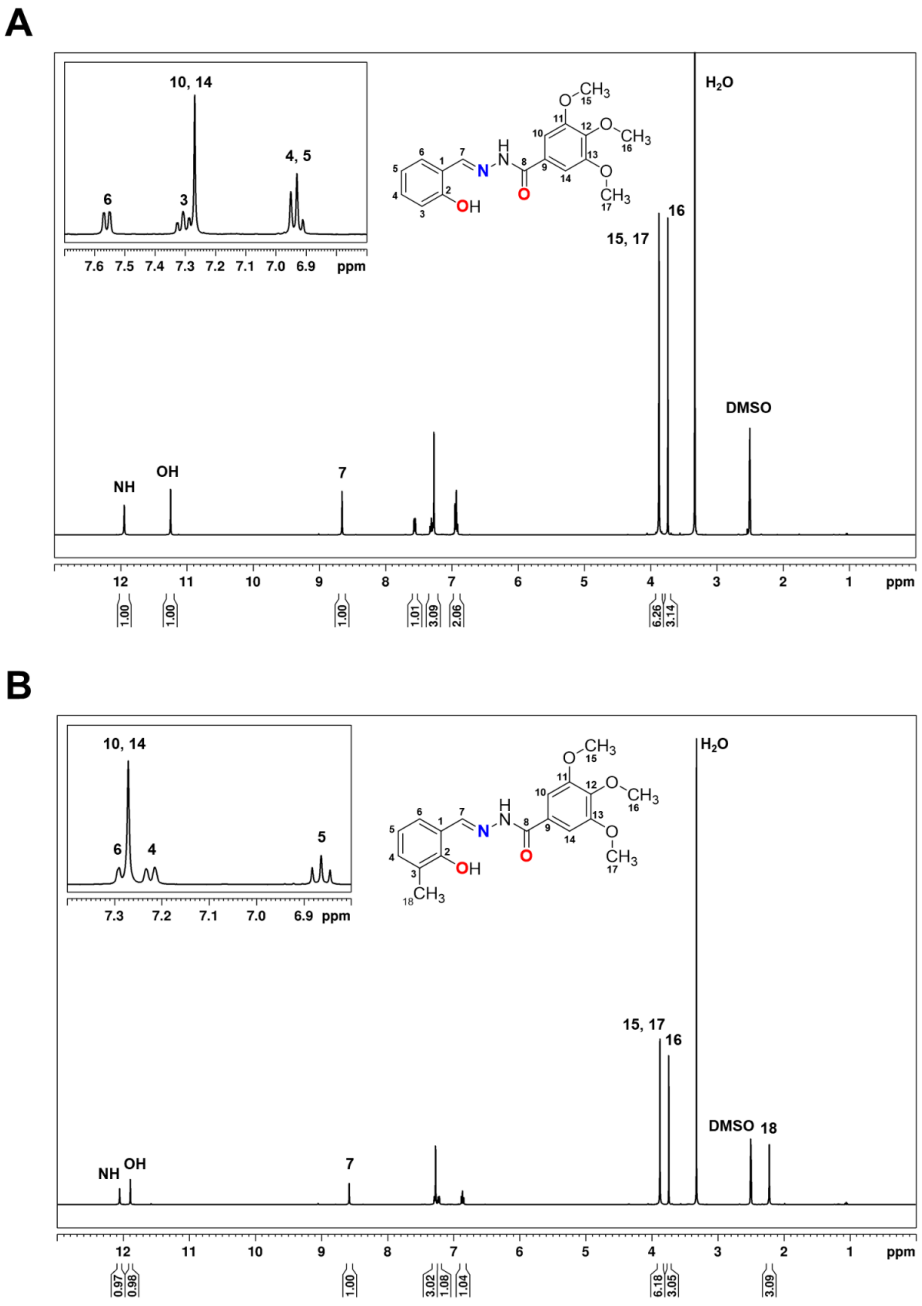

Figure 27. ^{1}H NMR (400 MHz) spectrum of (**A**) **1b** and (**B**) **3b** in DMSO-d_6 at 25 ºC.

5.2.3. Compounds 1c, 2c, 3c and 5c: Furoic acid hydrazide *N*-acylhydrazones

Compounds **1c**, **3c** and **5c** were obtained as yellow crystalline solids in yields between 38 and 77%. Compound **2c**, on the other hand, was obtained as a white solid with a yield of 35%. The crystal structures of **1c** and **2c** were previously described by Bikas *et al*., (2010); Malheiros, (2018); and Parra *et al*., (2024) respectively, so only the XRD structural characterization of **3c** and **5c** will be explored here.

Compound **2c** has been extensively studied previously by Malheiros, (2018); Kumar & Nath, (2018). In this sense, the experimental data obtained for this compound in the present study can be found in Appendices A25-A28 and Table A19, but its characterizations will not be discussed again in this document.

The crystal structure of **3c** was obtained from recrystallization in acetonitrile at room temperature, while the crystal of **5c** was acquired from the mother-liquor of the synthesis. The isolated compounds crystallize in different systems and space groups. Compound **3c** crystallized in the monoclinic system and $P2_1/n$ group, while the crystalline system of **5c** is orthorhombic and belongs to the $Pna2_1$ space group. Both are crystallized with a water molecule as a hydrate linked *via* a hydrogen bond in the C=O amide fagment. Crystal characteristics, data collection parameters, and refinement parameters are summarized in Table 12 and ORTEP representations of the crystal structures are displayed in Figure 28.

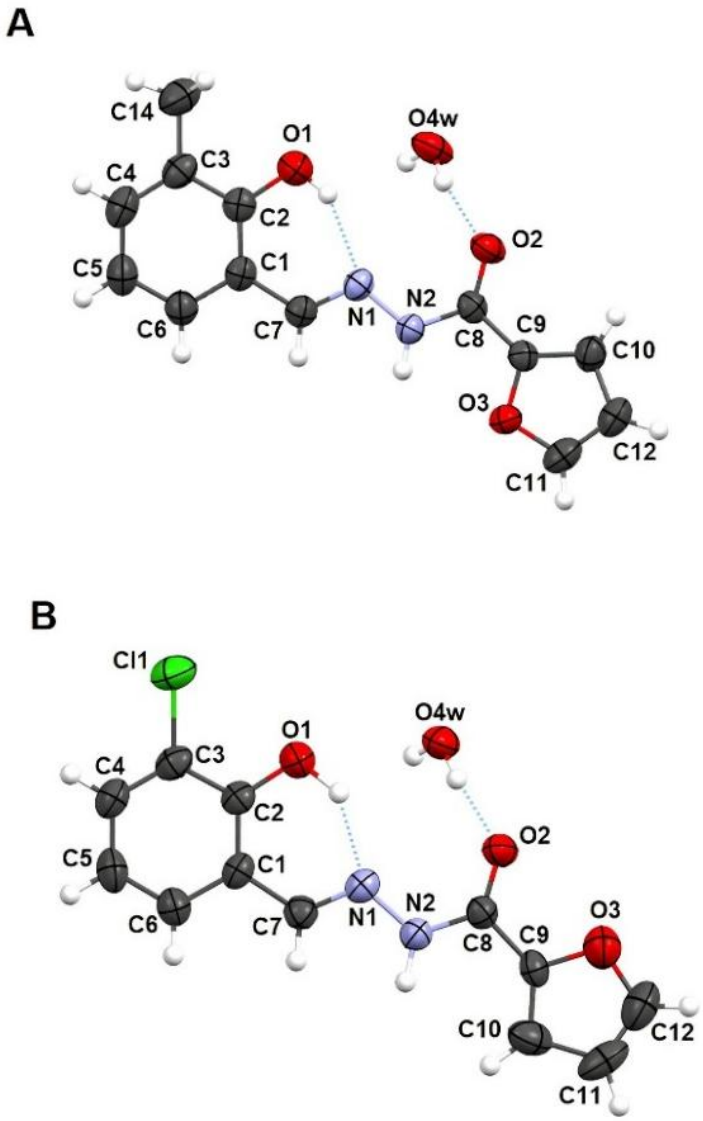

Figure 28. ORTEP representation of the crystal structures of (**A**) **3c** and (**B**) **5c**. The ellipsoids were drawn with 50% probability level.

Table 12. Crystal data, collection and refinement parameters for compounds **3c** and **5c**.

Compound	**3c**	**5c**
Crystal size (mm)	0.06 x 0.27 x 0.61	0.07 x 0.12 x 0.90
Empirical formula	$C_{13}H_{12}N_2O_3 \cdot H_2O$	$C_{12}H_9ClN_2O_3 \cdot H_2O$
Formula weight (g mol^{-1})	262.26	282.68
F(000)	552	584
Temperature (K)	546	273
Absorption coefficient μ (mm^{-1})	0.103	0.311
Calculated density ($g.cm^{-3}$)	1.363	1.472
Crystal System	Monoclinic	Orthorhombic
Space group	$P2_1/n$ (n°. 14)	$Pna2_1$ (n°. 33)
a, b, c (Å)	4.6207(1)	21.4293(14)
	21.8530(6)	4.6935(4)
	12.6957(3)	12.6841(8)
α, β, γ (°)	90	90
	94.741(1)	90
	90	90
Cell volume ($Å^3$)	1277.58(5)	1275.75(16)
Z, Z'	4, 1	4
Reflections collected, R_{int}	33132, 0.040	27744, 0.223
Independent reflections	2418	2309
Index Ranges	$-5 < h < 5$	$-25 < h < 25$
	$-26 < k < 26$	$-5 < k < 5$
	$-15 < l < 15$	$-15 < l < 15$
Data/parameters	1899/225	1488/184
Final residual factor [I>2σ(I)]	R_1: 0.0439	R_1: 0.0497
	wR_2: 0.1243	wR_2: 0.0934
Goodness-of-fit on F^2	1.10	0.98
T_{min}, T_{max}	1.9, 25.7	1.9, 25.3
Largest diff. peak and hole ($e.Å^{-3}$)	-0.17, 0.29	-0.18, 0.24

a, *b*, *c*, *α*, *β*, *γ*: unit cell parameters; *Z*: formula unit per unit cell; *Z'*: number of formula units in the crystallographic unit cell divided by the number of independent general positions; F(000): structure factor in the zero-order case; F: structure factor; F^2: squared structure factor; T: transmission factor.

In the structure of compound **3c** there is a positional disorder in the furoyl ring, derived from free rotation around the C8–C9 bond, which culminates in the coexistence of two crystal structures for this compound, namely: **3cA** and **3cB** (Figure 29). The largest component **3cA** (86%) has intermolecular hydrogen bonds of the N–H···O type that stabilize the furoyl ring with O3A pointing in the opposite direction to O2 [O2–C8–C9–O3A torsion angle of -170.6(5)°]. In the case of the smaller component **3cB** (14%), the O2–C8–C9–O3B torsion angle of -1,47(5)° indicates the *cis* configuration of the O2 atom in relation to O3B. However, both structures have an *E* configuration around the C=N bond [C1–C7–N1–N2 torsion angle -178.76(16)°] and show that the dihedral angles between the benzene and furoyl rings are 12.16° and 6.05°, respectively, indicating that both molecular structures are almost coplanar.

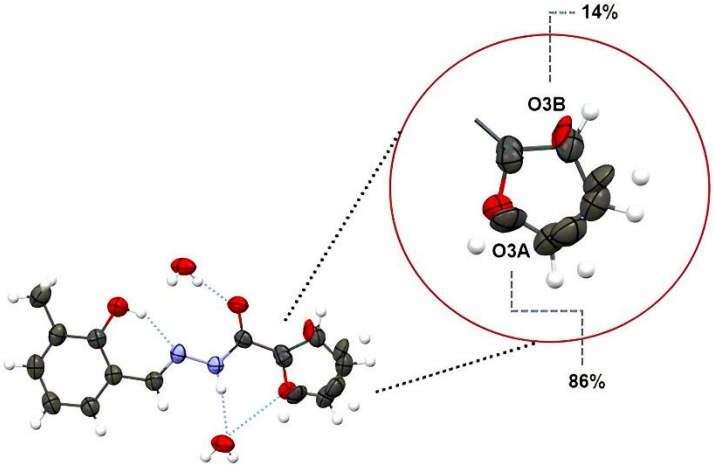

Figure 29. ORTEP representation of the crystal structures of **3cA** and **3cB**. The disorder in the equatorial furoyl ring is highlighted. The ellipsoids were drawn with 50% probability level.

Compound **5c** exists as the (*E*)-isomer with respect to the C7=N1 bond, with the C1–C7–N1–N2 torsion angle of 179.5(4)°. The furanic ring makes a dihedral angle of 1.85° with the six-membered ring, suggesting that the molecule is not completely flat. The bond distances C7=N1 [1.284(6) Å] and C8=O2 [1.240(5) Å] are very close to the formal double bond lengths C=N and C=O (Vineetha *et al*., 2019). In addition, the N1–N2–C8–O2 torsion angle of -0.2(7)° confirms the *trans* configuration of the O2 atom with respect to N2 (Chantrapromma *et al*., 2019). Both pieces of information indicate that, in the solid state, **5c** exists as an amide tautomer. The geometric parameters selected for the compound are shown in Table 13 (complete data in the Appendice Table A20-A29)

Table 13. Select bond distances and angles for compounds **3c** and **5c**.

	Bond distance (Å)	
	3c	**5c**
C1–C7	1.448(3)	1.443(6)
C7–N1	1.285(3)	1.284(6)
N1–N2	1.383(2)	1.386(5)
N2–C8	1.341(2)	1.333(6)
C8–O2	1.237(2)	1.240(5)
C8–C9A	1.442(9)	4.470(6)
C8–C9B	1.59(6)	–
C9A-C10A	1.369(13)	1.333(6)
C9B-C10B	1.36(6)	–
C9A-O3A	1.369(6)	1.365(5)
C9B- O3B	1.370(6)	–
	Bond angle (°)	
C1–C7–N1	123.02(18)	123.2(4)
C7–N1–N2	114.65(16)	114.9(4)
N1–N2–C8	119.97(16)	119.8(4)
N2–C8–O2	124.12(18)	124.5(4)
N2–C8–C9A	116.7(3)	114.8(4)
N2–C8–C9B	111.3(15)	–
C9A–C8–O2	119.2(3)	120.8(4)
C9B–C8–O2	124.4(15)	–
C8–C9A–O3A	118.9(6)	116.0(4)
C8–C9B–O3B	105(3)	–
	Torsion angle (°)	
C1–C7–N1–N2	-178.76(16)	179.5(4)
C7–N1–N2–C8	-179.18(17)	179.8(4)
N1–N2–C8–C9A	-177.8(4)	179.0(4)
N1–N2–C8–O2	1.4(3)	-0.2(7)
N2–C8–C9A–O3A	8.6(8)	-178.4(4)

In the crystal structure of **3c**, there are two intramolecular hydrogen bonding interactions: O1–H1···N1 and N2–H1A···O3A, and three intermolecular

interactions linking one molecule to two others through bonds between N2–H1···O4 and O4–H4···O2. Finally, the structure also has an unconventional hydrogen bond between C7–H7···O4 (angle=142.0º), which helps stabilize the molecular structure in an anti-parallel organization. The bond distances are shown in Table 14, while the interactions present in the crystal (unconventional hydrogen bond in green) are illustrated in Figure 30.

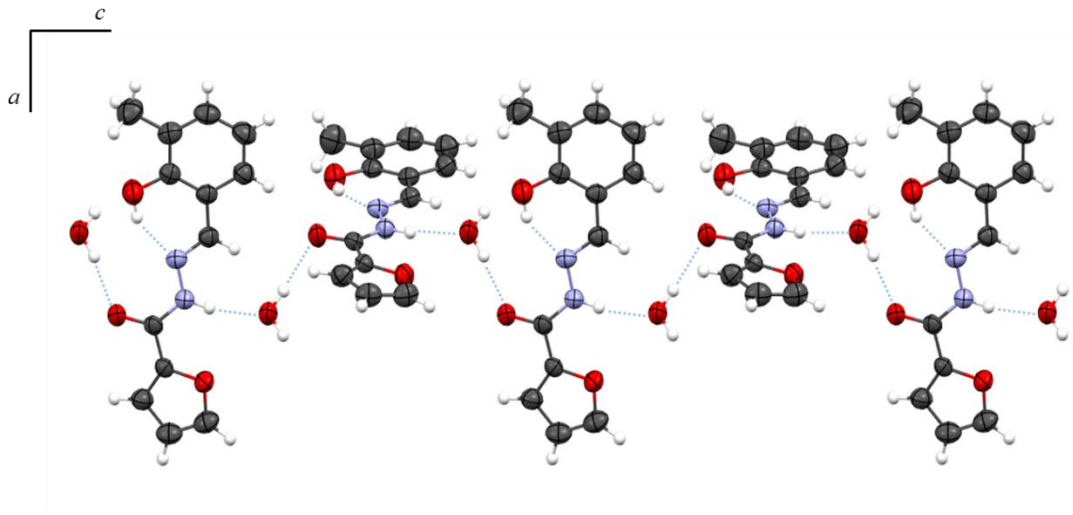

Figure 30. Hydrogen bond interactions in the crystal networks of compound **3c** ao longo do eixo cristalográfico *c*.

Table 14. Hydrogen bond geometric parameters for compound **3c**.

D–H···A	D–H (Å)	H···A (Å)	D···A (Å)	D–H···A (°)
O1–H1···N1	0.85(2)	1.95(2)	2.702(2)	147(2)
N2–H1A···O3A	0.855(19)	2.36(2)	2.712(4)	104.9(17)
N2–H1A···O4^{ii}	0.855(19)	1.939(18)	2.782(2)	168(2)
O4–H4A···O2	0.87(2)	1.90(2)	2.741(2)	166(2)
O4–H4B···O2^{i}	0.85(2)	1.97(2)	2.817(2)	176(3)
C7–H7···O4^{ii}	0.9300	2.5000	3.286(3)	142.00

Symmetry code: *i* (-1+x,y,z); *ii* (1/2+x,3/2-y,1/2+z).

The structure of **5c** contains an intramolecular hydrogen bond involving O1–H1···N1 with a angle of 136(5)° (Table 15). The molecule also has stronger non-covalent intermolecular interactions, such as the classic hydrogen bonds between N2–H2···O4; O4–H4A···O2 and O4–H4B···O2, and unusual hydrogen bonds C7–H7···O4 and C10–H10···O4, with the classic hydrogen bonds being responsible for the two-dimensional ordering of the crystal. An illustration of the

general packing is shown in Figure 31, where the conventional hydrogen bond is highlighted in blue.

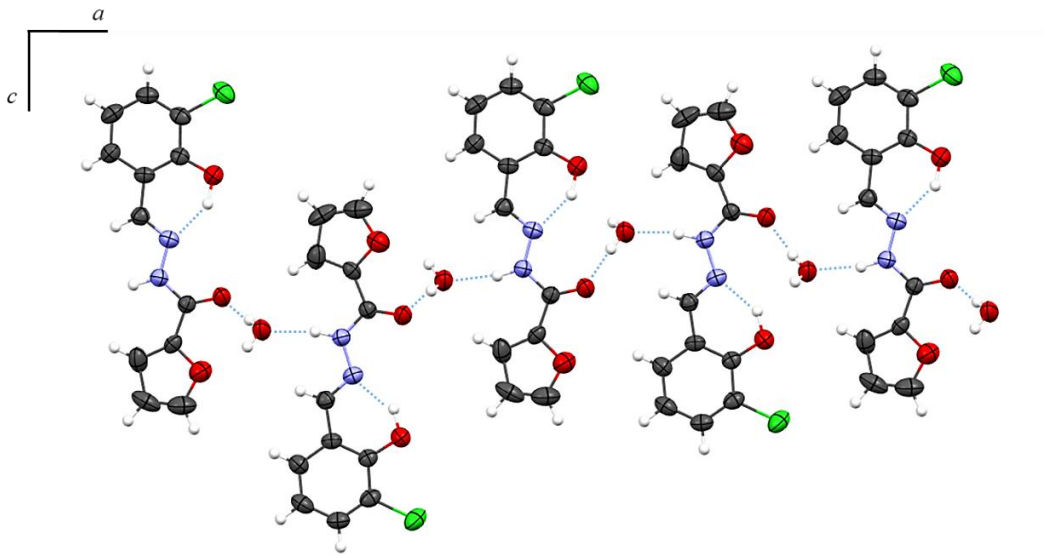

Figure 31. Hydrogen bond interactions in the crystal networks of compound **5c** ao longo do eixo cristalográfico *a*.

Table 15. Hydrogen bond geometric parameters for compound **5c**.

D–H···A	D–H (Å)	H···A (Å)	D···A (Å)	D–H···A (°)
O1–H1···N1	1.06(7)	1.86(6)	2.720(5)	136(5)
N2–H2···O4^{ii}	0.94(6)	1.87(6)	2.795(5)	170(5)
O4–H4A···O2	0.84(5)	1.91(5)	2.739(5)	169(6)
O4–H4B ···O2^{i}	0.84(7)	2.01(7)	2.847(5)	178(9)
C7–H7 ···O4^{ii}	0.9300	2.5300	3.316(6)	142.00
C10–H10···O4^{ii}	0.9300	2.3500	3.182(7)	148.00

Symmetry code: *i* (1-x,1-y,1/2+z); *ii* (x,-1+y,z).

Melting points of **1c**, **3c** and **5c** suggest high purity of the compounds in the solid state, since the replicas were obtained in a range below 5 ºC. The compounds were confirmed through CG-MS, showing a peak at *m/z* 230.06 (calculated 230.07) for **1c**, *m/z* 244.11 (calculated 244.08) for **3c** and at *m/z* 264.05 (calculated 264.03) for **5c** (Chromatrogram in Appendix Figures A29-A31).

Thermal analysis of **1c** showed the absence of solvation molecules in the structure of the compound in the solid state ($C_{12}H_{10}N_2O_3$, MW = 230.22 g mol^{-1}) TGA curve of **1c** can be seen in Appendix Figure A32. The losses observed in the TGA of compound **3c** could not be attributed perfectly, which is why the molar

mass considered in the subsequent studies was based on the GC-MS. The TGA of compound **3c** can be seen in Appendix Figure A33. Finally, in the TGA of compound **5c** (Appendix Figure A34), a loss of approximately 4.94% was observed between 60 and 150 °C, consistent with the presence of one hydration molecule of water per molecule of compound (Calcd.: 4.76% for $C_{12}H_9ClN_2O_3 \cdot H_2O$, MW = 282.69 g mol^{-1}).

Regarding their vibrational characterization, infrared spectra, stretching bands in the regions of 3233cm^{-1}, 3134 cm^{-1} and 3128 cm^{-1} confirm the presence of –NH groups in **1c**, **3c** and **5c**, respectively. The bending of phenol and stretching -CH=N- were observed, respectivamente, at 1360 band at 1620 cm^{-1} for compound **1c** (1372 and 1610 cm^{-1} for compound **3c**). In compound **5c**, the shift in the carbonyl band was observed in comparison to the other compounds. A similar trend is observed in the case of the C=N vibrational mode, where the band is significantly red-shifted, which may be related to the presence of the -Cl group in the structure of this hydrazone. The aromatic C-H stretchings of the ligands were observed at 3055 cm^{-1} for the three ligands. Other important functional groups were also characterized in their respective IR regions and the values can be seen in Table 16. The spectra of the compounds can be seen in Appendix Figures A35-A37.

Table 16. Selected infrared frequencies of compounds **1c**, **3c** and **5c**, along with their assignments. Samples were prepared as KBr pellets.

Assignment	**1c**	**3c**	**5c**
		IR (cm^{-1})	
$\nu(O–H)_{water}$	3435	3436	3437
$\nu(N–H)_{hydrazone}$	3233	3134	3128
$\nu(C–H)_{azomethine}$	3054	3117	2997
$\nu(C=O)_{carbonyl}$	1672/1654	1634/1646	1650
$\nu(C=N)_{azomethine}$	1620	1610	1615
$\nu(C=N)_{pyridine}$	1610	1563	1555
$\nu(C–C)_{aromatic}$	1477	1471	1465
$\delta(C–OH)_{phenol}$	1360	1372	1367
$\nu(N–N)$	1153	1143	1147
$\delta_{out\text{-}of\text{-}plane}(C–O–C)_{furan}$	588	617	611

As observed for the hydrazones derived from isoniazid, the NMR spectra of the solution of **1c** and **3c** showed the existence of two sets of signals, which can be attributed to the presence of conformations in the amide bond (*anti/syn*). The condensation reaction led to the formation of (*E*)-isomer, identified by the singlet around 12 ppm corresponding to the NH proton in all the compounds in this family (Moura *et al*., 2023). The absence of precursor signals in the spectra indicates high purity of the compounds. The relative integration of the **1c** (98.33% of the *anti* conformation and 1.33% of the *syn* conformation) and **3c** (96.63% of the *anti* conformation and 3.36% of the *syn* conformation) signals led to the conclusion that the *antiperiplanar* conformation is mostly present.

The *N*-acylhydrazones **1c**, **3c** and **5c** show the peak for the N=CH proton of the imine at 8.64, 8.57 and 8.61 ppm, respectively. The OH proton can be seen at 11.13 ppm for **1c** and 11.79 for compound **3c**. For compound **5c**, on the other hand, this signal is more de-shielded (12.40 ppm) due to the presence of the Cl group, which was mentioned above in compound **5a** (isoniazid family). Additionally, the aromatic signal regions for compounds **1c**, **3c** and **5c** were 6.71-7.96 ppm, 6.73-7.98 ppm and 6.74-7.99 ppm, respectively, agreeing with what was described by Li *et al*., (2009) for structures containing the furoyl ring and similar to salicylaldehyde. The ^{1}H spectrum of compounds **1c**, **3c** and **5c**, along with the corresponding assignments, is shown in Figure 32A-C. All signals and attributions made for the ^{1}H spectra of the compounds are summarized in Appendix Table A30.

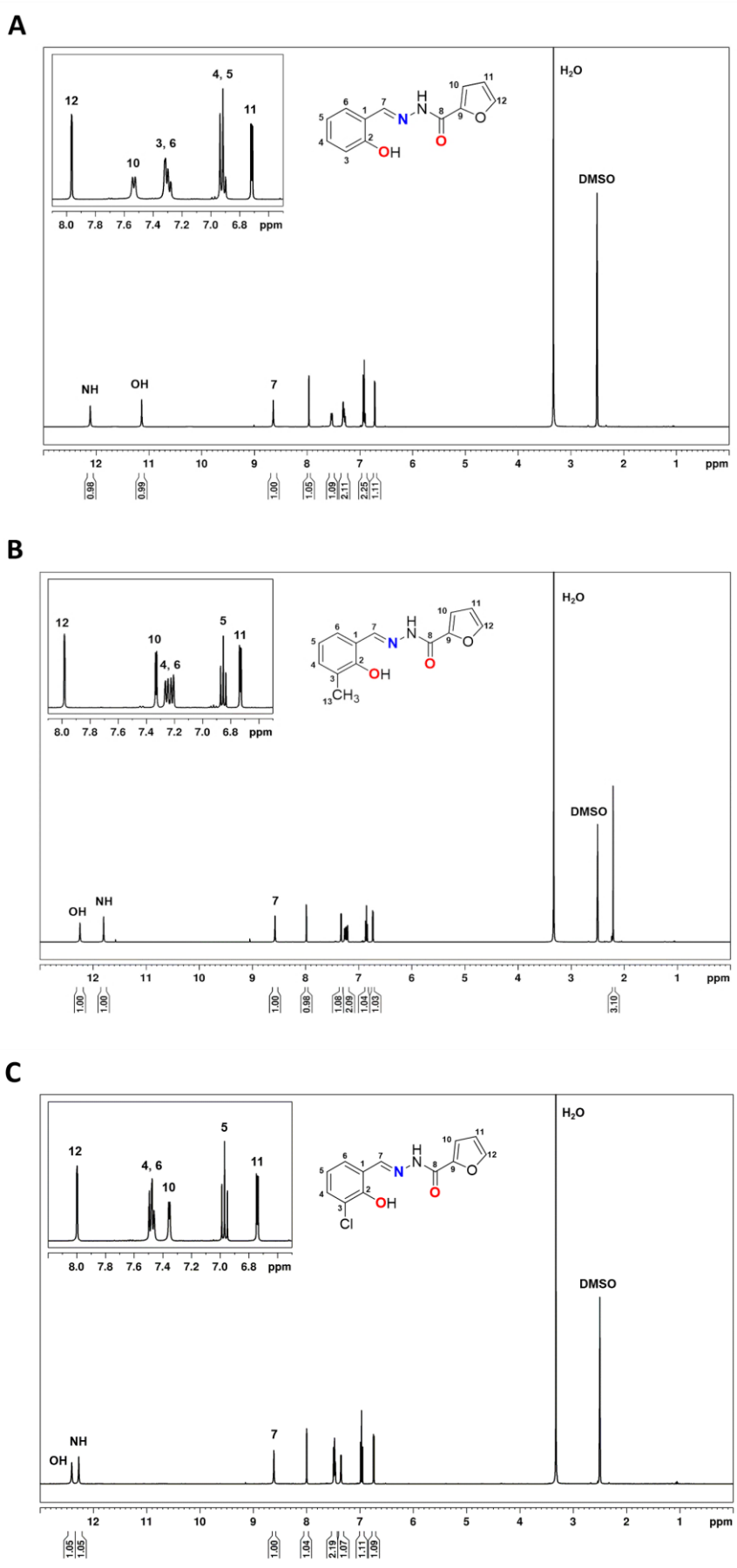

Figure 32. ^{1}H NMR (400 MHz) spectrum of (**A**) **1c**, (**B**) **3c** and (**C**) **5c** in DMSO-d_6 at 25 ºC

5.3. Experimental Solubility

All previously characterized compounds were evaluated for their solubility in aqueous media. Since it was not possible to solubilize the compounds directly in buffer solution, solubility tests were performed in pure DMSO and/or mixtures containing specific DMSO/buffer ratios. Cytotoxicity tests performed by (Helena *et al*., 2024a) demonstrated suitability at up to 1% of this solvent for *in vitro* cellular assays. These same authors found tolerability of this solvent at 10% *in vivo* (Cukierman *et al*., 2017). Thus, the solubility, as well as other studies in solution with the compounds were evaluated in mixtures containing 1%, 5% and 10% DMSO/buffer, at a concentration of 5×10^{-5} mol L^{-1}, as used in works with *N*-acylhydrazones previously published by the group (Carvalho *et al*., 2023a; Cukierman *et al*., 2020a; Martins *et al*., 2023).

Compounds **1a**, **2a**, **3a**, **1b**, **1c** and **2c** (Figure 33) showed good solubility in only 1% DMSO/buffer, while compounds **5a**, **3b** and **5c** could only be solubilized at the tolerable threshold of this solvent (10% DMSO). Compound **3c**, on the other hand, was eliminated at this step because it was not soluble under these conditions.

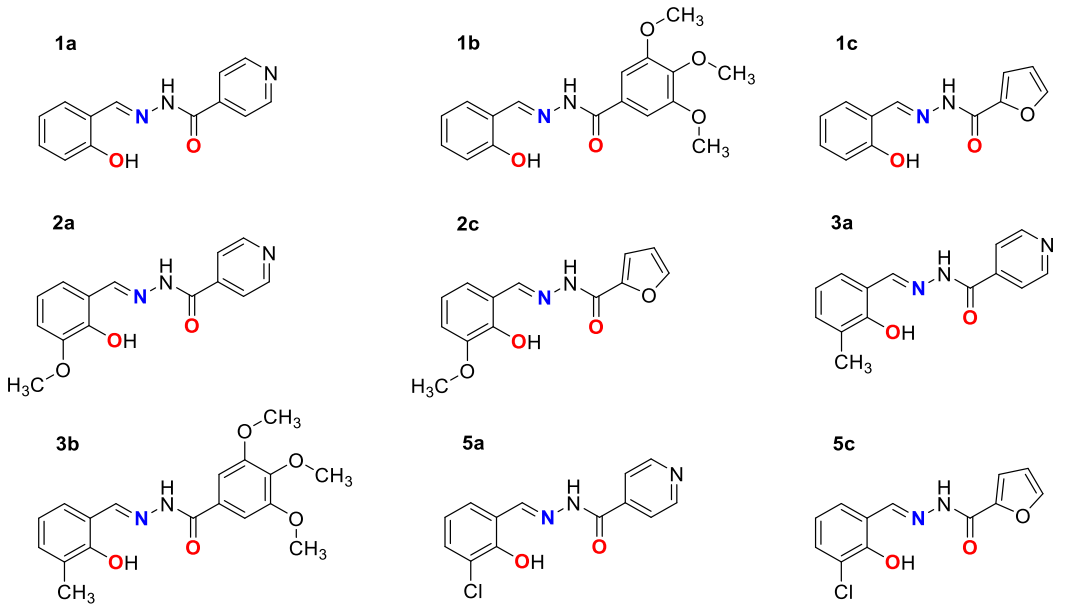

Figure 33. Structures of the 9 *N*-acylhydrazones selected for the next steps of the present work.

5.4. Stability Study

The mechanism associated with the hydrolysis of hydrazones generally involves the protonation of the azomethine nitrogen (N1), followed by the addition of an H_2O molecule to the compound's structure, generating a carbinolamine intermediate. An intramolecular attack of N1 under H_2O favors the decomposition of carbinolamine into its respective aldehyde/ketone and hydrazide (Figure 34) (Ji *et al.*, 2015; Kalia; Raines, 2008). *N*-acylhydrazones derived from salicylaldehyde are structurally and pharmacokinetically impaired by autohydrolysis caused by an intramolecular interaction between the phenolic hydrogen and the azomethine nitrogen present in their structure. Therefore, evaluating the stability of the compounds proposed in this study in aqueous media is an important step in the development of new bioactive hydrazone derivatives capable of targeting trivalent metal ions such as Al^{3+}.

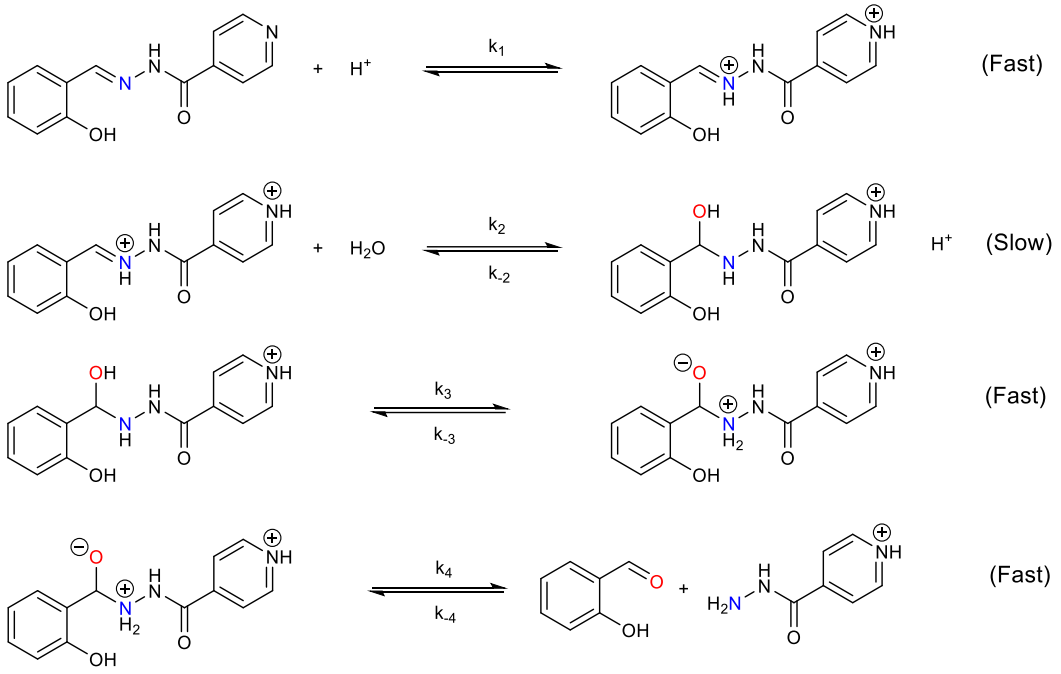

Figure 34. Proposed mechanism of acid hydrolysis of hydrazones studied.

As this is a study related to the development of Al^{3+} chelators and due to the conditions in which this metal is found in its free form (Martin, 1986), the studies in solution were carried out simulating both physiological and environmental

conditions. Thus, the compounds were evaluated for their stability in 1% DMSO/buffer mixture (pH 4.5 and 7.4; C = 5×10^{-5} mol L^{-1}), except for compounds **5a**, **3b** and **5c** in which the 10% DMSO/buffer ratio was used, according to the result obtained in the solubility assay. The compounds were monitored initially at regular intervals for 12 hours, and readings were also taken after 48 hours. In the first- and 12-hour spectrum, a Gaussian curve fitting was performed in order to obtain the exact wavelengths of maximum absorptions. The other spectra can be found in Appendix Figure A38-A46.

The exclusion criterion used in this phase of the study assumes that compounds with a loss of more than 15% of absorbance in a period of 12 hours, in one or both conditions tested, are pharmacokinetically unfavorable and will therefore not be considered for the following phases.

5.4.1. Compound 1a

The electronic spectra of **1a** in 1% DMSO/acetate buffer, pH 4.5 (Figure 35A) show three apparent absorptions characterized by two overlapping higher energy bands at 287 (8.700 ± 70 L mol^{-1} cm^{-1}) and 300 nm (7.600 ± 60 L mol^{-1} cm^{-1}), and a shoulder at 330 nm (6.500 ± 52 L mol^{-1} cm^{-1}). With the deconvolution of the bands, it was possible to confirm that there are in fact three contributions in the profile of **1a**. The band at 330 nm was attributed by comparison to electronic transitions involving the 2-HBA precursor (Figure 35B, dotted brown curve) similar to that observed by (Galić *et al*., 2011, 2012), while the absorptions at 287 and 300 nm correspond to intra-ligand hydrazone transitions highlighted earlier by Lu *et al*., (2006).

In 1% DMSO/HEPES buffer (pH 7.4), it also showed three absorption bands at 287 nm (8.000 ± 100 L mol^{-1} cm^{-1}), 300 nm (7.300 ± 100 L mol^{-1} cm^{-1}) and 330 nm (6.300 ± 100 L mol^{-1} cm^{-1}) (Figure 36A and 36B).

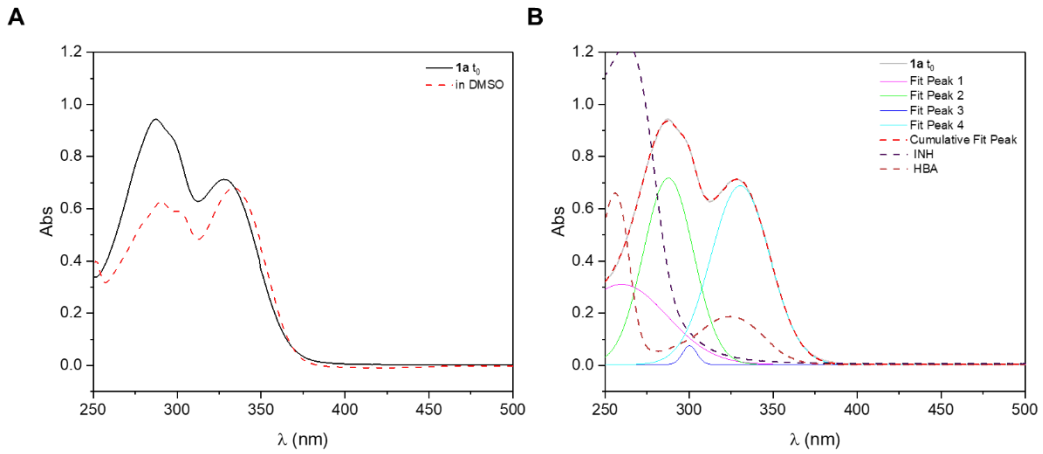

Figure 35. Electronic absorption spectra in selected wavelength regions for a 5×10^{-5} mol L^{-1} solution of **1a**. (**A**) Spectra measured at t_0 in 1% DMSO/acetate buffer mixture, pH 4.5 (black solid curve) and in pure DMSO (red dotted curve). (**B**) Gaussian fitting of the bands in the spectrum at t_0**,** along with the spectra of precursors INH and 2-HBA. Deconvolution was performed with Origin software.

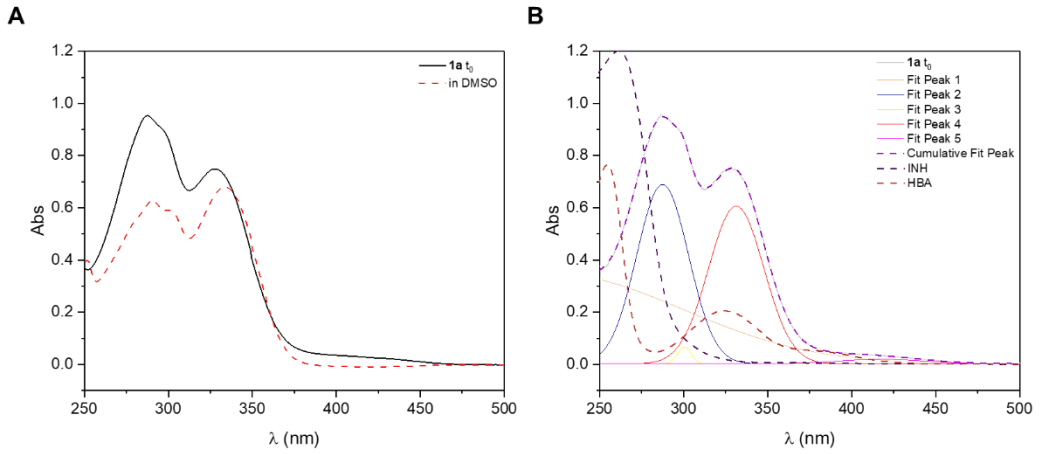

Figure 36. Electronic absorption spectra in selected wavelength regions for a 5×10^{-5} mol L^{-1} solution of **1a**. (**A**) Spectra measured at t_0 in 1% DMSO/HEPES buffer mixture, pH 7.4 (black solid curve) and in pure DMSO (red dotted curve). (**B**) Gaussian fitting of the ba bands in the spectrum at t_0, along with the spectra of precursors INH and 2-HBA. Deconvolution was performed with Origin software.

In the 1% DMSO/HEPES buffer solution (pH 7.4), hydrazone **1a** showed great stability (Figure 37A, Gaussian fitting in Figure 37B), on the other hand, in acidic media (i.e. 1% DMSO/acetate buffer, pH 4.5), there was a 25.5% and 24.7% decrease in the absorption of the bands at 287 and 300 nm, respectively. In addition, a loss of 22.2% was also observed in the lowest intensity band (330 nm), and the appearance of a new band at 255 nm was observed after 12 hours of monitoring (Figure 38A), suggesting that in this latter condition the hydrolysis of the compound into its precursors INH and 2-HBA is favored. The Gaussian fitting of the bands in

the spectrum in 1% DMSO/acetate buffer at t_{12} can be seen in Figure 38B.

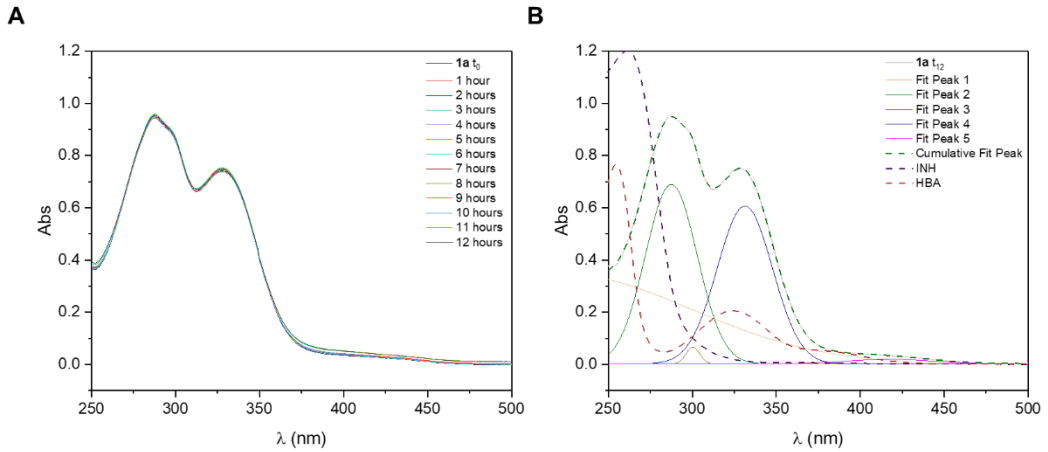

Figure 37. Electronic absorption spectra in selected wavelength regions for a 5×10^{-5} mol L^{-1} solution of **1a**. (**A**) Spectra measured at t_0 and after 12h in 1% DMSO/HEPES buffer mixture, pH 7.4. (**B**) Gaussian fitting of the bands in the spectrum at t_{12}, along with the spectra of precursors INH and 2-HBA. Deconvolution was performed with Origin software.

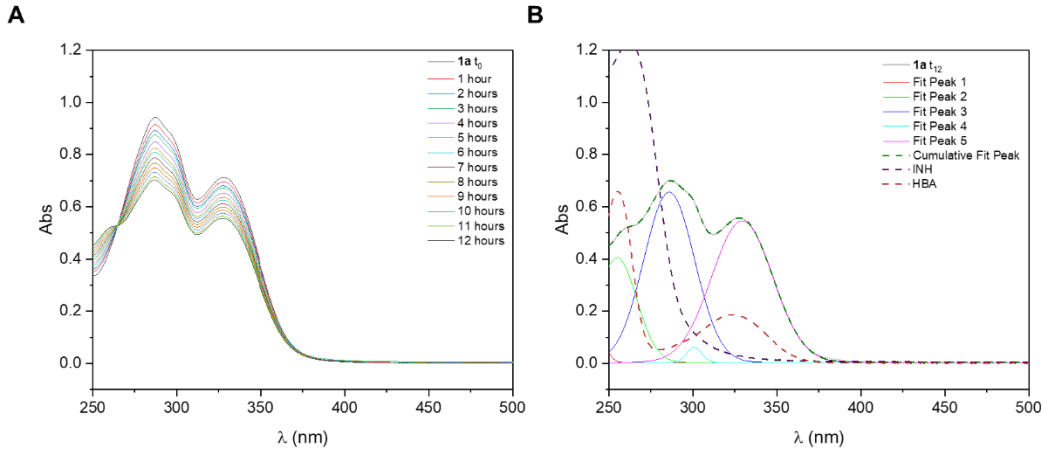

Figure 38. Electronic absorption spectra in selected wavelength regions for a 5×10^{-5} mol L^{-1} solution of **1a**. (**A**) Spectra measured at t_0 and after 12h in 1% DMSO/acetate buffer mixture, pH 4.5. (**B**) Gaussian fitting of the bands in the spectrum at t_{12}, along with the spectra of precursors INH and 2-HBA. Deconvolution was performed with Origin software.

5.4.2. Compound 1b

In the 1% DMSO solution/acetate buffer (pH 4.5) mixture (Figure 39A), compound **1b** shows the presence of three apparent bands at 292 (27,300 ± 430 L mol^{-1} cm^{-1}) and 300 nm (27,300 ± 426 L mol^{-1} cm^{-1}) and 328 nm (20,600 ± 312 L mol^{-1} cm^{-1}). The Gaussian fitting of the curve also showed the contribution of only 3 absorptions in the spectrum, of which the intense bands (292 and 300 nm) probably correspond to the hydrazone part, since they are completely absent in the precursor spectra. Furthermore, a comparison of the spectra allowed the component

at 266 nm and the broad band at 328 nm to be attributed to transitions involving the TMP and 2-HBA rings Figure 39B, dark purple and brown dotted curves, respectively).

A similar profile was obtained in 1% DMSO/HEPES buffer, pH 7.4, with three absorptions (i.e. three overlapping bands and a shoulder) centered at 292 (27,200 ± 490 L mol^{-1} cm^{-1}) and and 300 nm (27,200 ± 490 L mol^{-1} cm^{-1}) and 328 nm (20,500 ± 370 L mol^{-1} cm^{-1}), respectively (Figure 40A and 40B).

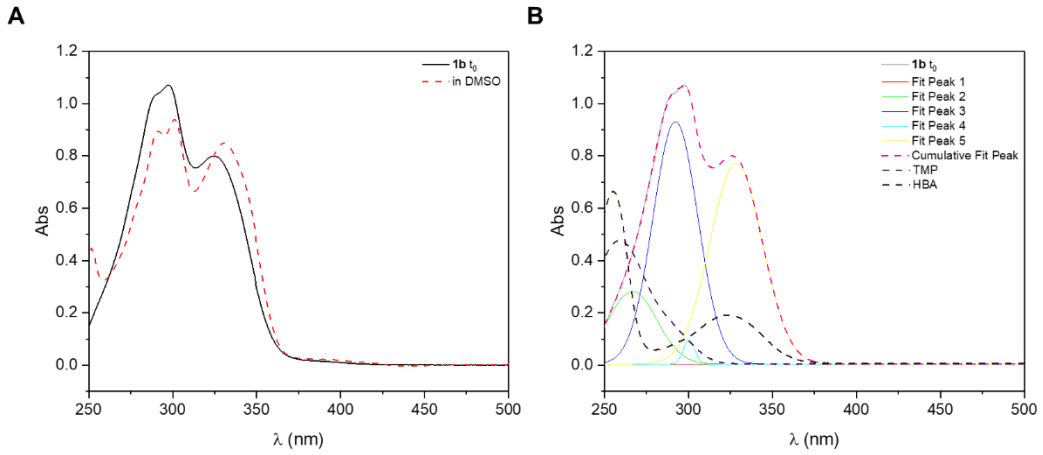

Figure 39. Electronic absorption spectra in selected wavelength regions for a 5×10^{-5} mol L^{-1} solution of **1b**. (**A**) Spectra measured at t_0 in 1% DMSO/acetate buffer mixture, pH 4.5 (black solid curve) and in pure DMSO (red dotted curve). (**B**) Gaussian fitting of the bands in the spectrum at t_0, along with the spectra of precursors TMP and 2-HBA. Deconvolution was performed with Origin software.

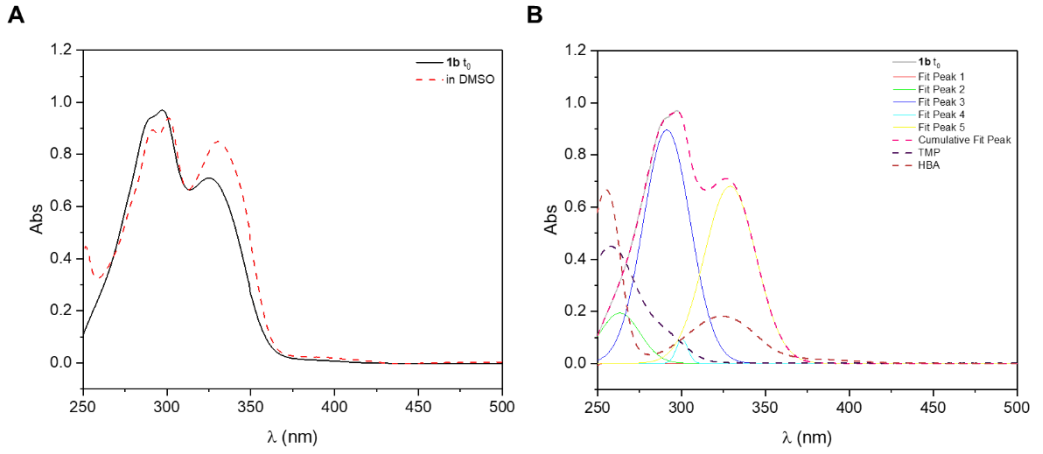

Figure 40. Electronic absorption spectra in selected wavelength regions for a 5×10^{-5} mol L^{-1} solution of **1b**. (**A**) Spectra measured at t_0 in 1% DMSO/HEPES buffer mixture, pH 7.4 (black solid curve) and in pure DMSO (red dotted curve). (**B**) Gaussian fitting of the bands in the spectrum at t_0, along with the spectra of precursors TMP and 2-HBA. Deconvolution was performed with Origin software.

Although it showed stability in 1% DMSO/HEPES buffer, pH 7.4 (Figure 41A and 41B), compound **1b** showed a decrease of around 33.9% in the absorbance of the main bands at 292 and 300 nm after 12 hours of monitoring at 1% DMSO/acetate buffer. The lowest energy band at 330 nm also suffered a decrease in absorbance of around 32.1% (Figure 42A). An isosbestic point can be clearly observed in the spectrum at 267 nm, and a new band was observed at 258 nm (2-HBA transitions) with an increase of 54.5% compared to the t_0 spectrum. The adjustment carried out on a 1% DMSO/acetate buffer mixture for t_{12} can be seen in Figure 42B.

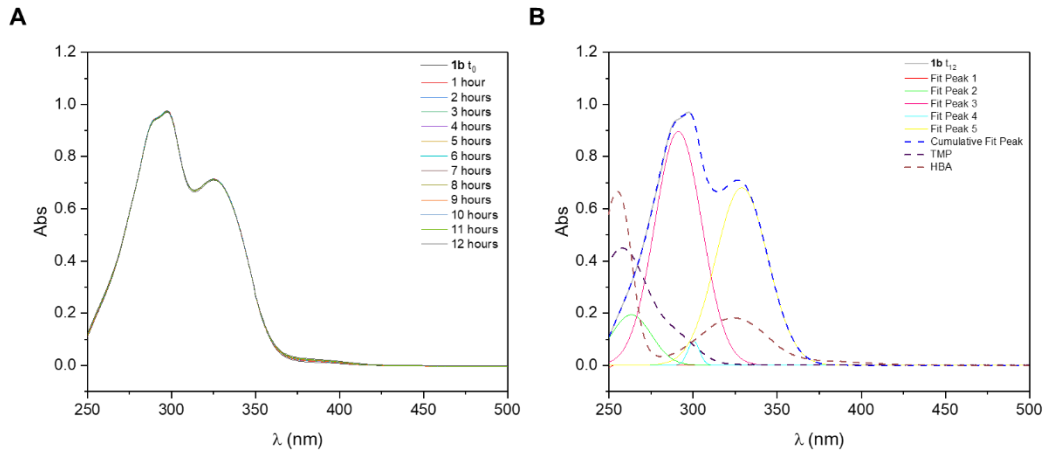

Figure 41. Electronic absorption spectra in selected wavelength regions for a 5×10^{-5} mol L^{-1} solution of **1b**. (**A**) Spectra measured at t_0 and after 12h in 1% DMSO/HEPES buffer mixture, pH 7.4. (**B**) Gaussian fitting of the bands in the spectrum at t_{12}, along with the spectra of precursors TMP and 2-HBA. Deconvolution was performed with Origin software.

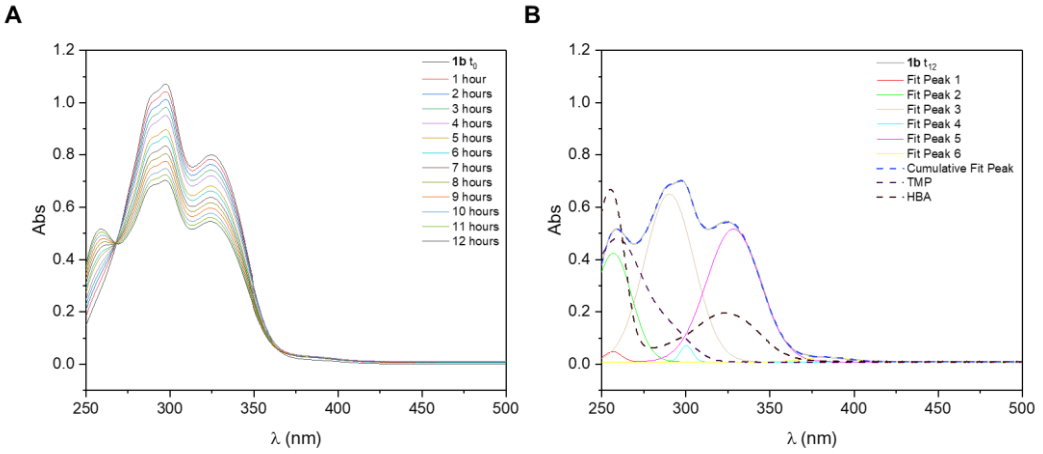

Figure 42. Electronic absorption spectra in selected wavelength regions for a 5×10^{-5} mol L^{-1} solution of **1b**. (**A**) Spectra measured at t_0 and after 12h in 1% DMSO/acetate buffer mixture, pH 4.5. (**B**) Gaussian fitting of the bands in the spectrum at t_{12}, along with the spectra of precursors TMP and 2-HBA. Deconvolution was performed with Origin software.

5.4.3. Compound 1c

In aqueous medium at pH 4.5 (Figure 43A), compound **1c** shows three strongly asymmetrical apparent bands centered at 297 (22.200 ± 315 L mol^{-1} cm^{-1}) and 302 nm (23.300 ± 330 L mol^{-1} cm^{-1}) and 334 nm (17.500 ± 240 L mol^{-1} cm^{-1}), which were satisfactorily fitted as the sum of five gaussian components (Figure 43B). The absorption at 334 nm is also present in the spectrum of the 2-HBA precursor and is probably related to transitions involving this portion of the hydrazone. The intense and clear bands at 297 and 302 nm were related to processes strictly associated with hydrazone, since they are completely absent from the precursors' spectra.

The profile of the compound in 1% DMSO/HEPES buffer is identical to that observed in the more acidic condition (pH 4.5) (Figure 44A). The main bands observed are: 297 (22,800 ± 330 L mol^{-1} cm^{-1}), 302 (23,800 ± 343 L mol^{-1} cm^{-1}) and 334 (17,900 ± 250 L mol^{-1} cm^{-1}) nm (Figure 44B). For the profile in DMSO, a difference in intensity was observed in relation to the profile in buffer, related to a hypochromic effect in this solvent.

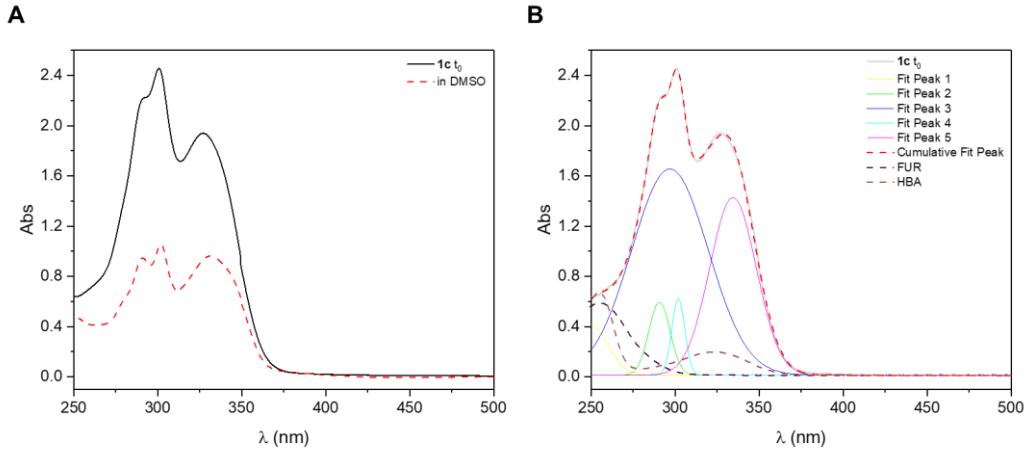

Figure 43. Electronic absorption spectra in selected wavelength regions for a 5×10^{-5} mol L^{-1} solution of **1c**. (**A**) Spectra measured at t_0 in 1% DMSO/acetate buffer mixture, pH 4.5 (black solid curve) and in pure DMSO (red dotted curve). (**B**) Gaussian fitting of the bands in the spectrum at t_0**,** along with the spectra of precursors FUR and 2-HBA. Deconvolution was performed with Origin software.

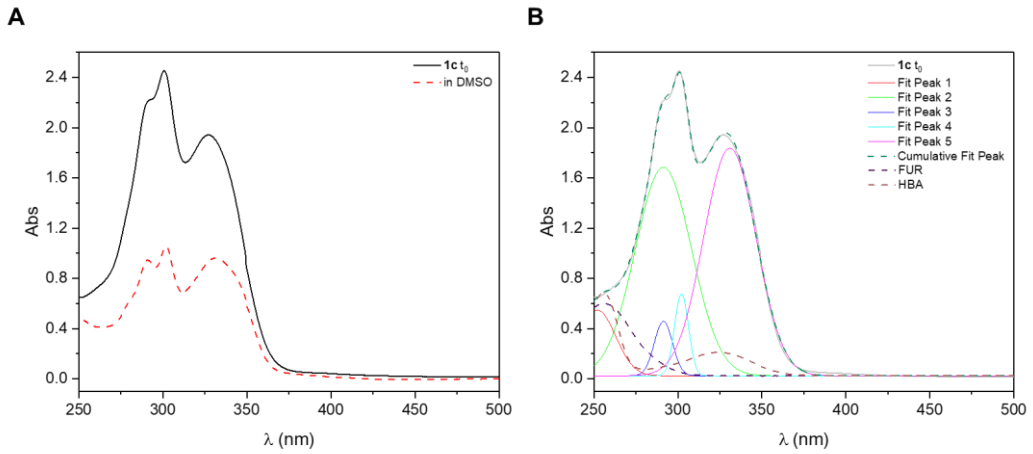

Figure 44. Electronic absorption spectra in selected wavelength regions for a 5×10^{-5} mol L^{-1} solution of **1c**. (**A**) Spectra measured at t_0 in 1% DMSO/HEPES buffer mixture, pH 7.4 (black solid curve) and in pure DMSO (red dotted curve). (**B**) Gaussian fitting of the bands in the spectrum at t_0, along with the spectra of precursors FUR and 2-HBA. Deconvolution was performed with Origin software.

In a mixture containing 1% DMSO/HEPES buffer at physiological pH 7.4, **1c** is highly resistant to the hydrolytic process (Figure 45A and 45B). At pH 4.5, on the other hand, the rate of hydrolysis of **1c** in the first 12 hours of experiments is very high (Figure 46A), there is a reduction in the absorption of the main band (at 302 nm) by around 19.60%, and a new absorption can be observed at 257 nm (Figure 46B). In addition, the presence of an isosbestic point (at 271 nm) suggests the presence of other absorbing species in equilibrium in the solution, related to hydrazone and the precursors 2-HBA and FUR, since they absorb in the same region.

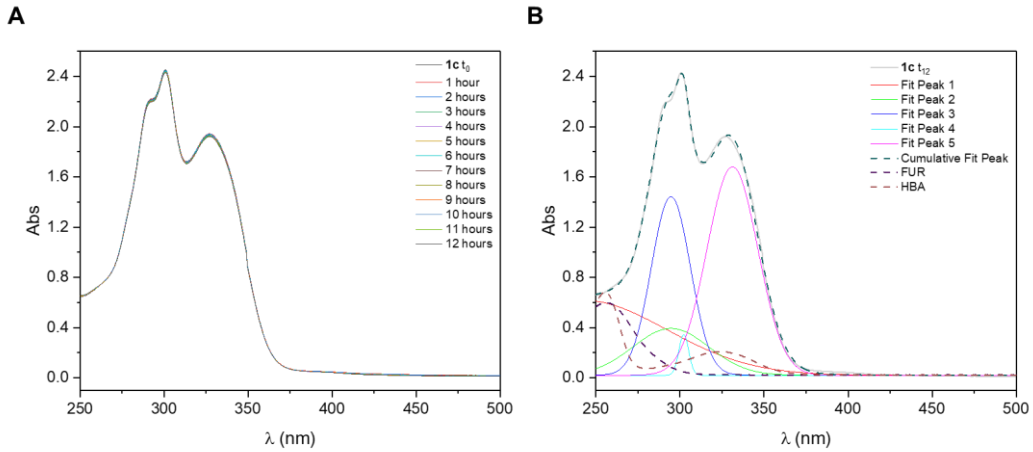

Figure 45. Electronic absorption spectra in selected wavelength regions for a 5×10^{-5} mol L^{-1} solution of **1c**. (**A**) Spectra measured at t_0 and after 12h in 1% DMSO/HEPES buffer mixture, pH 7.4. (**B**) Gaussian fitting of the bands in the spectrum at t_{12}, along with the spectra of precursors FUR and 2-HBA. Deconvolution was performed with Origin software.

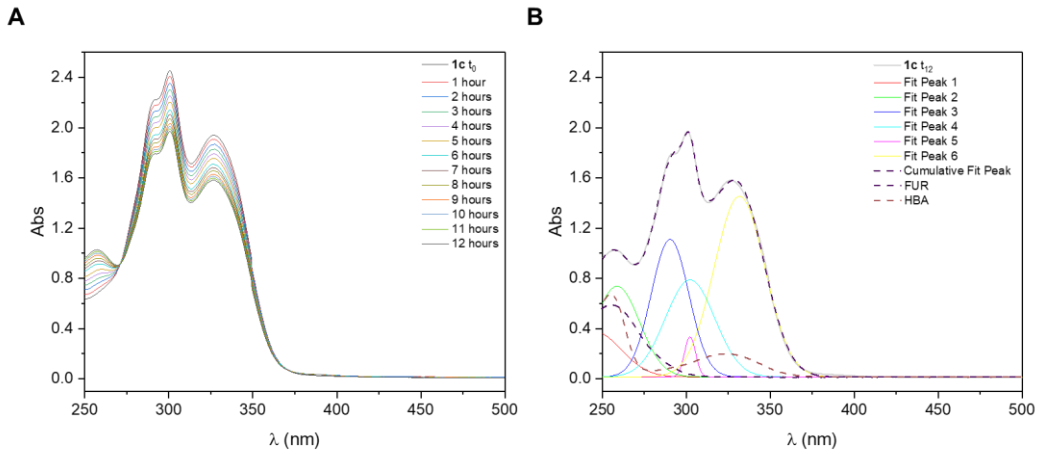

Figure 46. Electronic absorption spectra in selected wavelength regions for a 5×10^{-5} mol L^{-1} solution of **1c**. (**A**) Spectra measured at t_0 and after 12h in 1% DMSO/acetate buffer mixture, pH 4.5. (**B**) Gaussian fitting of the bands in the spectrum at t_{12}, along with the spectra of precursors FUR and 2-HBA. Deconvolution was performed with Origin software.

5.4.4. Compounds 2a and 2c

The compounds **2a** and **2c** were thoroughly studied in solution by our research group, which confirmed the instability of compounds with the OBA moiety in an aqueous medium (Anna De Falco, 2017). In fact, in the electronic spectrum in 1% DMSO/acetate buffer mixture (pH 4.5) (Figure 47A and 47B), it is possible to observe intraligand transitions centered at 302 and 342 nm for compound **2a** (at 302 and 334 nm for **2c,** Figure 48A and 48B) and, over the course of 12 hours, a drastic decrease in the absorption of the hydrazone in Figure 49A for compound **2a** (Figure 50A for compound **2c**). In both spectra, it is also possible to notice the appearance of a new band, at 268 nm for **2a** and 263 nm for **2c (**Figure 49B and 50B, respectively) related to the hydrolysis product of the aldehyde, in agreement with what was previously reported by us.

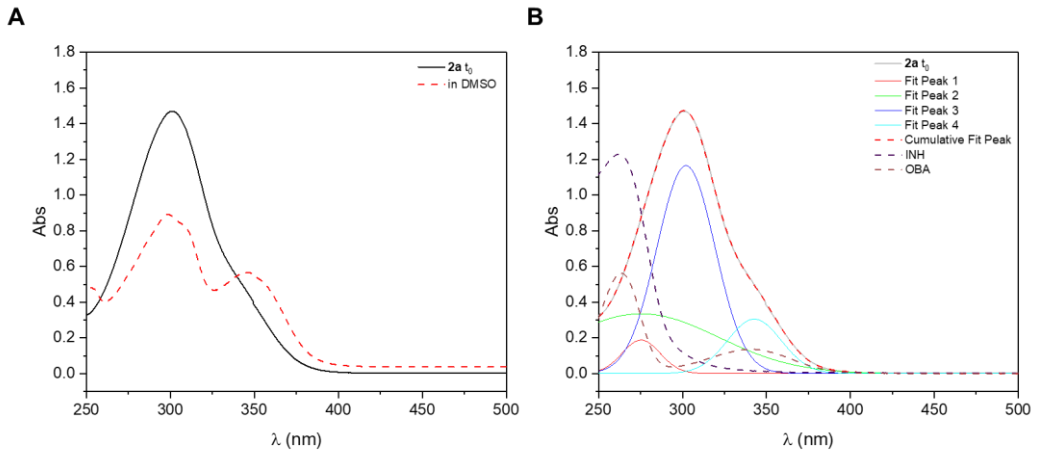

Figure 47. Electronic absorption spectra in selected wavelength regions for a 5×10^{-5} mol L^{-1} solution of **2a**. (**A**) Spectra measured at t_0 in 1% DMSO/acetate buffer mixture, pH 4.5 (black solid curve) and in pure DMSO (red dotted curve). (**B**) Gaussian fitting of the bands in the spectrum at t_0, along with the spectra of precursors INH and OBA. Deconvolution was performed with Origin software.

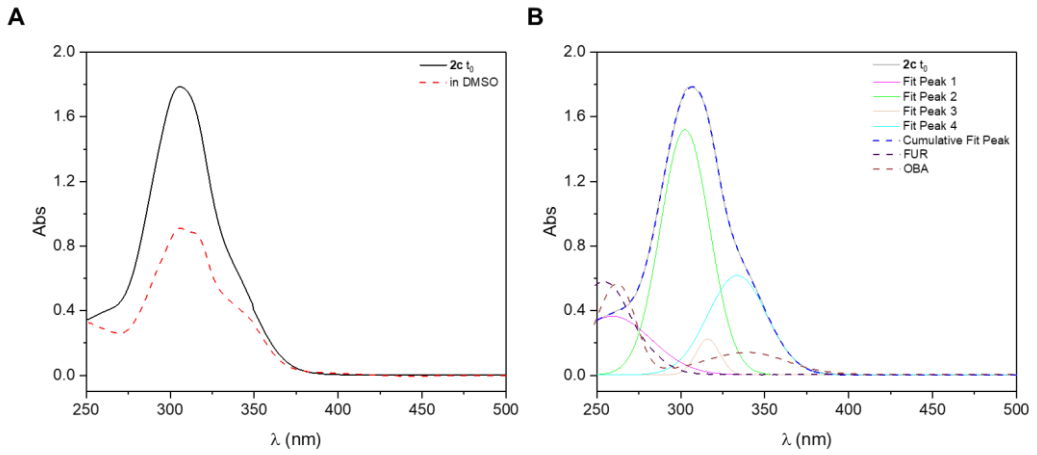

Figure 48. Electronic absorption spectra in selected wavelength regions for a 5×10^{-5} mol L^{-1} solution of **2c**. (**A**) Spectra measured at t_0 in 1% DMSO/acetate buffer mixture, pH 4.5 (black solid curve) and in pure DMSO (red dotted curve). (**B**) Gaussian fitting of the bands in the spectrum at t_0, along with the spectra of precursors FUR and OBA. Deconvolution was performed with Origin software.

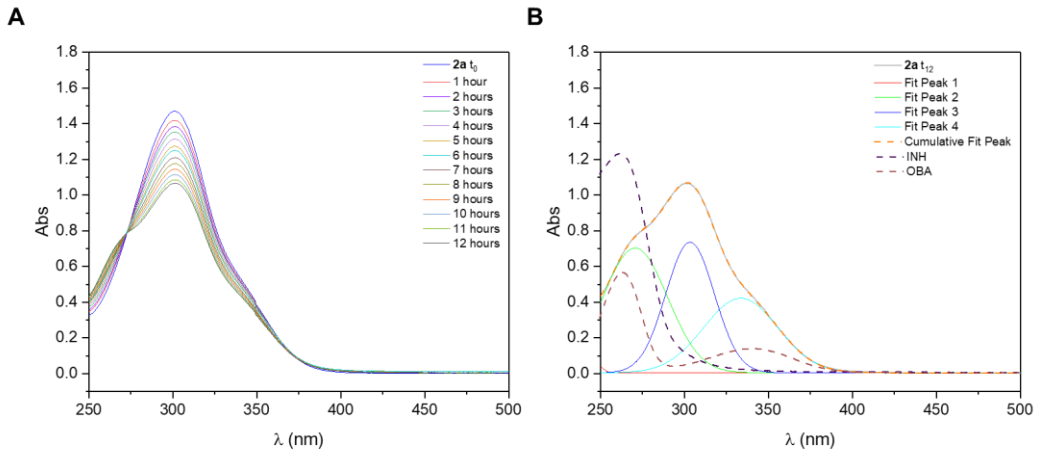

Figure 49. Electronic absorption spectra in selected wavelength regions for a 5×10^{-5} mol L^{-1} solution of **2a**. (**A**) Spectra measured at t_0 and after 12h in 1% DMSO/acetate buffer mixture, pH 4.5. (**B**) Gaussian fitting of the bands in the spectrum at t_{12}, along with the spectra of precursors INH and OBA. Deconvolution was performed with Origin software.

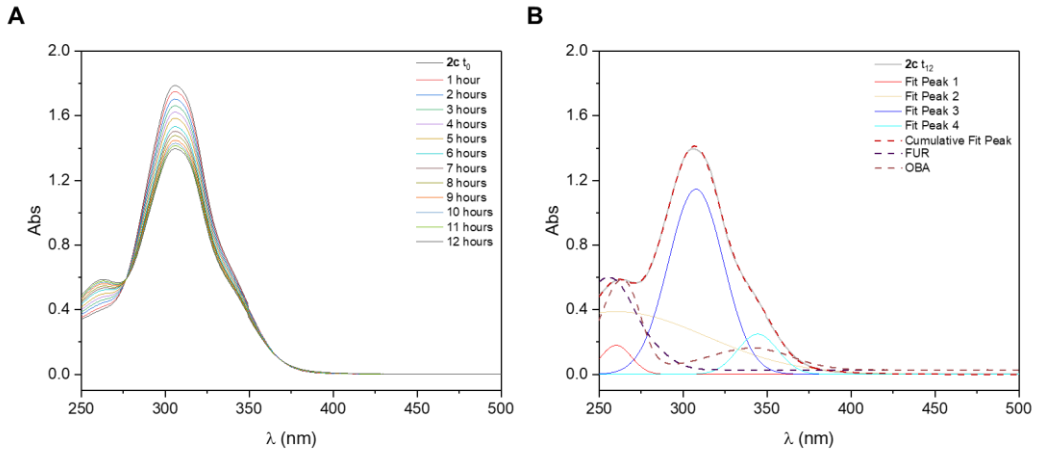

Figure 50. Electronic absorption spectra in selected wavelength regions for a 5×10^{-5} mol L^{-1} solution of **2c**. (**A**) Spectra measured at t_0 and after 12h in 1% DMSO/acetate buffer mixture, pH 4.5. (**B**) Gaussian fitting of the bands in the spectrum at t_{12}, along with the spectra of precursors FUR and OBA. Deconvolution was performed with Origin software.

The profile of both compounds in 1% DMSO/HEPES buffer, pH 7.4 (Figure 51A and Figure 52A), is similar to the unhydrolyzed profile at pH 4.5, with two absorptions centered at 302 and 342 nm (individually, 24.560 ± 134 and 10.278 ± 65 L mol^{-1} cm^{-1}) for **2a** and at 302 nm and 334 nm (32.000 ± 405 and 14.471 ± 248 L mol^{-1} cm^{-1}) for **2c** (Figure 51B and Figure 52B, respectively). Also, for both, these bands appear better defined in 100% DMSO medium.

Under these conditions, the compounds showed high stability in aqueous media, as can be seen in Figures 53A and 54A. The deconvolution of the bands is shown in Figures 53B and 54B.

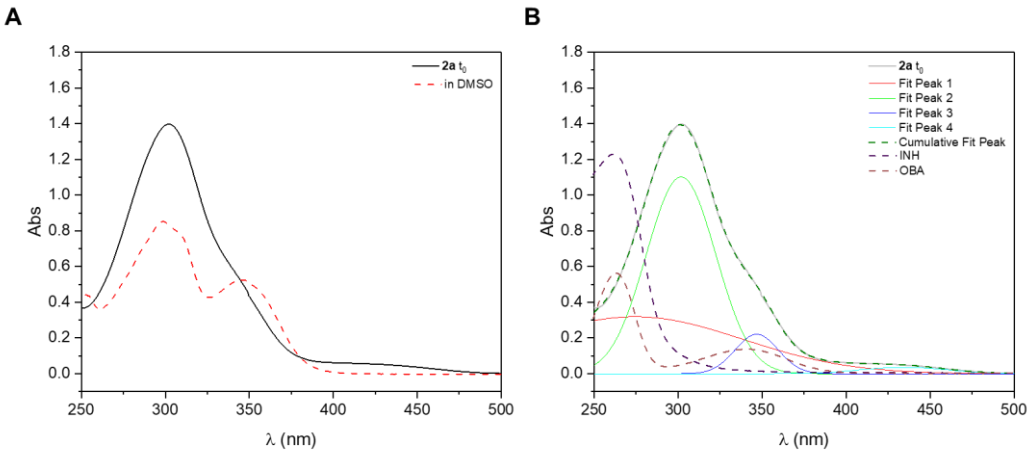

Figure 51. Electronic absorption spectra in selected wavelength regions for a 5×10^{-5} mol L^{-1} solution of **2a**. (**A**) Spectra measured at t_0 in 1% DMSO/HEPES buffer mixture, pH 7.4 (black solid curve) and in pure DMSO (red dotted curve). (**B**) Gaussian fitting of the bands in the spectrum at t_0**,** along with the spectra of precursors INH and OBA. Deconvolution was performed with Origin software.

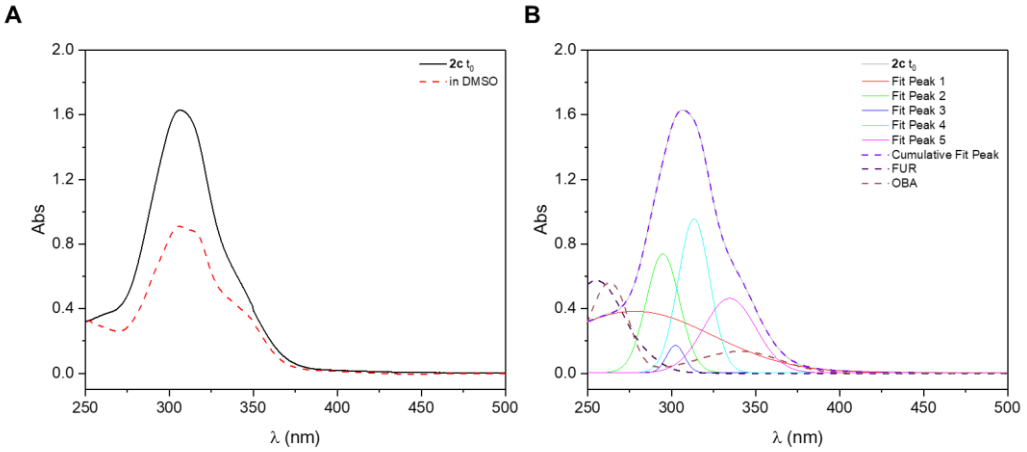

Figure 52. Electronic absorption spectra in selected wavelength regions for a 5×10^{-5} mol L^{-1} solution of **2c**. (**A**) Spectra measured at t_0 in 1% DMSO/HEPES buffer mixture, pH 7.4 (black solid curve) and in pure DMSO (red dotted curve). (**B**) Gaussian fitting of the bands in the spectrum at t_0**,** along with the spectra of precursors FUR and OBA. Deconvolution was performed with Origin software.

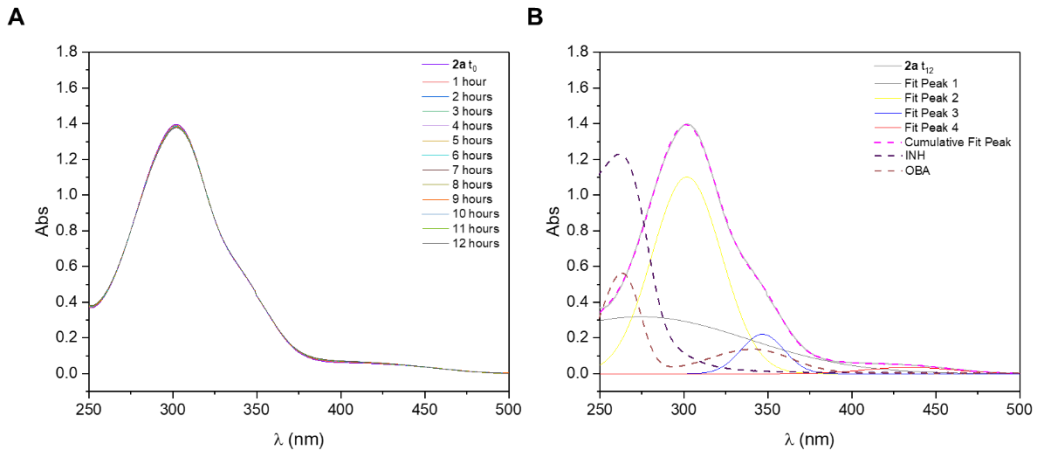

Figure 53. Electronic absorption spectra in selected wavelength regions for a 5×10^{-5} mol L^{-1} solution of **2a**. (**A**) Spectra measured at t_0 and after 12h in 1% DMSO/HEPES buffer mixture, pH 7.4. (**B**) Gaussian fitting of the bands in the spectrum at t_{12}, along with the spectra of precursors INH and OBA. Deconvolution was performed with Origin software.

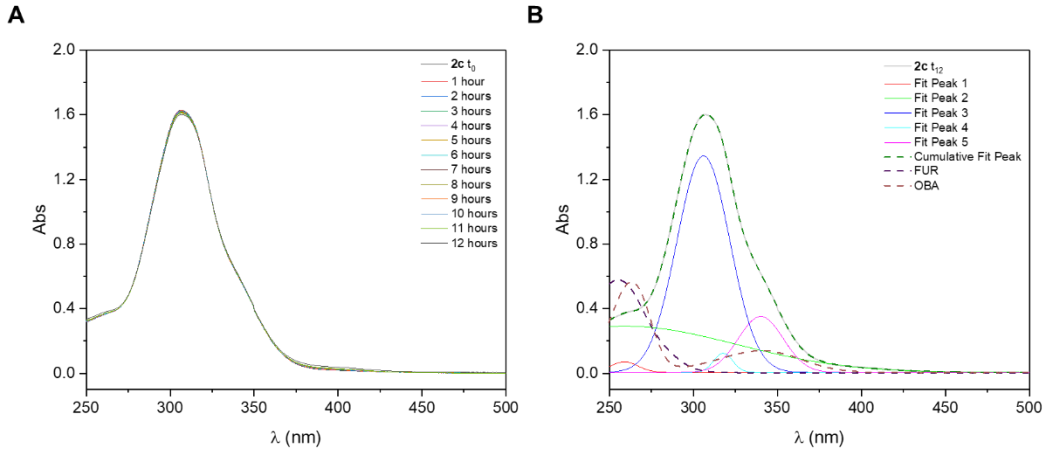

Figure 54. Electronic absorption spectra in selected wavelength regions for a 5×10^{-5} mol L^{-1} solution of **2c**. (**A**) Spectra measured at t_0 and after 12h in 1% DMSO/HEPES buffer mixture, pH 7.4. (**B**) Gaussian fitting of the bands in the spectrum at t_{12}, along with the spectra of precursors INH and OBA. Deconvolution was performed with Origin software.

5.4.5. Compound 3a

The t_0 absorption spectrum of **3a** in the rich aqueous medium at pH 4.5 (Figure 55A) shows a multicomponent band and a shoulder centered, correspondingly, at 291 (20,900 ± 280 L mol^{-1} cm^{-1}) and 333 nm (11,700 ± 150 L mol^{-1} cm^{-1}). The gaussian component at 291 nm and the very low intensity component at 306 nm have no association with the absorptions of the INH and MBA precursor profiles, so these bands were assigned exclusively to hydrazone-centered

transitions. The absorption at 333 nm was related to MBA ring transitions by comparison with the spectrum of this precursor under the proposed experimental conditions (dotted brown curve in Figure 55B).

The spectrum of **3a** in 1% DMSO/HEPES buffer mixture (pH 7.4) (Figure 56A), shows a band of greater intensity at 292 (20,940 ± 396 L mol^{-1} cm^{-1}) and a shoulder at 336 nm (11,438 ± 206 L mol^{-1} cm^{-1}), also related to contributions from the hydrazone and the MBA aldehyde derivative (Figure 56B). No significant changes were observed in the absorption bands of **3a** in pure DMSO (same concentration) when compared to **3a** in a rich aqueous medium. In this case, only the hypochromic effect of DMSO was observed, caused by changes in the intramolecular interactions between the solute and the solvent.

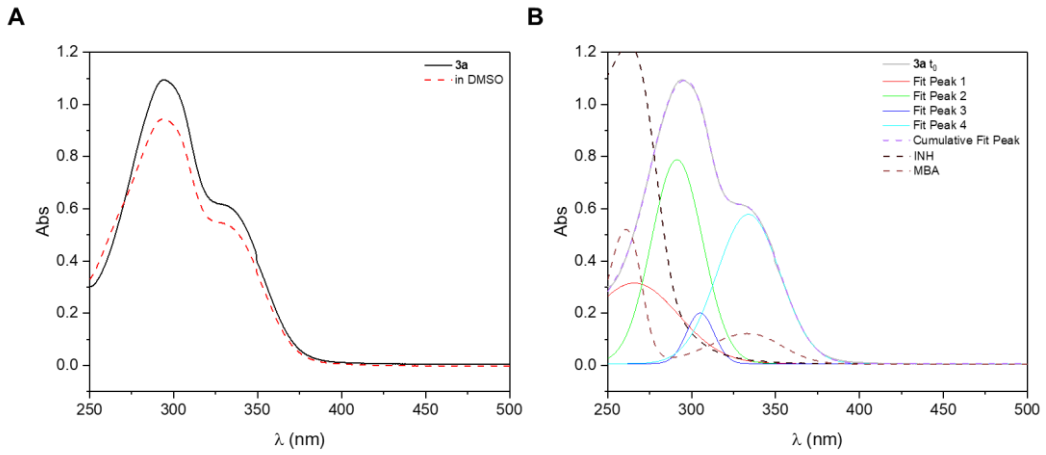

Figure 55. Electronic absorption spectra in selected wavelength regions for a 5×10^{-5} mol L^{-1} solution of **3a**. (**A**) Spectra measured at t_0 in 1% DMSO/acetate buffer mixture, pH 4.5 (black solid curve) and in pure DMSO (red dotted curve). (**B**) Gaussian fitting of the bands in the spectrum at t_0**,** along with the spectra of precursors INH and MBA. Deconvolution was performed with Origin software.

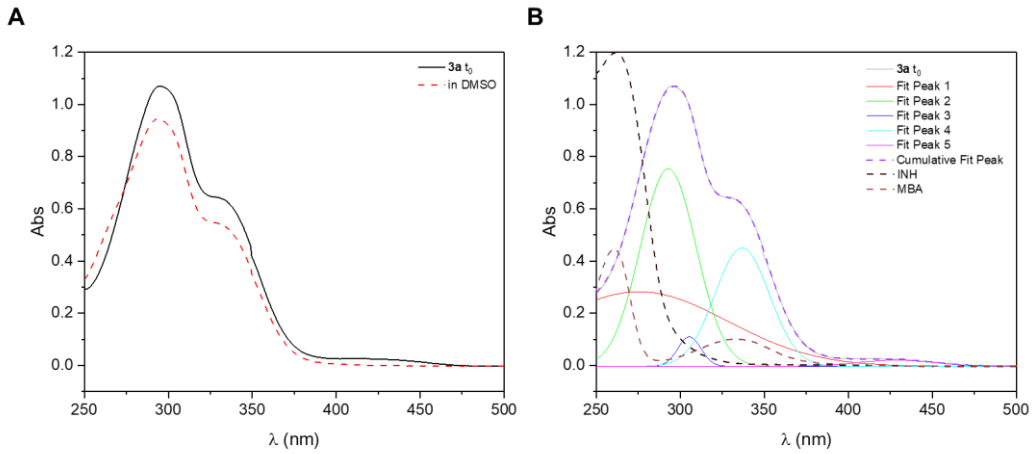

Figure 56. Electronic absorption spectra in selected wavelength regions for a 5×10^{-5} mol L^{-1} solution of **3a**. (**A**) Spectra measured at t_0 in 1% DMSO/HEPES buffer mixture, pH 7.4 (black solid curve) and in pure DMSO (red dotted curve). (**B**) Gaussian fitting of the bands in the spectrum at t_0, along with the spectra of precursors INH and MBA. Deconvolution was performed with Origin software.

No significant changes were observed in the **3a** spectra during the 12-hour follow-up study in solution at pH 7.4 (Figure 57A and 57B). In contrast, during the first 12 hours of the experiment in 1% DMSO/acetate buffer (pH 4.5), a 6% reduction in the absorbance of the main band (hydrazonic) was observed, accompanied by a slight increase at 261 nm (Figure 58A). The latter is probably related to the presence of the MBA precursor in equilibrium with **3a** (Figure 58B). Despite this, 94% of the compound remains unchanged in solution after the first 12 hours of monitoring, indicating that the compound is quite stable in a water-rich environment.

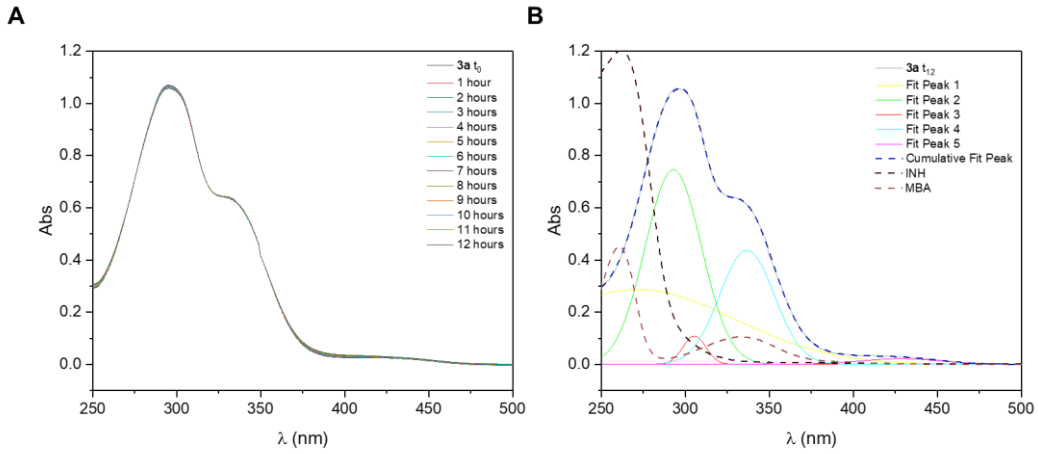

Figure 57. Electronic absorption spectra in selected wavelength regions for a 5×10^{-5} mol L^{-1} solution of **3a**. (**A**) Spectra measured at t_0 and after 12h in 1% DMSO/HEPES buffer mixture, pH 7.4. (**B**) Gaussian fitting of the bands in the spectrum at t_{12}, along with the spectra of precursors INH and MBA. Deconvolution was performed with Origin software.

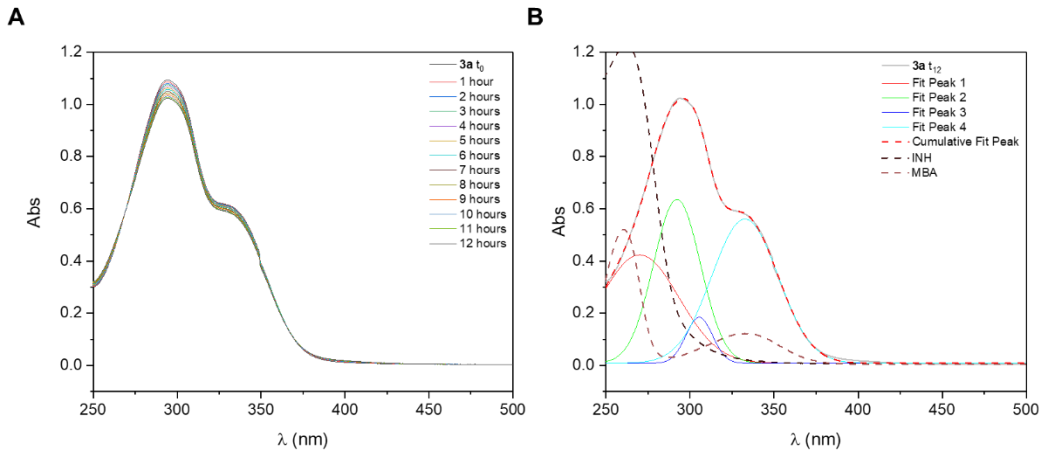

Figure 58. Electronic absorption spectra in selected wavelength regions for a 5×10^{-5} mol L^{-1} solution of **3a**. (**A**) Spectra measured at t_0 and after 12h in 1% DMSO/acetate buffer mixture, pH 4.5. (B) Gaussian fitting of the bands in the spectrum at t_{12}, along with the spectra of precursors INH and MBA. Deconvolution was performed with Origin software.

5.4.6. Compound 3b

In the 10% DMSO/acetate buffer mixture (pH 4.5) (Figure 59A), the compound **3b** shows two multicomponent absorptions centered at 297 (23.700 ± 160 L mol^{-1} cm^{-1}) and 335 nm (12,500 ± 80 L mol^{-1} cm^{-1}), which could be fitted to the sum of five gaussian bands. Of these, the one at 276 nm and that of very low intensity at 307 nm were tentatively assigned by comparison with the spectra of precursors to transitions mainly localized in the TMP ring. Nevertheless, a contribution of the phenol-containing MBA ring to the component at 276 nm cannot be ruled out. On the other hand, the constituent at 335 nm was attributed to transitions from MBA. Finally, the component at 297 nm possesses no correlates in the precursors' absorption profiles, being consequently assigned to the hydrazone moiety, meaning that it probably involves a transition delocalized throughout the molecule (i.e., electronic density moving from one ring to the other) (Figure 59B).

Under more physiological-like conditions (i.e., 10% DMSO/HEPES buffer, pH 7.4), the spectra of **3b** (Figure 60A) is very similar to that obtained in 10% DMSO solution/acetate buffer (pH 4.5), with a main band and a shoulder at 297 (20,700 ± 40 L mol^{-1} cm^{-1}) and 335 nm (10,000 ± 25 L mol^{-1} cm^{-1}), respectively (Figure 60B). For comparison purposes, a spectrum was recorded in pure DMSO (same concentration) and, although with much lower intensity, the profile observed was very similar to that of the aqueous medium.

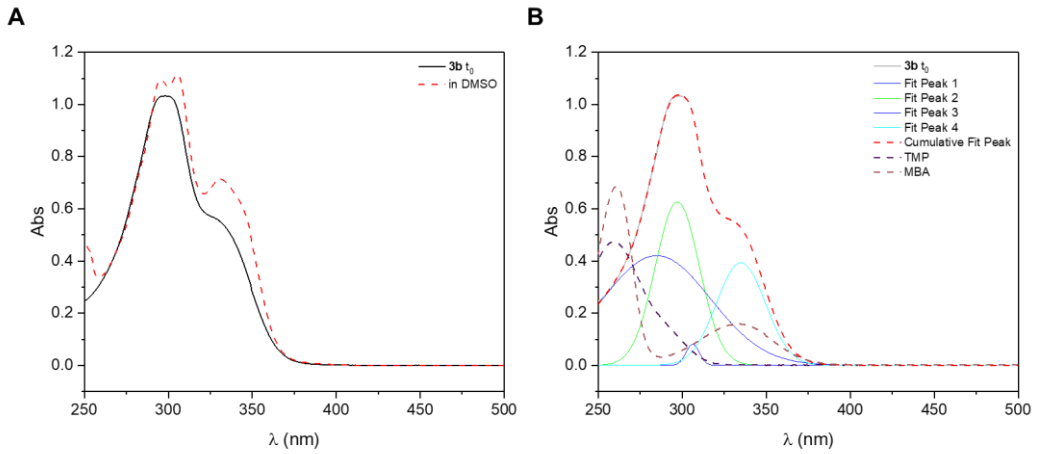

Figure 59. Electronic absorption spectra in selected wavelength regions for a 5×10^{-5} mol L^{-1} solution of **3b**. (**A**) Spectra measured at t_0 in 10% DMSO/acetate buffer mixture, pH 4.5 (black solid curve) and in pure DMSO (red dotted curve). (**B**) Gaussian fitting of the bands in the spectrum at t_0, along with the spectra of precursors TMP and MBA. Deconvolution was performed with Origin software.

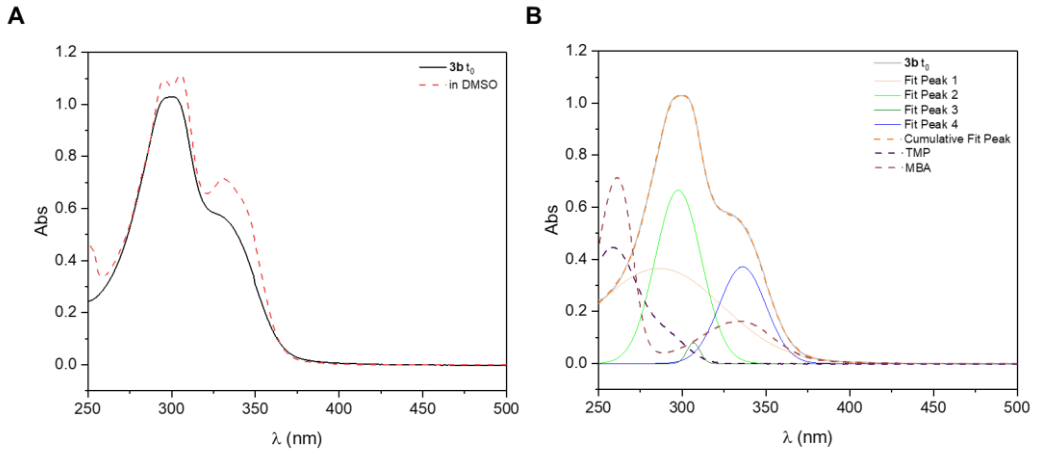

Figure 60. Electronic absorption spectra in selected wavelength regions for a 5×10^{-5} mol L_{-1} solution of **3b**. (**A**) Spectra measured at t_0 in 10% DMSO/HEPES buffer mixture, pH 7.4 (black solid curve) and in pure DMSO (red dotted curve). (**B**) Gaussian fitting of the bands in the spectrum at t_0, along with the spectra of precursors TMP and MBA. Deconvolution was performed with Origin software.

Compound **3b** showed high stability in more physiological-like conditions (i.e. 10% DMSO/HEPES buffer, pH 7.4) (Figure 61A and 61B). On the other hand, a decrease of around 11% in the absorbance of the compound's main band was observed in the first 12 hours of the experiment in 10% DMSO/acetate buffer solution (pH 4.5) (Figure 62A). In this interval, the formation of an isosbestic point at 268 nm was observed, indicating the presence of two absorbing species in solution. The slight increase in absorption at 259 nm suggests the presence of an equilibrium between the hydrazone and the free MBA precursor, assigned by

comparison (Figure 62B). Despite the decrease in absorbance, around 89% of the compound was kept in solution, indicating the high stability of **3b** in aqueous media.

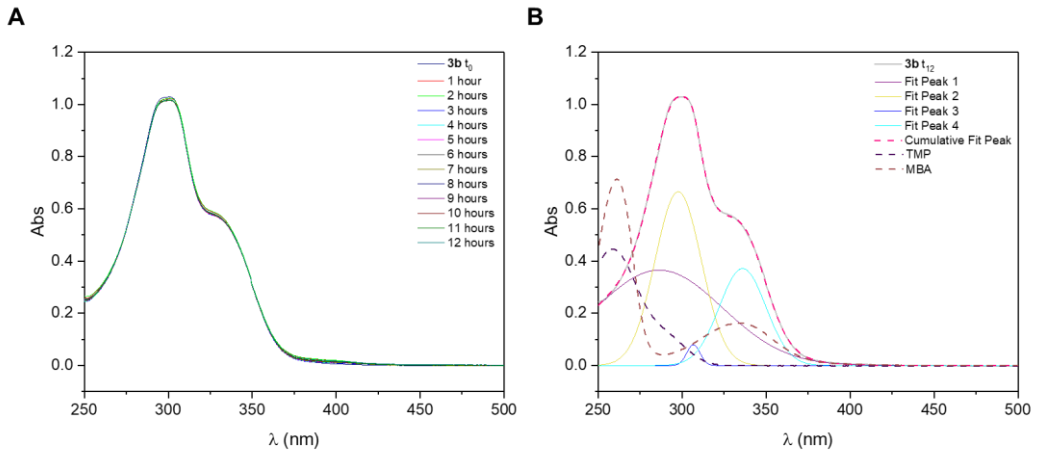

Figure 61. Electronic absorption spectra in selected wavelength regions for a 5×10^{-5} mol L^{-1} solution of **3b**. (**A**) Spectra measured at t_0 and after 12h in 10% DMSO/HEPES buffer mixture, pH 7.4. (**B**) Gaussian fitting of the bands in the spectrum at t_{12}, along with the spectra of precursors TMP and MBA. Deconvolution was performed with Origin software.

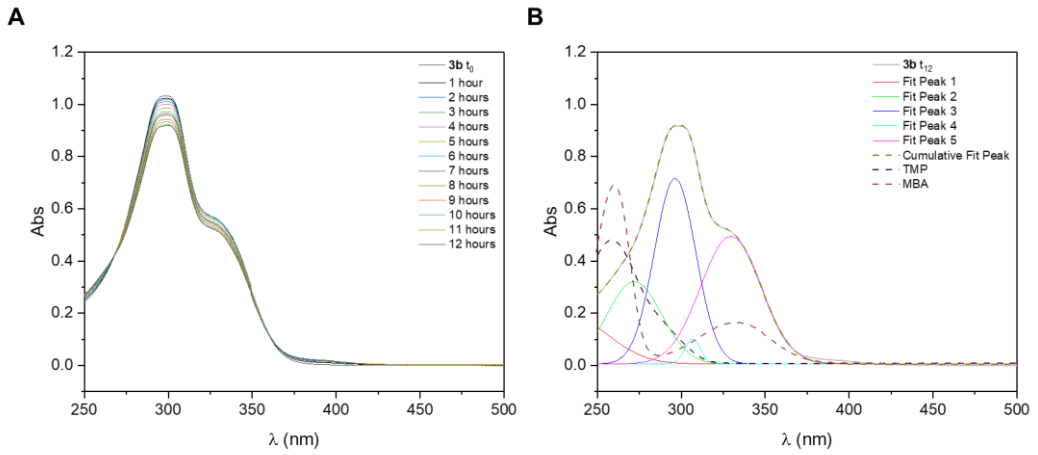

Figure 62. Electronic absorption spectra in selected wavelength regions for a 5×10^{-5} mol L^{-1} solution of **3b**. (**A**) Spectra measured at t_0 and after 12h in 10% DMSO/acetate buffer mixture, pH 4.5. (**B**) Gaussian fitting of the bands in the spectrum at t_{12}, along with the spectra of precursors TMP and MBA. Deconvolution was performed with Origin software.

5.4.7. Compounds 5a and 5c

The UV-Vis spectrum of **5a** shown in Figure 63A is composed of a multiple absorption that displays two apparent bands at 294 (21.500 ± 224 L mol^{-1} cm^{-1}) and 335 nm (11.600 ± 85 L mol^{-1} cm^{-1}), which can be completely fitted to the sum of three Gaussian curves. The Gaussian component at 335 nm was attributed to a protonated CBA transition by comparison with the spectrum of this precursor at pH

4.5 (Figure 63B, dotted brown curve). The components at 294 nm (intense absorption) and 305 nm are not similar to the precursor spectra and have therefore been attributed to a process involving hydrazone, probably related to a delocalized transition throughout the molecule. The spectra in DMSO of both compounds were also recorded and are included in Figure 63A for comparison purposes.

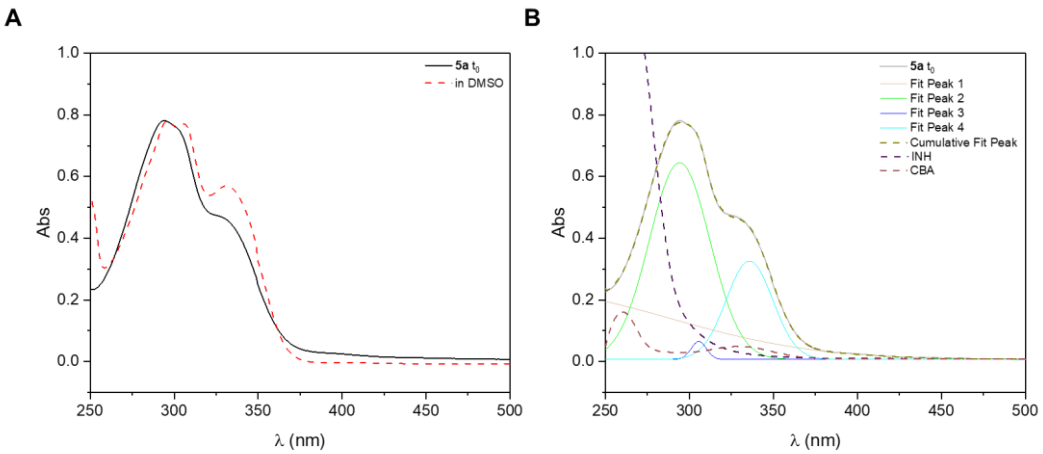

Figure 63. Electronic absorption spectra in selected wavelength regions for a 5×10^{-5} mol L^{-1} solution of **5a**. (**A**) Spectra measured at t_0 in 10% DMSO/acetate buffer mixture, pH 4.5 (black solid curve) and in pure DMSO (red dotted curve). (**B**) Gaussian fitting of the bands in the spectrum at t_0, along with the spectra of precursors INH and CBA. Deconvolution was performed with Origin software.

The electronic spectrum of compound **5c**, in the rich aqueous medium at pH 4.5 (Figure 64A), shows three absorptions centered at 301 (23.470 ± 530 L mol^{-1} cm^{-1}) and 308 nm (24,900 ± 562 L mol^{-1} cm^{-1}) and 334 nm (14,546 ± 338 L mol^{-1} cm^{-1}, attributed to intra-ligand $\pi\rightarrow\pi^*$ transitions due to the high molar absorptivity value. In addition, the Gaussian fit revealed a component at 305 nm which was mainly attributed to electronic transitions involving the CBA fragment (Figure 64B).

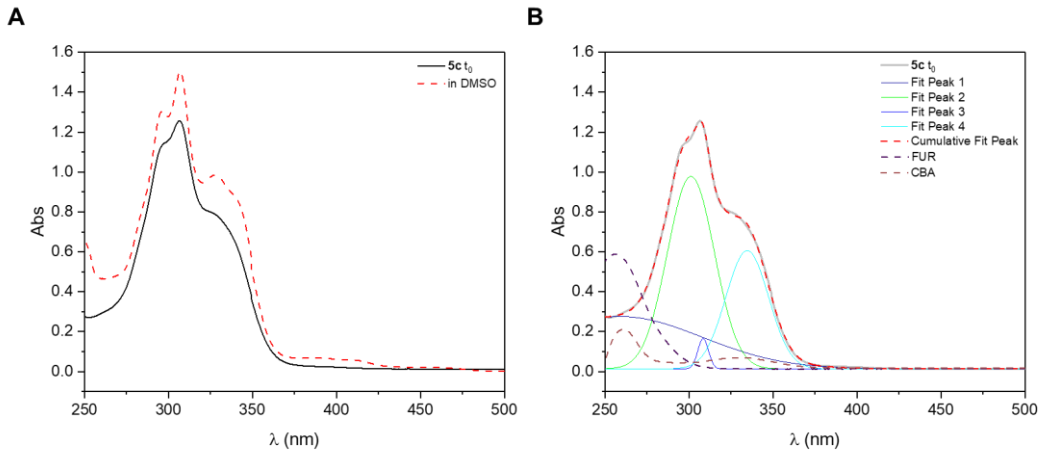

Figure 64. Electronic absorption spectra in selected wavelength regions for a 5×10^{-5} mol L^{-1} solution of **5c**. (**A**) Spectra measured at t_0 in 10% DMSO/acetate buffer mixture, pH 4.5 (black solid curve) and in pure DMSO (red dotted curve). (**B**) Gaussian fitting of the bands in the spectrum at t_0, along with the spectra of precursors FUR and CBA. Deconvolution was performed with Origin software.

During the 12-hour follow-up study in a more acidic aqueous medium (pH 4.5), **5a** showed a slight reduction in the absorbance of the hydrazone band (294 nm) (Figure 65A). As a result, a lower energy band appeared at 268 nm, related to the CBA precursor by comparison (dotted brown curve in Figure 65B). A similar behavior can be observed for **5c** in this same interval, showing an 8% decrease in absorbance in the band at 308 nm, as can be seen in Figure 66A. Gaussian fitting of the bands in the spectrum at t12, along with the spectra of precursors FUR and CBA in Figure 66B. Despite this, more than 92% of the absorbance of the main band was maintained for both compounds. This observation suggests that the compounds have a high degree of stability in acidic aqueous medium.

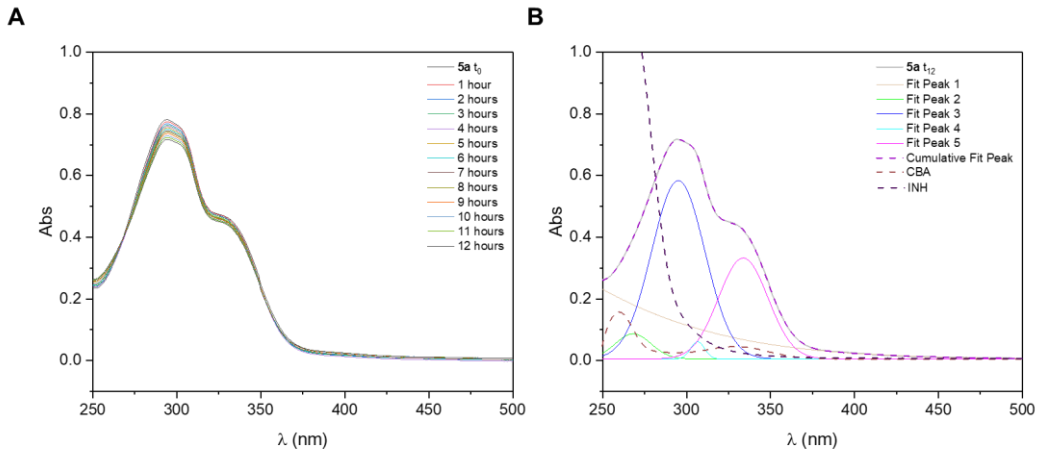

Figure 65. Electronic absorption spectra in selected wavelength regions for a 5×10^{-5} mol L^{-1} solution of **5a**. (**A**) Spectra measured at t_0 and after 12h in 10% DMSO/acetate buffer mixture, pH 4.5. (**B**) Gaussian fitting of the bands in the spectrum at t_{12}, along with the spectra of precursors INH and CBA. Deconvolution was performed with Origin software.

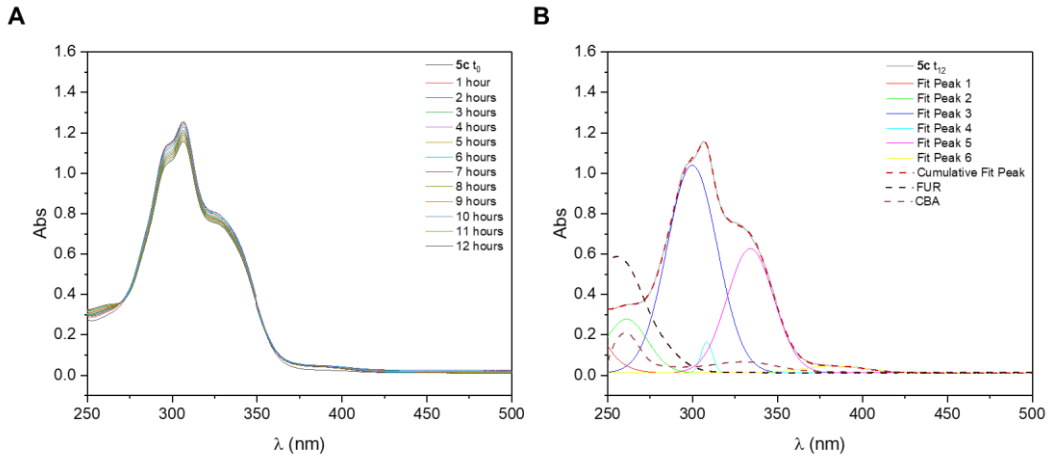

Figure 66. Electronic absorption spectra in selected wavelength regions for a 5×10^{-5} mol L^{-1} solution of **5c**. (**A**) Spectra measured at t_0 and after 12h in 10% DMSO/acetate buffer mixture, pH 4.5. (**B**) Gaussian fitting of the bands in the spectrum at t_{12}, along with the spectra of precursors FUR and CBA. Deconvolution was performed with Origin software.

A particular feature was observed in the profile of compounds **5a** and **5c** under more physiological-like conditions (i.e., 10% DMSO/HEPES buffer, pH 7.4) (Figure 67A and 67B). A new absorption around 400 nm was identified for both compounds, associated with the deprotonation of the phenolic portion present in the structures. For this reason, the absorption patterns of both compounds were analyzed individually for the fully protonated and deprotonated states, using solutions containing 10% DMSO/buffer solutions (acetate, PBS or HEPES) at different pH values, in the range of 3.8 to 9.0.

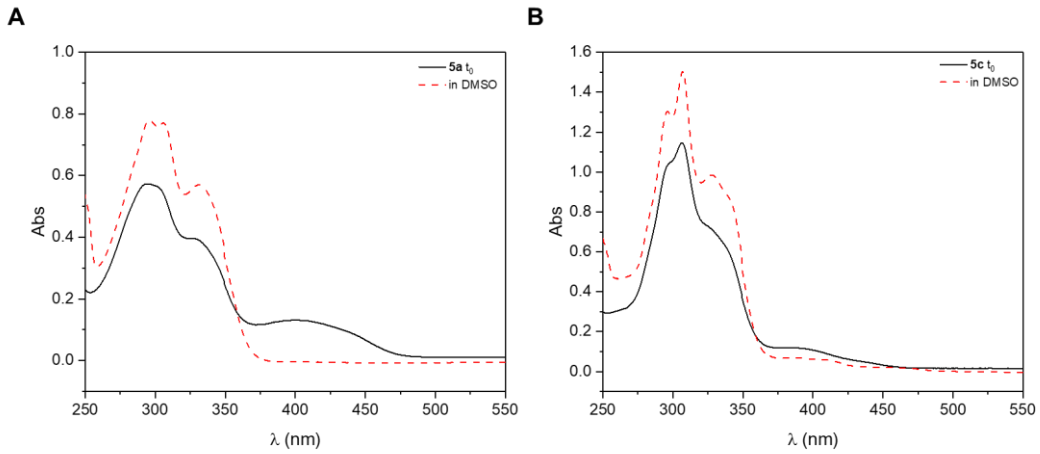

Figure 67. Electronic absorption spectra in selected wavelength regions for a 5×10^{-5} mol L^{-1} solution. (**A**) Spectra measured of **5a** at t_0 in 10% DMSO/HEPES buffer mixture, pH 7.4 (black solid curve) and in pure DMSO (red dotted curve). (**B**) Spectra measured of **5c** at t_0 in 10% DMSO/HEPES buffer mixture, pH 7.4 (black solid curve) and in pure DMSO (red dotted curve).

For a more specific investigation, the absorption patterns of compounds **5a** and **5c** fully protonated and deprotonated with phenol were examined individually. For **5a** we selected the profile at pH 3.8 and 9.0, while for **5c** we analyzed the profiles at pH 3.8 and 8.2, since for the latter we observed a second process referring to the deprotonation of amide NH starting between pH 8.6 and 9.0.

When protonated (pH 3.8), the spectrum of **5a** and **5c** is very similar to that observed in the experiment in 10% DMSO/acetate buffer, pH 4.5 (Figures 68A and Figure 69A). The change in profile, in other words the deprotonation of phenol into phenolate, begins to be observed around pH 4.2 for **5a** (pH 4.6 for **5c**), with a subtle increase in absorbance between 375 and 500 nm (375 and 450 nm for **5c**), and both reach their maximum intensity at pH 8.2.

In the complete deprotonation profile of **5a** (i.e.; pH 9.0, Figure 68B), five apparent bands were observed, namely: 289, 316, 327, 343 and 400 nm. The bands at 316 and 327 nm were proposed as processes involving the hydrazone portion displaced by the formation of the enolate, while the bands at 289 and 343 nm were inferred as contributions from the CBA portion, since they can also be observed in the deprotonated precursor (dark yellow dashed curve).

For the deprotonated profile of **5c** (i.e.; pH 8.2, Figure 69B), three apparent bands were observed at 306, 343 and 385 nm, in a complex system containing 7 Gaussian components. We propose that the contributions observed in the band centered at 306 nm come from an overlap of bands referring to transitions of both

the aldehyde ring and the hydrazone portion. In addition, the absorption at 343 nm was suggested as a contribution from the batochromically shifted hydrazone band to the deprotonation of the compound, with small contributions from the aldehyde portion. Finally, by comparison, we infer that the intense absorption at 385 nm is related to contributions from the deprotonated CBA ring (dotted dark yellow curve).

By graphing the absorbance at the maximum point (λmax) as a function of varying pH values and then employing a sigmoidal curve fitting procedure (as shown in Figure 68C, *inset*), we determined an apparent pKa value of 6.07 ± 0.02 for compound **5a** (6.25 ± 0.02 for **5c**, Figure 69C, *inset*), which means that, under the physiological conditions used in the stability study, both compounds are completely deprotonated, which can impair their BBB-crossing abilities. Despite this peculiarity, both compounds were stable.

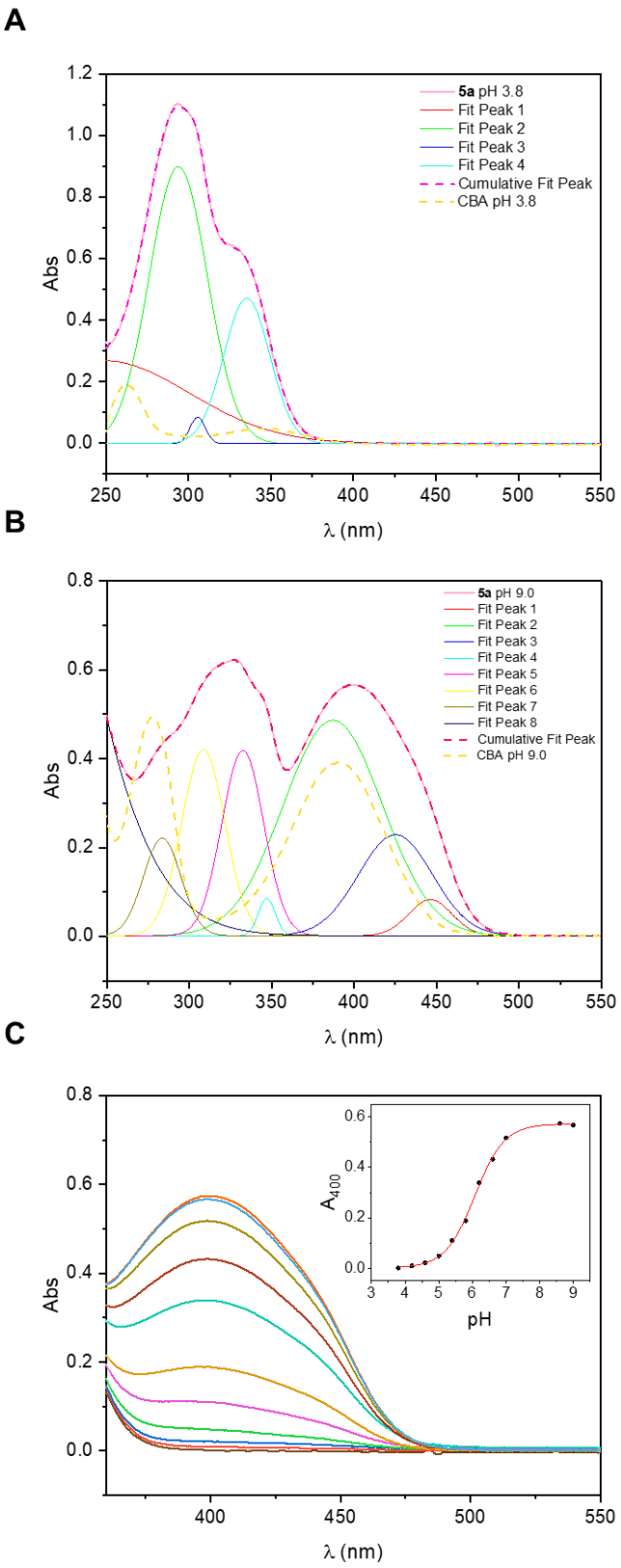

Figure 68. Electronic absorption spectra in selected wavelength regions for a 5×10^{-5} mol L^{-1} solution of **5a**. (**A**) Gaussian fitting of the bands in a solution of the hydrazone in 10% DMSO/acetate buffer (pH 3.8) and (**B**) 10% DMSO/HEPES buffer (pH 9.0). Deconvolution was performed with Origin software. (**C**) Deprotonation band centered at 400 nm, measured in different 10% DMSO/buffer mixtures (pH range from 3.8 to 9.0). *Inset*: A_{400} versus pH with sigmoidal fitting.

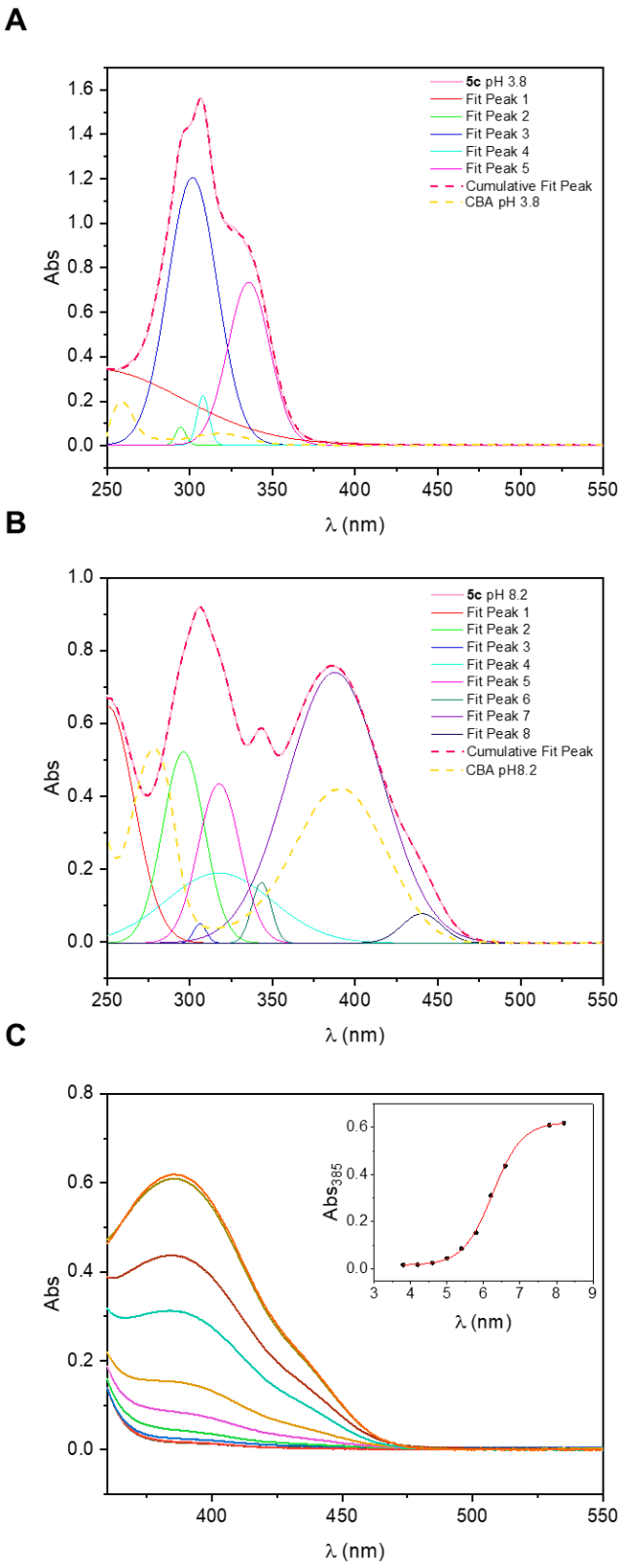

Figure 69. Electronic absorption spectra in selected wavelength regions for a 5×10^{-5} mol L^{-1} solution of **5c**. (**A**) Gaussian fitting of the bands in a solution of the hydrazone in 10% DMSO/acetate buffer (pH 3.8) and (**B**) 10% DMSO/HEPES buffer (pH 8.2). Deconvolution was performed with Origin software. (**C**) Deprotonation band centered at 385 nm, measured in different 10% DMSO/buffer mixtures (pH range from 3.8 to 8.2). *Inset*: A_{385} versus pH with sigmoidal fitting.

5.5. Influence of the substituent on the stability

Structurally, the hydroxyl group plays an important role as a strong electron donor, forming an intramolecular hydrogen bond with the azomethine nitrogen of the hydrazone. This has two main effects, the first being related to the stabilization of the hydrazone formed, restricting its conformation by steric and electronic effects. The second is related to the more basic character attributed to azomethine due to the intramolecular O1-H1···N1 interaction, which causes this nitrogen to retain its electronic density. Thus, the double bond between C7=N1 is more polarized, which makes the azomethine carbon susceptible to nucleophilic attack by a solvent molecule as described above.

Besides the fact that the experimental pKa values (Table 17, spectra in Appendix Figure A47-A55) were within the expected range for the structures derived from salicialdehyde (Liu *et al.*, 2016), it was noted that *meta* position substitutions also exert a strong influence on the degradation of these compounds.

Table 17. Experimental pKa values of the *N*-acylhydrazones studied.

Compound	λ_{abs}/nm	experimental pK_a
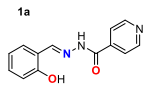	400	7.61 ± 0.05
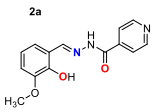	406	7.51 ± 0.01
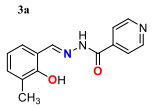	418	7.62 ± 0.03
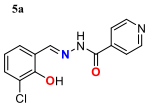	400	6.07 ± 0.02
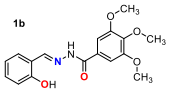	380	8.46 ± 0.07
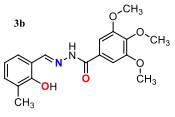	400	8.79 ± 0.06

Table 17. Experimental pKa values of the *N*-acylhydrazones studied.

Compound	λ_{abs}/nm	experimental pK_a
1c 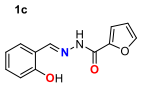	390	8.42 ± 0.05
2c 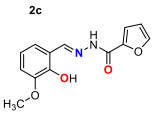	393	8.15 ± 0.07
5c 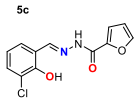	385	6.25 ± 0.02

For structures without substituents in position 3, we would expect intermediate stability for the compounds formed, since the presence of the -OH group in position 2 may favor the formation of hydrazone through intramolecular interactions, stabilizing the conformation, but may also induce tautomerism under certain experimental conditions. However, the results showed low stability in solution, with hydrolysis greater than 15%, indicating that, in these cases, the factors leading to instability are predominant.

For methyl-substituted compounds (3-Me), the slight increase in the electronic density of the carbonyl carbon facilitates the hydrazone formation reaction and the system is additionally stabilized by hyperconjugation. This is probably why 3-Me derivatives showed great stability under the experimental conditions used.

The experimental results showed that substituted 3-OMe compounds are more unstable than 3-H and 3-Me, with absorption reductions of more than 20% in 12 hours of experimentation. Although the methoxy group is a strong electron donor by resonance, in the meta position the inductive effect of electron withdrawal is predominant. This effect removes the electron density from the carbonyl carbon, making the aldehyde precursor more electrophilic and, consequently, more reactive to nucleophilic attack. However, the stability of the final product is thermodynamically dependent. It is likely that the electron-donating nature of the methoxy group increases the electron density around the C=N bond of the formed hydrazone, making it more basic and therefore more susceptible to reverse hydrolysis.

Unlike compounds with electron-donating groups (such as 3-Me or 3-OMe), in compounds substituted at 3-Cl, the predominant effect is the withdrawal of electrons by chlorine. This not only increases the electrophilicity of the carbonyl carbon, making the aldehyde precursor more reactive, but also makes the final product, the hydrazone, less susceptible to reverse hydrolysis. In this sense, it is expected that the withdrawal of electrons by chlorine decreases the electron density of the azomethine bond, making it less basic and less prone to protonation. Since reverse hydrolysis depends on this protonation, the lower basicity of the C=N bond hinders the process, resulting in a more stable compound in solution. Additionally, for these structures, the modulation of reactivity and the stabilizing role of the hydroxyl was fundamental in obtaining compounds with high stability in solution.

Finally, based on the compounds' behavior in solution, only four compounds (Figure 70) proved suitable for the step involving binding properties to Al^{3+} ions.

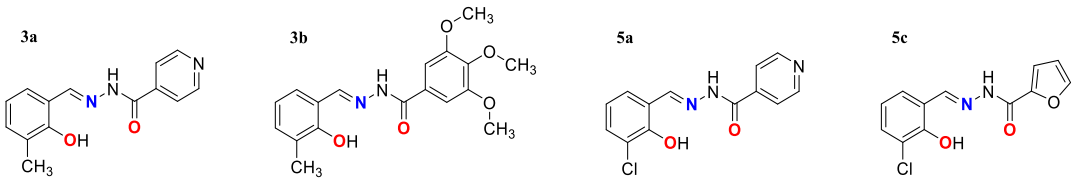

Figure 70. Structures of 2-hydroxy-3-methylbenzaldehyde isonicotinoyl hydrazone (**3a**), 2-hydroxy-3-methylbenzaldehyde-3,4,5-trimethoxybenzoyl hydrazone (**3b**), 3-chloro-2-hydroxybenzaldehyde isonicotinoyl hydrazone (**5a**) and 3-chloro-2-hydroxybenzaldehyde-2-furoyl hydrazone (**5c**). The potential coordination atoms are highlighted in color.

6. Cytotoxicity in eukaryotic cell models

6.1. Cytotoxicity in *Saccharomyces cerevisiae* cell line

In initial tests, *Saccharomyces cerevisiae* cells were exposed to increasing percentages of DMSO, which is the chosen vehicle for cytotoxicity assay in cells, to evaluate its effect and tolerance limits in this cell line. The studies were carried out considering increasing concentration of the vehicle (0.5 to 12 %) in solution. For the negative control, ultra-pure water was used, while H_2O_2 served as the sensitivity control.

After 24 hours of incubation, a marked decrease in cell viability was observed following exposure to 8% DMSO onwards (Figure 71). The calculated

half-maximal inhibitory concentration (IC_{50}) for *Saccharomyces cerevisiae* was 7.7 ± 0.10 DMSO, with a coefficient of determination (R^2) of 0.9994.

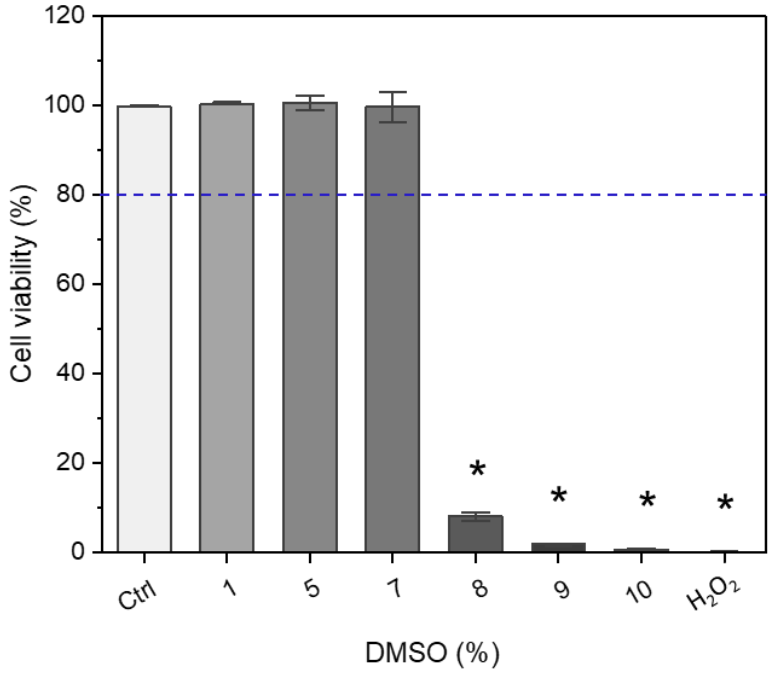

Figure 71. Toxicity profile of exposure to selected concentrations of DMSO in *Saccharomyces cerevisiae* cells. The mean standard deviation is shown and results have been normalized relative to the positive control. Symbol (*) represents a statistical differen in relation to the control, with $p < 0.05$. Hydrogen peroxide was included as a positive control since it kills almost all the cells at 15%.

As previously mentioned, due to the low solubility of the compounds in aqueous media, it was necessary to use a percentage of organic solvent for studies in solution. In this work we chose DMSO as the solvent based on previous data obtained in our research group (Helena *et al*., 2024b). However, from the point of view of drug development, the need for high volumes of organic solvent represents a major pharmacological limitation regarding solubility in water-rich media. In addition, the need to use 10% DMSO to solubilize compounds **3b**, **5a** and **5c**, even at low concentrations, presented an experimental obstacle due to the high cytotoxicity observed in the previous experiment and, for these reasons, these compounds were eliminated from this study.

Compound **3a** was evaluated for its cytotoxicity against the *Saccharomyces cerevisiae* cell line, in a 1% DMSO-containing vehicle solution. The data obtained was normalized by the vehicle-treated group in order to assess the cytotoxic effect of the compound on the cell line, regardless of the impact of the vehicle. The

toxicity of compound **3a** was found to be statistically significant only at very high concentrations (1000 µmol L^{-1}) (Figure 72), suggesting that, *in vivo*, at the expected active doses, this compound will not show intrinsic toxicity. Therefore, it was not possible to calculate the IC_{50}, as higher concentrations would be needed to do so.

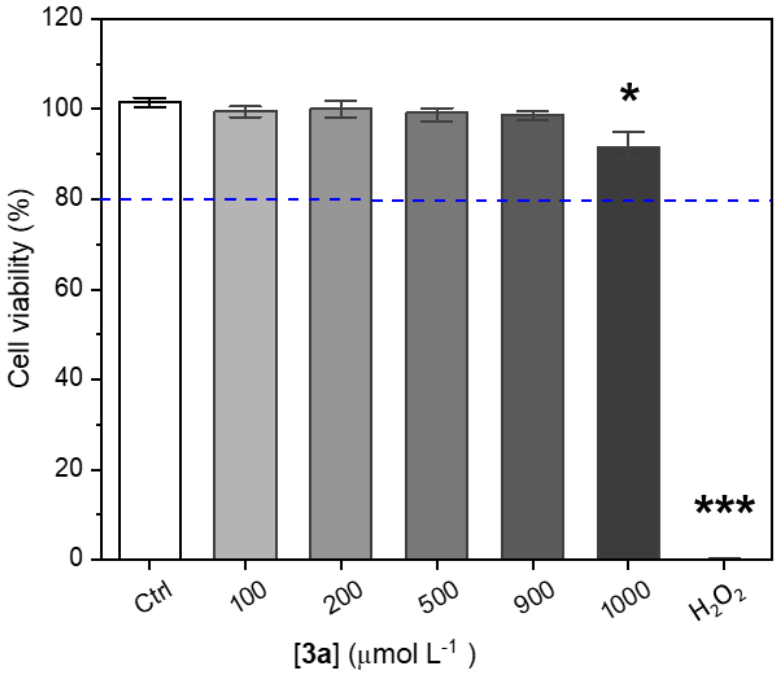

Figure 72. Cytotoxic effects of **3a** on *Saccharomyces cerevisiae* cells. The cells were pre-treated with 100, 20, 500, 900 and 1000 µmol L^{-1} of **3a** for 24 h. The columns and error bars represent the mean ± standard derivation of the mean of three independent experiments. The results were normalized with respect to the control and the symbols (*) and (***) represent, respectively, lower and higher statistically significant differences with respect to the control, with $p < 0.05$.

6.2. Cytotoxicity in SH-SY5Y neuroblastoma cells

The cytotoxicity of the compound was evaluated against SH-SY5Y cells, a neuroblastoma lineage that is widely employed as an *in vitro* model for Parkinson's disease (Xicoy; Wieringa; Martens, 2017). The viability of cells treated with various concentrations of **3a** for 24 h was assessed using the MTT assay.

Treatment with 1% DMSO reduced cell viability of approximately 5% after 24 h of incubation, indicating that the presence of DMSO in the culture medium reduces cell growth compared to control cells (Figure 73). Regarding exposure to compound **3a**, a more important reduction in cell viability was observed only in the presence of 90 µmol L^{-1} of compound, with growth reduced by 40% compared to

control cells. The results indicate that compound **3a** has cytotoxic effects on SH-SY5Y neuroblastoma cells in a dose-dependent manner.

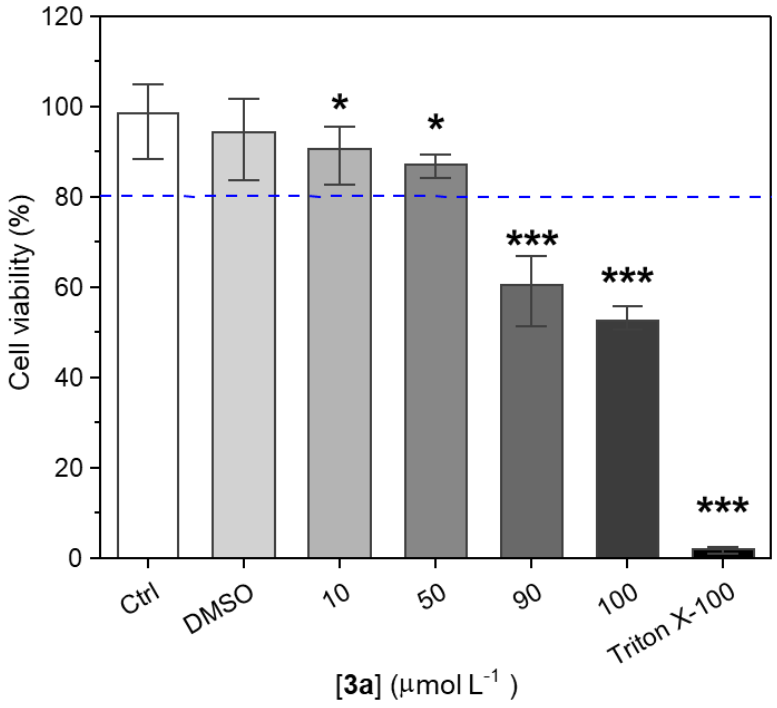

Figure 73. Cytotoxic effects of **3a** on SH-SY5Y neuroblastoma cells. Cell viability was measured using the MTT assay. The cells were pre-treated with 10, 50, 90 and 100 µmol L^{-1} of **3a** for 24 h. The mean± standard deviation is presented. The results were normalized with respect to the control and the symbols (*) and (***) represent, respectively, lower and higher statistically significant differences with respect to the control, with $p < 0.05$.

7. 3a–aluminum(III) interactions: insights into coordination features

7.1. Reaction kinetics and complexation study

Complexation studies were performed to estimate the stoichiometric ratio of the complexes formed between ligand **3a** and Al^{3+} ions. A preliminary study was carried out to explore the kinetics of the reaction in solution, since aluminum(III) complexes exhibit high thermodynamic stability, yet they are characterized by high kinetic inertia due to the relatively slow ligand exchange reactions (Callegari *et al*., 2023; Dalla Torre *et al*., 2019b). To this end, the complexation was monitored using stoichiometries proposed in the literature for coordination compounds of this metal (M_2L, ML and ML_2) by UV-vis electron spectroscopy (Appendix Figures A56; A57

and A58, respectively). The band around 400 nm, associated with the phenolate group in the ligand, was closely monitored as a reliable indicator of complexation, since phenol usually undergoes deprotonation upon coordination to strong Lewis acids. Aluminum chloride was used as the metal source.

Analyzing the profiles obtained for the **3a**:Al^{3+} (1:1, ML) and **3a**:Al^{3+} (2:1, ML_2) mixtures, it can be seen that there is no clear stabilization in the followed band and the absence of clear isosbestic points indicates the intricate dynamics of species in solution under these stoichiometric ratios. On the other hand, for the **3a**:Al^{3+} (1:2, M_2L) mixture, a stabilization is observed at around 5-6 hours of monitoring. In the latter case, the spectral changes observed were time-dependent and stable up to 10 hours after the metal salt dissolution. For this reason, the methodology adopted for the complexation studies follows the spectra obtained approximately 6 hours after preparing the solutions.

During the complexation study (titration of the ligand with a solution of the metal), the electronic spectra of **3a** (Figure 74A) showed a bathochromic shift of the hydrazonic absorption from 294 to 317 nm upon complexation, and appearance of a new band attributed to a ligand-to-metal charge transfer (LMCT) process. The constant absorbance value at the absorption maximum of the complex was reached approximately 6 hours after mixing the reactants in solution. The dependence of the absorbance at the spectral maximum at 384 nm in **3a** (phenolate-associated LMCT band) on aluminum concentration (Figure 74B) indicates complexation with the addition of two metal equivalents on the ligand, which suggests the formation of a complex with an M_2L stoichiometry.

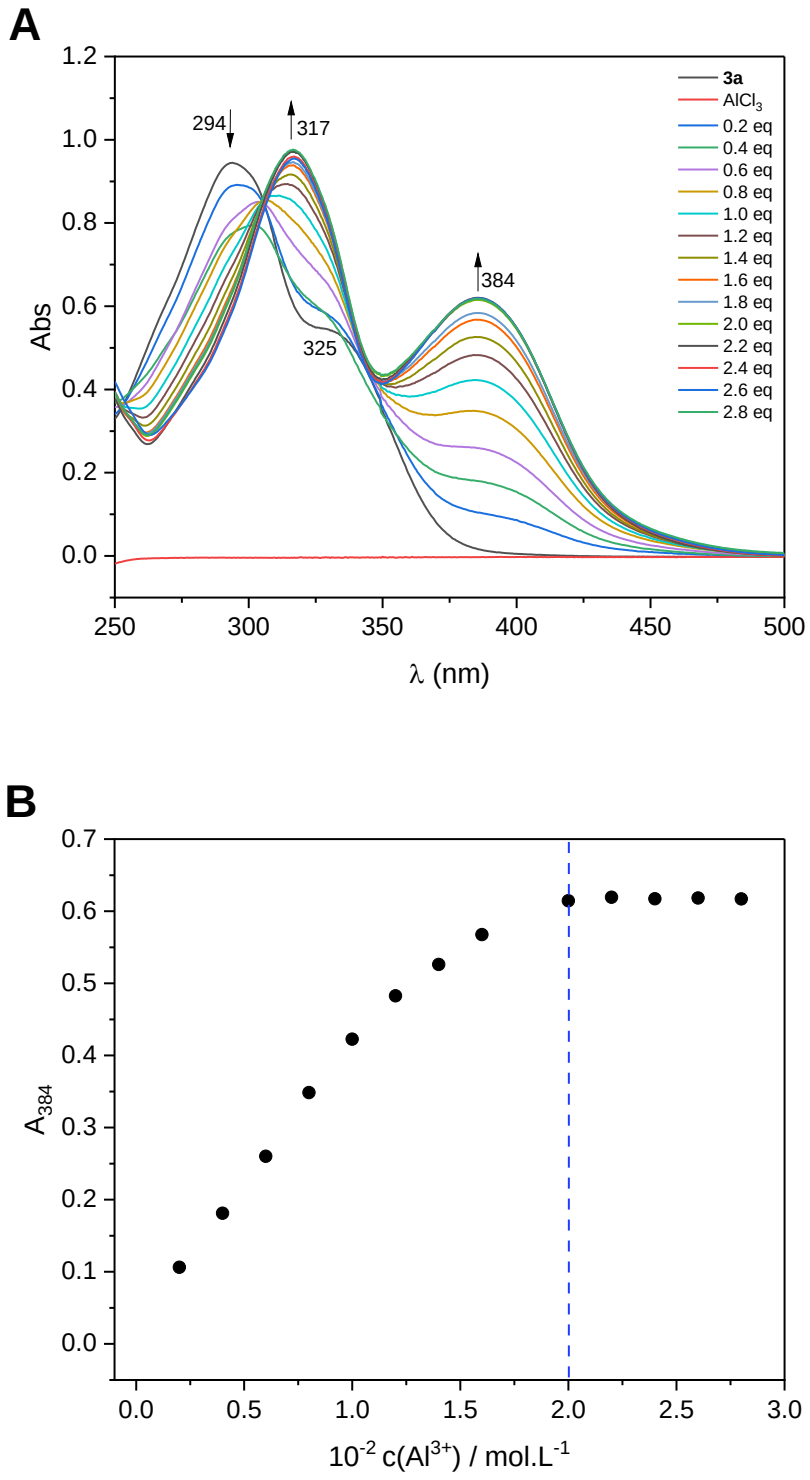

Figure 74. (**A**) Electronic absorption spectra in selected wavelength regions from the complexation study of **3a**:Al^{3+}, in a 1% DMSO/acetate buffer mixture (pH = 4.5). Experimental conditions: l = 1 cm and θ = (25.0 ± 0.1) °C. (**B**) Dependence of absorption at 384 nm on Al^{3+} concentration.

7.2. Study of the interaction mode using ^{1}H NMR

The ^{1}H NMR studies of compound **3a** in the absence and presence of 0.5, 1 and 2 equivalents of Al^{3+} are shown in Figure 75. Spectra were recorded in D_2O / DMSO-d_6 (50:50, v/v), 6 hours after the mixtures were prepared. The different ligand:aluminum mixtures show a unique set of signals related to complexed forms, regardless of the amount of metal added. This indicates that only one complex is formed. Upon addition of 2 equivalents of metal, there was no more free ligand in solution and the system seems to stabilize, in accordance to the UV-vis results.

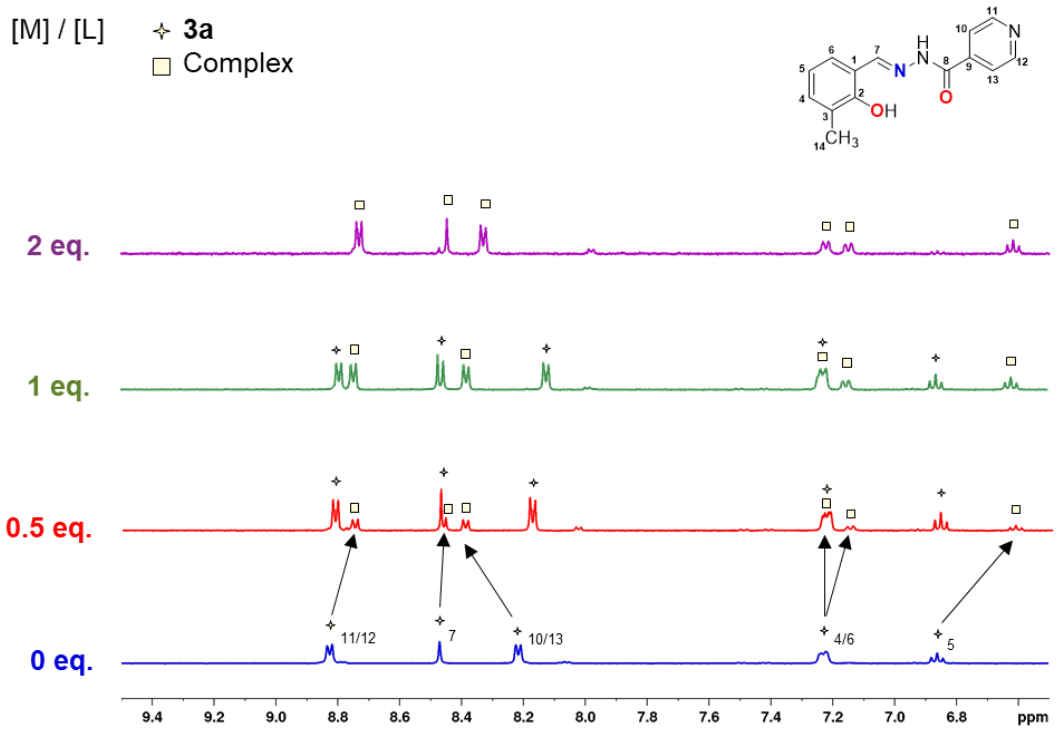

Figure 75. ^{1}H NMR spectra (400 MHz) of **3a** in the absence (blue) and presence of 0.5 eq. (red), 1.0 eq. (green), 2.0 eq. (purple) of Al^{3+}. Spectra recorded in DMSO-d_6/D_2O (50:50, v/v) at 25 ºC.

Concerning the chemical shifts in the free ligand, the azomethine hydrogen appears as a singlet at 8.47 ppm. Equivalent hydrogens of the pyridine ring were identified as a pair of doublets at 8.21 and 8.82 ppm. Other aromatic hydrogen signals were observed at 7.22 (doublet) for H4 and H6, at 6.86 (triplet) for H5.

All the complex signals are shifted downwards in relation to those of the free ligand. The main changes observed in the spectra are related to aromatic hydrogens displacements, for example, H10 and H13 (displacement from 8.21 ppm to 8.33 ppm), as well as H5, displaced to 6.62 ppm. The azomethine proton was

slightly shifted to 8.44 ppm. The spectral changes during the ^{1}H NMR titration are summarized in Appendix Table A31.

The coordination chemistry of aluminum chloride has still been well studied, both for isolated $AlCl_3$ and in solution in coordination solvents (Edwards; Farwell; Johnson, 1995). This system has been described by several authors as a complex system due to the existence of aluminium species in dimeric molecular forms, a result of its electron-deficient nature, behaviour as a Lewis acid and the stabilizing interactions that occur within the dimeric structure (Lanzani *et al*., 2012).

The dimer is formed by the coordinated bond between the chloride and aluminum ions, so that each aluminum has eight electrons in its outer shell. The molecular formation process of Al_2Cl_6 is thermodynamically favoured, as it helps to lower the overall energy of the system and stabilizes the structure (Jasien, 1995; Melissen *et al*., 2013; Volkov; Timoshkin; Suvorov, 2004, 2005). We therefore attribute the formation of the M_2L stoichiometry complex to the dimerization of $AlCl_3$ mediated by chlorido-bridges and the subsequent coordination of one of the metal centers to the hydrazonic ligand **3a**.

7.3. Relative affinity with aluminum(III) in aqueous solutions

Determining the binding constant associated with the binding stoichiometry is important from a biological point of view. To do this, an analysis using the Job's method was carried out to obtain the apparent interaction constant between **3a** and Al^{3+} ions. In this experiment, aluminum nitrate was used as the metal source in order to avoid the formation of the aluminum dimers observed in the presence of chloride.

Since ligand **3a** has a pKa value of 7.62 ± 0.03, consequently, at pH 7.4 it is possible to observe the absorbance of the partially deprotonated phenol group at around 400 nm, with the ligand contributing to the absorption band of the complex. However, in order to apply the Job's method, it is essential that the analysis is carried out at a wavelength where the ligand does not absorb, minimizing its contribution to the total absorbance and allowing an accurate determination of the stoichiometry of the complex. Because of this, the condition of 1% DMSO / acetate buffer mixture (pH = 4.5) was used.

As previously observed, the profile of **3a** shows two bands centered at 294 (20,700 ± 40 L mol^{-1} cm^{-1}) and 300 nm (10,000 ± 25 L mol^{-1} cm^{-1}). A bathochromic

shift was observed in the hydrazone profile from 294 to 314 nm in proportion to the addition of metal. The 400 nm point was used for monitoring and used in the plot, since this point does not show absorption contributions from the ligand. The plots of absorbance *versus* the ligand mole fraction, [**3a**]/([Al^{3+}]+[**3a**]), are shown in Figure 76.

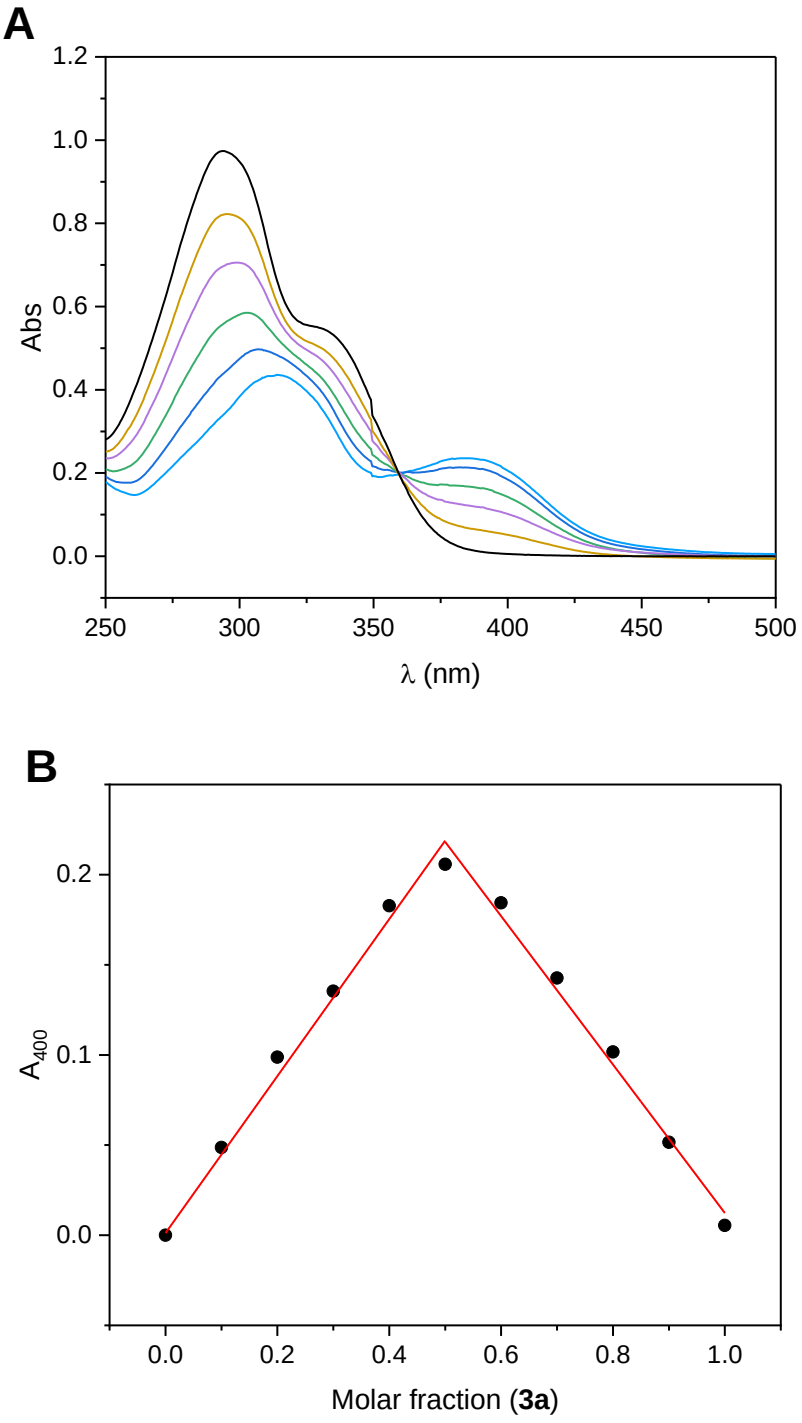

Figure 76. Method of Continuous Variations for the ligand **3a** with metal ions. (**A**) Selected UV-Visible spectra of molar fractions from 0.5 to 1.0 of **3a**:$Al(NO_3)_3 \cdot 9H_2O$. (**B**) absorbance *versus* molar fraction at 400 nm. Conditions: 1%DMSO/acetate buffer (20 mmol L^{-1}, pH 4.5), 25 °C.

The intensity of the absorbance measured showed a maximum when the molar fraction of **3a** was 0.5, which demonstrated the formation of a 1:1 complex. We infer that the complex formed probably adopts an octahedral geometry, with **3a** acting as a tridentate ONO-donor ligand and the coordination sphere of the metal ion being completed by one or more oxygen atoms from the solvent.

The apparent affinity constant (K_{app}) were determined considering the equilibrium concentrations of the complex, the ligand and the metal by means of [ML]/([L] x [M]) and presented a log K_{app} value of 4.60 ± 0.08, calculated from triplicate experiments. This constant value reflects the high concentration of H^+ ions, which promotes direct competition with metals ions for the coordination sites available on ligand **3a**, as well as the relatively low thermodynamic stability of Al^{3+} complexes. At pH 4.5, it is plausible that there is a significant reduction in the electronic density of the donor groups, due to the protonation of the ligand. As a consequence, the ability to complex with metals ions is compromised, since the coordination sites become partially or totally unavailable in this condition. This phenomenon directly affects both the formation and stability of the complexes in solution, limiting the efficiency of the metal-ligand interaction.

7.4. Coordination chemistry in the solid state

The structural formation of the complex (hereinafter called complex **1**) was confirmed when it was obtained in the solid state. The synthesis, using aluminum nitrate as the metal source, resulted in very low yields, and new methodological conditions are needed to optimize and maximize the amount of complex isolated. On the other hand, the crystals obtained could be adequately characterized br XRD, and the results are presented below.

With regard to the crystal structure, X-ray data from the single crystal revealed a monoclinic cell crystallization with space group $P2_1/c$ (Table 18). The complete data, bond distances, bond angles and torsion angles are shown in Tables A33-A34 (Appendix). Crystal structure revealed octahedral geometry of aluminum by coordinating with one nitrogen and two oxygen atoms of hydrazones in equatorial position, forming five- and six-membered metallocycles, and three water molecules (one in the equatorial position and two in axial positions) which complete the coordination sphere. Additionally, the crystal structure contains two NO_3^-

counterions and two lattice water molecules (Figure 77).

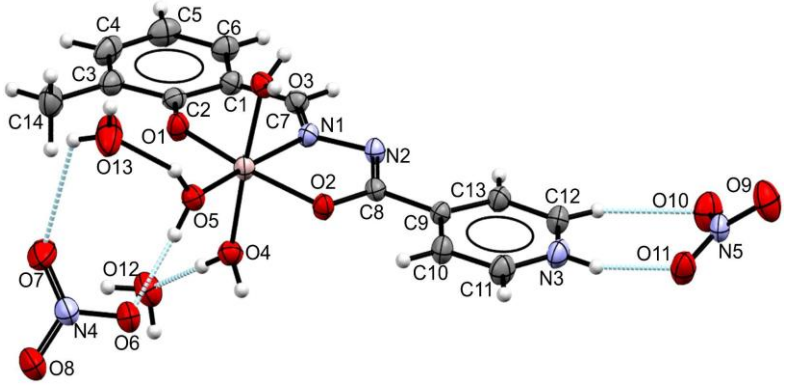

Figure 77. The asymmetric unit of complex **1** with 50% probability displacement ellipsoid.

Table 18. Single-crystal diffraction and structural refinement data for complex **1**.

Formula of the monomer	$C_{14}H_{22}N_5O_{13}Al$
Moiety formula	$C_{14}H_{18}AlN_3O_5 \cdot 2\ NO_3 \cdot 2H_2O$
Mr / g mol^{-1}	495.35
Crystal system, space group	Monoclinic, $P2_1/c$
Temperature / K	273
a / Å	6.8141(9)
b / Å	15.607(2)
c / Å	19.944(3)
α / °	90
β / °	95.415(4)
γ / °	90
V / Å^3	2111.6(5)
Z	4
Radiation type	MoK⟨
μ / mm^{-1}	0.175
Crystal size / mm	0,05 x 0,10 x 0,28
Data	-8: 8 ; -18: 18 ; -24: 24
Reflections collected, R_{int}	31210, 0.105
Data/parameters	3856/ 332
R_1, wR_2, S (I > 2.0 sigma(I))	0.0627, 0.1542, 1.19
R_1, wR_2 (all data)	0.1245, 0.2225
Δρmax, Δρmin / e Å^{-3}	-0.37, 0.39

The supramolecular structure of complex **1** is primarily organized by hydrogen bonds, as shown in Table 19. A more detailed analysis was carried out using Hirshfeld surface analysis (HS). Typically, the HS is visualized as a color map based on intermolecular distances: reddish regions appear where these distances are shorter than the sum of the van der Waals radii ($\sum \mathbf{r}_{vdW}$), indicating stronger interactions, while bluish regions correspond to weaker, longer-range contacts. Intermolecular distances can also be represented as two-dimensional fingerprint plots. These plots highlight specific types of interactions with characteristic patterns as sharp spikes for hydrogen and halogen bonds, lateral wings for C–H···π interactions, and a central spot for π···π and π stacking interactions. As shown in the HS maps filtered by interaction type (Figure 78), the strongest interactions arise from O···H and N···H hydrogen bonds, which together account for nearly 40% of the Hirshfeld surface. π stacking and C–H···π interactions also play a significant role in the supramolecular organization.

Table 19. Hydrogen bond geometric parameters for complex **1**.

D	**H**	**A**	**D-H (Å)**	**H···A**	**D···A**	**D-H···A**	**symmetry**	$\sum \mathbf{r}_{vdW}$ (%)
O3	H3B	O9	0.82(4)	1.92(4)	2.717(5)	164(5)	1-x,1-y,1-z	70.6
O3	H3C	N2	0.82(4)	2.06(4)	2.864(4)	168(4)	1-x,1-y,1-z	74.9
O4	H4A	O12	0.81(5)	1.83(5)	2.632(5)	170(5)	2-x,1-y,1-z	67.3
O4	H4B	O11	0.82(4)	1.95(4)	2.754(5)	167(5)	2-x,1-y,1-z	71.7
O5	H5A	O6	0.82(4)	1.86(4)	2.683(5)	175(5)	1-x,1-y,1-z	68.4
O5	H5B	O13	0.82(3)	1.80(4)	2.581(6)	157(4)	1-x,1-y,1-z	66.2
O12	H12A	O8	0.87(8)	1.94(8)	2.805(6)	176(8)	1-x,2-y,1-z	71.3
O13	H13A	O6	0.82(5)	2.10(4)	2.914(6)	169(5)	1+x,y,z	76.4
O13	H13B	O7	0.82(7)	2.55(9)	3.048(6)	121(8)	-	93.8
O13	H13B	O7	0.82(7)	2.25(7)	3.018(8)	158(8)	1-x,2-y,1-z	82.7
C7	H7	O9	0.93	2.25	3.169(6)	169	-	82.7

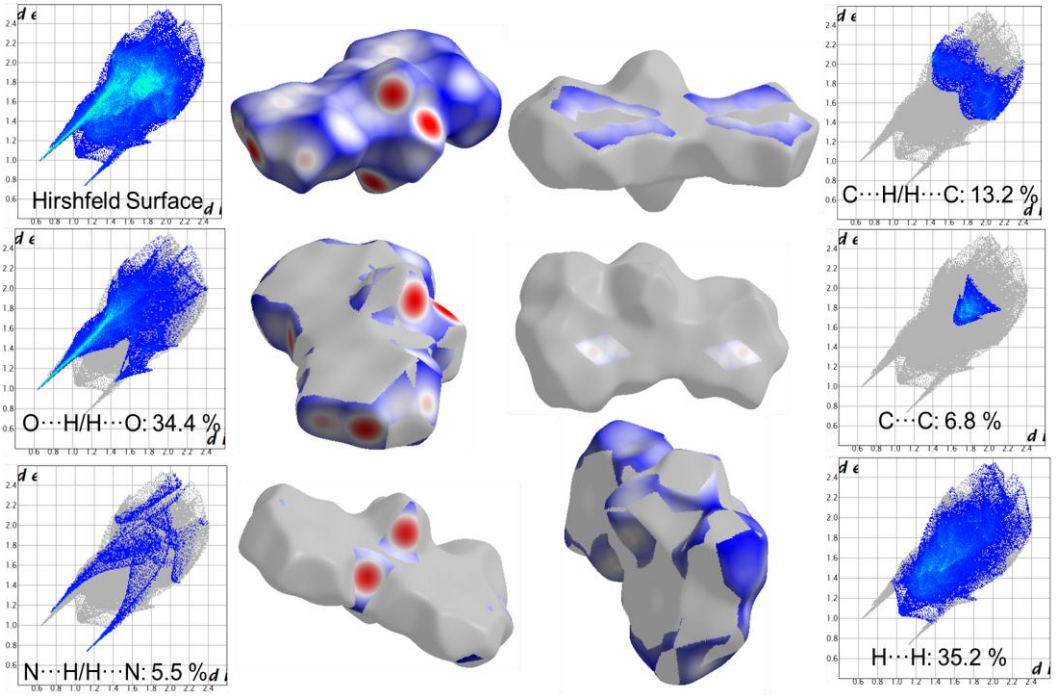

Figure 78. Hirshfeld surface (d_{norm}, -0.6317 to 1.1550) and fingerprint plots to complex **1**, filtered by contact type.

Being a charged species, most of the hydrogen bonds occur with the complex **1** acting as a hydrogen bond donor and nitrate anions and water molecules as the acceptors. These contacts are highlighted in HS shown in Figure 79A. These strong hydrogen bonds are characterized by the distance donator (D) from 66 to 75 % of the sum of their van der Waals radii.

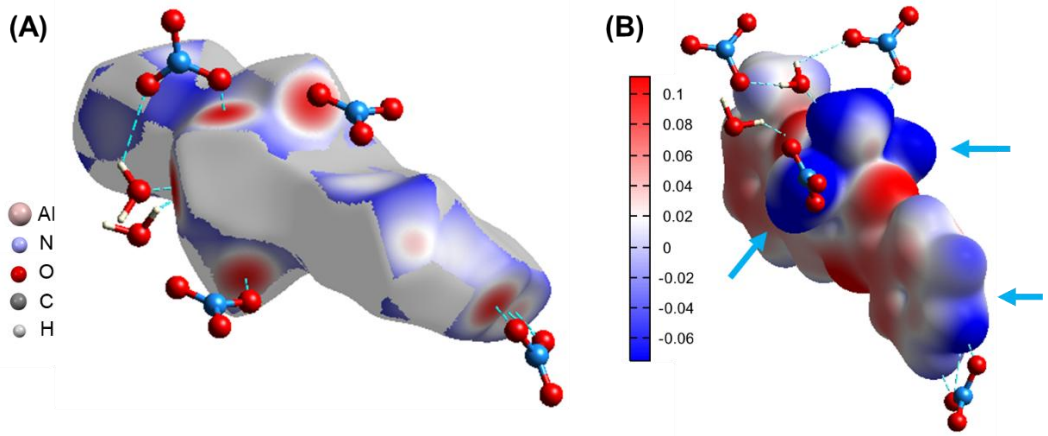

Figure 79. Some hydrogen bonds of complex **1** with the counterions: (**A**) electrostatic potential map plotted over a electron density surface; (**B**) Hirshfeld surface (d_{norm}, -0.7429 to 1.3340) filtered by O···H (left) and unfiltered (right).

The electrostatic potential map overlaid on the electron density surface

(Figure 79B) highlights, using red-blue color gradients, the regions with more positive electrostatic potential in blue, particularly corresponding to the areas involved in these hydrogen bonds.

Pyridinic ring is protonated and establishes an hydrogen bond N3-H3A···O11 with one of the nitro groups (Figure 80A). This connection is complemented by a non-conventional C12-H12···O1, giving a seven-member ring. The same nitro group also forms a hydrogen bond with the relatively acidic C7-H7. Repetition of this pattern gives rise to an extended zigzag motif propagating along the *c* axis. These contacts are highlighted in HS shown in Figure 80B.

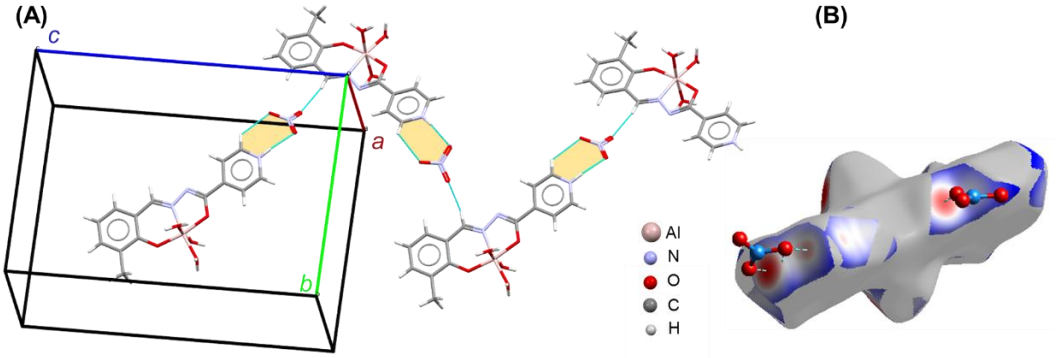

Figure 80. HB motive along with *c* axis: (**A**) electrostatic potential map plotted over a electron density surface; (**B**) Hirshfeld surface (d_{norm}, -0.7429 to 1.3340) filtered by O···H (left) and unfiltered (right).

Complex **1** presents interaction resulting in stacking along with *a* axis. In this motive, two complex units form π···π a slipped inverse π···π interaction with vertical distance of 3.275(2) Å and slippage of 2.278 Å (Figure 81A). This motive is intercalated by a second slipped inverse π···π interaction, with a perpendicular distance of 3.441(2) Å and slippage of 1.135 Å. The further motive is stabilized by a pair of reciprocal O3-H3C···N2 hydrogen bonds. This HB can be described by the graphset $R_2^2(10)$, as shown in Figure 81B. The hydrogen bond acceptor, N2, is located in the region of complex **1** that exhibits the most negative electrostatic potential, indicated by the reddish color in the electrostatic potential map (Figure 81C). The superposition of these motifs is visualized using the HS map in Figure 81D, while the overall stacking along the unit cell axis *a* is shown in Figure 81E.

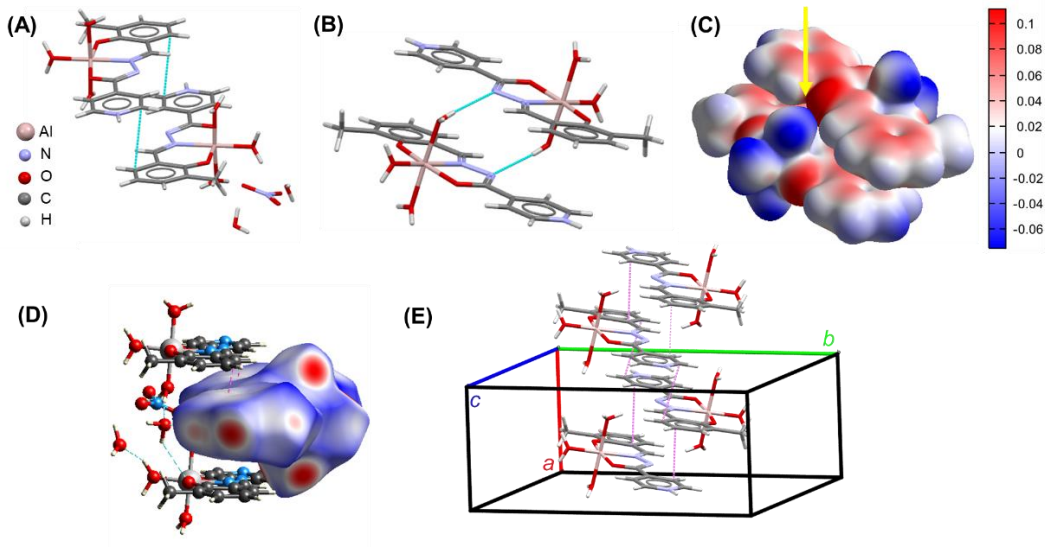

Figure 81. (**A**) stacking π···π along with *a* axis. (**B**) Graphset $R_2^2(10)$. (**C**) Electrostatic potential map of the complex (**D**) HS map and (**E**) general stacking along the *a* axis of the unit cell.

Mid-infrared analysis of **3a** and complex **1** was carried out to compare and elucidate coordination in the solid state. The typical absorptions of hydrazones are present in the spectrum of **3a**, for example, the band at 3189 cm^{-1} attributed to the symmetrical stretching of ν(N–H), as well as the stretching of C=O at 1681 cm^{-1}. As shown in Figure 82, the characteristic stretching of C=O present in the spectrum of **3a** (in blue) is not observed after coordination of the metal ion by the compound (in red). On the other hand, the detection of vibrational modes associated with ν(C=N–N=C) in 1615 cm^{-1} and ν(C–O) in 1223 cm^{-1} indicates a clear iminolization by coordination with the metal ion. Finally, the appearance of two new ν(N–O) stretching vibration bands at 1311 and 1380 cm^{-1} (symmetrical and asymmetrical, respectively) confirms the presence of nitrate groups in the crystal structure of the complex.

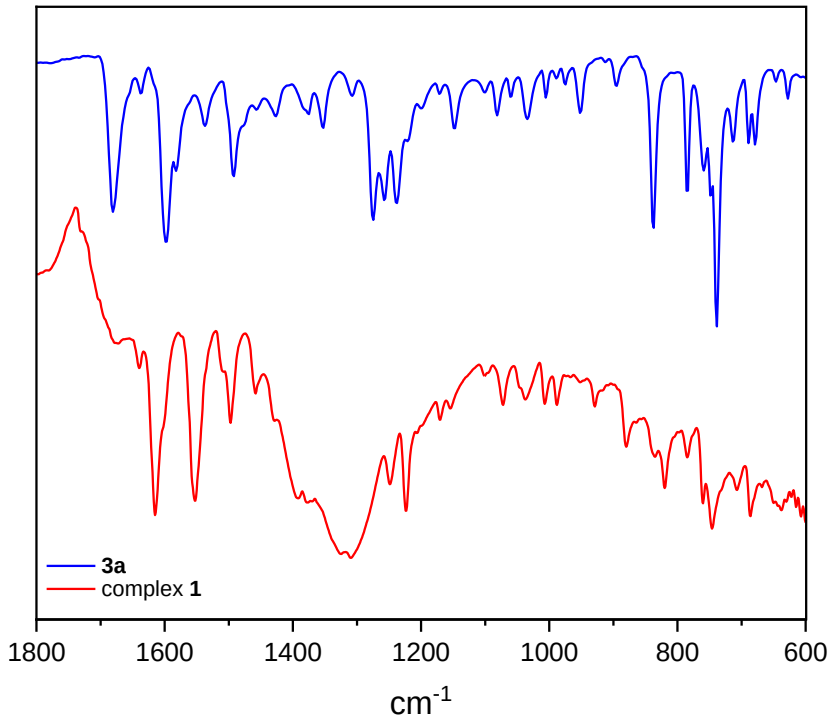

Figure 82. Overlapping of the mid-infrared spectra of **3a** and complex **1**, at room temperature.

The ^{1}H NMR spectrum of complex **1** (in crystalline form) was obtained in a mixture of D_2O/DMSO-*d*$_6$ (50:50, v/v). For comparative purposes, the same type of analysis was carried out for ligand **3a**. Both ^{1}H NMR spectra were duly assigned, as shown in Figure 83. Full assignments, with the chemical shifts and coupling constants, can be found in Appendix Table A35.

Comparative analysis of the spectra shows that coordination to the aluminum(III) ion promotes deprotonation of the phenolic hydroxyl group, leading to the formation of phenolate. This is confirmed in solution, since this species acts as a σ donor for the metal and, additionally, allows the partial transfer of electronic density to the adjacent aromatic ring. The consequent increase in electronic density in the aromatic ring results in a shielding effect on the proton signals, which manifests itself moderately for H4 and H6, and more markedly for H5, due to its position relative to the phenolic oxygen. This electronic delocalization is also perceived by the imine proton (-CH=N-) and the pyridine ring, since the structure is fully conjugated. As a result, the signal corresponding to these protons is shifted to lower frequencies (greater shielding) in the spectrum of the complex, compared to the non-coordinated ligand **3a**.

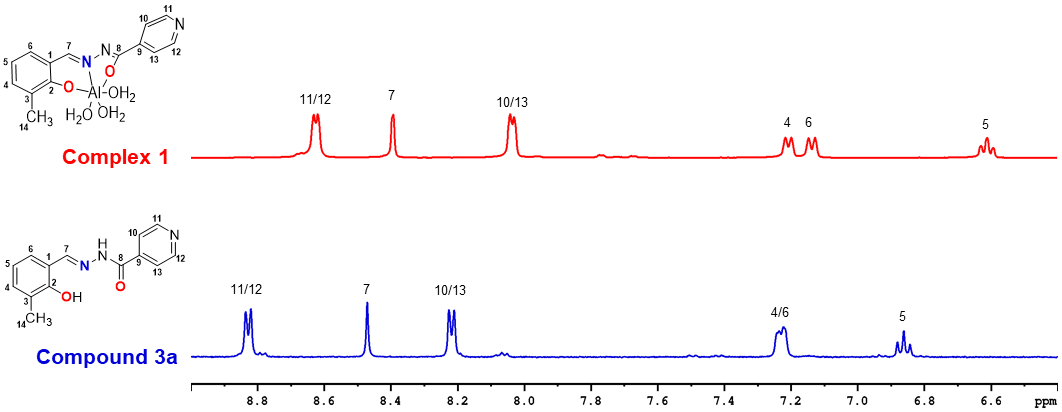

Figure 83. ^{1}H NMR spectra (400 MHz) of **3a** (blue) and complex **1** (red). Spectra obtained in DMSO-d_6/D_2O (50:50 v/v) at 25 ºC.

In general, the spectrum of complex **1** is quite similar to the one obtained after the addition of two equivalents of Al^{3+} in a solution of **3a** (Figure 75), although with some differences concerning the respective chemical shifts.

8. Studies of Ternary Metal-Protein-Hydrazone Systems through high-field NMR

Following the establishment of the pathophysiological association between α-Syn and Parkinson's disease by Polymeropoulos *et al*., (1997) and Spillantini *et al*., (1997b), the effects of metal ions on this protein began to attract increasing scientific interest. To the best of our knowledge, the first reference addressing the interaction between aluminum ions and a protein related to α-Syn was published in the same year by Paik *et al*., (1997a). The article, entitled "Aluminum-Induced Structural Alterations of the Precursor of the Non-Aβ Component of Alzheimer's Disease Amyloid" describes a study performed on a presynaptic protein that shares structural similarities with α-Syn. Work on the structural changes caused by the interaction between Al^{3+} and α-Syn was published in the following years by Uversky *et al*., (2001b); Yamin *et al*., (2003) and others (Bai *et al*., 2015; Khan *et al*., 2005; Kostka *et al*., 2008; Ly; Julian, 2008; Nübling *et al*., 2012; Paik *et al*., 1997b; Uversky *et al*., 2002; Venati; Uversky, 2024). However, to date, there is no good understanding of the real impact of this metal on the protein and its implications for PD. Based on this assumption, we decided to investigate this system by first analyzing this binary interaction.

Although some authors consider Al^{3+} labile, this metal ion tends to participate in relatively slow reactions, especially in biological systems (Boullemant *et al.*, 2009; Hémadi *et al.*, 2003; Kuiper *et al.*, 2022; Zhao; Campbell; Wilkinson, 2016). For this reason, it is likely that a certain amount of time is required for the metal to bind to specific sites on the protein and reach a local concentration sufficient to initiate conformational changes. Therefore, the binding kinetics can be slow, especially when there is competition with other ions or the accessibility of the binding sites is initially limited.

Given the need to elucidate this interaction kinetics between aluminum and α-Syn and to ensure the detection and quantification of the effects induced by the metal, we decided to use a five-fold higher concentration of Al^{3+} in the investigation, performing a ^{1}H x ^{15}N HSQC experiment. This concentration was determined to optimize the observation of any disturbances that would be manifested over time, ensuring that the accumulation and interaction of the metal ion reaches a detectable threshold within the experimental period.

The addition of 5 equivalents of Al^{3+} to the α-Syn sample did not induce immediate spectral changes, as evidenced by the blue/red contours in Figure 84A. However, analysis of the same sample 34 hours after exposure to the metal revealed changes in the C-terminal region of protein (Figure 84B -blue/red contours).

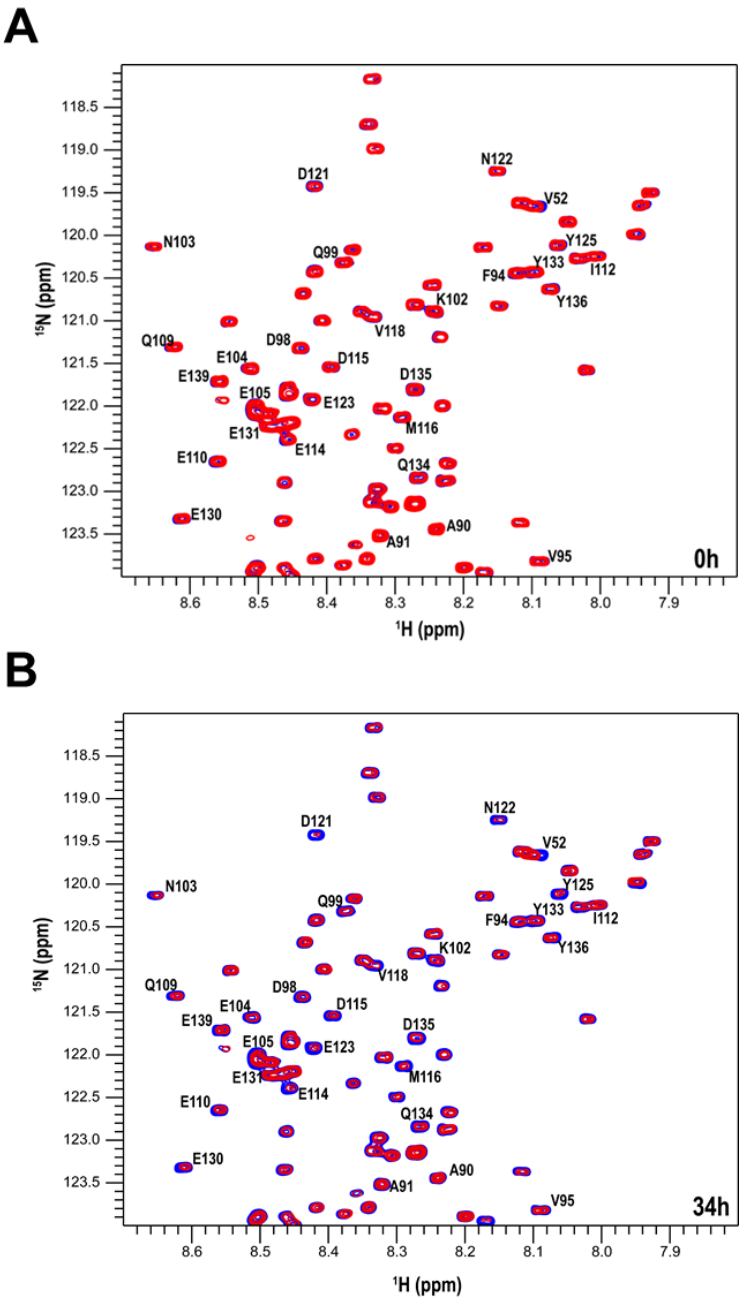

Figure 84. NMR analysis of the interaction between Al^{3+} and α-Syn. Overlaid contour plots of the ^{1}H x ^{15}N HSQC spectra of α-Syn in the absence (blue) and in the presence of 5 eq. (red) of Al^{3+}. (**A**) Spectrum obtained immediately after mixing and (**B**) Spectrum obtained 34 hours after mixing. All the experiments were recorded at 15 °C (100 µmol L^{-1} α-Syn in MES 20 mM pH 6.5).

For a short-term assessment, tests were conducted involving exposure of α-Syn to high concentrations of metal, namely: 10, 15, and 20 equivalents of Al^{3+}. Spectral changes were monitored using ^{1}H x ^{15}N HSQC spectroscopy immediately and after 24 hours of the addition. The results demonstrated that there were no significant spectral changes during this interval, *i.e.*, at higher aluminum concentrations, coordination seems to be immediate and stable.

Among the conditions tested, the addition of 15 equivalents of the metal was chosen for further studies because it represents an intermediate point between concentrations of 10 and 20 equivalents, providing a more balanced and effective evaluation of the system. Under this condition, a significant broadening of the C-terminal amino acid residues' signals was observed, as shown in Figure 85A (red contours), an effect that is also seen in the other concentrations tested, as shown in the I/I_0 graph (Figure 85B), which confirms the main effect of the metal under the C-terminal, but also shows small changes at the N-terminal and NAC domain.

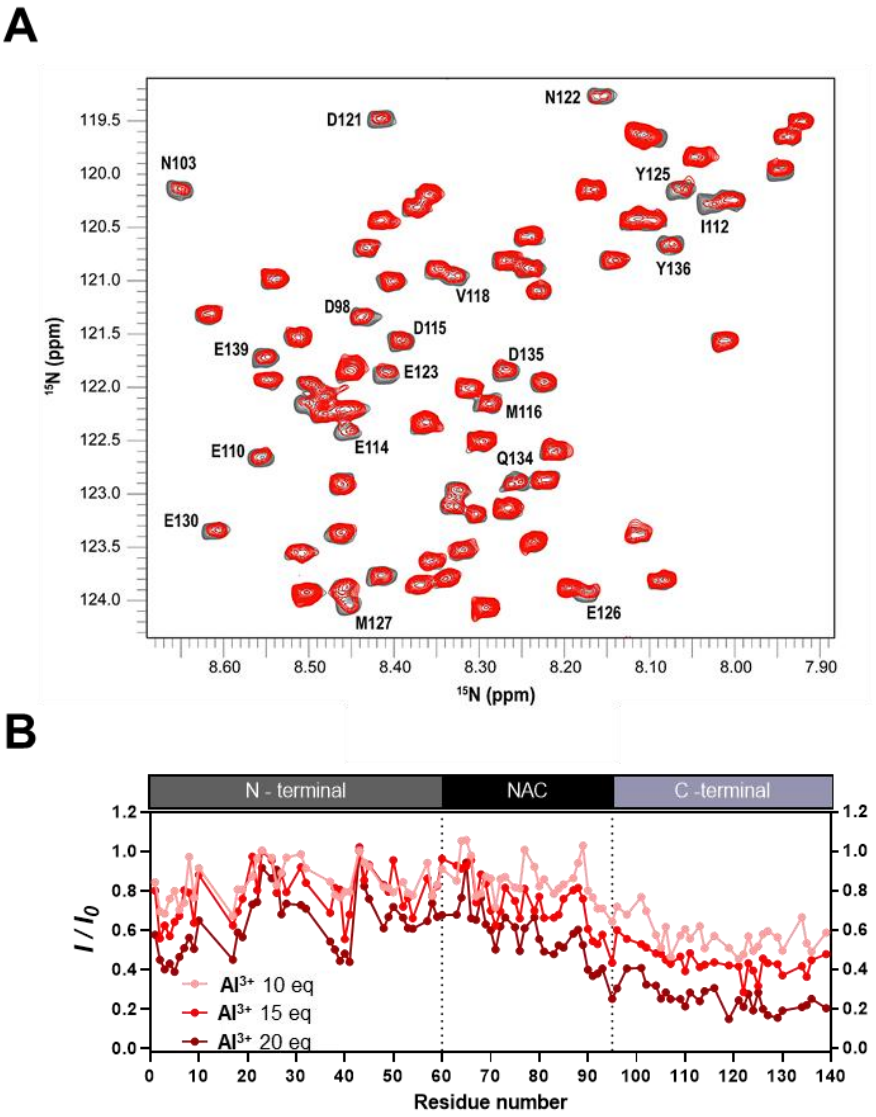

Figure 85. NMR analysis of the interaction between Al^{3+} and α-Syn. (**A**) Overlaid contour plots of the $^{1}H^{15}N$ HSQC spectra of α-Syn in the absence (gray) and in the presence of 15 eq. (red) of Al^{3+}. (**B**) The I/I_0 profiles of the amide groups of the α-Syn backbone were plotted as a function of the number of residues in different molar ratios of Al^{3+} (10 eq. (light red); 15 eq. (red) and 20 eq. (red wine)). Experiments were recorded at 15 °C (100 µmol L^{-1} α-Syn in MES 20 mM pH 6.5).

Observing the overlaid contour plots shown in Figure 85A, it is possible to infer the amino acid residues predominantly affected by this interaction, which include: tyrosine (Y125, Y133 and Y136), whose phenolic side chain, due to its chemical characteristics, has a greater affinity for the metal ion; and the residues of aspartic acid (D98, D115 and D121) and glutamic acid (E104-E131), with their negatively charged carboxylate groups acting as high-affinity binding sites for Al^{3+}. Additionally, phenylalanine (F94) and asparagine (N103 and N122) also seem to be involved, suggesting the participation of other interactions besides the predominantly ionic ones in this interaction.

Before evaluating the ternary system involving α-Syn, Al^{3+} and hydrazone, we decided to investigate the interactions of **3a** directly with the protein, also by ^{1}H x ^{15}N HSQC experiments. A detailed analysis of the amide signals of the backbone showed that 15 eq. of the compound did not interact directly with the protein (Figure 86A, green contours). This result is confirmed by the I/I_0 graph (Figure 86B) even for other concentrations (10 and 20 eq.).

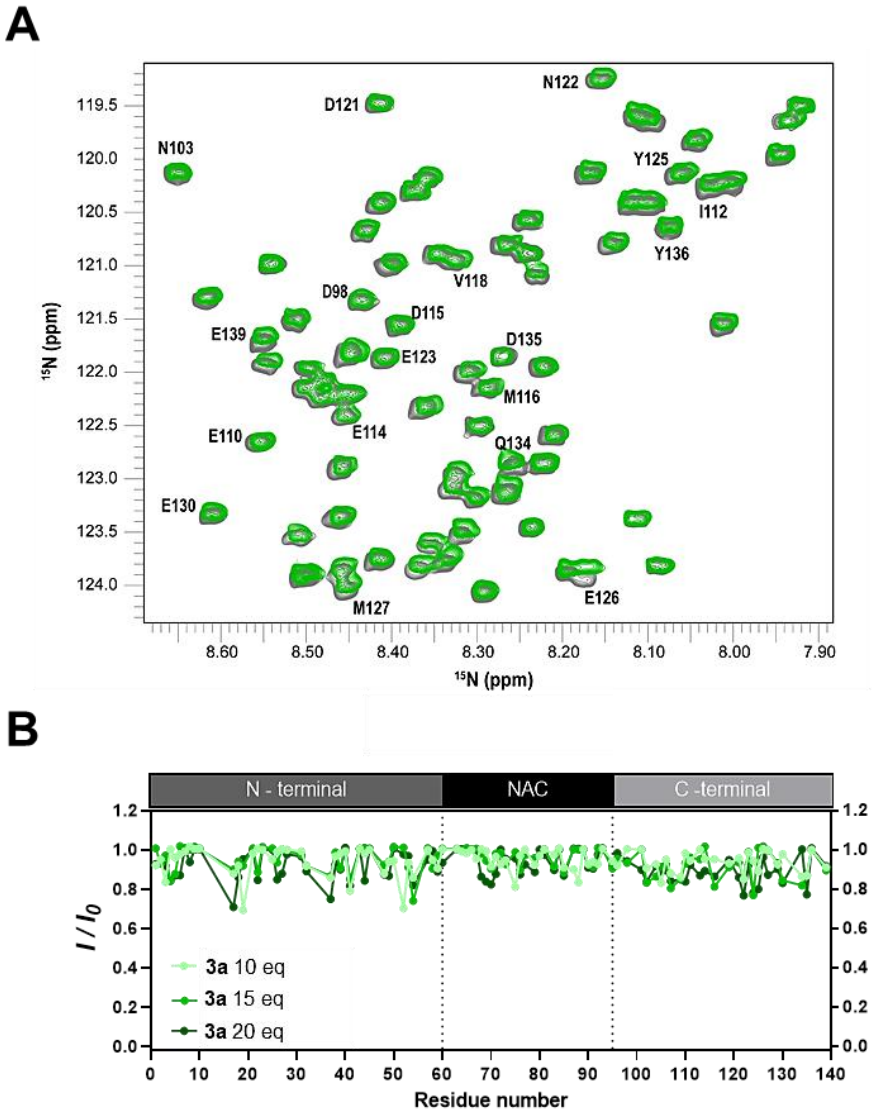

Figure 86. NMR analysis of the interaction between **3a** and α-Syn. (A) Overlaid contour plots of the $^{1}H^{15}N$ HSQC spectra of α-Syn in the absence (gray) and in the presence of 15 eq. (green) of **3a**. (**B**) The I/I_0 profiles of the amide groups of the α-Syn backbone were plotted as a function of the number of residues in different molar ratios of **3a** [10 eq. (light green); 15 eq. (green) and 20 eq. (dark green)]. Experiments recorded at 15 °C (100 μmol L^{-1} α-Syn in MES 20 mM pH 6.5).

The potential for aluminum(III) sequestration by **3a** in relation to α-Syn was also explored by ^{1}H x ^{15}N HSQC. As previously demonstrated, the addition of 15 eq. of the metal ion to the α-Syn samples caused severe broadening of specific amide crosspeaks, mainly in the C-terminal portion of the protein, clearly indicating its involvement as a metal coordination site. Interestingly, increasing amounts, even in equimolar proportions, of compound **3a** were not efficient in removing the aluminum-induced perturbations in the α-Syn backbone amide signals. On the opposite: a broadening effect was observed in the signals involved in the interaction

with Al^{3+} after the addition of the compound, with the Asp, Glu, and Tyr residues being the most affected (Figure 87A, blue contours). This interaction-induced broadening is further supported by the I/I_0 plot, which clearly reflects the reduction in signal intensity (Figure 87B). This behavior suggests the formation of a ternary species of the α-Syn-Al^{3+}-**3a** type, in which the compound associates with the metal ion already coordinated to the protein instead of removing it. This result is similar to the findings previously reported by the group regarding the formation of ternary complexes involving *N*-acylhydrazones and physiological metal ions such as Cu^{2+} (Carvalho *et al*., 2023, 2025; Cukierman *et al*., 2019b, 2022b).

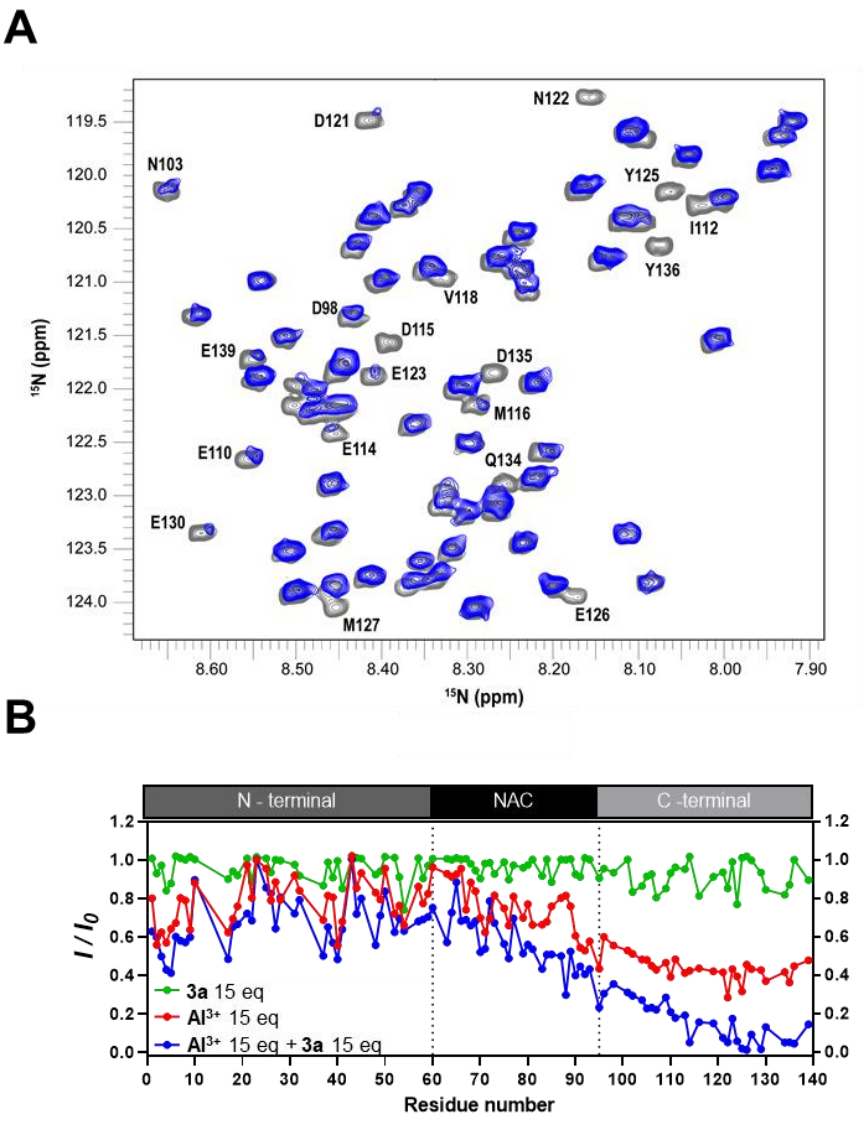

Figure 87. NMR analysis of the interaction between α-Syn, Al^{3+} and **3a**. (**A**) Overlaid contour plots of the $^{1}H^{15}N$ HSQC spectra of α-Syn (gray) and α-Syn+Al^{3+}+3a (green). (**B**) The I/I_0 profiles of the amide groups of the α-Syn backbone were plotted as a function of the number of residues contend 15 eq. (green); 15 eq. (red) of Al^{3+} and 15 eq. (blue) of the Al^{3+}+3a. Experiments were recorded at 15 °C (100 µmol L^{-1} α-Syn in MES 20 mM pH 6.5).

The effects of the α-Syn-Al^{3+}-**3a** ternary complex on the formation of protein aggregates was also investigated through aggregation kinetics experiments. Figure 88 shows the process of α-Syn aggregation monitored by thioflavin-T (ThT) fluorescence over time, in which the curves represent the protein in the absence or presence of Al^{3+} and compound **3a**. Table 20 shows the kinetic parameters extracted from the α-Syn aggregation curves under the different experimental conditions.

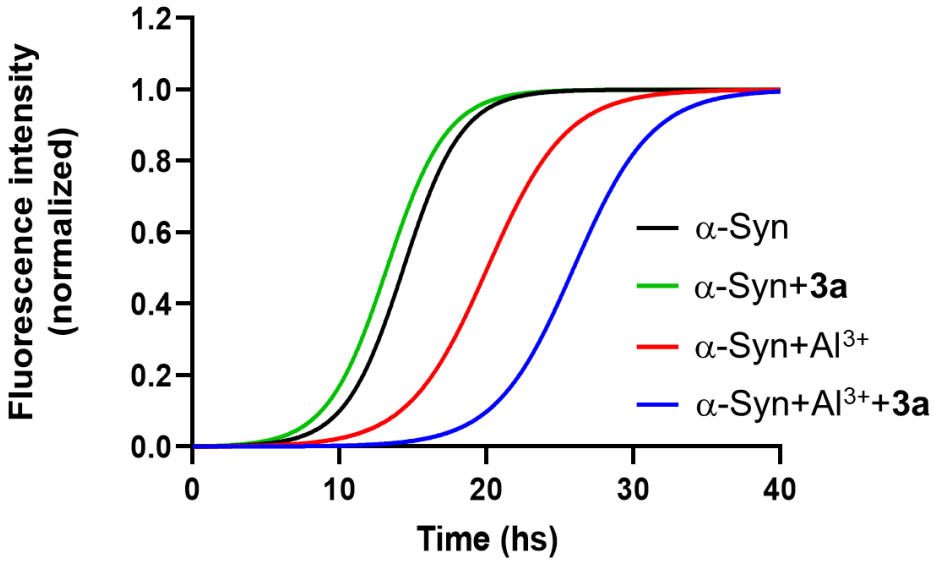

Figure 88. Aggregation kinetics of α-Syn (50 μmol L^{-1}) in the absence (black) and presence of 15 eq. de **3a** (green), 15 eq. de Al^{3+} (red) and 15 eq. de Al^{3+}+**3a** (blue), performed in triplicate using the thioflavin-T fluorescence assay.

Table 20. Aggregation kinetic parameters of α-Syn under the different experimental conditions.

Sample	$T_{1/2}$ (h)	Elongation factor (h^{-1})
α-Syn	14.36 (± 0.24)	0.503 (± 0.052)
α-Syn + Al^{3+}	20.07 (± 0.39)	0.370 (± 0034)
α-Syn + **3a**	13.23 (± 0.31)	0.488 (± 0.064)
α-Syn + Al^{3+} + **3a**	25.95 (± 0.45)	0.374 (± 0.040)

α-Syn without additives (Figure 88, black curve), shows a typical sigmoidal curve (Buratti; Fernández; Zweckstetter, 2023), with aggregation starting around 10 h and reaching a plateau around 25 h. The presence of the evaluated hydrazone

(Figure 88, green curve) did not cause any major variation in the protein aggregation process, as the curves are almost superimposed, indicating that the compound alone does not significantly affect the protein aggregation kinetics. On the other hand, in the presence of Al^{3+} (Figure 88, red curve), the change in aggregation kinetics ($T_{1/2}$ from 14.36 h to 20.07 h) suggests that the metal affects the primary nucleation phase, increasing the nucleation time, so that the protein can remain in intermediate conformational states for longer before the formation of fibrillar aggregates detectable by ThT fluorescence. This behavior is compatible with the stabilization of soluble oligomeric species, commonly described as transient intermediates along the amyloidogenic aggregation pathway (Uversky; Li; Fink, 2001c).

In the system containing α-syn, Al^{3+} and compound **3a** (Figure 88, curve blue), there was an even more pronounced shift in the aggregation curve compared to the other tested conditions ($T_{1/2}$, reaching 25.95 h). This kinetic profile indicates a further delay in the formation of fibrillar aggregates, suggesting that the formation of the α-Syn-Al^{3+}-**3a** ternary complex acts synergistically in inhibiting the aggregation process. This effect may be related to the stabilization of conformations that are less prone to nucleation or to direct interference in intermolecular interactions that are crucial for fibrillar progression.

After the aggregation experiment, the α-Syn content in both the pellet and the supernatant of each sample was analyzed by SDS-PAGE. In the samples containing only the protein, the protein and **3a**, and the ternary complex, α-Syn appears almost completely in the pellets, as shown in the wells marked in black, green and blue in Figure 89, respectively. For samples containing only protein and Al^{3+} (wells marked in red), however, α-Syn can be seen in the supernatant, indicating that this condition probably favors the formation of toxic soluble intermediates (such as oligomers or protofibrils).

The absence of interaction between α-Syn and compound **3a** observed in the kinetic aggregation and NMR studies is corroborated by the results of the SDS-PAGE analysis. On the other hand, the presence of soluble intermediate species in the condition with Al^{3+} may represent a significant risk, since these protein forms can interact intensely with cellular components. These interactions promote mitochondrial dysfunction by destabilizing the membrane and increasing ROS production, as well as inducing apoptosis (Deas *et al.*, 2016). In the central nervous

system, oligomers are also capable of activating glial cells, such as microglia, stimulating the release of inflammatory cytokines and aggravating neuronal damage (Bucciantini *et al*., 2002; Kandel; Jung; Neal, 2024; Kayed *et al*., 2003; Santos *et al*., 2025). In addition, they can negatively interfere with protein degradation pathways such as the proteasome and autophagy, contributing to the accumulation of misfolded proteins and perpetuating proteotoxic stress (Brown, 2009; Saberzadeh; Arabsolghar; Takhshid, 2016).

The formation of the α-Syn-Al^{3+}-**3a** ternary complex seems to mitigate the deleterious effects associated with the soluble intermediates generated by the direct interaction between the protein and aluminum. The simultaneous α-Syn-Al^{3+}-**3a** coordination may act as a containment system, neutralizing potentially hazardous bioactive intermediates that could otherwise interact with cell components.

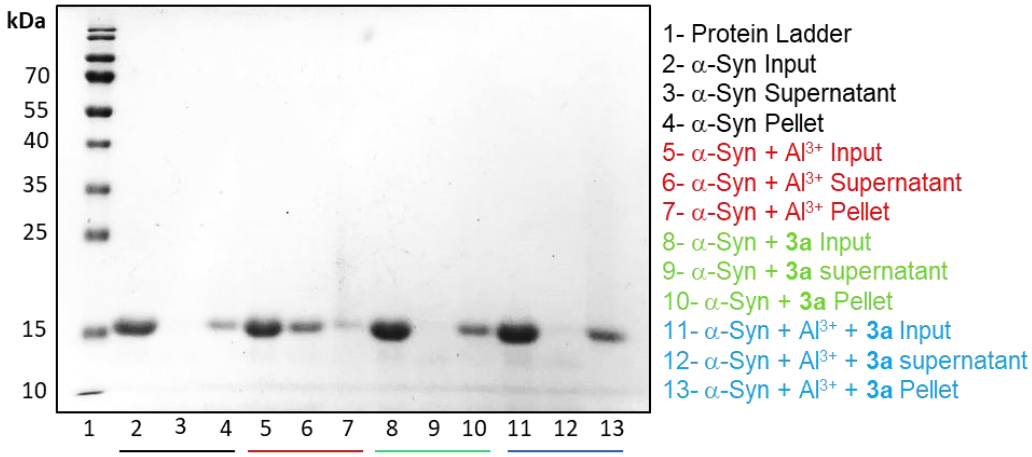

Figure 89. Coomassie-stained SDS-PAGE showing monomeric α-synuclein and final aggregation products, separated into supernatant and pellet fractions, under conditions with Al^{3+} and with the Al^{3+}+**3a** combination.

9. *In vivo* evaluation of the selected *N*-acylhydrazone: Biological effects and therapeutic potential

9.1. Penetration of the blood-brain barrier

Penetration of biological membranes is an important criterion for the successful application of drugs. Considering that **3a** is a therapeutic agent targeting PD that must act at the brain level, crossing the blood-brain barrier is mandatory. For the BBB penetration study, a separation method was initially optimized using

high-performance liquid chromatography to obtain well-defined retention times for compound **3a** and its precursors. The mobile phase, consisting of acetonitrile and water under gradient conditions, was selected for the analyses in this experiment, providing signals well separated from the dead volume and retention times within a suitable range. To confirm the method's applicability and compound detectability in complex matrices, fortified biological samples were prepared by spiking the matrix with known concentrations of compound **3a** and its precursors INH and MBA. The chromatogram obtained for the pure substances in the presence of biological matrix is shown in Figure 90, in which compound **3a**, INH, and MBA show distinct and characteristic retention times, allowing their unequivocal identification in the biological samples.

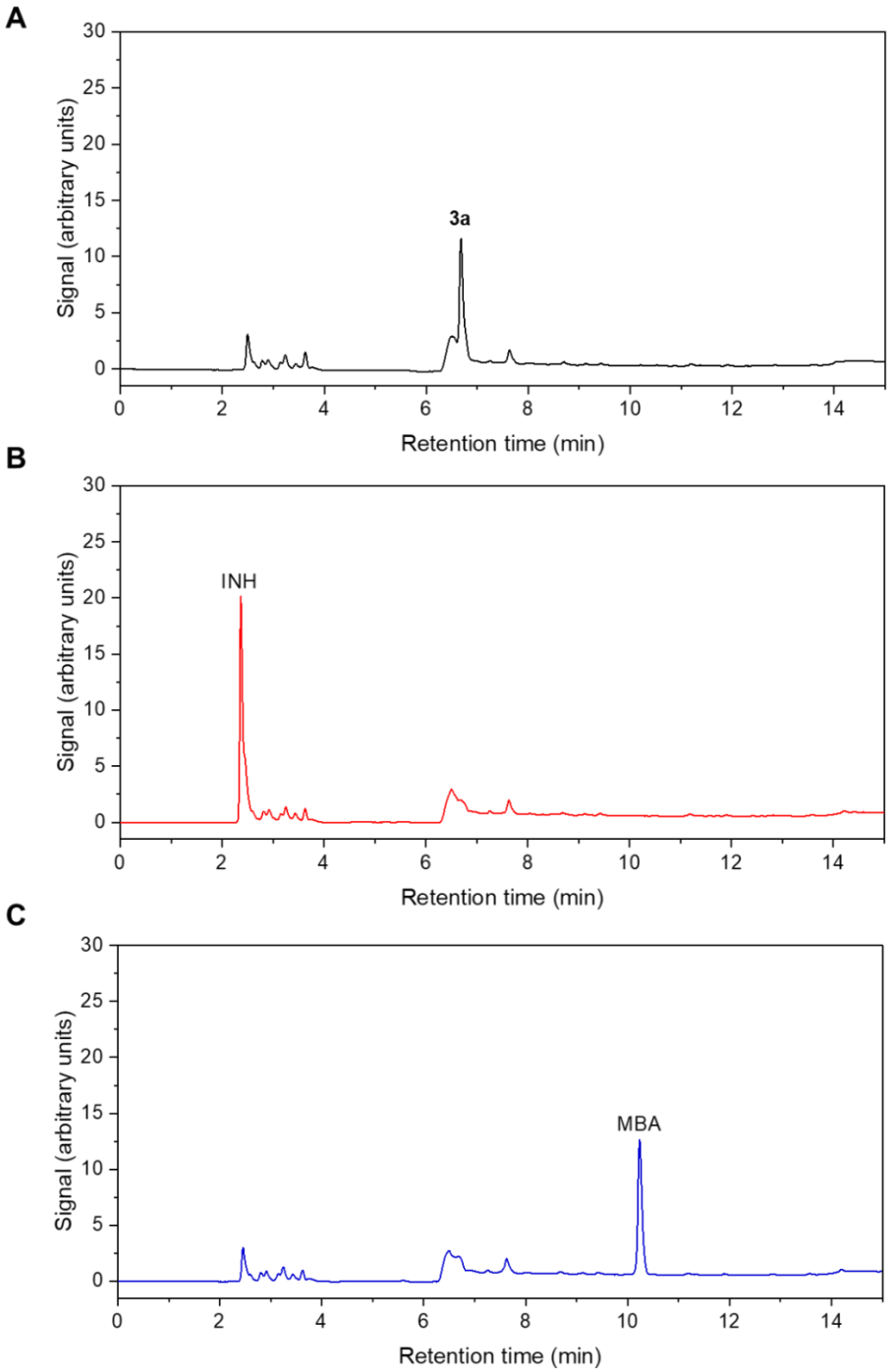

Figure 90. Chromatograms of brain tissue extracts fortified with (**A**) INH, (**B**) MBA, and (**C**) compound **3a** were obtained using a gradient elution of acetonitrile and water as the mobile phase at a flow rate of 1.0 mLmin^{-1}. Injection volume of 20 μL and column temperature maintained at 30 °C.

Figure 91 displays the chromatograms of the brain extracts obtained 1 hour after administration of 50 mg kg^{-1} of compound **3a**. The results show the clear presence of **3a** in the brain tissue, with no detection of signals corresponding to its precursors, INH and MBA. These data indicate that the compound definitely

crosses the BBB and maintain its chemical integrity in brain throughout this period.

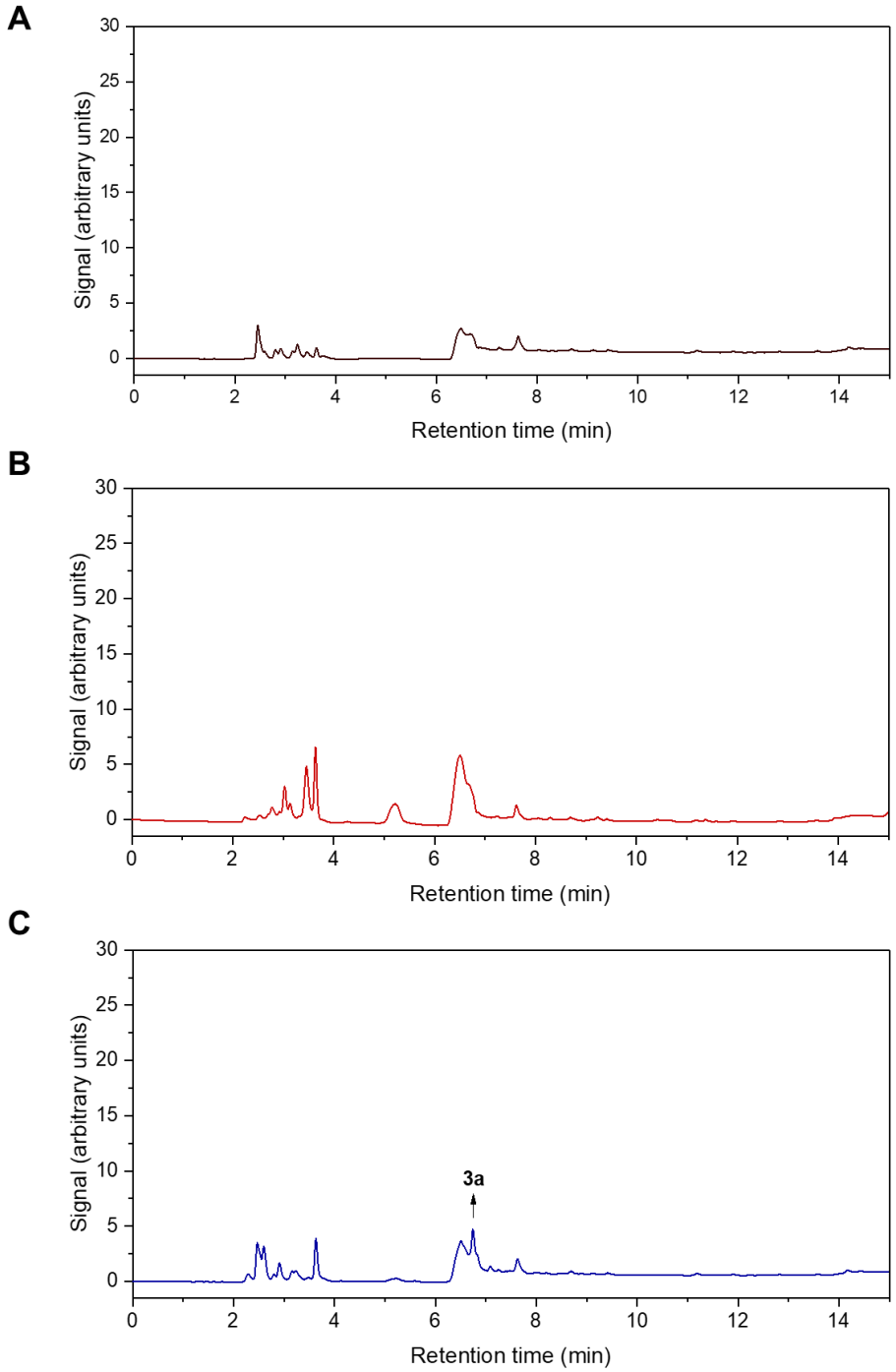

Figure 91. Chromatograms of brain tissue extract from Wistar rats (**A**) control, (**B**) vehicle, and (**C**) exposed to 50 mg/kg of **3a** were obtained using a gradient elution of acetonitrile and water as the mobile phase at a flow rate of 1.0 $mLmin^{-1}$. Injection volume of 20 µL and column temperature maintained at 30 °C.

9.2. Chronic toxicity of compound 3a in healthy rats

The rats treated with **3a** (5, 25 and 50 mg/kg/day) for 7 days showed no significant changes in behavior, excreta or body weight. The complete data weight of the rats per group throughout the experiment can be found in Appendix Table A36. Furthermore, no apparent physiological abnormalities were observed in the organs between the groups, nor were there any differences in the distribution profile of the weights of the brains and kidneys analyzed (wet weight) between the control, vehicle, and those subjected to doses of 5 and 25 mg/kg/day of compound **3a** (Figure 92A and C). However, statistically significant reductions in liver weight were observed in all groups treated with compound **3a** compared to the control group (Figure 92B). The liver weights were as follows: control group, 15.51 ± 0.44 g; 5 mg/kg/day, 13.80 ± 0.50 g (p = 0.0229); 25 mg/kg/day, 13.28 ± 0.40 g (p = 0.0020); and 50 mg/kg/day, 13.53 ± 0.27 g (p = 0.0068).

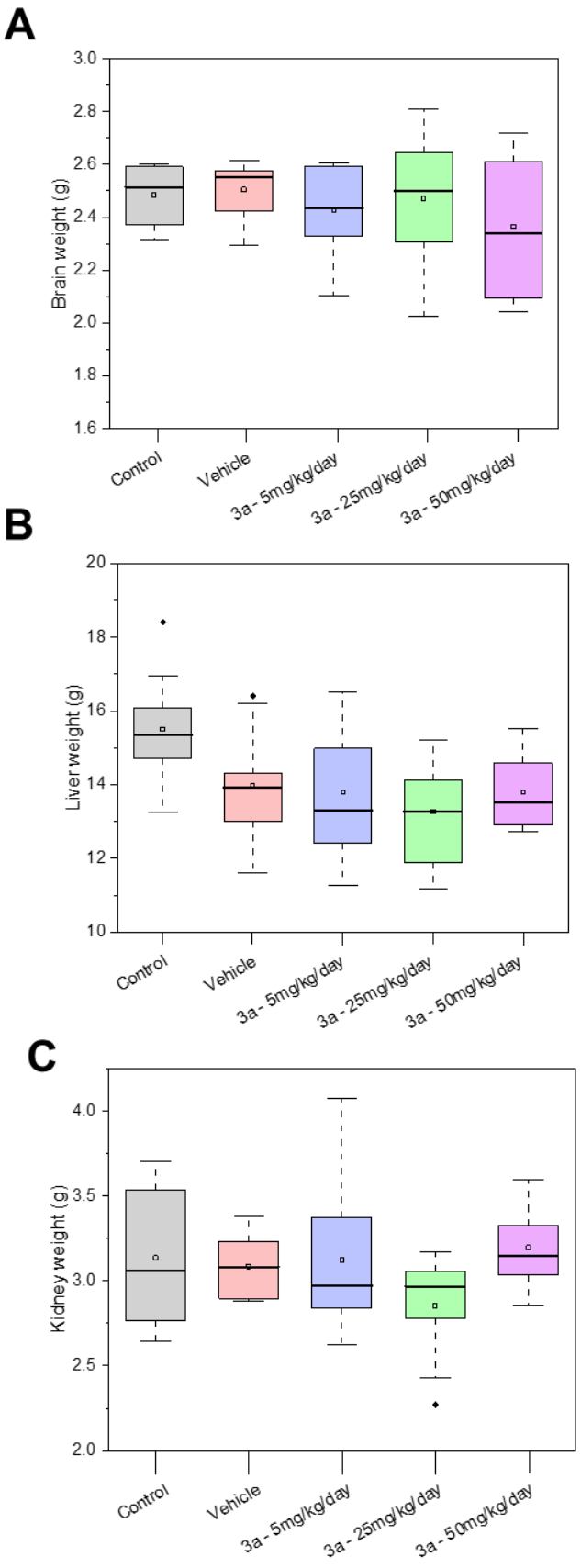

Figure 92. Distribution profile of the analyzed organ weights (wet weight) of the (**A**) Brain, (**B**) Liver and (**C**) Kidney in healthy male *Wistar* rats. Kidney weights are given as the sum of the left and right organs. The "♦" symbol represents outliers.

Since compound **3a** was rationally designed to act as an Al^{3+} chelator, the possibility of nonspecific interactions with essential metals cannot be ruled out. At this stage of the study, we decided to investigate whether **3a** would be capable of interfering with the homeostasis of physiologically relevant metal ions (iron, zinc, and copper) since changes in the availability of these ions can compromise fundamental cellular processes, including energy metabolism, intracellular signaling, and the activity of metal-dependent enzymes (Martín Giménez *et al*., 2021; Peters *et al*., 2024; Zhou *et al*., 2024). To this end, we performed quantitative analyses of metal levels in different organs using inductively coupled plasma optical emission spectrometry after the chronic exposure of male *Wistar* rats to increasing concentrations of compound **3a**.

The suitability of the method used for quantification was confirmed by comparing the values obtained experimentally with the certified values for each analyte in the BB184 and BB422 references materials used. All analytical curves presented correlation coefficients greater than 0.999. No statistically significant differences were observed between them and obtained values and recoveries (ranging from 78 to 119%), indicated the reliability of the method for quantifying the selected elements, as shown in Table 21.

Table 21. Element concentrations (mg kg^{-1} dry wt) in certified reference materials (BB184 and BB422). Values are displayed as mean ± SD (*n*= 3 for BB184 and for BB422).

Element	**BB184 (Bovine Muscle)**		**BB422 (Fish muscle)**	
	Certified value	Found value	Certified value	Found value
Zn	146 ± 7	149.42 ± 1.3	16 ± 1.1	19.22 ± 0.9
Cu	2.31± 0.09	2.26 ± 0.02	1.67 ± 0.16	1.79 ± 0.1
Fe	75 ± 4	72.40 ± 0.7	9.4 ± 1.4	12.58 ± 0.04

Aluminum concentrations in organs were evaluated; however, the signals obtained by ICP-OES were close to or below the method's quantification limit, which compromised the reliability and reproducibility of the measurements. Thus, the results were not considered sufficiently robust for interpretation, and for this reason, it was decided not to report the aluminum concentrations determined by this technique.

The affinity of compound **3a** for bivalent metals, which predominantly act as soft and/or intermediate Lewis acids, as described by Pearson's hard and soft

acid-base principle, is expected to be significantly lower. Figures 93A-C and 93D-F show, respectively, the levels of zinc and copper in different organs of control rats, those treated with vehicle and with compound **3a** (5, 25, and 50 mg/kg/day) for 7 days. No statistically significant differences in the levels of these metal ions were observed between the groups in any of the organs analyzed.

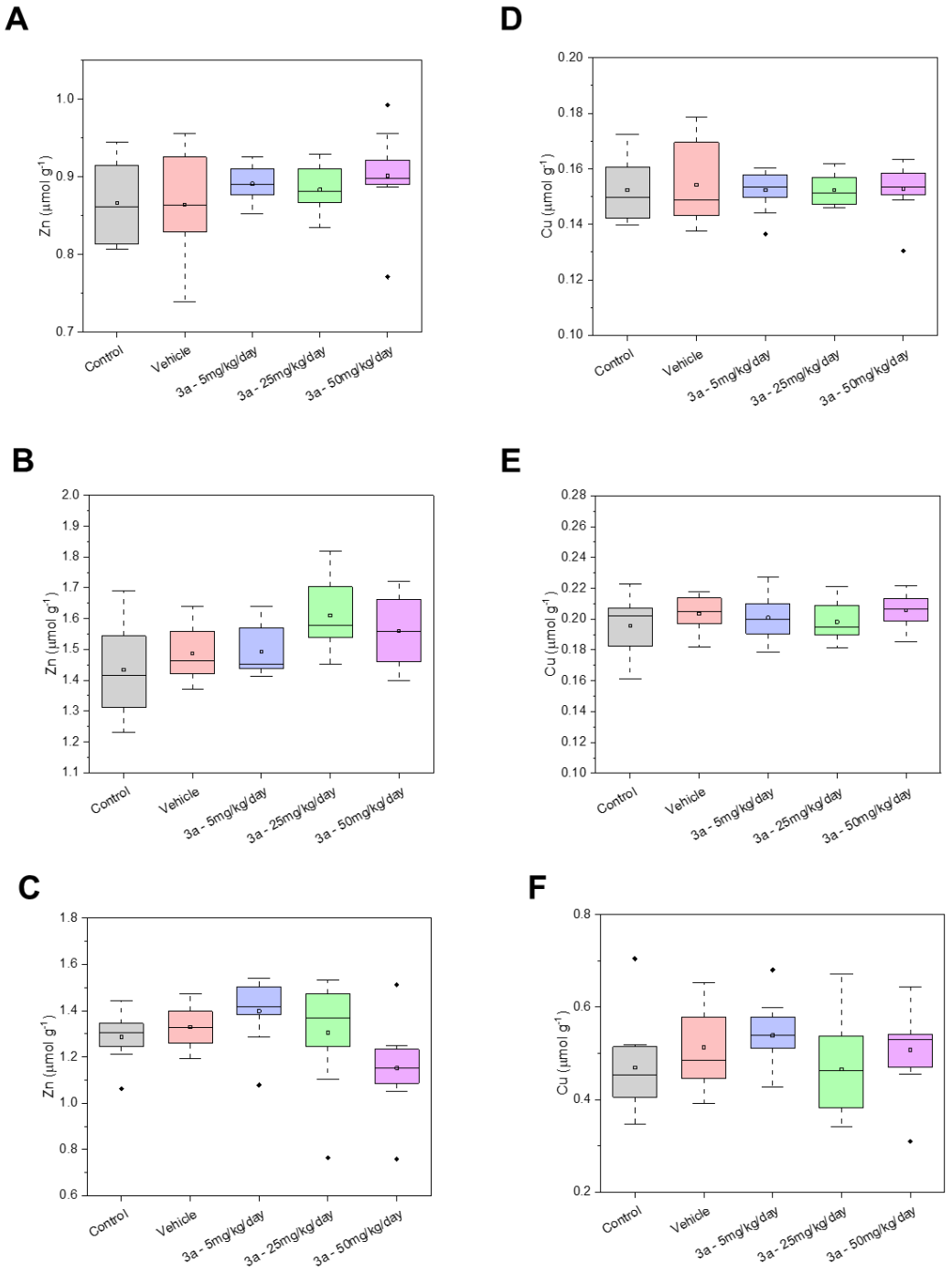

Figure 93. Whisker plot showing the distribution profile of total bivalent metal concentrations (dry weight) in the analyzed organs of male, healthy Wistar rats from control, vehicle, and compound 3a-treated groups. Zinc concentrations are shown in (**A**) brain, (**B**) liver, and (**C**) kidneys; copper concentrations are shown in (**D**) brain, (**E**) liver, and (**F**) kidneys. The "♦" symbol represents outliers.

In the case of iron, the levels determined in the brain and kidneys remained statistically similar between the control, vehicle, and compound **3a**-treated groups (Figure 94A and C). On the other hand, on the liver samples, a statistically significant difference was observed associated with the highest dose tested (group 3, 50 mg/kg/day), which showed a reduction in metal levels compared to the other groups: control (7.95 ± 0.16 $\mu molg^{-1}$, $p = 0.0010$), vehicle (8.20 ± 0.38 $\mu molg^{-1}$, $p = 0.0002$), group 1 – 5 mg/kg/day (7.80 ± 0.33 $\mu molg^{-1}$, $p = 0.0029$) and group 2 – 25 mg/kg/day (7.45 ± 0.33 $\mu molg^{-1}$, $p = 0.0243$) (Figure 94B). Considering the liver's central role in systemic iron storage and regulation, this decrease may reflect a direct effect of compound **3a** on hepatic metal availability. Notably, the group exposed to 50 mg/kg/day also showed a significant reduction in liver weight compared to controls, suggesting a possible correlation between the loss of hepatic iron content and structural or metabolic changes in the organ.

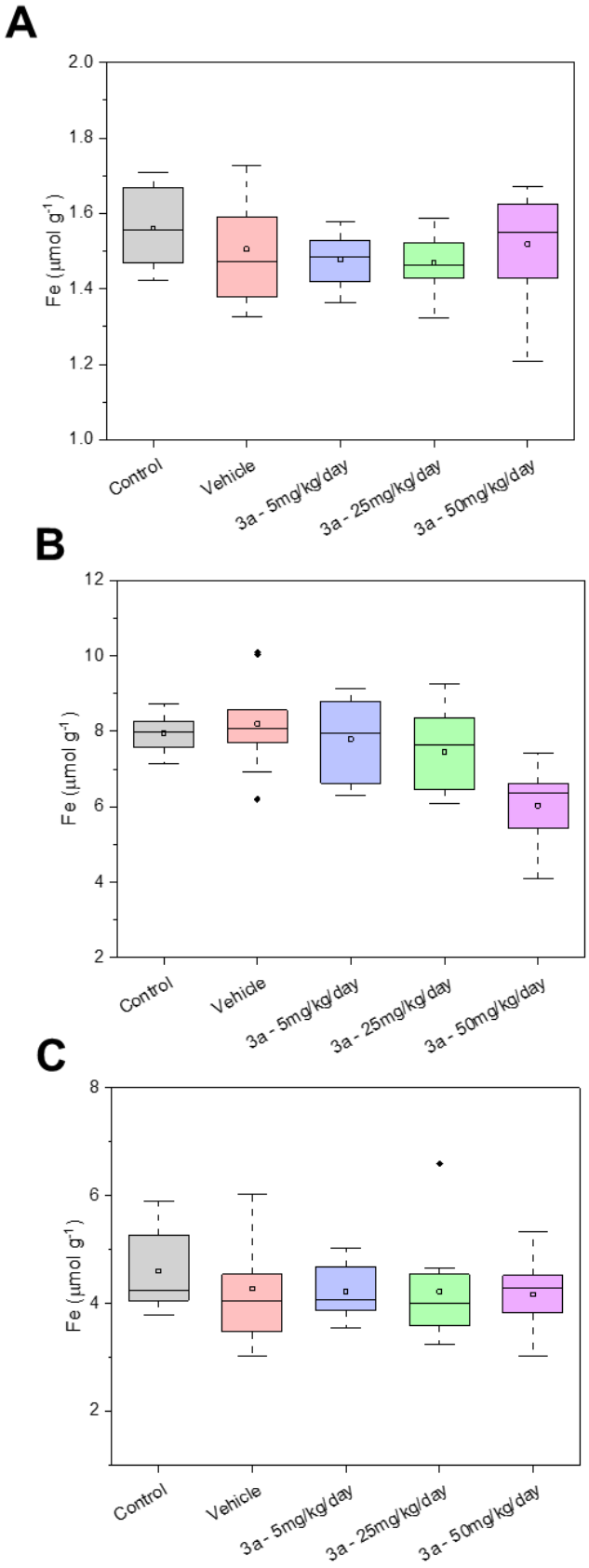

Figure 94. Whiskers Graph istribution profile of total iron concentration in the analyzed organs (dry weight) of control, vehicle- and compound 3a male, healthy, *Wistar* rats. (**A**) Brain (**B**) Liver and (**C**) Kidneys. The "♦" symbol represents outliers.

It is worth noting that, under physiological conditions, iron(III) is predominantly bound to proteins, such as ferritin in the liver.Thus, the reduction in hepatic iron levels observed following exposure to the highest dose of compound **3a** suggests that the compound may be able to compete, to some extent, with these storage systems, promoting mobilization or removal of the metal. Given the predicted high affinity of the ligand for Al^{3+}, it is plausible to assume that, in the presence of this metal, its interaction with Fe^{3+} would be reduced or even inhibited, thereby contributing to the preservation of iron homeostasis. In this context, further investigations using aluminum intoxication models are essential to assess the compound's selectivity under pathological conditions and its safety regarding the mobilization of endogenous metals.

Another important factor to consider is the dose administered to the animals. Given that the average weight of the animals in group 3 was 264.2 g, the dose of 50 mg corresponds to approximately 13.21 mg/day per animal. To estimate the human equivalent dose (HED), an interspecies conversion factor based on body surface area was applied, as recommended by the Food and Drug Administration (FDA) (Saadh; Haddad; Dababneh, 2020), which suggests dividing the rodent dose by a factor of 6.2. Based on this calculation, the dose administered to the rats is equivalent to 8.06 mg/kg in humans. Multiplying this value by the average adult body weight (70 kg) yields an estimated total daily dose of 564.2 mg. It is important to highlight that the dose employed in this study is substantially higher than those used in approved medications for Parkinson's disease, such as Levodopa, which typically has a daily therapeutic dose of approximately 150 mg. This discrepancy suggests that the effects observed at elevated doses reflect an extreme experimental condition, not directly comparable to the therapeutic range commonly applied in clinical settings. As a future perspective, it is essential to adjust the compound's dosage in order to minimize the adverse effects observed at elevated concentrations and to ensure the safety and efficacy of the treatment at levels compatible with clinical application.

10. Conclusions

In this study, 15 bioinspired *N*-acylhydrazones were initially considered as possible aluminum(III) chelators for the treatment of parkinsonism syndrome caused by occupational exposure. After an *in silico* pharmacological analysis, 10 of those compounds were selected as those with the greatest potential for this study. These hydrazones were synthesized and fully characterized, both in solution and in the solid state. In the solid state, new crystalline structures were determined by XRD. An intramolecular H-bond involving the phenolic hydroxy group and the azomethine nitrogen N1 was identified in the solid state for all of them, and it seems to be maintained in DMSO-d_6 solution.

Solubility in aqueous media was assessed considering a percentage of organic solvent (DMSO) of no more than 10%. Only 9 compounds could be studied, under these conditions, for stability in acidic and neutral aqueous conditions. After this assessment, only 4 of the structures initially proposed were satisfactorily stable under both conditions. The use of transport and controlled delivery systems, such as β-CDs, can help increase the solubility and stability of compounds. This remains as a suggestion for future work.

A DMSO vehicle tolerance test on *Saccharomyces cerevisiae* yeast cell line showed a maximum tolerance of 7% of the organic solvent. Due to lack of cellular tolerance to the vehicle (DMSO), only compound **3a** was tested *in vitro*, showing low toxicity to eukaryotic yeast cells at concentrations up to 900 μM. In studies with SH-SY5Y human neuroblastoma cells, this compound demonstrated a dose-dependent cytotoxic effect, showing a 40% reduction in cell viability at 90 μM. This result suggests its potential for use in cell-based and *in vivo* systems, though requiring careful dose optimization to ensure a safe therapeutic window.

Compound **3a** was also tested for its chelation properties against aluminum ions. An unexpected M_2L stoichiometry was observed at pH 4.5, when chloride ions were present in solution. We attribute this stoichiometry to the dimerization of the $AlCl_3$ salt *via* formation of chloride-bridges prior to coordination. In addition, the Method of Continuous Variations was used to obtain the apparent affinity value of the ligand for the metal ion. In order to avoid dimerization, we used aluminum nitrate, and the obtained value ($\log K_{app} = 4.60 \pm 0.08$) indicates a good chelating potential of compound **3a** against Al^{3+} ions, even in acidic conditions.

A complex derived from **3a**, [Al(**3a**)(OH_2)$_3$](NO_3)$_2$·2H_2O, which is highly soluble in water, was isolated in its crystalline form. In the refined structure, the *N*-acylhydrazone is fully deprotonated and coordinates aluminum(III) as a tridentate meridional O_2N-donor ligand.

Biophysical studies investigating the interaction between α-Syn and Al^{3+} at a residue-specific level of resolution demonstrated a time-dependent behavior. This observation suggests a dynamic process that can impact or influence the onset of synucleinopathies, in which aluminum could contribute to the gradual accumulation of misfolded proteins over decades. Moreover, the binary interactions of α-Syn with compound **3a** as well as the ternary interactions between α-Syn, Al^{3+} and **3a** were also studied in solution. The results showed that the *N*-acylhydrazone does not interact directly with the protein. On the other hand, in the presence of aluminum, we identified the formation of an unprecedented ternary complex involving α-Syn.

In healthy animal studies, we verified the ability of compound **3a** to cross the blood-brain barrier using high-resolution chromatography. The results showed that the compound can be detected in the brains of animals after oral administration. Chronic toxicity tests *in vivo* showed that compound **3a** is well tolerated at low concentrations by the animal model. Regarding the distribution of metal ions, compound **3a** did not significantly alter zinc and copper levels in the analyzed organs, suggesting low affinity for these metals under physiological conditions. On the other hand, the reduction in hepatic iron levels, along with the decrease in relative liver weight observed in the group treated with the highest dose, indicates that the compound may interfere with iron homeostasis in the liver. However, it is important to note that these effects were associated with high hydrazone concentrations, highlighting the need for further investigation with doses compatible with therapeutic use, preferably using *in vivo* models chronically exposed to the target metal. Given the results obtained herein, we strongly believe that compound **3a** may indeed constitute a promising candidate for additional pre-clinical studies in the context of aluminum-associated synucleinopathy.

11. Future perspective

The results obtained provide a foundation for designing the next stages of investigation, which will focus on methodological refinements, dosage definition, and compound validation in pathologically relevant models.

As a first step, it is essential to conduct the optimization of the solid-state synthesis methodology of the complex. Enhancing the synthetic protocol aims to increase reaction yield, improve material purity and reproducibility, and thus facilitate a more robust characterization using techniques such as CHN elemental analysis, for example. Simultaneously, studies involving compound dosage adjustment can be conducted. The observation of adverse effects at high concentrations makes it mandatory to determine the maximum tolerated dose and the minimum effective dose, thereby establishing a safe therapeutic window. This step is crucial for preventing issues observed in this work, such as the removal of important endogenous metals.

Finally, and critical for validating the compound against the proposed chelation and reduction of aluminum-induced parkinsonism, it is fundamental to perform studies utilizing optimized *in vitro* and *in vivo* aluminum intoxication models. These assays are crucial for assessing the compound's selectivity under pathological conditions, confirming that its chelating activity is directed toward aluminum without inducing the mobilization of essential endogenous metals. The demonstration of this selectivity and safety in a disease context is a vital indicator for advancing the compound as a potential therapeutic agent.

12. Bibliography

AARSLAND, Dag; ZACCAI, Julia; BRAYNE, Carol. A systematic review of prevalence studies of dementia in Parkinson's disease. **Movement Disorders**, v. 20, n. 10, p. 1255–1263, 22 out. 2005.

ABEYAWARDHANE, Dinendra L. *et al.* Iron Redox Chemistry Promotes Antiparallel Oligomerization of α-Synuclein. **Journal of the American Chemical Society**, v. 140, n. 15, p. 5028–5032, 18 abr. 2018.

ABOGHAZLEH, Refat *et al.* Rodent brain extraction and dissection: A comprehensive approach. **MethodsX**, v. 12, p. 102516, jun. 2024.

ABULKHAIR, Hamada S. *et al.* Novel triazolophthalazine-hydrazone hybrids as potential PCAF inhibitors: Design, synthesis, *in vitro* anticancer evaluation, apoptosis, and molecular docking studies. **Bioorganic Chemistry**, v. 100, p. 103899, jul. 2020.

ABUMELHA, Hana M. A. Synthesis and Spectroscopic Characterization of Some Hydrazone and 2 *H* -benzopyranone Derivatives as Antitumor Agents. **Journal of Heterocyclic Chemistry**, v. 55, n. 7, p. 1738–1745, 24 jul. 2018.

AIDE, Michael. Aluminum Soil Chemistry: Influence on Soil Health and Forest Ecosystem Productivity. **Agricultural Sciences**, v. 13, n. 08, p. 917–935, 2022.

AITMAN, Timothy J. *et al.* Progress and prospects in rat genetics: a community view. **Nature Genetics**, v. 40, n. 5, p. 516–522, 28 maio 2008.

ALASFAR, Reema H.; ISAIFAN, Rima J. Aluminum environmental pollution: the silent killer. **Environmental Science and Pollution Research**, v. 28, n. 33, p. 44587–44597, 1 set. 2021.

ALHARBI, Mashael M. *et al.* Synthesis and lewis acidity of fluorinated triaryl borates. **Dalton Transactions**, v. 52, n. 6, p. 1820–1825, 2023.

AL-THANI, Hanadi; KOÇ, Muammer; ISAIFAN, Rima J. A review on the direct effect of particulate atmospheric pollution on materials and its mitigation for sustainable cities and societies. **Environmental Science and Pollution Research**, v. 25, n. 28, p. 27839–27857, 20 out. 2018.

ANGELOVA, Violina T. *et al.* Development of New Antimycobacterial Sulfonyl Hydrazones and 4-Methyl-1,2,3-thiadiazole-Based Hydrazone Derivatives. **Antibiotics**, v. 11, n. 5, p. 562, 22 abr. 2022.

ANNA DE FALCO. **Activity evaluation and toxicological profile of new potential "Metal Protein Attenuating Compounds" in biological models of Alzheimer's disease**. Rio de Janeiro: Pontifícia Universidade Católica do Rio de Janeiro, 2017.

APEX3. **Bruker: Madison**. EUA, 2012.

ARUNAGIRI, C. *et al.* Crystal Structure, Vibrational, Optical, and Photoluminescence Analyses of Schiff Base 4-Bromo-N′-[(5-bromo-2-hydroxyphenyl)methylidene]benzohydrazide Single Crystals. **Journal of Electronic Materials**, v. 53, n. 12, p. 7937–7945, 27 dez. 2024.

ASLANHAN, Özlem *et al.* Design, synthesis, antioxidant and anticholinesterase activities of novel isonicotinic hydrazide-hydrazone derivatives. **Journal of Molecular Structure**, v. 1279, p. 135037, maio 2023.

BAHAR AKIN, Semra. The Effects of Total Parenteral Nutrition on Plasma Aluminum Levels in Premature. **SiSli Etfal Hastanesi Tip Bulteni / The Medical Bulletin of Sisli Hospital**, p. 106–112, 2025.

BAI, Jia *et al.* α-synuclein-lanthanide metal ions interaction: binding sites, conformation and fibrillation. **BMC Biophysics**, v. 9, n. 1, p. 1, 3 dez. 2015.

BARABASZ, W. ;. Albinska, D. ;. Jaskowska, M. ;. Lipiec, J. Ecotoxicology of

aluminium. **Pol. J. Environ. Stud.**, v. 3, n. 11, p. 199–203, 2002.

BARBUTI, Peter A. A-Syn(ful) MAM: A Fresh Perspective on a Converging Domain in Parkinson's Disease. **International Journal of Molecular Sciences**, v. 25, n. 12, p. 6525, 13 jun. 2024.

BARBUTI, Peter A. *et al.* The role of alpha-synuclein in synucleinopathy: Impact on lipid regulation at mitochondria–ER membranes. **npj Parkinson's Disease**, v. 11, n. 1, p. 103, 30 abr. 2025.

BARTOLIĆ, Marija *et al.* Evaluation of hydrazone and *N* -acylhydrazone derivatives of vitamin B6 and pyridine-4-carbaldehyde as potential drugs against Alzheimer's disease. **Journal of Enzyme Inhibition and Medicinal Chemistry**, v. 39, n. 1, 31 dez. 2024.

BARTZOKIS, George *et al.* Increased Basal Ganglia Iron Levels in Huntington Disease. **Archives of Neurology**, v. 56, n. 5, p. 569, 1 maio 1999.

BELLUCCI, Arianna *et al.* From α-synuclein to synaptic dysfunctions: New insights into the pathophysiology of Parkinson's disease. **Brain Research**, v. 1476, p. 183–202, out. 2012.

BENET, Leslie Z. *et al.* BDDCS, the Rule of 5 and drugability. **Advanced Drug Delivery Reviews**, v. 101, p. 89–98, jun. 2016.

BENKOVIĆ, T. *et al.* Aromatic hydrazones derived from nicotinic acid hydrazide as fluorimetric pH sensing molecules: Structural analysis by computational and spectroscopic methods in solid phase and in solution. **Spectrochimica Acta Part A: Molecular and Biomolecular Spectroscopy**, v. 190, p. 259–267, fev. 2018.

BERLANA, David *et al.* Comparing Aluminum Concentrations in Adult and Pediatric Parenteral Nutrition Solutions: Multichamber-Bag versus Compounded Parenteral Nutrition. **Nutrients**, v. 16, n. 7, p. 1024, 1 abr. 2024.

BICKERTON, G. Richard *et al.* Quantifying the chemical beauty of drugs. **Nature Chemistry**, v. 4, n. 2, p. 90–98, 24 fev. 2012.

BIELIAUSKAS, Aurimas *et al.* Synthesis of electroactive hydrazones derived from carbazolyl-based 2-propenals for optoelectronics. **Synthetic Metals**, v. 179, p. 27–33, set. 2013.

BIGHAM, J. M.; NORDSTROM, D. K. Iron and Aluminum Hydroxysulfates from Acid Sulfate Waters. **Reviews in Mineralogy and Geochemistry**, v. 40, n. 1, p. 351–403, 1 jan. 2000.

BIKAS, Rahman *et al.* (*E*)- *N* ′-(2-Hydroxybenzylidene)furan-2-carbohydrazide. **Acta Crystallographica Section E Structure Reports Online**, v. 66, n. 8, p. o2015–o2015, 15 ago. 2010.

BINOLFI, Andrés *et al.* Interaction of α-Synuclein with Divalent Metal Ions Reveals Key Differences: A Link between Structure, Binding Specificity and Fibrillation Enhancement. **Journal of the American Chemical Society**, v. 128, n. 30, p. 9893–9901, 1 ago. 2006.

BLOWES, D. W. *et al.* The Geochemistry of Acid Mine Drainage. *In*: **Treatise on Geochemistry**. *[S.l.]*: Elsevier, 2003. p. 149–204.

BONATO, Giulia *et al.* Genetic mutations in Parkinson's disease: screening of a selected population from North-Eastern Italy. **Neurological Sciences**, v. 46, n. 1, p. 165–174, 22 jan. 2025.

BONFIGLIO, Rita; SCIMECA, Manuel; MAURIELLO, Alessandro. The impact of aluminum exposure on human health. **Archives of Toxicology**, v. 97, n. 11, p. 2997–2998, 19 nov. 2023.

BOTTÉ, Audrey *et al.* Aluminium in aquatic environments: abundance and ecotoxicological impacts. **Aquatic Ecology**, v. 56, n. 3, p. 751–773, 27 set. 2022.

BOULLEMANT, Amiel *et al.* Uptake of Hydrophobic Metal Complexes by Three Freshwater Algae: Unexpected Influence of pH. **Environmental Science & Technology**, v. 43, n. 9, p. 3308–3314, 1 maio 2009.

BRAMMER, L.; ZHAO, D. Low-Temperature Structures of [py2H]+[Co(CO)4]− (py = Pyridine) and [(tmen)H]+[Co(CO)4]− (tmen = N,N,N',N'-Tetramethylethylenediamine). **Acta Crystallographica Section C Crystal Structure Communications**, v. 51, n. 1, p. 45–48, 15 jan. 1995.

BREUKER, Kathrin; MCLAFFERTY, Fred W. Stepwise evolution of protein native structure with electrospray into the gas phase, 10^{-12} to 10^{2} s. **Proceedings of the National Academy of Sciences**, v. 105, n. 47, p. 18145–18152, 25 nov. 2008.

BREYDO, Leonid; WU, Jessica W.; UVERSKY, Vladimir N. α-Synuclein misfolding and Parkinson's disease. **Biochimica et Biophysica Acta (BBA) - Molecular Basis of Disease**, v. 1822, n. 2, p. 261–285, fev. 2012.

BROCKIE, Penelope J. *et al.* Differential Expression of Glutamate Receptor Subunits in the Nervous System of *Caenorhabditis elegans* and Their Regulation by the Homeodomain Protein UNC-42. **The Journal of Neuroscience**, v. 21, n. 5, p. 1510–1522, 1 mar. 2001.

BROWN, David R. Metal binding to alpha-synuclein peptides and its contribution to toxicity. **Biochemical and Biophysical Research Communications**, v. 380, n. 2, p. 377–381, mar. 2009.

BRYLIŃSKI, Łukasz *et al.* Aluminium in the Human Brain: Routes of Penetration, Toxicity, and Resulting Complications. **International Journal of Molecular Sciences**, v. 24, n. 8, p. 7228, 13 abr. 2023.

BUCCIANTINI, Monica *et al.* Inherent toxicity of aggregates implies a common mechanism for protein misfolding diseases. **Nature**, v. 416, n. 6880, p. 507–511, abr. 2002.

BULK, Marjolein *et al.* Postmortem MRI and histology demonstrate differential iron accumulation and cortical myelin organization in early- and late-onset Alzheimer's disease. **Neurobiology of Aging**, v. 62, p. 231–242, fev. 2018.

BURATTI, Fiamma A.; FERNÁNDEZ, Claudio Oscar; ZWECKSTETTER, Markus. Parkinson's disease-linked V15A mutation facilitates α-synuclein aggregation by reducing membrane affinity. **Protein Science**, v. 32, n. 8, 20 ago. 2023.

BURROWS, W. Dickinson; HEM, John D. Aquatic aluminum: Chemistry, toxicology, and environmental prevalence∗. **C R C Critical Reviews in Environmental Control**, v. 7, n. 2, p. 167–216, jun. 1977.

CALLEGARI, Edoardo *et al.* Thermodynamic and Kinetic Stabilities of Al(III) Complexes with N2O3 Pentadentate Ligands. **Molecules**, v. 28, n. 9, p. 3764, 27 abr. 2023.

CARVALHO, Alessandra *et al.* New mescaline-related N-acylhydrazone and its unsubstituted benzoyl derivative: Promising metallophores for copper-associated deleterious effects relief in Alzheimer's disease. **Journal of Inorganic Biochemistry**, v. 238, p. 112033, jan. 2023a.

CARVALHO, Alessandra *et al.* New mescaline-related N-acylhydrazone and its unsubstituted benzoyl derivative: Promising metallophores for copper-associated deleterious effects relief in Alzheimer's disease. **Journal of Inorganic Biochemistry**, v. 238, p. 112033, jan. 2023b.

CARVALHO, Alessandra *et al.* Differential Modulation of Copper(II) Interactions with the 18–22 Coordinating Amylin Fragment by the Geometric Isomers of a New Nicotinoyl Hydrazone: A First Study. **ACS Omega**, v. 10, n. 28, p. 31115–31127, 22 jul. 2025.

CHAI, Qing *et al.* Multiple luminescent switching of pyrenyl-substituted

acylhydrazone derivative. **Dyes and Pigments**, v. 152, p. 93–99, maio 2018.

CHANTRAPROMMA, Suchada *et al.* Crystal structure of (*E*)- *N* ′-(3,4-dihydroxybenzylidene)-4-hydroxybenzohydrazide. **Acta Crystallographica Section E Crystallographic Communications**, v. 75, n. 8, p. 1280–1283, 1 ago. 2019.

CHARKOUDIAN, Louise K. *et al.* Modifications of boronic ester pro-chelators triggered by hydrogen peroxide tune reactivity to inhibit metal-promoted oxidative stress. **Dalton Transactions**, n. 43, p. 5031, 2007.

CHEN, Fengjiao *et al.* α-Synuclein aggregation in the olfactory bulb induces olfactory deficits by perturbing granule cells and granular–mitral synaptic transmission. **npj Parkinson's Disease**, v. 7, n. 1, p. 114, 13 dez. 2021.

CHEN, Pan *et al.* Metal-induced neurodegeneration in C. elegans. **Frontiers in aging neuroscience**, v. 5, p. 18, 2013.

CHEN, Zhaoyang *et al.* Effect of total aluminum concentration on the formation and transformation of nanosized Al13 and Al30 in hydrolytic polymeric aluminum aqueous solutions. **Science Bulletin**, v. 50, n. 18, p. 2010–2015, 16 set. 2005.

CHIANG, Shannon *et al.* Frataxin and the molecular mechanism of mitochondrial iron-loading in Friedreich's ataxia. **Clinical Science**, v. 130, n. 11, p. 853–870, 1 jun. 2016.

CIAMPELLI, Cristina *et al.* LRRK2 in Drosophila Melanogaster Model: Insights into Cellular Dysfunction and Neuroinflammation in Parkinson's Disease. **International Journal of Molecular Sciences**, v. 26, n. 5, p. 2093, 27 fev. 2025.

CONNOR, J. R. *et al.* Cellular distribution of transferrin, ferritin, and iron in normal and aged human brains. **Journal of Neuroscience Research**, v. 27, n. 4, p. 595–611, 11 dez. 1990.

CRAPPER, D. R.; DALTON, A. J. Alterations in short-term retention, conditioned avoidance response acquisition and motivation following aluminum induced neurofibrillary degeneration. **Physiology & Behavior**, v. 10, n. 5, p. 925–933, maio 1973.

CRISTINA, Tejera-Parrado *et al.* A genetic analysis of a Spanish population with early onset Parkinson's disease. **PLOS ONE**, v. 15, n. 9, p. e0238098, 1 set. 2020.

CUKIERMAN, D. S. **Physico-chemical optimization and Structure-Activity Relationship studies of aldehyde-derived N-acylhydrazones: towards the improvement of moderate metal chelators as a strategy against metal-enhanced aggregopathies**. Rio de Janeiro: Pontifícia Universidade Católica do Rio de Janeiro, 2021.

CUKIERMAN, Daphne S. *et al.* Aroylhydrazones constitute a promising class of 'metal-protein attenuating compounds' for the treatment of Alzheimer's disease: a proof-of-concept based on the study of the interactions between zinc(II) and pyridine-2-carboxaldehyde isonicotinoyl hydrazone. **JBIC Journal of Biological Inorganic Chemistry**, v. 23, n. 8, p. 1227–1241, 25 dez. 2018.

CUKIERMAN, Daphne S. *et al.* Impact of pyridine-2-carboxaldehyde-derived aroylhydrazones on the copper-catalyzed oxidation of the M112A PrP103–112 mutant fragment. **JBIC Journal of Biological Inorganic Chemistry**, v. 24, n. 8, p. 1231–1244, 10 dez. 2019a.

CUKIERMAN, Daphne S. *et al.* Impact of pyridine-2-carboxaldehyde-derived aroylhydrazones on the copper-catalyzed oxidation of the M112A PrP103–112 mutant fragment. **JBIC Journal of Biological Inorganic Chemistry**, v. 24, n. 8, p. 1231–1244, 10 dez. 2019b.

CUKIERMAN, Daphne S. *et al.* X1INH, an improved next-generation affinity-optimized hydrazonic ligand, attenuates abnormal copper(<scp>i</scp>)/copper(<scp>ii</scp>)-α-Syn interactions and affects protein aggregation in a cellular model of synucleinopathy. **Dalton Transactions**, v. 49, n. 45, p. 16252–16267,

2020a.

CUKIERMAN, Daphne S. *et al.* X1INH, an improved next-generation affinity-optimized hydrazonic ligand, attenuates abnormal copper(<scp>i</scp>)/copper(<scp>ii</scp>)-α-Syn interactions and affects protein aggregation in a cellular model of synucleinopathy. **Dalton Transactions**, v. 49, n. 45, p. 16252–16267, 2020b.

CUKIERMAN, Daphne S. *et al.* Full Equilibrium Picture in Aqueous Binary and Ternary Systems Involving Copper(II), 1-Methylimidazole-Containing Hydrazonic Ligands, and the 103–112 Human Prion Protein Fragment. **Inorganic Chemistry**, v. 61, n. 1, p. 723–737, 10 jan. 2022a.

CUKIERMAN, Daphne S. *et al.* Full Equilibrium Picture in Aqueous Binary and Ternary Systems Involving Copper(II), 1-Methylimidazole-Containing Hydrazonic Ligands, and the 103–112 Human Prion Protein Fragment. **Inorganic Chemistry**, v. 61, n. 1, p. 723–737, 10 jan. 2022b.

CUKIERMAN, Daphne S.; REY, Nicolás A. Tridentate N-Acylhydrazones as Moderate Ligands for the Potential Management of Cognitive Decline Associated With Metal-Enhanced Neuroaggregopathies. **Frontiers in Neurology**, v. 13, 16 fev. 2022.

CUKIERMAN, Daphne Schneider *et al.* A moderate metal-binding hydrazone meets the criteria for a bioinorganic approach towards Parkinson's disease: Therapeutic potential, blood-brain barrier crossing evaluation and preliminary toxicological studies. **Journal of Inorganic Biochemistry**, v. 170, p. 160–168, maio 2017.

CUNAT, Lisiane *et al.* Bioavailability and Intestinal Absorption of Aluminum in Rats : Effects of Aluminum Compounds and Some Dietary Constituents. **Biological Trace Element Research**, v. 76, n. 1, p. 31–56, 2000.

CUPERTINO, Marli do Carmo *et al.* Cadmium-induced testicular damage is

associated with mineral imbalance, increased antioxidant enzymes activity and protein oxidation in rats. **Life Sciences**, v. 175, p. 23–30, abr. 2017.

DA COSTA SALOMÉ, Dayana *et al.* Novel Regioisomeric Analogues of Naphthyl-N-Acylhydrazone Derivatives and Their Anti-Inflammatory Effects. **International Journal of Molecular Sciences**, v. 23, n. 21, p. 13562, 5 nov. 2022.

DALLA TORRE, Gabriele *et al.* Tuning the affinity of catechols and salicylic acids towards Al(<scp>iii</scp>): characterization of Al–chelator interactions. **Dalton Transactions**, v. 47, n. 29, p. 9592–9607, 2018.

DALLA TORRE, Gabriele *et al.* The interaction of aluminum with catecholamine-based neurotransmitters: can the formation of these species be considered a potential risk factor for neurodegenerative diseases? **Dalton Transactions**, v. 48, n. 18, p. 6003–6018, 2019a.

DALLA TORRE, Gabriele *et al.* The interaction of aluminum with catecholamine-based neurotransmitters: can the formation of these species be considered a potential risk factor for neurodegenerative diseases? **Dalton Transactions**, v. 48, n. 18, p. 6003–6018, 2019b.

DASCALU, Anca-Elena *et al.* Design, synthesis and evaluation of hydrazine and acyl hydrazone derivatives of 5-pyrrolidin-2-one as antifungal agents. **Bioorganic & Medicinal Chemistry Letters**, v. 30, n. 13, p. 127220, jul. 2020.

DATTA, Riya *et al. N '*-[(*E*)-Furan-2-ylmethylidene]-4-hydroxybenzohydrazide. **Acta Crystallographica Section E Structure Reports Online**, v. 70, n. 3, p. o242–o242, 1 mar. 2014.

DE FALCO, Anna *et al.* The aroylhydrazone INHHQ prevents memory impairment induced by Alzheimer's-linked amyloid-β oligomers in mice. **Behavioural Pharmacology**, v. 31, n. 8, p. 738–747, 6 dez. 2020.

DE FALCO, Anna *et al.* Luminescence imaging and toxicity assessment of

graphene quantum dots using *in vitro* models. **Fullerenes, Nanotubes and Carbon Nanostructures**, v. 30, n. 6, p. 657–666, 3 jun. 2022.

DE FREITAS, Leonardo Viana *et al.* Structural and vibrational study of 8-hydroxyquinoline-2-carboxaldehyde isonicotinoyl hydrazone – A potential metal–protein attenuating compound (MPAC) for the treatment of Alzheimer's disease. **Spectrochimica Acta Part A: Molecular and Biomolecular Spectroscopy**, v. 116, p. 41–48, dez. 2013.

DE QUEIROZ, Aline Cavalcanti *et al.* Pre-clinical evaluation of LASSBio-1491: From *in vitro* pharmacokinetic study to *in vivo* leishmanicidal activity. **PLOS ONE**, v. 17, n. 6, p. e0269447, 6 jun. 2022.

DE RIJK, M. C. *et al.* Prevalence of parkinsonism and Parkinson's disease in Europe: the EUROPARKINSON Collaborative Study. European Community Concerted Action on the Epidemiology of Parkinson's disease. **Journal of Neurology, Neurosurgery & Psychiatry**, v. 62, n. 1, p. 10–15, 1 jan. 1997.

DEAS, Emma *et al.* Alpha-Synuclein Oligomers Interact with Metal Ions to Induce Oxidative Stress and Neuronal Death in Parkinson's Disease. **Antioxidants & Redox Signaling**, v. 24, n. 7, p. 376–391, mar. 2016.

DELEERS, Michel; SERVAIS, Jean-Paul; WÜLFERT, Ernst. Neurotoxic cations induce membrane rigidification and membrane fusion at micromolar concentrations. **Biochimica et Biophysica Acta (BBA) - Biomembranes**, v. 855, n. 2, p. 271–276, fev. 1986.

DEMIR, Yeliz *et al.* Synthesis and characterization of novel acyl hydrazones derived from vanillin as potential aldose reductase inhibitors. **Molecular Diversity**, v. 27, n. 4, p. 1713–1733, 14 ago. 2023.

DEVOS, David *et al.* Targeting Chelatable Iron as a Therapeutic Modality in Parkinson's Disease. **Antioxidants & Redox Signaling**, v. 21, n. 2, p. 195–210, 10 jul. 2014.

DING, Yongjie *et al.* Ortho-Vanillin-based fluorescent sensor with ESIPT characteristics for selective detection of Al(III) in aqueous solutions and its application for plant and live-cell imaging. **Journal of Molecular Structure**, v. 1299, p. 137159, mar. 2024.

DITTRICH, Jonas *et al.* Converging a Knowledge-Based Scoring Function: DrugScore ^{2018}. **Journal of Chemical Information and Modeling**, v. 59, n. 1, p. 509–521, 28 jan. 2019.

DONGARE, Gajanan; ASWAR, Anand. Synthesis of new heterocyclic N'-(2-hydroxy-3-methoxybenzylidene)-4-oxopiperidine-1-carbohydrazide and its mononuclear metal (II) complexes: Spectroscopic characterization, fluorescence, DFT, thermo-kinetic, and antimicrobial studies. **Journal of Molecular Structure**, v. 1281, p. 135107, jun. 2023.

DOUGLAS, Samuel P. *et al.* Tris(β-ketoiminate) Aluminium(III) Compounds as Aluminium Oxide Precursors. **ChemPlusChem**, v. 88, n. 1, 16 jan. 2023.

DRABEK, Ondrej *et al.* Possible method of aluminium speciation in forest soils. **Journal of Inorganic Biochemistry**, v. 97, n. 1, p. 8–15, set. 2003.

DRUI, G. *et al.* Loss of dopaminergic nigrostriatal neurons accounts for the motivational and affective deficits in Parkinson's disease. **Molecular Psychiatry**, v. 19, n. 3, p. 358–367, 12 mar. 2014.

EDWARDS, H. G. M.; FARWELL, D. W.; JOHNSON, A. F. FT-Raman spectroscopic study of aluminium(III) chloride in acetonitrile and dichloromethane solutions containing water. **Journal of Molecular Structure**, v. 344, n. 1–2, p. 37–44, jan. 1995.

EGAN, William J.; MERZ, , Kenneth M.; BALDWIN, John J. Prediction of Drug Absorption Using Multivariate Statistics. **Journal of Medicinal Chemistry**, v. 43, n. 21, p. 3867–3877, 1 out. 2000.

EL-SAYED, Wael M.; AL-KAHTANI, Mohamed A.; ABDEL-MONEIM, Ashraf M. Prophylactic and therapeutic effects of taurine against aluminum-induced acute hepatotoxicity in mice. **Journal of Hazardous Materials**, v. 192, n. 2, p. 880–886, ago. 2011.

EXLEY, C. A biogeochemical cycle for aluminium? **Journal of Inorganic Biochemistry**, v. 97, n. 1, p. 1–7, 15 set. 2003.

EXLEY, C. The toxicity of aluminium in humans. **Morphologie**, v. 100, n. 329, p. 51–55, jun. 2016.

EXLEY, Christopher *et al.* Aluminum in Tobacco and Cannabis and Smoking-Related Disease. **The American Journal of Medicine**, v. 119, n. 3, p. 276.e9-276.e11, mar. 2006.

EXLEY, Christopher; MOLD, Matthew J. The binding, transport and fate of aluminium in biological cells. **Journal of Trace Elements in Medicine and Biology**, v. 30, p. 90–95, abr. 2015.

EXLEY, Christopher; MOLD, Matthew J. Aluminium in human brain tissue: how much is too much? **JBIC Journal of Biological Inorganic Chemistry**, v. 24, n. 8, p. 1279–1282, 29 dez. 2019.

EXLEY, Christopher; VICKERS, Thomas. Elevated brain aluminium and early onset Alzheimer's disease in an individual occupationally exposed to aluminium: a case report. **Journal of Medical Case Reports**, v. 8, n. 1, p. 41, 10 dez. 2014.

FAN, Long *et al.* A colorimetric and turn-on fluorescent chemosensor for Al(III) based on a chromone Schiff-base. **Spectrochimica Acta Part A: Molecular and Biomolecular Spectroscopy**, v. 118, p. 760–764, jan. 2014.

FARMER, V. C. Sources and Speciation of Aluminium and Silicon in Natural Waters. *In*: *[S.l.: S.n.]*. p. 4–23.

FARRUGIA, Louis J. *WinGX* and *ORTEP for Windows*: an update. **Journal of Applied Crystallography**, v. 45, n. 4, p. 849–854, 1 ago. 2012.

FATTORETTI, PATRIZIA *et al.* Chronic Aluminum Administration to Old Rats Results in Increased Levels of Brain Metal Ions and Enlarged Hippocampal Mossy Fibers. **Annals of the New York Academy of Sciences**, v. 1019, n. 1, p. 44–47, 12 jun. 2004.

FERNÁNDEZ-PALACIOS, Sara *et al.* New Insights into Acylhydrazones E/Z Isomerization: An Experimental and Theoretical Approach. **International Journal of Molecular Sciences**, v. 24, n. 19, p. 14739, 29 set. 2023.

FIRMINO, Gisele dos S. S. *et al. In vitro* assessment of the cytotoxicity of Gallium(III) complexes with Isoniazid-Derived Hydrazones: Effects on clonogenic survival of HCT-116 cells. **Inorganica Chimica Acta**, v. 497, p. 119079, nov. 2019.

FLORES-LEÓN, Manuel; OUTEIRO, Tiago F. Expanding our understanding of synucleinopathies: proteinopathy, proteinopenia, and lipidopathy. **The FEBS Journal**, 25 fev. 2025.

FRANCO, Lucas Silva *et al.* Exploring the Conformational Effects of *N* - and *C* -Methylation of *N* -Acylhydrazones. **ACS Omega**, v. 10, n. 17, p. 17993–18004, 6 maio 2025.

GALIĆ, N. *et al.* Structural and spectroscopic characteristics of aroylhydrazones derived from nicotinic acid hydrazide. **Journal of Molecular Structure**, v. 559, n. 1–3, p. 187–194, jan. 2001.

GALIĆ, Nives *et al.* Solution and solid-state studies of complexation of transition-metal cations and Al(III) by aroylhydrazones derived from nicotinic acid hydrazide. **Inorganica Chimica Acta**, v. 366, n. 1, p. 98–104, jan. 2011.

GALIĆ, Nives *et al.* Structural investigation of aroylhydrazones in dimethylsulphoxide/water mixtures. **Spectrochimica Acta Part A: Molecular and Biomolecular Spectroscopy**, v. 95, p. 347–353, set. 2012.

GALIĆ, Nives; CIMERMAN, Zvjezdana; TOMIŠIĆ, Vladislav. Spectrometric study of tautomeric and protonation equilibria of o-vanillin Schiff base derivatives and their complexes with Cu(II). **Spectrochimica Acta Part A: Molecular and Biomolecular Spectroscopy**, v. 71, n. 4, p. 1274–1280, dez. 2008.

GALLO, Elisa *et al.* Aluminium 8-Hydroxyquinolinate N-Oxide as a Precursor to Heterometallic Aluminium–Lanthanide Complexes. **Molecules**, v. 29, n. 2, p. 451, 17 jan. 2024.

GANHÖR, Clara *et al.* Airborne Aluminum as an Underestimated Source of Human Exposure: Quantification of Aluminum in 24 Human Tissue Types Reveals High Aluminum Concentrations in Lung and Hilar Lymph Node Tissues. **Environmental Science & Technology**, v. 58, n. 26, p. 11292–11300, 2 jul. 2024.

GEIBL, Fanni F. *et al.* α-Synuclein pathology disrupts mitochondrial function in dopaminergic and cholinergic neurons at-risk in Parkinson's disease. **Molecular Neurodegeneration**, v. 19, n. 1, p. 69, 8 out. 2024.

GENTILE, Iñaki *et al.* Interaction of Cu(<scp>i</scp>) with the Met-X3-Met motif of alpha-synuclein: binding ligands, affinity and structural features. **Metallomics**, v. 10, n. 10, p. 1383–1389, 17 out. 2018.

GHOSE, Arup K.; VISWANADHAN, Vellarkad N.; WENDOLOSKI, John J. A Knowledge-Based Approach in Designing Combinatorial or Medicinal Chemistry Libraries for Drug Discovery. 1. A Qualitative and Quantitative Characterization of Known Drug Databases. **Journal of Combinatorial Chemistry**, v. 1, n. 1, p. 55–68, 12 jan. 1999.

GIACOBELLO, Fausta *et al.* Hydrolysis of Al3+ in Aqueous Solutions: Experiments and Ab Initio Simulations. **Liquids**, v. 2, n. 1, p. 26–38, 3 mar. 2022.

GLEESON, M. Paul. Generation of a Set of Simple, Interpretable ADMET Rules of Thumb. **Journal of Medicinal Chemistry**, v. 51, n. 4, p. 817–834, 1 fev. 2008.

GOEDERT, Michel. Alpha-synuclein and neurodegenerative diseases. **Nature Reviews Neuroscience**, v. 2, n. 7, p. 492–501, jul. 2001.

GÓMEZ-BENITO, Mónica *et al.* Modeling Parkinson's Disease With the Alpha-Synuclein Protein. **Frontiers in Pharmacology**, v. 11, 23 abr. 2020.

GONZÁLEZ, Nazareno *et al.* Effects of alpha-synuclein post-translational modifications on metal binding. **Journal of Neurochemistry**, v. 150, n. 5, p. 507–521, 9 set. 2019.

GONZÁLEZ-BARÓ, Ana C. *et al.* Spectroscopic and theoretical study of the o-vanillin hydrazone of the mycobactericidal drug isoniazid. **Journal of Molecular Structure**, v. 1007, p. 95–101, jan. 2012.

GOOD, Paul F.; OLANOW, C. W.; PERL, Daniel P. Neuromelanin-containing neurons of the substantia nigra accumulate iron and aluminum in Parkinson's disease: a LAMMA study. **Brain Research**, v. 593, n. 2, p. 343–346, out. 1992.

GU, Yaxin *et al.* DBPP-Predictor: a novel strategy for prediction of chemical drug-likeness based on property profiles. **Journal of Cheminformatics**, v. 16, n. 1, p. 4, 5 jan. 2024.

GUATTEO, Ezia *et al.* Pathophysiological Features of Nigral Dopaminergic Neurons in Animal Models of Parkinson's Disease. **International Journal of Molecular Sciences**, v. 23, n. 9, p. 4508, 19 abr. 2022.

GUILHERME DOS SANTOS MALHEIROS. **Síntese e caracterização de potenciais 'Metal- Protein Attenuating Compounds' hidrazônicos e avaliação da complexação ao íon vanadila como possível forma de administração no con- texto da doença de Alzheimer**. Rio de Janeiro: Pontifícia Universidade

Católica do Rio de Janeiro, 2018.

GUIMARÃES, Cristiano R. W. *et al.* Use of 3D Properties to Characterize Beyond Rule-of-5 Property Space for Passive Permeation. **Journal of Chemical Information and Modeling**, v. 52, n. 4, p. 882–890, 23 abr. 2012.

GUPTA, Nidhi; GAURAV, Shailendra Singh; KUMAR, Ashwani. Molecular Basis of Aluminium Toxicity in Plants: A Review. **American Journal of Plant Sciences**, v. 04, n. 12, p. 21–37, 2013.

HANSCH, Corwin; BJÖRKROTH, J. P.; LEO, A. Hydrophobicity and Central Nervous System Agents: On the Principle of Minimal Hydrophobicity in Drug Design. **Journal of Pharmaceutical Sciences**, v. 76, n. 9, p. 663–687, set. 1987.

HAUSER-DAVIS, R. A. *et al.* Disruption of zinc and copper interactions with Aβ(1–40) by a non-toxic, isoniazid-derived, hydrazone: a novel biometal homeostasis restoring agent in Alzheimer's disease therapy? **Metallomics**, v. 7, n. 5, p. 743–747, 2015.

HAYFLICK, Susan J.; KURIAN, Manju A.; HOGARTH, Penelope. Neurodegeneration with brain iron accumulation. *In*: *[S.l.: S.n.]*. p. 293–305.

HELENA, Eduarda Santa *et al.* Cardiotoxicity and ROS Protection Assessment of three Structure-Related *N* -Acylhydrazones with Potential for the Treatment of Neurodegenerative Diseases. **Chemistry & Biodiversity**, v. 21, n. 3, 29 mar. 2024a.

HELENA, Eduarda Santa *et al.* Cardiotoxicity and ROS Protection Assessment of three Structure-Related *N* -Acylhydrazones with Potential for the Treatment of Neurodegenerative Diseases. **Chemistry & Biodiversity**, v. 21, n. 3, 29 mar. 2024b.

HÉMADI, Miryana *et al.* Aluminum Exchange between Citrate and Human Serum Transferrin and Interaction with Transferrin Receptor 1. **Biochemistry**, v. 42, n. 10,

p. 3120–3130, 1 mar. 2003.

HIZLI, Sezin *et al.* Identifying Geogenic and Anthropogenic Aluminum Pollution on Different Spatial Distributions and Removal of Natural Waters and Soil in Çanakkale, Turkey. **ACS Omega**, v. 8, n. 9, p. 8557–8568, 7 mar. 2023.

HORVITZ, H. Robert *et al.* Serotonin and Octopamine in the Nematode *Caenorhabditis elegans*. **Science**, v. 216, n. 4549, p. 1012–1014, 28 maio 1982.

HOYER, Wolfgang *et al.* Impact of the Acidic C-Terminal Region Comprising Amino Acids 109−140 on α-Synuclein Aggregation *in Vitro*. **Biochemistry**, v. 43, n. 51, p. 16233–16242, 1 dez. 2004.

HÜBSCHLE, Christian B.; SHELDRICK, George M.; DITTRICH, Birger. *ShelXle* : a Qt graphical user interface for *SHELXL*. **Journal of Applied Crystallography**, v. 44, n. 6, p. 1281–1284, 1 dez. 2011.

HUH, Young Eun *et al.* GBA1 Variants and Parkinson's Disease: Paving the Way for Targeted Therapy. **Journal of Movement Disorders**, v. 16, n. 3, p. 261–278, 30 set. 2023.

IANNACCONE, Philip M.; JACOB, Howard J. Rats! **Disease Models & Mechanisms**, v. 2, n. 5–6, p. 206–210, 30 abr. 2009.

IGBOKWE, Ikechukwu Onyebuchi; IGWENAGU, Ephraim; IGBOKWE, Nanacha Afifi. Aluminium toxicosis: a review of toxic actions and effects. **Interdisciplinary Toxicology**, v. 12, n. 2, p. 45–70, 1 out. 2019.

INAN-EROGLU, Elif; AYAZ, Aylin. Is aluminum exposure a risk factor for neurological disorders? **Journal of Research in Medical Sciences**, v. 23, n. 1, p. 51, 2018.

IRWIN, David J.; LEE, Virginia M. Y.; TROJANOWSKI, John Q. Parkinson's disease dementia: convergence of α-synuclein, tau and amyloid-β pathologies.

Nature Reviews Neuroscience, v. 14, n. 9, p. 626–636, 31 set. 2013.

JACKSON JS, Rout P. **Aluminum Toxicity**. Disponível em: <https://www.ncbi.nlm.nih.gov/books/NBK609094/>. Acesso em: 24 maio. 2025.

JASIEN, Paul G. The Role of AlCl3 and Al2Cl6 in the Catalyzed Decomposition of Organic Halides. **The Journal of Physical Chemistry**, v. 99, n. 17, p. 6502–6508, 1 abr. 1995.

JAYANTHI M, Thirunavukkarasu SV. Effect of Manasamitra Vatakam Against Aluminium Induced Learning and Memory Impairment of Apoptosis in Rat's Hippocampus and Cortex. **Journal of Drug Metabolism & Toxicology**, v. 04, n. 04, 2013.

JERŠEK, Miha *et al.* Intriguing minerals: corundum in the world of rubies and sapphires with special attention to Macedonian rubies. **ChemTexts**, v. 7, n. 3, p. 19, 28 set. 2021.

JI, Kun *et al.* Triazine-Substituted and Acyl Hydrazones: Experiment and Computation Reveal a Stability Inversion at Low pH. **Molecular Pharmaceutics**, v. 12, n. 8, p. 2924–2927, 3 ago. 2015.

JOMOVA, Klaudia *et al.* Heavy metals: toxicity and human health effects. **Archives of Toxicology**, v. 99, n. 1, p. 153–209, 20 jan. 2025.

KADYAN, Kulbir *et al.* Exploring the Structural Versatility and Dynamic Behavior of Acyl/Aroyl Hydrazones: A Comprehensive Review. **Topics in Current Chemistry**, v. 383, n. 2, p. 18, 8 abr. 2025.

KALIA, Jeet; RAINES, Ronald T. Hydrolytic Stability of Hydrazones and Oximes. **Angewandte Chemie International Edition**, v. 47, n. 39, p. 7523–7526, 15 set. 2008.

KANDEL, Rachel; JUNG, Jasmine; NEAL, Sonya. Proteotoxic stress and the

ubiquitin proteasome system. **Seminars in Cell & Developmental Biology**, v. 156, p. 107–120, mar. 2024.

KARIMI-MOGHADAM, Amin *et al.* Parkinson Disease from Mendelian Forms to Genetic Susceptibility: New Molecular Insights into the Neurodegeneration Process. **Cellular and Molecular Neurobiology**, v. 38, n. 6, p. 1153–1178, 26 ago. 2018.

KAYED, Rakez *et al.* Common Structure of Soluble Amyloid Oligomers Implies Common Mechanism of Pathogenesis. **Science**, v. 300, n. 5618, p. 486–489, 18 abr. 2003.

KHAN, Ayesha *et al.* Metals accelerate the formation and direct the structure of amyloid fibrils of NAC. **Journal of Inorganic Biochemistry**, v. 99, n. 9, p. 1920–1927, set. 2005.

KIJAK, Ewelina *et al. Drosophila melanogaster* as a model system of aluminum toxicity and aging. **Insect Science**, v. 21, n. 2, p. 189–202, 10 abr. 2014.

KOSTKA, Marcus *et al.* Single Particle Characterization of Iron-induced Pore-forming α-Synuclein Oligomers. **Journal of Biological Chemistry**, v. 283, n. 16, p. 10992–11003, abr. 2008.

KOSTOVA, Irena; SASO, Luciano. Advances in Research of Schiff-Base Metal Complexes as Potent Antioxidants. **Current Medicinal Chemistry**, v. 20, n. 36, p. 4609–4632, 31 nov. 2013.

KOULI, Antonina; TORSNEY, Kelli M.; KUAN, Wei-Li. Parkinson's Disease: Etiology, Neuropathology, and Pathogenesis. *In*: **Parkinson's Disease: Pathogenesis and Clinical Aspects**. *[S.l.]*: Codon Publications, 2018. p. 3–26.

KRALJ, Sebastjan; JUKIČ, Marko; BREN, Urban. Molecular Filters in Medicinal Chemistry. **Encyclopedia**, v. 3, n. 2, p. 501–511, 18 abr. 2023.

KRAUSE, Lennard *et al.* Comparison of silver and molybdenum microfocus X-ray sources for single-crystal structure determination. **Journal of Applied Crystallography**, v. 48, n. 1, p. 3–10, 1 fev. 2015.

KUIPER, Sander G. *et al.* Ceftriaxone for the Treatment of Chronic Bacterial Prostatitis: A Case Series and Literature Review. **Antibiotics**, v. 11, n. 1, p. 83, 11 jan. 2022.

KUMAR, S. Aluminium-induced changes in the rat brain serotonin system. **Food and Chemical Toxicology**, v. 40, n. 12, p. 1875–1880, dez. 2002.

KUMAR, Sundeep; NATH, Mala. New diorganotin(IV) complexes of salicylaldehyde based hydrazones bearing furan heterocycle moiety: X-ray structural investigation of dimethyltin(IV) and diphenyltin(IV) complexes. **Journal of Organometallic Chemistry**, v. 856, p. 87–99, fev. 2018.

KUMAR, Vijay; BAL, Amanjit; GILL, Kiran Dip. Impairment of mitochondrial energy metabolism in different regions of rat brain following chronic exposure to aluminium. **Brain Research**, v. 1232, p. 94–103, set. 2008.

LANE, Darius J. R.; AYTON, Scott; BUSH, Ashley I. Iron and Alzheimer's Disease: An Update on Emerging Mechanisms. **Journal of Alzheimer's Disease**, v. 64, n. s1, p. S379–S395, 12 jun. 2018.

LANZANI, G. *et al.* Study of the stability of aluminium trimeric clusters in aqueous solutions. **Molecular Simulation**, v. 38, n. 11, p. 934–943, set. 2012.

LÁZARO, Diana F.; PAVLOU, Maria Angeliki S.; OUTEIRO, Tiago Fleming. Cellular models as tools for the study of the role of alpha-synuclein in Parkinson's disease. **Experimental Neurology**, v. 298, p. 162–171, dez. 2017.

LEE, Seung Ha *et al.* Brain regional iron contents in progressive supranuclear palsy. **Parkinsonism & Related Disorders**, v. 45, p. 28–32, dez. 2017.

LEE, Shin Jung C. *et al.* Probing Conformational Change of Intrinsically Disordered α-Synuclein to Helical Structures by Distinctive Regional Interactions with Lipid Membranes. **Analytical Chemistry**, v. 86, n. 3, p. 1909–1916, 4 fev. 2014.

LEESON, Paul D.; YOUNG, Robert J. Molecular Property Design: Does Everyone Get It? **ACS Medicinal Chemistry Letters**, v. 6, n. 7, p. 722–725, 9 jul. 2015.

LENZ, Sarah *et al. Drosophila* as a screening tool to study human neurodegenerative diseases. **Journal of Neurochemistry**, v. 127, n. 4, p. 453–460, 21 nov. 2013.

LI, Ai-Fang *et al.* Oxidative cyclization of N-acylhydrazones. Development of highly selective turn-on fluorescent chemodosimeters for Cu^{2+}. **Org. Biomol. Chem.**, v. 7, n. 1, p. 193–200, 2009.

LI, Bowen *et al.* DrugMetric: quantitative drug-likeness scoring based on chemical space distance. **Briefings in Bioinformatics**, v. 25, n. 4, 23 maio 2024.

LI, Can *et al.* Health Risk Assessment of Inhalable Dust Exposure during the Welding and Grinding Process of Subway Aluminum Alloy Components. **Buildings**, v. 13, n. 10, p. 2469, 28 set. 2023.

LI, Meng *et al.* Design, Synthesis, and Biological Evaluation of Novel Acylhydrazone Derivatives as Potent Neuraminidase Inhibitors. **ACS Medicinal Chemistry Letters**, v. 11, n. 9, p. 1745–1750, 10 set. 2020.

LI, Yong *et al.* Temporal and geographical dynamics of early-onset Parkinson's disease burden: insights from the Global Burden of Disease Study 2021. **Frontiers in Neurology**, v. 16, 30 jan. 2025.

LIM, Shen-Yang *et al.* Parkinson's disease in the Western Pacific Region. **The Lancet Neurology**, v. 18, n. 9, p. 865–879, set. 2019.

LIPINSKI, Christopher A. *et al.* Experimental and computational approaches to estimate solubility and permeability in drug discovery and development settings. **Advanced Drug Delivery Reviews**, v. 23, n. 1–3, p. 3–25, jan. 1997.

LIU, Jiaoyan *et al.* Photophysical properties and pH sensing applications of luminescent salicylaldehyde derivatives. **Research on Chemical Intermediates**, v. 42, n. 5, p. 5027–5048, 16 maio 2016.

LIU, Li-mei; YANG, Zheng-yin. A new off-on fluorescent sensor for the detection of Al(III) based on a chromone-derived Schiff-base. **Inorganica Chimica Acta**, v. 469, p. 588–592, jan. 2018.

LU, Yi-Heng *et al.* UV-visible spectroscopic study of the salicyladehyde benzoylhydrazone and its cobalt complexes. **Spectrochimica acta. Part A, Molecular and biomolecular spectroscopy**, v. 65, n. 3–4, p. 695–701, nov. 2006.

LY, Tony; JULIAN, Ryan R. Protein-metal interactions of calmodulin and α-synuclein monitored by selective noncovalent adduct protein probing mass spectrometry. **Journal of the American Society for Mass Spectrometry**, v. 19, n. 11, p. 1663–1672, 1 nov. 2008.

MACRAE, Clare F. *et al. Mercury* : visualization and analysis of crystal structures. **Journal of Applied Crystallography**, v. 39, n. 3, p. 453–457, 1 jun. 2006.

MAJUMDAR, AnuradhaS; NIRWANE, Abhijit; KAMBLE, Rahul. Coenzyme Q10 abrogated the 28 days aluminium chloride induced oxidative changes in rat cerebral cortex. **Toxicology International**, v. 21, n. 2, p. 214, 2014.

MARTÍN GIMÉNEZ, Virna M. *et al.* Metal ion homeostasis with emphasis on zinc and copper: Potential crucial link to explain the non-classical antioxidative properties of vitamin D and melatonin. **Life Sciences**, v. 281, p. 119770, set. 2021.

MARTIN, R. B. The chemistry of aluminum as related to biology and medicine. **Clinical Chemistry**, v. 32, n. 10, p. 1797–1806, 1 out. 1986.

MARTIN-BASTIDA, A. *et al.* Motor associations of iron accumulation in deep grey matter nuclei in Parkinson's disease: a cross-sectional study of iron-related magnetic resonance imaging susceptibility. **European Journal of Neurology**, v. 24, n. 2, p. 357–365, 16 fev. 2017.

MARTINS, Cláudia Rocha; LOPES, Wilson Araújo; ANDRADE, Jailson Bittencourt de. Solubilidade das substâncias orgânicas. **Química Nova**, v. 36, n. 8, p. 1248–1255, 2013.

MARTINS, Dayanne *et al.* Effects of the aldehyde-derived ring substituent on the properties of two new bioinspired trimethoxybenzoylhydrazones: methyl vs nitro groups. **Beilstein Journal of Organic Chemistry**, v. 19, p. 1713–1727, 10 nov. 2023.

MASATO, Anna *et al.* Impaired dopamine metabolism in Parkinson's disease pathogenesis. **Molecular Neurodegeneration**, v. 14, n. 1, p. 35, 20 dez. 2019.

MATHIVANAN, Moorthy *et al.* A new *7* -diethylamino- *4* -hydroxycoumarin based reversible colorimetric/fluorometric probe for sequential detection of Al^{3+} /PPi and its potential use in biodetection and bioimaging applications. **New Journal of Chemistry**, v. 45, n. 13, p. 6067–6079, 2021.

MCGUIRE, Sean E.; DESHAZER, Mitch; DAVIS, Ronald L. Thirty years of olfactory learning and memory research in Drosophila melanogaster. **Progress in Neurobiology**, v. 76, n. 5, p. 328–347, ago. 2005.

MEANWELL, Nicholas A. Improving Drug Candidates by Design: A Focus on Physicochemical Properties As a Means of Improving Compound Disposition and Safety. **Chemical Research in Toxicology**, v. 24, n. 9, p. 1420–1456, 19 set. 2011.

MEHRA, Surabhi; SAHAY, Shruti; MAJI, Samir K. α-Synuclein misfolding and aggregation: Implications in Parkinson's disease pathogenesis. **Biochimica et Biophysica Acta (BBA) - Proteins and Proteomics**, v. 1867, n. 10, p. 890–908,

out. 2019.

MELISSEN, Sigismund T. A. G. *et al.* A DFT study of the Al2Cl6-catalyzed Friedel–Crafts acylation of phenyl aromatic compounds. **Journal of Molecular Modeling**, v. 19, n. 11, p. 4947–4958, 20 nov. 2013.

MELLEM, Jerry E. *et al.* Decoding of Polymodal Sensory Stimuli by Postsynaptic Glutamate Receptors in C. elegans. **Neuron**, v. 36, n. 5, p. 933–944, dez. 2002.

MENG, Guangrong *et al.* Reversible Twisting of Primary Amides via Ground State N–C(O) Destabilization: Highly Twisted Rotationally Inverted Acyclic Amides. **Journal of the American Chemical Society**, v. 140, n. 2, p. 727–734, 17 jan. 2018.

MENZEL BARRAQUETA, Jan-Lukas *et al.* Aluminium in the North Atlantic Ocean and the Labrador Sea (GEOTRACES GA01 section): roles of continental inputs and biogenic particle removal. **Biogeosciences**, v. 15, n. 16, p. 5271–5286, 30 ago. 2018.

MICHAEL J. FOX FOUNDATION FOR PARKINSON'S RESEARCH. **New Estimate Suggests 25 Million People with Parkinson's by 2050**. Disponível em: <https://www.michaeljfox.org/news/new-estimate-suggests-25-million-people-parkinsons-2050?utm_source=chatgpt.com>. Acesso em: 24 maio. 2025.

MIOTTO, Marco C. *et al.* Bioinorganic chemistry of synucleinopathies: Deciphering the binding features of Met motifs and His-50 in AS–Cu(I) interactions. **Journal of Inorganic Biochemistry**, v. 141, p. 208–211, dez. 2014.

MIOTTO, Marco C. *et al.* Copper Binding to the N-Terminally Acetylated, Naturally Occurring Form of Alpha-Synuclein Induces Local Helical Folding. **Journal of the American Chemical Society**, v. 137, n. 20, p. 6444–6447, 27 maio 2015.

MOHAMED JAMAL SAADH; MANSOUR HADDAD; MOEEN DABABNEH. A Guide for Estimating the Maximum Safe Starting Dose and Conversion it

between Animals and Humans. **Systematic Reviews in Pharmacy**, v. 8, n. 11, p. 98–101, 2020.

MOHAMMAD, Fathia S.; AL ZUBAIDY, Isam A. H.; BASSIONI, Ghada. A comparison of Aluminum Leaching Processes in Tap and Drinking Water. **International Journal of Electrochemical Science**, v. 9, n. 6, p. 3118–3129, jun. 2014.

MOLD, Matthew *et al.* Intracellular Aluminium in Inflammatory and Glial Cells in Cerebral Amyloid Angiopathy: A Case Report. **International Journal of Environmental Research and Public Health**, v. 16, n. 8, p. 1459, 24 abr. 2019.

MORAES, Rafaela S. *et al.* Luminescent properties of a di-hydrazone derived from the antituberculosis agent isoniazid: Potentiality as an emitting layer constituent for OLED fabrication. **Optical Materials**, v. 52, p. 186–191, fev. 2016.

MORIARTY, Gina M. *et al.* A Revised Picture of the Cu(II)−α-Synuclein Complex: The Role of N-Terminal Acetylation. **Biochemistry**, v. 53, n. 17, p. 2815–2817, 6 maio 2014.

MORJAN, Rami Y. *et al.* Antibacterial activities of novel nicotinic acid hydrazides and their conversion into N-acetyl-1,3,4-oxadiazoles. **Bioorganic & Medicinal Chemistry Letters**, v. 24, n. 24, p. 5796–5800, dez. 2014a.

MORJAN, Rami Y. *et al.* Antibacterial activities of novel nicotinic acid hydrazides and their conversion into N-acetyl-1,3,4-oxadiazoles. **Bioorganic & Medicinal Chemistry Letters**, v. 24, n. 24, p. 5796–5800, dez. 2014b.

MOURA, Fagner da Silva *et al.* Copper(<scp>ii</scp>) complexes of a furan-containing aroylhydrazonic ligand: syntheses, structural studies, solution chemistry and interaction with HSA. **Dalton Transactions**, v. 52, n. 47, p. 17731–17746, 2023.

MULLER, Michelle; LEAVITT, Blair R. Iron dysregulation in Huntington’s

disease. **Journal of Neurochemistry**, v. 130, n. 3, p. 328–350, 28 ago. 2014.

MUNIR, Rubina *et al.* Synthesis of Novel N-Acylhydrazones and Their C-N/N-N Bond Conformational Characterization by NMR Spectroscopy. **Molecules**, v. 26, n. 16, p. 4908, 13 ago. 2021a.

MUNIR, Rubina *et al.* Synthesis of Novel N-Acylhydrazones and Their C-N/N-N Bond Conformational Characterization by NMR Spectroscopy. **Molecules**, v. 26, n. 16, p. 4908, 13 ago. 2021b.

NAGATSU, Toshiharu *et al.* Neuromelanin in Parkinson's Disease: Tyrosine Hydroxylase and Tyrosinase. **International Journal of Molecular Sciences**, v. 23, n. 8, p. 4176, 10 abr. 2022.

NIKOLAYCHUK, Pavel Anatolyevich; KOZESCHNIK, Ernst. Thermodynamic evaluation of the aerial and aqueous oxidation of Al – Mg, Al – Si and Al – Mg – Si system alloys at 298 K. **npj Materials Degradation**, v. 8, n. 1, p. 94, 6 set. 2024.

NÜBLING, Georg *et al.* Synergistic influence of phosphorylation and metal ions on tau oligomer formation and coaggregation with α-synuclein at the single molecule level. **Molecular Neurodegeneration**, v. 7, n. 1, p. 35, 23 dez. 2012.

O GLOBO. **Experimento usa células de porcos para tratar o mal de Parkinson**. Disponível em: <https://oglobo.globo.com/saude/ciencia/experimento-usa-celulas-de-porcos-para-tratar-mal-de-parkinson-21471546>. Acesso em: 24 maio. 2025.

PAIK, Seung R. *et al.* Aluminum-Induced Structural Alterations of the Precursor of the Non-Aβ Component of Alzheimer's Disease Amyloid. **Archives of Biochemistry and Biophysics**, v. 344, n. 2, p. 325–334, ago. 1997a.

PAIK, Seung R. *et al.* Aluminum-Induced Structural Alterations of the Precursor of the Non-Aβ Component of Alzheimer's Disease Amyloid. **Archives of Biochemistry and Biophysics**, v. 344, n. 2, p. 325–334, ago. 1997b.

PALANIMUTHU, Duraippandi *et al.* Novel chelators based on adamantane-derived semicarbazones and hydrazones that target multiple hallmarks of Alzheimer's disease. **Dalton Transactions**, v. 47, n. 21, p. 7190–7205, 2018.

PALM, Katrin *et al.* Polar molecular surface properties predict the intestinal absorption of drugs in humans. **Pharmaceutical Research**, v. 14, n. 5, p. 568–571, 1997.

PARKINSON, James. An Essay on the Shaking Palsy. **The Journal of Neuropsychiatry and Clinical Neurosciences**, v. 14, n. 2, p. 223–236, maio 2002.

PARKINSON'S FOUNDATION. **In the United States alone, approximately 90,000 new cases are diagnosed each year, a 50% increase on previous estimates, which indicated around 60,000 new cases annually**. Disponível em: <https://www.parkinson.org/about-us/news/incidence-2022>. Acesso em: 24 maio. 2025.

PARSONS, Leo W. T.; BERBEN, Louise A. Expanding the Scope of Aluminum Chemistry with Noninnocent Ligands. **Accounts of Chemical Research**, v. 57, n. 8, p. 1087–1097, 16 abr. 2024.

PEARSON, Ralph G. **Hard and Soft Acids and Bases**. **Journal of the American Chemical Society**, v. 85, n. 22, p. 3533–3539, 1 nov. 1963.

PEARSON, Ralph G. Acids and Bases. **Science**, v. 151, n. 3707, p. 172–177, 14 jan. 1966.

PENG, Huanan *et al.* Synthesis and crystal structure of a novel pyridine acylhydrazone derivative as a "turn on" fluorescent probe for Al3+. **Journal of Molecular Structure**, v. 1212, p. 128138, jul. 2020.

PETERS, Kirsten *et al.* Impact of Metal Ions on Cellular Functions: A Focus on Mesenchymal Stem/Stromal Cell Differentiation. **International Journal of Molecular Sciences**, v. 25, n. 18, p. 10127, 20 set. 2024.

PICKLES, Christopher; LU, Ting. Microwave Dewatering of Gibbsite-Type Bauxite Ores: Permittivities, Heating Behavior and Strength Indices. **Minerals**, v. 12, n. 5, p. 648, 20 maio 2022.

PITZ, Vanessa *et al.* Analysis of rare Parkinson's disease variants in millions of people. **npj Parkinson's Disease**, v. 10, n. 1, p. 11, 8 jan. 2024.

POLLASTRI, Michael P. Overview on the Rule of Five. **Current Protocols in Pharmacology**, v. 49, n. 1, jun. 2010.

POLO-CERÓN, Dorian; HINCAPIÉ-OTERO, María Mercedes; JOAQUI-JOAQUI, Andrey. Synthesis and characterization of four N-acylhydrazones as potential O,N,O donors for Cu2+: An experimental and theoretical study. **Universitas Scientiarum**, v. 26, n. 2, 19 jul. 2021.

POLYMEROPOULOS, Mihael H. *et al.* Mutation in the α-Synuclein Gene Identified in Families with Parkinson's Disease. **Science**, v. 276, n. 5321, p. 2045–2047, 27 jun. 1997.

POŇKA, Přemysl *et al.* A study of intracellular iron metabolism using pyridoxal isonicotinoyl hydrazone and other synthetic chelating agents. **Biochimica et Biophysica Acta (BBA) - General Subjects**, v. 586, n. 2, p. 278–297, ago. 1979.

POPŁAWSKA-DOMASZEWICZ, Karolina; FLORCZAK-WYSPIAŃSKA, Jolanta; KOZUBSKI, Wojciech. Update on neurodegeneration with brain iron accumulation. **Neurologia i Neurochirurgia Polska**, v. 48, n. 3, p. 206–213, maio 2014.

POST, Bart *et al.* Young Onset Parkinson's Disease: A Modern and Tailored Approach. **Journal of Parkinson's Disease**, v. 10, n. s1, p. S29–S36, 29 jul. 2020.

POULSON, Benjamin Gabriel *et al.* Aggregation of biologically important peptides and proteins: inhibition or acceleration depending on protein and metal ion

concentrations. **RSC Advances**, v. 10, n. 1, p. 215–227, 2020.

PRÜSSING, Katja; VOIGT, Aaron; SCHULZ, Jörg B. Drosophila melanogaster as a model organism for Alzheimer's disease. **Molecular Neurodegeneration**, v. 8, n. 1, p. 35, 22 dez. 2013.

PUENTES-DÍAZ, Nicolás *et al.* Role of Metal Cations of Copper, Iron, and Aluminum and Multifunctional Ligands in Alzheimer's Disease: Experimental and Computational Insights. **ACS Omega**, v. 8, n. 5, p. 4508–4526, 7 fev. 2023.

PURANDARA, H.; FORO, Sabine; THIMME GOWDA, B. Crystal structures of three *ortho* -substituted *N* -acylhydrazone derivatives. **Acta Crystallographica Section E Crystallographic Communications**, v. 73, n. 12, p. 1946–1951, 1 dez. 2017.

RACZUK, Edyta *et al.* Different Schiff Bases—Structure, Importance and Classification. **Molecules**, v. 27, n. 3, p. 787, 25 jan. 2022.

RADA, Jesica Paola *et al.* Binucleating Hydrazonic Ligands and Their μ-Hydroxodicopper(II) Complexes as Promising Structural Motifs for Enhanced Antitumor Activity. **Inorganic Chemistry**, v. 58, n. 13, p. 8800–8819, 1 jul. 2019.

RADA, Jesica Paola *et al.* Isoxazole-Derived Aroylhydrazones and Their Dinuclear Copper(II) Complexes Show Antiproliferative Activity on Breast Cancer Cells with a Potentially Alternative Mechanism Of Action. **ChemBioChem**, v. 21, n. 17, p. 2474–2486, 19 set. 2020.

RADA, Jesica Paola *et al.* Novel luminescent benzopyranothiophene- and BODIPY-derived aroylhydrazonic ligands and their dicopper(II) complexes: syntheses, antiproliferative activity and cellular uptake studies. **JBIC Journal of Biological Inorganic Chemistry**, v. 26, n. 6, p. 675–688, 20 set. 2021.

RAHIMZADEH, Mehrdad Rafati *et al.* Aluminum Poisoning with Emphasis on Its Mechanism and Treatment of Intoxication. **Emergency Medicine International**,

v. 2022, p. 1–13, 11 jan. 2022.

RAVINDRA B. MALABADI *et al.* Tea (Camellia sinensis) leaves accumulate higher levels of Aluminum: Potential Health Risk- Alzheimer's disease (AD): An updated review of evidence. **GSC Advanced Research and Reviews**, v. 20, n. 1, p. 313–337, 30 jul. 2024.

REZKI, Nadjet *et al.* A novel dicationic ionic liquids encompassing pyridinium hydrazone-phenoxy conjugates as antimicrobial agents targeting diverse high resistant microbial strains. **Journal of Molecular Liquids**, v. 284, p. 431–444, jun. 2019.

RICHARDSON, D. R. *et al.* Iron chelators of the pyridoxal isonicotinoyl hydrazone class. **Biology of Metals**, v. 2, n. 3, p. 161–167, 1989.

RICHARDSON, D. R.; BECKER, E.; BERNHARDT, P. V. The biologically active iron chelators 2-pyridylcarboxaldehyde isonicotinoylhydrazone, 2-pyridylcarboxaldehyde benzoylhydrazone monohydrate and 2-furaldehyde isonicotinoylhydrazone. **Acta Crystallographica Section C Crystal Structure Communications**, v. 55, n. 12, p. 2102–2105, 15 dez. 1999.

RICHARDSON, DR. Friedreich's ataxia: iron chelators that target the mitochondrion as a therapeutic strategy? **Expert Opinion on Investigational Drugs**, v. 12, n. 2, p. 235–245, 2 fev. 2003.

ROCHA, Emily M.; DE MIRANDA, Briana; SANDERS, Laurie H. Alpha-synuclein: Pathology, mitochondrial dysfunction and neuroinflammation in Parkinson's disease. **Neurobiology of Disease**, v. 109, p. 249–257, jan. 2018.

ROCHMAN, Mika *et al.* Aluminum Content of Human Milk and Antiperspirant Use. **Breastfeeding Medicine**, v. 16, n. 8, p. 654–659, 1 ago. 2021.

RODRIGUEZ, Patricio H. *et al.* Determination of Bioavailable Aluminum in Natural Waters in the Presence of Suspended Solids. **Environmental Toxicology**

and Chemistry, v. 38, n. 8, p. 1668–1681, 29 abr. 2019.

ROGERS, Candida M. *et al.* Regulation of the pharynx of *Caenorhabditis elegans* by 5-HT, octopamine, and FMRFamide-like neuropeptides. **Journal of Neurobiology**, v. 49, n. 3, p. 235–244, 15 nov. 2001.

ROHANE, Sachin H. *et al.* Synthesis and *in vitro* antimycobacterial potential of novel hydrazones of eugenol. **Arabian Journal of Chemistry**, v. 13, n. 2, p. 4495–4504, fev. 2020.

ROMANOWSKA, Hanna *et al.* Unexpected Serum and Urine Aluminum Concentrations in Pediatric Patients on Home Parenteral Nutrition. **Nutrients**, v. 15, n. 16, p. 3597, 17 ago. 2023.

RUBINI, Patrice *et al.* Speciation and structural aspects of interactions of Al(III) with small biomolecules. **Coordination Chemistry Reviews**, v. 228, n. 2, p. 137–152, jun. 2002.

SABERZADEH, Jamileh; ARABSOLGHAR, Rita; TAKHSHID, Mohammad Ali. Alpha synuclein protein is involved in Aluminum-induced cell death and oxidative stress in PC12 cells. **Brain Research**, v. 1635, p. 153–160, mar. 2016.

SABIR, Deema K. *et al.* Modulating oxidative stress, apoptosis, and mitochondrial dysfunctions on cardiotoxicity induced by aluminum phosphide pesticide using resveratrol. **Toxicology Mechanisms and Methods**, v. 34, n. 6, p. 727–735, 23 jul. 2024.

SÁNCHEZ-IGLESIAS, Sofía *et al.* Brain oxidative stress and selective behaviour of aluminium in specific areas of rat brain: potential effects in a 6-OHDA-induced model of Parkinson's disease. **Journal of Neurochemistry**, v. 109, n. 3, p. 879–888, 7 maio 2009.

SANGHERA, M. K.; TRULSON, M. E.; GERMAN, D. C. Electrophysiological properties of mouse dopamine neurons: *In vivo* and *in vitro* studies. **Neuroscience**,

v. 12, n. 3, p. 793–801, jul. 1984.

SANLUCA, Chiara *et al.* Interaction between α-Synuclein and Bioactive Lipids: Neurodegeneration, Disease Biomarkers and Emerging Therapies. **Metabolites**, v. 14, n. 7, p. 352, 22 jun. 2024.

SANTA MARIA DE LA PARRA, Lucía *et al.* Promising Dual Anticancer and Antimetastatic Action by a Cu(II) Complex Derived from Acylhydrazone on Human Osteosarcoma Models. **Inorganic Chemistry**, v. 63, n. 11, p. 4925–4938, 18 mar. 2024.

SANTOS, Luana Stephany *et al.* Autophagy Pathways, Ubiquitin-Proteasome System and Neurodegenerative Diseases: a Scopus Review. **Brazilian Journal of Biological Sciences**, v. 12, n. 26, p. e149, 17 mar. 2025.

SAVENKO, A. V.; SAVENKO, V. S. Aluminum hydroxide's solubility and the forms of dissolved aluminum's occurrence in seawater. **Oceanology**, v. 51, n. 2, p. 231–234, 30 abr. 2011.

SAWIN, Elizabeth R.; RANGANATHAN, Rajesh; HORVITZ, H. Robert. C. elegans Locomotory Rate Is Modulated by the Environment through a Dopaminergic Pathway and by Experience through a Serotonergic Pathway. **Neuron**, v. 26, n. 3, p. 619–631, jun. 2000.

SCHEPERS, Jana; LÖSER, Timo; BEHL, Christian. Lipids and α-Synuclein: adding further variables to the equation. **Frontiers in Molecular Biosciences**, v. 11, 12 ago. 2024.

SCHÖNENBERGER, Katja A. *et al.* Aluminum and other chemical elements in parenteral nutrition components and all-in-one admixtures. **Clinical Nutrition**, v. 42, n. 12, p. 2475–2483, dez. 2023.

SÉGALAT, Laurent; ELKES, Daniel A.; KAPLAN, Joshua M. Modulation of Serotonin-Controlled Behaviors by G $_{o}$ in *Caenorhabditis elegans*. **Science**, v. 267,

n. 5204, p. 1648–1651, 17 mar. 1995.

SHAN, Wenfei *et al.* Synthesis and luminescence properties of salicylaldehyde isonicotinoyl hydrazone derivatives and their europium complexes. **Journal of Inorganic Biochemistry**, v. 150, p. 100–107, set. 2015.

SHARMA, Shivani *et al.* 2-Hydroxy-naphthalene hydrazone based dual-functional chemosensor for ultrasensitive colorimetric detection of Cu2+ and highly selective fluorescence sensing and bioimaging of Al3+. **Journal of Photochemistry and Photobiology A: Chemistry**, v. 437, p. 114408, mar. 2023.

SHATI, A. A.; ELSAID, F. G.; HAFEZ, E. E. Biochemical and molecular aspects of aluminium chloride-induced neurotoxicity in mice and the protective role of Crocus sativus L. extraction and honey syrup. **Neuroscience**, v. 175, p. 66–74, fev. 2011.

SHAW, Christopher A.; MARLER, Thomas E. Aluminum and the human diet revisited. **Communicative & Integrative Biology**, v. 6, n. 6, p. e26369, 9 nov. 2013.

SHELDRICK, George M. *SHELXT* – Integrated space-group and crystal-structure determination. **Acta Crystallographica Section A Foundations and Advances**, v. 71, n. 1, p. 3–8, 1 jan. 2015.

SIEGEL, N.; HAUG, A. Aluminum interaction with calmodulin. **Biochimica et Biophysica Acta (BBA) - Protein Structure and Molecular Enzymology**, v. 744, n. 1, p. 36–45, abr. 1983.

SILVA, Thaiane Pereira da; CARVALHO, Claudia Reinoso Araujo de. Doença de Parkinson: o tratamento terapêutico ocupacional na perspectiva dos profissionais e dos idosos. **Cadernos Brasileiros de Terapia Ocupacional**, v. 27, n. 2, p. 331–344, 2019.

SINGH, Tanveer; GOEL, Rajesh Kumar. Neuroprotective effect of Allium cepa L.

in aluminium chloride induced neurotoxicity. **NeuroToxicology**, v. 49, p. 1–7, jul. 2015.

SINGH, Udaya Pratap *et al.* Phenyl hydrazone bearing pyrazole and pyrimidine scaffolds: design and discovery of a novel class of non-nucleoside reverse transcriptase inhibitors (NNRTIs) against HIV-1 and their antibacterial properties. **RSC Advances**, v. 3, n. 38, p. 17335, 2013.

SIVAKUMAR, S.; SIVASUBRAMANIAN, J.; RAJA, B. Aluminium induced structural, metabolic alterations and protective effects of desferrioxamine in the brain tissue of mice: An FTIR study. **Spectrochimica Acta Part A: Molecular and Biomolecular Spectroscopy**, v. 99, p. 252–258, dez. 2012.

SKALNY, Anatoly V. *et al.* Molecular mechanisms of aluminum neurotoxicity: Update on adverse effects and therapeutic strategies. *In*: *[S.l.: S.n.]*. p. 1–34.

SKRAHIN, Aliaksandr *et al.* GBA1-Associated Parkinson's Disease Is a Distinct Entity. **International Journal of Molecular Sciences**, v. 25, n. 13, p. 7102, 28 jun. 2024.

SLITER, Brian; MORGAN, Jessica; GREENBERG, Arthur. 1-Azabicyclo[3.3.1]nonan-2-one: Nitrogen Versus Oxygen Protonation. **The Journal of Organic Chemistry**, v. 76, n. 8, p. 2770–2781, 15 abr. 2011.

SOMAYAJI, Mahalakshmi *et al.* Roles for α-Synuclein in Gene Expression. **Genes**, v. 12, n. 8, p. 1166, 29 jul. 2021.

SONG, Zhengyu *et al.* Prevalence of Parkinson's Disease in Adults Aged 65 Years and Older in China: A Multicenter Population-Based Survey. **Neuroepidemiology**, v. 56, n. 1, p. 50–58, 2022.

SPACKMAN, Peter R. *et al. CrystalExplorer* : a program for Hirshfeld surface analysis, visualization and quantitative analysis of molecular crystals. **Journal of Applied Crystallography**, v. 54, n. 3, p. 1006–1011, 1 jun. 2021.

SPEK, Anthony L. Structure validation in chemical crystallography. **Acta Crystallographica Section D Biological Crystallography**, v. 65, n. 2, p. 148–155, 1 fev. 2009.

SPILLANTINI, Maria Grazia *et al.* α-Synuclein in Lewy bodies. **Nature**, v. 388, n. 6645, p. 839–840, 28 ago. 1997a.

SPILLANTINI, Maria Grazia *et al.* α-Synuclein in Lewy bodies. **Nature**, v. 388, n. 6645, p. 839–840, 28 ago. 1997b.

STEVANOVIĆ, Ivana D. *et al.* The effect of inhibition of nitric oxide synthase on aluminium-induced toxicity in the rat brain. **General physiology and biophysics**, v. 28 Spec No, p. 235–42, 2009.

SU, Dongning *et al.* Projections for prevalence of Parkinson's disease and its driving factors in 195 countries and territories to 2050: modelling study of Global Burden of Disease Study 2021. **BMJ**, p. e080952, 5 mar. 2025.

SU, Xin; APRAHAMIAN, Ivan. Hydrazone-based switches, metallo-assemblies and sensors. **Chemical Society Reviews**, v. 43, n. 6, p. 1963, 2014.

SULE, Kevin; UMBSAAR, Jenelle; PRENNER, Elmar J. Mechanisms of Co, Ni, and Mn toxicity: From exposure and homeostasis to their interactions with and impact on lipids and biomembranes. **Biochimica et Biophysica Acta (BBA) - Biomembranes**, v. 1862, n. 8, p. 183250, ago. 2020.

SUMATHI, Thangarajan *et al.* Protective effect of L-Theanine against aluminium induced neurotoxicity in cerebral cortex, hippocampus and cerebellum of rat brain – histopathological, and biochemical approach. **Drug and Chemical Toxicology**, v. 38, n. 1, p. 22–31, 2 jan. 2015.

SUMRRA, Sajjad Hussain *et al.* Synthesis, Spectral Characterization, and Biological Evaluation of Transition Metal Complexes of Bidentate N, O Donor

Schiff Bases. **Bioinorganic Chemistry and Applications**, v. 2014, p. 1–10, 2014.

SZCZEPANIK, Beata *et al.* The effect of chemical modification on the physico-chemical characteristics of halloysite: FTIR, XRF, and XRD studies. **Journal of Molecular Structure**, v. 1084, p. 16–22, mar. 2015.

TANG, Lijun *et al.* A new 2-(2′-hydroxyphenyl)quinazolin-4(3H)-one derived acylhydrazone for fluorescence recognition of Al 3+. **Spectrochimica Acta Part A: Molecular and Biomolecular Spectroscopy**, v. 174, p. 70–74, mar. 2017.

TATUM, Luke A.; SU, Xin; APRAHAMIAN, Ivan. Simple Hydrazone Building Blocks for Complicated Functional Materials. **Accounts of Chemical Research**, v. 47, n. 7, p. 2141–2149, 15 jul. 2014.

TENCHOV, Rumiana; SASSO, Janet M.; ZHOU, Qiongqiong Angela. Evolving Landscape of Parkinson's Disease Research: Challenges and Perspectives. **ACS Omega**, v. 10, n. 2, p. 1864–1892, 21 jan. 2025.

TERRY, ROBERT D.; PEÑA, CARLOS. EXPERIMENTAL PRODUCTION OF NEUROFIBRILLARY DEGENERATION. **Journal of Neuropathology and Experimental Neurology**, v. 24, n. 2, p. 200–210, abr. 1965.

THOTA, Sreekanth *et al.* N-Acylhydrazones as drugs. **Bioorganic & Medicinal Chemistry Letters**, v. 28, n. 17, p. 2797–2806, set. 2018.

TIAN, Yao *et al.* Copper $^{2+}$ Binding to α-Synuclein. Histidine50 Can Form a Ternary Complex with Cu $^{2+}$ at the N-Terminus but Not a Macrochelate. **Inorganic Chemistry**, v. 58, n. 22, p. 15580–15589, 18 nov. 2019.

TIBAR, Houyam *et al.* Non-Motor Symptoms of Parkinson's Disease and Their Impact on Quality of Life in a Cohort of Moroccan Patients. **Frontiers in Neurology**, v. 9, 4 abr. 2018.

TIETZ, Thomas *et al.* Aggregated aluminium exposure: risk assessment for the

general population. **Archives of Toxicology**, v. 93, n. 12, p. 3503–3521, 28 dez. 2019.

ŢÎNŢAŞ, Mihaela Liliana *et al.* Structural characterization of new 2-aryl-5-phenyl-1,3,4-oxadiazin-6-ones and their N-aroylhydrazone precursors. **Journal of Molecular Structure**, v. 1058, p. 106–113, jan. 2014.

TOMLJENOVIC, Lucija. Aluminum and Alzheimer's Disease: After a Century of Controversy, Is there a Plausible Link? **Journal of Alzheimer's Disease**, v. 23, n. 4, p. 567–598, 21 mar. 2011.

TOTH, M. L. *et al.* Neurite Sprouting and Synapse Deterioration in the Aging Caenorhabditis elegans Nervous System. **Journal of Neuroscience**, v. 32, n. 26, p. 8778–8790, 27 jun. 2012.

ULMER, Tobias S. *et al.* Structure and Dynamics of Micelle-bound Human α-Synuclein. **Journal of Biological Chemistry**, v. 280, n. 10, p. 9595–9603, mar. 2005.

UVERSKY, Vladimir N. *et al.* Synergistic Effects of Pesticides and Metals on the Fibrillation of α-Synuclein: Implications for Parkinson's Disease. **NeuroToxicology**, v. 23, n. 4–5, p. 527–536, out. 2002.

UVERSKY, Vladimir N.; LI, Jie; FINK, Anthony L. Metal-triggered Structural Transformations, Aggregation, and Fibrillation of Human α-Synuclein. **Journal of Biological Chemistry**, v. 276, n. 47, p. 44284–44296, nov. 2001a.

UVERSKY, Vladimir N.; LI, Jie; FINK, Anthony L. Metal-triggered Structural Transformations, Aggregation, and Fibrillation of Human α-Synuclein. **Journal of Biological Chemistry**, v. 276, n. 47, p. 44284–44296, nov. 2001b.

UVERSKY, Vladimir N.; LI, Jie; FINK, Anthony L. Metal-triggered Structural Transformations, Aggregation, and Fibrillation of Human α-Synuclein. **Journal of Biological Chemistry**, v. 276, n. 47, p. 44284–44296, nov. 2001c.

VANDUYN, Natalia *et al.* The metal transporter <scp>SMF</scp> -3/ <scp>DMT</scp> -1 mediates aluminum-induced dopamine neuron degeneration. **Journal of Neurochemistry**, v. 124, n. 1, p. 147–157, 21 jan. 2013.

VASQUEZ, Velmarini *et al.* Chromatin-Bound Oxidized α-Synuclein Causes Strand Breaks in Neuronal Genomes in *in vitro* Models of Parkinson's Disease. **Journal of Alzheimer's Disease**, v. 60, n. s1, p. S133–S150, 15 set. 2017.

VEBER, Daniel F. *et al.* Molecular Properties That Influence the Oral Bioavailability of Drug Candidates. **Journal of Medicinal Chemistry**, v. 45, n. 12, p. 2615–2623, 1 jun. 2002a.

VEBER, Daniel F. *et al.* Molecular Properties That Influence the Oral Bioavailability of Drug Candidates. **Journal of Medicinal Chemistry**, v. 45, n. 12, p. 2615–2623, 1 jun. 2002b.

VEGAS, Ángel *et al.* Anions in metallic matrices model: application to the aluminium crystal chemistry. **Acta Crystallographica Section B Structural Science**, v. 62, n. 2, p. 220–227, 1 abr. 2006.

VELEC, Hans F. G.; GOHLKE, Holger; KLEBE, Gerhard. DrugScore ^{CSD} Knowledge-Based Scoring Function Derived from Small Molecule Crystal Data with Superior Recognition Rate of Near-Native Ligand Poses and Better Affinity Prediction. **Journal of Medicinal Chemistry**, v. 48, n. 20, p. 6296–6303, 1 out. 2005.

VENATI, Sriya Reddy; UVERSKY, Vladimir N. Exploring Intrinsic Disorder in Human Synucleins and Associated Proteins. **International Journal of Molecular Sciences**, v. 25, n. 15, p. 8399, 1 ago. 2024.

VERBAAN, D. *et al.* Patient-reported autonomic symptoms in Parkinson disease. **Neurology**, v. 69, n. 4, p. 333–341, 24 jul. 2007.

VIDOVIĆ, Marija; RIKALOVIC, Milena G. Alpha-Synuclein Aggregation Pathway in Parkinson's Disease: Current Status and Novel Therapeutic Approaches. **Cells**, v. 11, n. 11, p. 1732, 24 maio 2022.

VIEIRA, Sophia R. L.; SCHAPIRA, Anthony H. V. Glucocerebrosidase mutations and Parkinson disease. **Journal of Neural Transmission**, v. 129, n. 9, p. 1105–1117, 6 set. 2022.

VILLAR-PIQUÉ, Anna *et al.* Molecular and Clinical Aspects of Protein Aggregation Assays in Neurodegenerative Diseases. **Molecular Neurobiology**, v. 55, n. 9, p. 7588–7605, 10 set. 2018.

VINEETHA, M. C. *et al.* Structural investigation of discrete solvent protonated vanadium and other transition metal complexes of N'-[(E)-(3-ethoxy-2-hydroxyphenyl)methylidene]benzohydrazide, synthetic, spectroscopic and cytotoxicity studies. **Inorganica Chimica Acta**, v. 491, p. 93–104, jun. 2019.

VOLKOV, Alexey N.; TIMOSHKIN, Alexey Y.; SUVOROV, Andrew V. On the importance of dimeric forms of Al and Ga trichlorides in the electrophilic aromatic substitution reactions: An ab initio study. **International Journal of Quantum Chemistry**, v. 100, n. 4, p. 412–418, 28 jan. 2004.

VOLKOV, Alexey N.; TIMOSHKIN, Alexey Y.; SUVOROV, Andrew V. Pathways of electrophilic aromatic substitution reactions catalyzed by group 13 trihalides: An *ab initio* study. **International Journal of Quantum Chemistry**, v. 104, n. 2, p. 256–260, 13 jan. 2005.

WANG, Dong-Fang *et al.* A novel highly selective colorimetric sensor for aluminum (III) ion using Schiff base derivative. **Spectrochimica Acta Part A: Molecular and Biomolecular Spectroscopy**, v. 122, p. 268–272, mar. 2014.

WANG, JianHua *et al.* A new 'turn-on' and reversible fluorescent sensor for Al^{3+} detection and live cell imaging. **Analytical Methods**, v. 11, n. 43, p. 5598–5606, 2019.

WANG, Pengfei *et al.* “Turn-On” Fluorescent Biosensors for High Selective and Sensitive Detection of Al3+ Ion. **Frontiers in Chemistry**, v. 8, 19 nov. 2020.

WEGERMANN, Camila A. *et al.* Unveiling geometrical isomers and tautomers of isatin-hydrazones by NMR spectroscopy. **Journal of Molecular Structure**, v. 1250, p. 131633, fev. 2022.

WEHBE, Mohamed *et al.* A Perspective – can copper complexes be developed as a novel class of therapeutics? **Dalton Transactions**, v. 46, n. 33, p. 10758–10773, 2017.

WEINSHENKER, D.; GARRIGA, G.; THOMAS, JH. Genetic and pharmacological analysis of neurotransmitters controlling egg laying in C. elegans. **The Journal of Neuroscience**, v. 15, n. 10, p. 6975–6985, 1 out. 1995.

WILLIAMS, David R.; LITVAN, Irene. Parkinsonian Syndromes. **CONTINUUM: Lifelong Learning in Neurology**, v. 19, p. 1189–1212, out. 2013.

WISCONSIN HOSPITAL ASSOCIATION. **Fast Facts from the WHA Information Center: April is Parkinson’s Awareness Month**. Disponível em: <https://www.wha.org/news/newsletters/2025/04-03-2025/5?utm_source=chatgpt.com>. Acesso em: 24 maio. 2025.

WIŚNIEWSKI, Henryk; NARKIEWICZ, Olgierd; WIŚNIEWSKA, Krystyna. Topography and dynamics of neurofibrillar degeneration in aluminum encephalopathy. **Acta Neuropathologica**, v. 9, n. 2, p. 127–133, jun. 1967.

WU, Zhihao *et al.* Aluminum induces neurodegeneration and its toxicity arises from increased iron accumulation and reactive oxygen species (ROS) production. **Neurobiology of Aging**, v. 33, n. 1, p. 199.e1-199.e12, jan. 2012.

WU, Zhixuan *et al.* Novel multifunctional iron chelators of the aroyl nicotinoyl hydrazone class that markedly enhance cellular NAD^+/NADH ratios. **British**

Journal of Pharmacology, v. 177, n. 9, p. 1967–1987, 12 maio 2020.

XIA, Lei *et al.* Benzaldehyde Schiff bases regulation to the metabolism, hemolysis, and virulence genes expression *in vitro* and their structure–microbicidal activity relationship. **European Journal of Medicinal Chemistry**, v. 97, p. 83–93, jun. 2015a.

XIA, Lei *et al.* Benzaldehyde Schiff bases regulation to the metabolism, hemolysis, and virulence genes expression *in vitro* and their structure–microbicidal activity relationship. **European Journal of Medicinal Chemistry**, v. 97, p. 83–93, jun. 2015b.

XICOY, Helena; WIERINGA, Bé; MARTENS, Gerard J. M. The SH-SY5Y cell line in Parkinson's disease research: a systematic review. **Molecular Neurodegeneration**, v. 12, n. 1, p. 10, 24 dez. 2017.

XU, Jun. Synthesis, Crystal Structure, and Antibacterial Activity of *N′*-(2-hydroxy-3-methoxybenzylidene)isonicotinohydrazide and Its Dinuclear Manganese(II) Complex with *N′* -(2-hydroxy-3-methoxybenzylidene)isonicotinohydrazide. **Synthesis and Reactivity in Inorganic, Metal-Organic, and Nano-Metal Chemistry**, v. 43, n. 10, p. 1329–1333, 26 nov. 2013.

XU, Yong-Ji; ZHAO, Shuang; BI, Sai. (*E*)- *N* -(2-Hydroxybenzylidene)isonicotinohydrazide. **Acta Crystallographica Section E Structure Reports Online**, v. 63, n. 12, p. o4633–o4633, 15 dez. 2007.

YAMIN, Ghiam *et al.* Certain Metals Trigger Fibrillation of Methionine-oxidized α-Synuclein. **Journal of Biological Chemistry**, v. 278, n. 30, p. 27630–27635, jul. 2003.

YANG, De-Suo. Syntheses, characterization and crystal structures of two structurally similar Schiff bases isonicotinic acid [1-(3-methoxy-2-hydroxyphenyl)methylidene]hydrazide and isonicotinic acid [1-(4-dimethylaminophenyl)methylidene]hydrazide monohydrate. **Journal of Chemical**

Crystallography, v. 37, n. 5, p. 343–348, 19 mar. 2007.

YANG, Yidong *et al.* Beyond Size, Ionization State, and Lipophilicity: Influence of Molecular Topology on Absorption, Distribution, Metabolism, Excretion, and Toxicity for Druglike Compounds. **Journal of Medicinal Chemistry**, v. 55, n. 8, p. 3667–3677, 26 abr. 2012.

YIN, Han Dong *et al.* Synthesis, characterization and structural studies of diorganotin(IV) complexes with Schiff base ligand salicylaldehyde isonicotinylhydrazone. **Journal of Organometallic Chemistry**, v. 690, n. 16, p. 3714–3719, ago. 2005.

YOKEL, R. A. The toxicology of aluminum in the brain: a review. **Neurotoxicology**, v. 21, n. 5, p. 813–28, out. 2000.

YOKEL, Robert A. Aluminum in beverages and foods: A comprehensive compilation of regulations; concentrations in raw, prepared, and stored beverages and foods; and intake. **Comprehensive Reviews in Food Science and Food Safety**, v. 24, n. 3, 6 maio 2025.

YU, Ming; CHEN, Xin; JING, Zuo-Liang. Isonicotinic acid (2-hydroxy-3-methoxybenzylidene)hydrazide. **Acta Crystallographica Section E Structure Reports Online**, v. 61, n. 5, p. o1345–o1346, 15 maio 2005.

ZARROCA, Mario *et al.* Natural acid rock drainage in alpine catchments: A side effect of climate warming. **Science of The Total Environment**, v. 778, p. 146070, jul. 2021.

ZHANG, Chen-Yang *et al.* Description of Si and Al Release from Aluminosilicate in the Acidic Condition Using Density Functional Theory: Protonated Terminal Oxygen. **Sustainability**, v. 14, n. 21, p. 14390, 3 nov. 2022.

ZHAO, Chun-Mei; CAMPBELL, Peter G. C.; WILKINSON, Kevin J. When are metal complexes bioavailable? **Environmental Chemistry**, v. 13, n. 3, p. 425,

2016.

ZHOU, Qi-yuan *et al.* The crosstalk between mitochondrial quality control and metal-dependent cell death. **Cell Death & Disease**, v. 15, n. 4, p. 299, 27 abr. 2024.

ZHU, Wenyu *et al.* Current Trends and Challenges in Drug-Likeness Prediction: Are They Generalizable and Interpretable? **Health Data Science**, v. 3, 10 jan. 2023.

12. Appendix

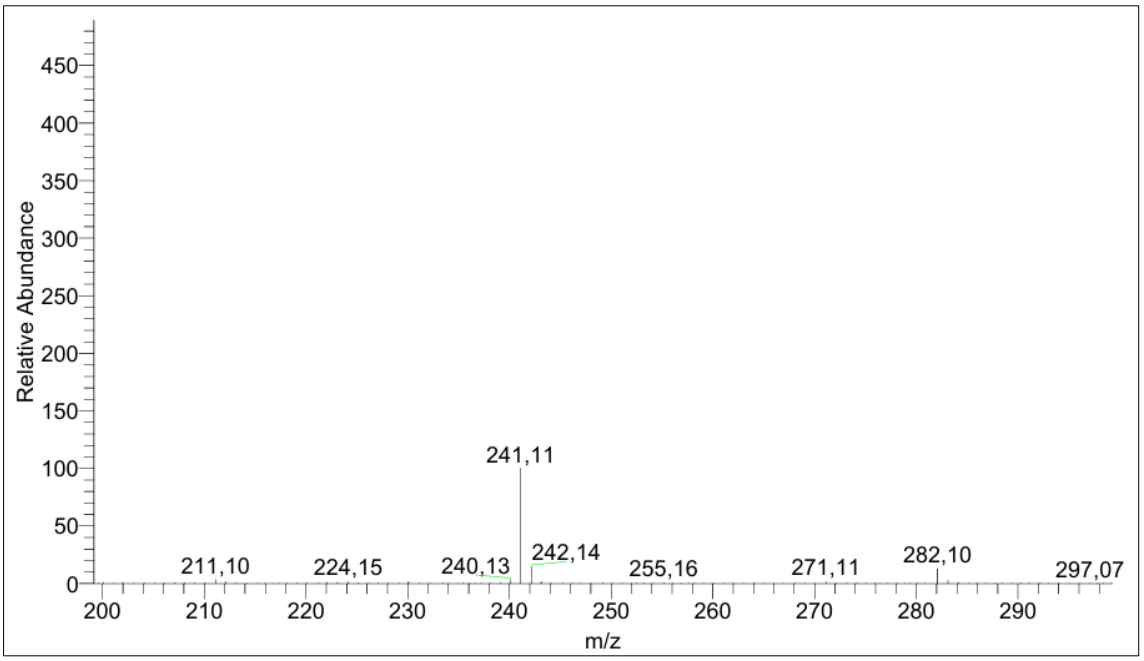

Figure A1. GC-MS chromatogram of the compound **1a**.

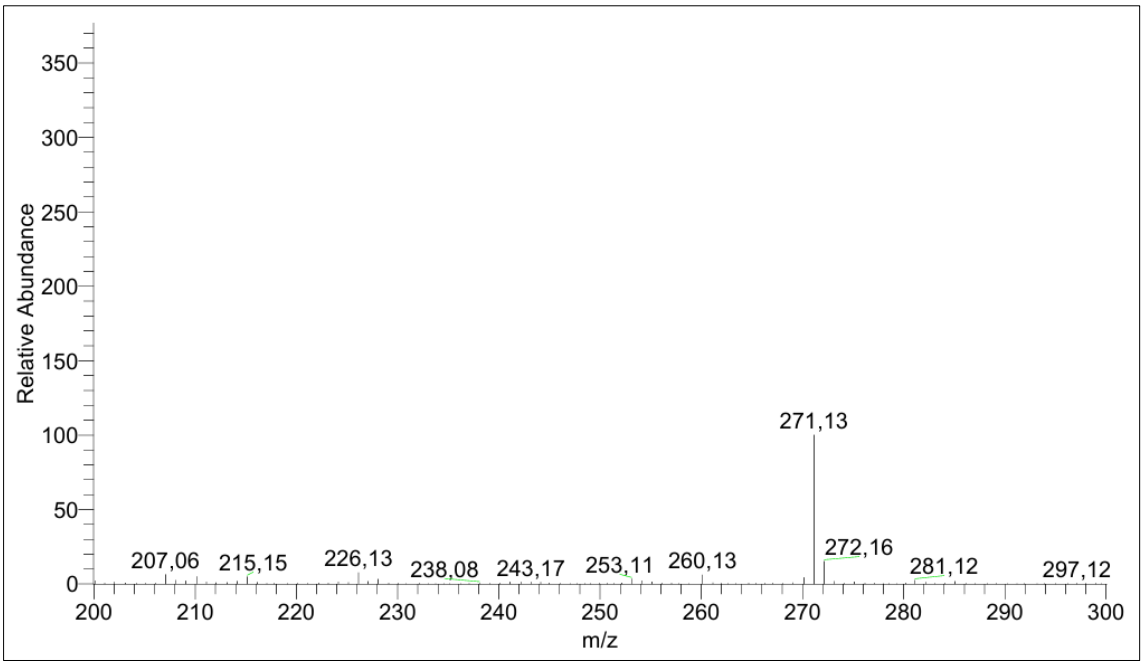

Figure A2.GC-MS chromatogram of the compound **2a**.

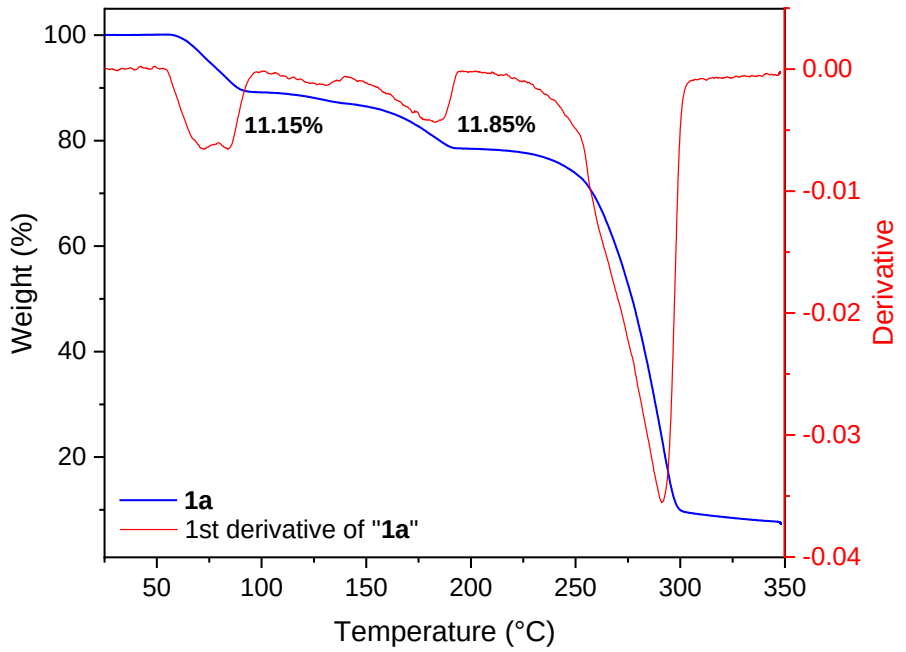

Figure A3. Thermogravimetric curve of **1a** between 25-350 ºC, under N_2 flow. Heating rate of 10 ºC min^{-1}.

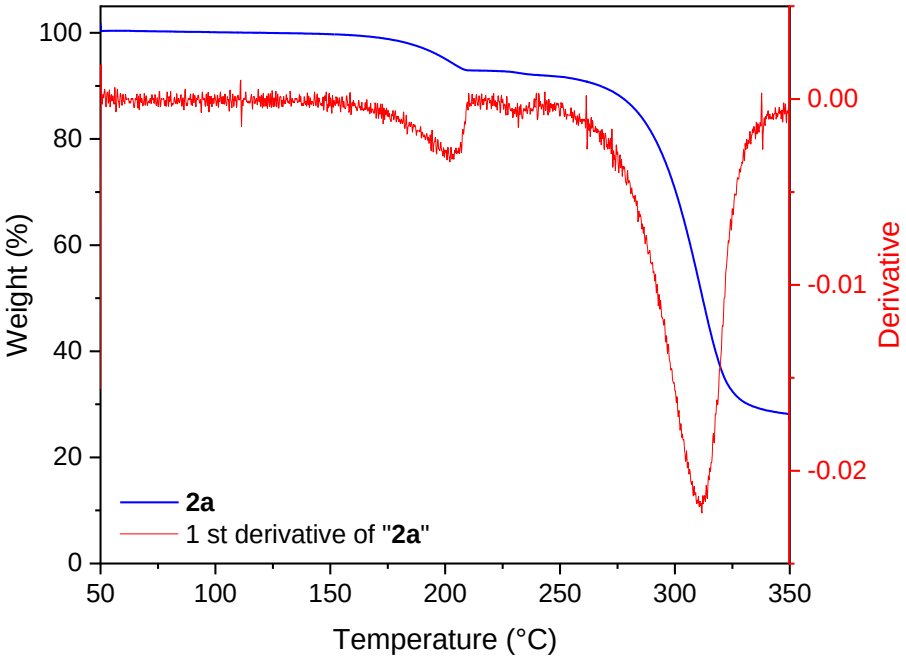

Figure A4. Thermogravimetric curve of **2a** between 50-350 ºC, under N_2 flow. Heating rate of 10 ºC min^{-1}.

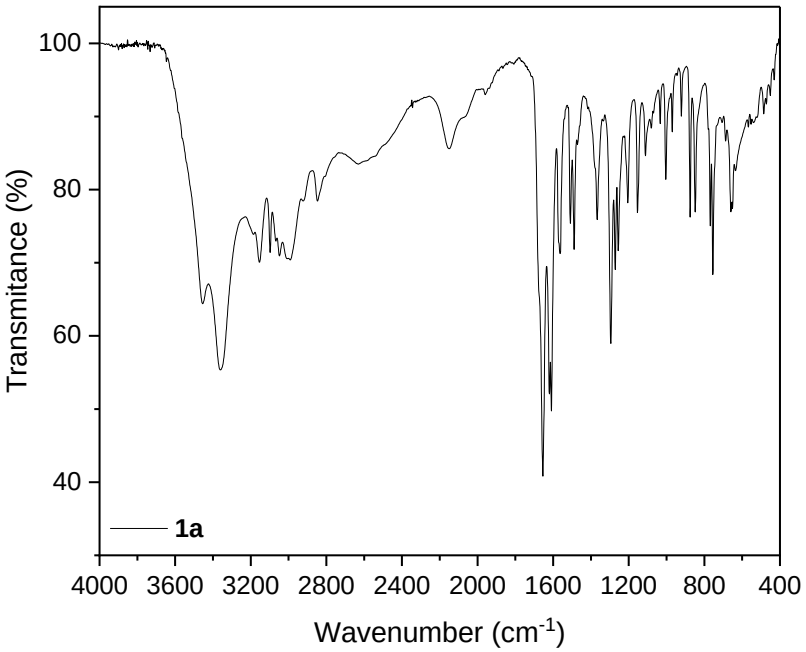

Figure A5. Mid-infrared spectra of **1a**. Experimental conditions: KBr pellets, room temperature.

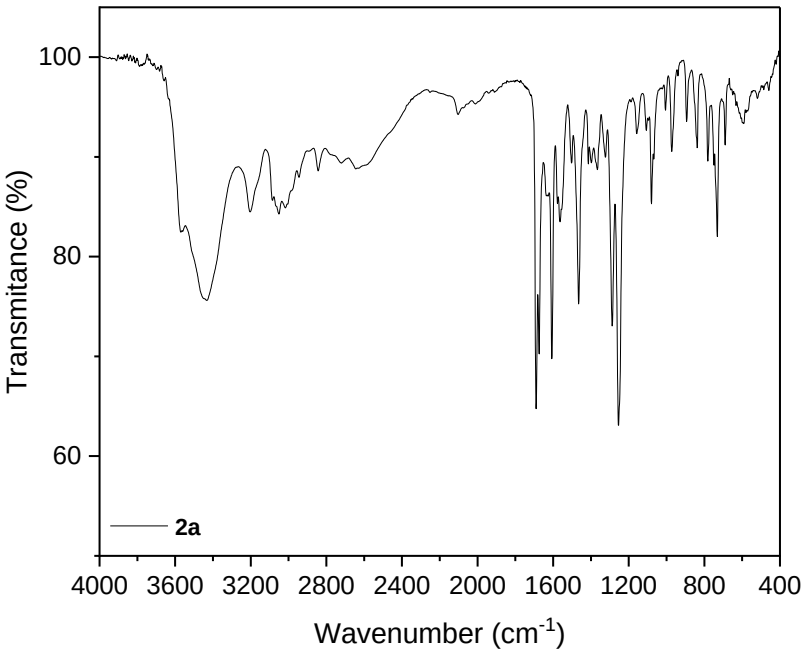

Figure A6. Mid-infrared spectra of **2a**. Experimental conditions: KBr pellets, room temperature.

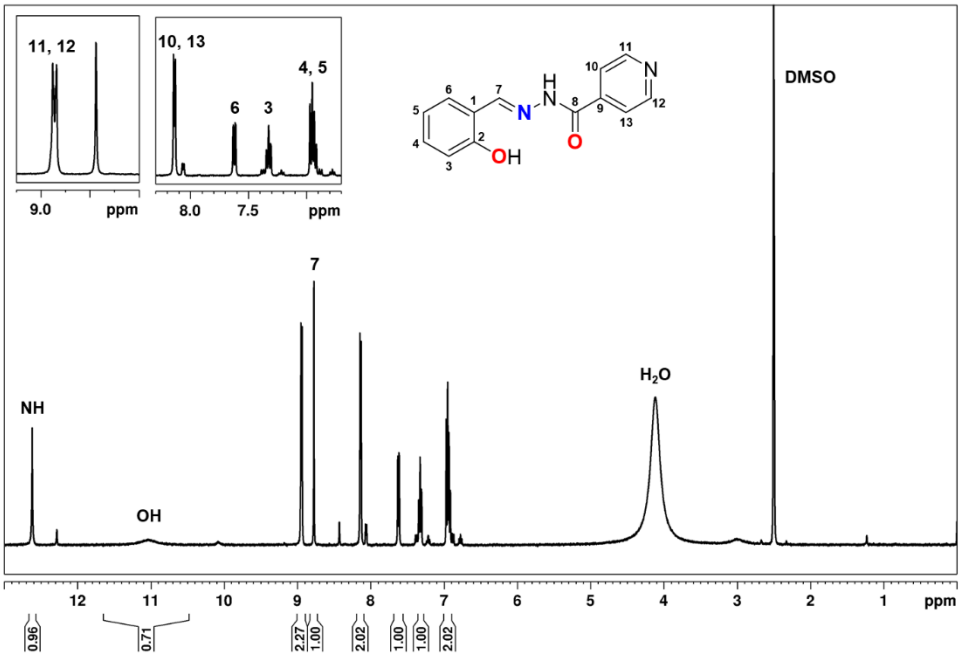

Figure A7. ^{1}H NMR (400 MHz) spectrum of **1a** in DMSO-d_6 at 25 ºC.

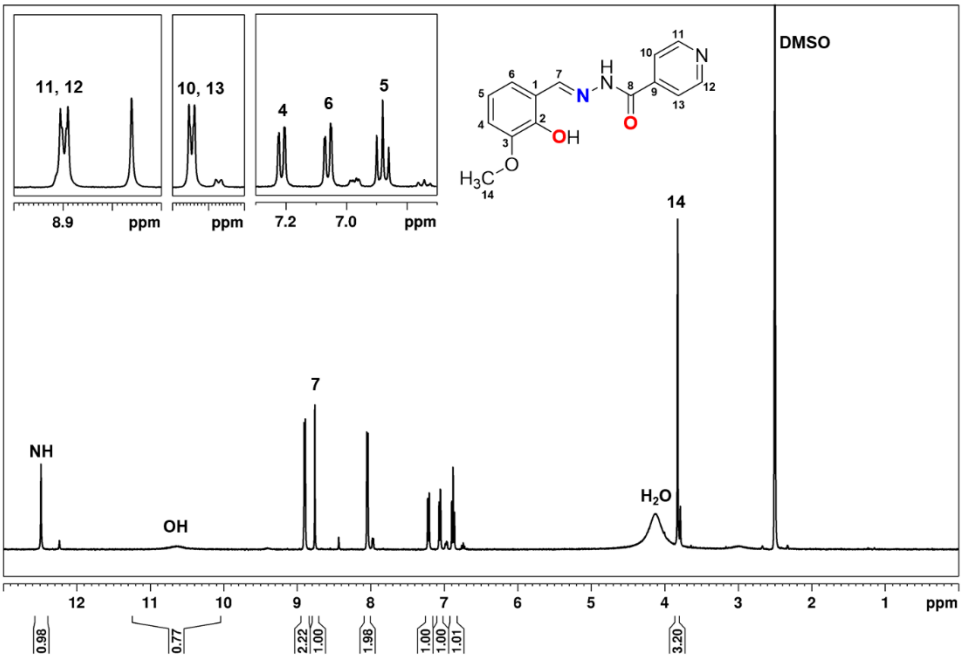

Figure A8. ^{1}H NMR (400 MHz) spectrum of **2a** in DMSO-d_6 at 25 ºC.

Table A1. ^{1}H (400 MHz) signal assignments for compounds **1a** and **2a**, in DMSO-d_6 solution at 25 ^{o}C.

	1a	**2a**
C/H	δ ^{1}H (ppm)	δ ^{1}H (ppm)
C1	-	-
C2	-	-
C3	7.3251 (td, 1H, $^{3}J_{H3\text{-}H4}$ = 6.96225 Hz)	-
C4	6.940875 (m, 2H, $^{3}J_{H4\text{-}H5}$ = 7.28235 Hz)	7.2129 (d, 1H, $^{3}J_{H4\text{-}H5}$ = 7.6025 Hz)
C5	6.940875 (m, 2H, $^{3}J_{H5\text{-}H4}$ = 7.28235 Hz)	6.8784 (t, 1H, $^{3}J_{H5\text{-}H4}$ = 7.9226 Hz)
C6	7.620875 (dd, 1H, $^{3}J_{H6\text{-}H5}$ = 7.7025 Hz)	7.0578 (d, 1H, $^{3}J_{H6\text{-}H5}$ = 7.7625 Hz)
C7	8.7747 (s, 1H)	8.7413 (s, 1H)
C8	-	-
C9	-	-
C10	8.1380 (d, 2H, $^{3}J_{H10\text{-}H11}$ = 6.2420 Hz)	8.0129 (d, 2H, $^{3}J_{H10\text{-}H11}$ = 4.8016 Hz)
C11	8.9438 (d, 2H, $^{3}J_{H11\text{-}H10}$ = 6.2420 Hz)	8.8804 (d, 2H, $^{3}J_{H11\text{-}H10}$ = 4.9616 Hz)
C12	8.9438 (d, 2H, $^{3}J_{H12\text{-}H13}$ = 6.2420 Hz)	8.8804 (d, 2H, $^{3}J_{H12\text{-}H13}$ = 4.9616 Hz)
C13	8.1380 (d, 2H, $^{3}J_{H13\text{-}H12}$ = 6.2420 Hz)	8.0129 (d, 2H, $^{3}J_{H13\text{-}H12}$ = 4.8016 Hz)
C14	-	3.8197 (s, 3H)
OH	11.0364 (*broad s*, 1H)	10.6305 (*broad s*, 1H)
NH	12.6189 (s, 1H)	12.4400 (s, 1H)

Multiplicity: s: singlet, d: doublet, dd: doublet of doublets, t: triplet, dt: doublet triplet m: multiplet.

Table A2. Final coordinates and equivalent isotropic displacement parameters of the non-Hydrogen atoms for compound **3a**.

Atom	x	y	z	U(eq)
O1A	0.36573(17)	0.23386(12)	0.37108(16)	0.0513(8)
O2A	0.0609(2)	0.37000(13)	0.35242(17)	0.0604(9)
N1A	0.3082(2)	0.38967(14)	0.35466(18)	0.0445(10)
N2A	0.2276(2)	0.45554(14)	0.35360(18)	0.0490(10)
N3A	-0.1236(2)	0.64753(16)	0.3892(2)	0.0514(11)
C1A	0.5133(3)	0.34009(18)	0.3500(2)	0.0394(11)
O1B	0.63489(17)	0.53527(12)	0.12664(16)	0.0505(8)
C2A	0.4843(3)	0.25810(19)	0.3658(2)	0.0399(11)
O2B	0.9344(2)	0.39645(13)	0.12572(17)	0.0611(9)
C3A	0.5773(3)	0.19694(19)	0.3775(2)	0.0449(11)
C4A	0.6984(3)	0.2199(2)	0.3721(2)	0.0540(14)
C5A	0.7295(3)	0.2995(2)	0.3560(2)	0.0554(15)
C6A	0.6376(3)	0.3597(2)	0.3454(2)	0.0510(11)
C7A	0.4196(3)	0.40467(19)	0.3417(2)	0.0466(11)
C8A	0.1054(3)	0.4393(2)	0.3567(2)	0.0435(12)
C9A	0.0279(3)	0.51323(18)	0.3672(2)	0.0389(11)
C10A	0.0757(3)	0.57644(18)	0.4290(2)	0.0468(11)
C11A	-0.0039(3)	0.64080(19)	0.4384(2)	0.0517(14)
C12A	-0.1669(3)	0.5867(2)	0.3300(2)	0.0563(14)
C13A	-0.0960(3)	0.51870(19)	0.3178(2)	0.0475(11)
C14A	0.5436(3)	0.10928(18)	0.3945(3)	0.0627(14)
N1B	0.6849(2)	0.37909(14)	0.11524(17)	0.0429(10)
N2B	0.7643(2)	0.31268(15)	0.11463(18)	0.0471(10)
N3B	1.1279(2)	0.11598(16)	0.12117(19)	0.0524(11)
C1B	0.4775(3)	0.42817(18)	0.1160(2)	0.0374(11)

C2B	0.5131(3)	0.51130(19)	0.1217(2)	0.0380(11)
C3B	0.4241(3)	0.57300(18)	0.1237(2)	0.0422(11)
C4B	0.2995(3)	0.5496(2)	0.1185(2)	0.0522(14)
C5B	0.2615(3)	0.4688(2)	0.1120(2)	0.0549(13)
C6B	0.3508(3)	0.40867(19)	0.1105(2)	0.0513(14)
C7B	0.5686(3)	0.36320(19)	0.1155(2)	0.0456(11)
C8B	0.8895(3)	0.32783(19)	0.1199(2)	0.0435(12)
C9B	0.9698(3)	0.25295(18)	0.1185(2)	0.0399(11)
C10B	0.9217(3)	0.17887(18)	0.0795(2)	0.0456(11)
C11B	1.0035(3)	0.11345(19)	0.0821(2)	0.0508(14)
C12B	1.1723(3)	0.1882(2)	0.1573(2)	0.0601(14)
C13B	1.0978(3)	0.25727(19)	0.1576(2)	0.0513(14)
C14B	0.4634(3)	0.66178(18)	0.1294(3)	0.0593(14)

Table A3. (An)isotropic Displacement Parameters for compound **3a**.

Atom	U(1,1)	U(2,2)	U(3,3)	U(2,3)	U(1,3)	U(1,2)
O1A	0.0299(12)	0.0418(14)	0.0838(17)	-0.0024(13)	0.0164(11)	0.0022(10)
O2A	0.0507(14)	0.0357(14)	0.100(2)	-0.0021(14)	0.0283(13)	-0.0006(12)
N1A	0.0342(15)	0.0373(16)	0.0633(19)	-0.0001(13)	0.0137(13)	0.0087(13)
N2A	0.0378(15)	0.0306(16)	0.083(2)	0.0040(14)	0.0227(14)	0.0058(13)
N3A	0.0422(17)	0.0444(18)	0.067(2)	-0.0074(16)	0.0113(14)	0.0076(14)
C1A	0.0347(18)	0.036(2)	0.048(2)	-0.0011(16)	0.0107(15)	0.0022(15)
O1B	0.0331(12)	0.0404(13)	0.0787(17)	-0.0081(12)	0.0144(11)	-0.0008(10)
C2A	0.0307(16)	0.045(2)	0.045(2)	-0.0037(16)	0.0110(14)	0.0032(16)
O2B	0.0516(14)	0.0327(14)	0.102(2)	-0.0021(13)	0.0237(13)	-0.0022(12)
C3A	0.0373(18)	0.042(2)	0.057(2)	-0.0013(17)	0.0140(16)	0.0088(16)
C4A	0.0365(19)	0.057(2)	0.069(3)	-0.004(2)	0.0129(17)	0.0096(18)
C5A	0.0330(19)	0.069(3)	0.067(3)	-0.003(2)	0.0174(17)	0.0037(19)
C6A	0.0375(19)	0.051(2)	0.067(2)	-0.0032(18)	0.0172(16)	-0.0042(17)
C7A	0.0424(19)	0.038(2)	0.061(2)	-0.0017(17)	0.0149(16)	0.0015(16)
C8A	0.043(2)	0.034(2)	0.056(2)	0.0016(17)	0.0166(17)	0.0037(16)
C9A	0.0375(18)	0.0303(19)	0.053(2)	0.0015(16)	0.0187(16)	0.0002(15)
C10A	0.0322(17)	0.038(2)	0.070(2)	-0.0014(19)	0.0110(16)	0.0037(16)
C11A	0.049(2)	0.041(2)	0.064(3)	-0.0091(18)	0.0109(18)	0.0008(18)
C12A	0.039(2)	0.053(2)	0.074(3)	-0.009(2)	0.0072(18)	0.0111(18)
C13A	0.0350(19)	0.041(2)	0.065(2)	-0.0116(17)	0.0081(16)	0.0012(16)
C14A	0.055(2)	0.043(2)	0.093(3)	0.006(2)	0.023(2)	0.0137(18)
N1B	0.0391(15)	0.0329(16)	0.0591(19)	-0.0015(13)	0.0161(13)	0.0074(13)
N2B	0.0398(15)	0.0290(15)	0.078(2)	-0.0009(14)	0.0247(14)	0.0020(13)
N3B	0.0467(18)	0.0408(18)	0.071(2)	-0.0030(15)	0.0161(15)	0.0086(14)
C1B	0.0326(17)	0.0327(19)	0.047(2)	-0.0025(15)	0.0096(14)	-0.0026(15)
C2B	0.0307(17)	0.040(2)	0.043(2)	-0.0027(16)	0.0081(14)	-0.0023(16)

C3B	0.0389(18)	0.037(2)	0.052(2)	-0.0025(16)	0.0128(15)	0.0007(16)
C4B	0.0379(19)	0.052(2)	0.067(3)	-0.0016(19)	0.0129(17)	0.0071(17)
C5B	0.0308(18)	0.055(2)	0.081(3)	0.000(2)	0.0172(17)	-0.0007(18)
C6B	0.040(2)	0.042(2)	0.073(3)	-0.0056(19)	0.0154(17)	-0.0104(17)
C7B	0.0400(19)	0.038(2)	0.061(2)	0.0005(17)	0.0164(17)	-0.0005(16)
C8B	0.043(2)	0.033(2)	0.058(2)	-0.0011(17)	0.0186(16)	0.0004(16)
C9B	0.0454(19)	0.0298(19)	0.049(2)	0.0010(16)	0.0201(16)	0.0030(16)
C10B	0.0389(18)	0.040(2)	0.059(2)	0.0004(18)	0.0133(16)	0.0026(17)
C11B	0.050(2)	0.035(2)	0.067(3)	-0.0072(17)	0.0123(18)	0.0029(17)
C12B	0.044(2)	0.050(2)	0.086(3)	-0.009(2)	0.0143(19)	0.0040(19)
C13B	0.039(2)	0.036(2)	0.080(3)	-0.0095(18)	0.0156(18)	-0.0026(16)
C14B	0.051(2)	0.041(2)	0.087(3)	-0.0045(19)	0.0179(19)	0.0055(17)

Table A4. Bond Distances (Angstrom) for compound **3a**.

O1A	C2A	1.359(4)	N3B	C12B	1.329(4)
O2A	C8A	1.219(4)	N3B	C11B	1.335(4)
N1A	N2A	1.377(3)	C1B	C6B	1.389(5)
N1A	C7A	1.283(4)	C1B	C7B	1.443(4)
O1A	H1A	0.81(3)	C1B	C2B	1.400(4)
N2A	C8A	1.357(4)	N2B	H2B	0.86
N3A	C12A	1.324(4)	C4A	C5A	1.368(5)
N3A	C11A	1.332(4)	C5A	C6A	1.376(5)
C1A	C6A	1.396(5)	C8A	C9A	1.491(4)
C1A	C7A	1.443(4)	C9A	C10A	1.385(4)
C1A	C2A	1.398(4)	C9A	C13A	1.370(5)
O1B	C2B	1.358(4)	C10A	C11A	1.379(4)
C2A	C3A	1.395(5)	C12A	C13A	1.378(5)
N2A	H2A	0.86	O1B	H1B	0.85(3)
O2B	C8B	1.210(4)	N1B	N2B	1.379(3)
C3A	C4A	1.380(5)	N1B	C7B	1.283(4)
C3A	C14A	1.503(4)	N2B	C8B	1.359(4)
C2B	C3B	1.393(4)	C9B	C10B	1.380(4)
C3B	C14B	1.499(4)	C9B	C13B	1.372(5)
C3B	C4B	1.384(5)	C10B	C11B	1.376(4)
C4B	C5B	1.371(5)	C12B	C13B	1.380(5)
C5B	C6B	1.376(5)	C8B	C9B	1.496(4)

Table A5. Bond Angles (Degrees) for compound **3a**.

N2A	N1A	C7A	117.6(2)	C9A	C13A	C12A	119.3(3)
C2A	O1A	H1A	109.1(17)	N2B	N1B	C7B	117.0(2)
N1A	N2A	C8A	117.8(2)	C2B	O1B	H1B	109.4(16)
C11A	N3A	C12A	116.4(3)	N1B	N2B	C8B	118.1(2)
C2A	C1A	C6A	118.6(3)	C11B	N3B	C12B	115.7(3)
C6A	C1A	C7A	119.6(3)	C4B	C3B	C14B	121.8(3)
C2A	C1A	C7A	121.7(3)	C3B	C4B	C5B	122.6(3)
O1A	C2A	C1A	122.3(3)	C4B	C5B	C6B	118.7(3)
O1A	C2A	C3A	116.7(3)	C1B	C6B	C5B	121.5(3)
N1A	N2A	H2A	121	N1B	C7B	C1B	121.5(3)
C8A	N2A	H2A	121	O2B	C8B	N2B	123.2(3)
C1A	C2A	C3A	121.0(3)	O2B	C8B	C9B	121.6(3)
C2A	C3A	C4A	117.8(3)	N2B	C8B	C9B	115.1(3)
C2A	C3A	C14A	119.9(3)	C10B	C9B	C13B	117.7(3)
C4A	C3A	C14A	122.3(3)	C8B	C9B	C10B	123.3(3)
C3A	C4A	C5A	122.5(3)	C8B	C9B	C13B	119.0(3)
C4A	C5A	C6A	119.4(3)	C9B	C10B	C11B	118.8(3)
C1A	C6A	C5A	120.7(3)	N3B	C11B	C10B	124.4(3)
N1A	C7A	C1A	120.9(3)	N3B	C12B	C13B	124.0(3)
O2A	C8A	N2A	123.6(3)	C2B	C1B	C6B	118.5(3)
O2A	C8A	C9A	121.6(3)	C9B	C13B	C12B	119.4(3)
N2A	C8A	C9A	114.9(3)	C1B	C2B	C3B	120.8(3)
C10A	C9A	C13A	117.9(3)	C2B	C3B	C4B	118.0(3)
C8A	C9A	C10A	121.9(3)	C2B	C3B	C14B	120.3(3)
C8A	C9A	C13A	120.2(3)	C2B	C1B	C7B	121.7(3)
C9A	C10A	C11A	118.5(3)	O1B	C2B	C1B	121.9(3)
N3A	C11A	C10A	124.0(3)	O1B	C2B	C3B	117.3(3)

N3A	C12A	C13A	123.9(3)	C6B	C1B	C7B	119.8(3)

Table A6. Torsion Angles (Degrees) for compound **3a**.

C7A	N1A	N2A	C8A	172.8(3)	N1B	N2B	C8B	C9B	179.8(2)
N2A	N1A	C7A	C1A	174.5(3)	C12B	N3B	C11B	C10B	1.6(4)
N1A	N2A	C8A	O2A	6.4(4)	C11B	N3B	C12B	C13B	1.2(4)
N1A	N2A	C8A	C9A	172.9(2)	C6B	C1B	C2B	O1B	179.6(3)
C12A	N3A	C11A	C10A	1.8(5)	C6B	C1B	C2B	C3B	1.3(4)
C11A	N3A	C12A	C13A	0.3(5)	C7B	C1B	C2B	O1B	0.3(4)
C6A	C1A	C2A	O1A	179.9(3)	C7B	C1B	C2B	C3B	178.9(3)
C6A	C1A	C2A	C3A	0.5(4)	C2B	C1B	C6B	C5B	1.0(4)
C7A	C1A	C2A	O1A	2.3(4)	C7B	C1B	C6B	C5B	179.2(3)
C7A	C1A	C2A	C3A	177.4(3)	C2B	C1B	C7B	N1B	3.7(4)
C2A	C1A	C6A	C5A	0.1(4)	C6B	C1B	C7B	N1B	176.1(3)
C7A	C1A	C6A	C5A	178.0(3)	O1B	C2B	C3B	C4B	179.9(3)
C2A	C1A	C7A	N1A	4.5(4)	O1B	C2B	C3B	C14B	1.0(4)
C6A	C1A	C7A	N1A	173.3(3)	C1B	C2B	C3B	C4B	0.9(4)
O1A	C2A	C3A	C4A	179.8(3)	C1B	C2B	C3B	C14B	179.7(3)
O1A	C2A	C3A	C14A	0.3(4)	C2B	C3B	C4B	C5B	0.3(4)
C1A	C2A	C3A	C4A	0.6(4)	C14B	C3B	C4B	C5B	179.1(3)
C1A	C2A	C3A	C14A	179.9(3)	C3B	C4B	C5B	C6B	0.1(4)
C2A	C3A	C4A	C5A	0.1(4)	C4B	C5B	C6B	C1B	0.4(4)
C14A	C3A	C4A	C5A	179.5(3)	O2B	C8B	C9B	C10B	156.0(3)
C3A	C4A	C5A	C6A	0.5(4)	O2B	C8B	C9B	C13B	23.9(4)
C4A	C5A	C6A	C1A	0.6(4)	N2B	C8B	C9B	C10B	24.3(4)
O2A	C8A	C9A	C10A	136.4(3)	N2B	C8B	C9B	C13B	155.8(3)
O2A	C8A	C9A	C13A	40.9(4)	C8B	C9B	C10B	C11B	179.8(3)
N2A	C8A	C9A	C10A	42.8(4)	C13B	C9B	C10B	C11B	0.3(4)

N2A	C8A	C9A	C13A	139.9(3)	C8B	C9B	C13B	C12B	179.4(3)
C8A	C9A	C10A	C11A	176.7(3)	C10B	C9B	C13B	C12B	0.6(4)
C13A	C9A	C10A	C11A	0.8(4)	C9B	C10B	C11B	N3B	0.8(5)
C8A	C9A	C13A	C12A	178.6(3)	N3B	C12B	C13B	C9B	0.2(5)
C10A	C9A	C13A	C12A	1.1(4)	C7B	N1B	N2B	C8B	176.2(3)
C9A	C10A	C11A	N3A	2.3(5)	N2B	N1B	C7B	C1B	179.9(2)
N3A	C12A	C13A	C9A	1.8(5)	N1B	N2B	C8B	O2B	0.5(4)

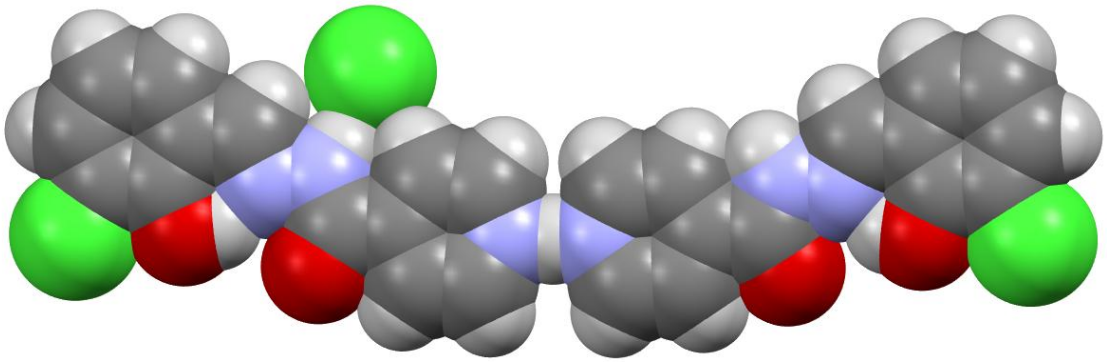

Figure A9. (X+X+H)+ dimers drawn with van der Waals radii (CPK model).

Table A7. Final coordinates and equivalent isotropic displacement parameters of the non-Hydrogen atoms for compound **5a**.

Atom	x	y	z	U(eq)
Cl1	0.29508(8)	0.16786(6)	0.11697(4)	0.045
Cl2	1/2	1/2	1/2	0.0584(4)
O1	0.3338(2)	0.18090(14)	0.26197(11)	0.0375(6)
O2	0.3733(2)	0.10609(15)	0.44144(9)	0.0405(7)
N1	0.3706(2)	0.28063(17)	0.37383(10)	0.0288(6)
N2	0.3986(2)	0.28065(18)	0.44231(11)	0.0291(7)
N3	0.4771(2)	0.16698(18)	0.68460(11)	0.0305(7)
C1	0.3269(2)	0.2754(2)	0.23297(13)	0.0284(8)
C2	0.3073(3)	0.2817(2)	0.16341(13)	0.0318(8)
C3	0.2967(3)	0.3764(2)	0.13058(14)	0.0357(9)
C4	0.3035(3)	0.4679(2)	0.16752(15)	0.0379(9)
C5	0.3237(3)	0.4635(2)	0.23656(14)	0.0338(8)
C6	0.3372(2)	0.3686(2)	0.27031(13)	0.0277(7)
C7	0.3636(2)	0.3681(2)	0.34302(13)	0.0291(8)
C8	0.3985(3)	0.1862(2)	0.47246(13)	0.0285(8)
C9	0.4278(3)	0.1851(2)	0.54736(13)	0.0270(7)
C10	0.4348(3)	0.0879(2)	0.57800(13)	0.0322(8)
C11	0.4602(3)	0.0817(2)	0.64665(13)	0.0334(8)
C12	0.4694(3)	0.2605(2)	0.65555(14)	0.0350(8)
C13	0.4452(3)	0.2733(2)	0.58721(13)	0.0321(8)

Table A8. (An)isotropic Displacement Parameters for compound **5a**.

Atom	U(1,1)	U(2,2)	U(3,3)	U(2,3)	U(1,3)	U(1,2)
Cl1	0.0596(5)	0.0422(5)	0.0355(4)	-0.0099(3)	0.0063(3)	0.0033(3)
Cl2	0.1141(11)	0.0287(6)	0.0341(5)	-0.0047(4)	0.0152(6)	-0.0224(6)
O1	0.0580(13)	0.0229(10)	0.0315(10)	0.0027(7)	0.0037(9)	-0.0045(8)
O2	0.0655(14)	0.0269(11)	0.0279(10)	-0.0034(8)	-0.0012(9)	-0.0042(9)
N1	0.0364(11)	0.0282(12)	0.0220(10)	0.0017(8)	0.0033(8)	-0.0012(9)
N2	0.0394(12)	0.0267(12)	0.0211(10)	-0.0002(8)	0.0024(8)	-0.0010(9)
N3	0.0360(12)	0.0321(13)	0.0234(10)	-0.0001(8)	0.0030(9)	0.0000(9)
C1	0.0283(12)	0.0273(14)	0.0304(13)	0.0031(10)	0.0071(10)	-0.0004(10)
C2	0.0321(13)	0.0342(15)	0.0298(13)	-0.0007(11)	0.0060(10)	0.0011(11)
C3	0.0358(14)	0.0444(17)	0.0272(13)	0.0078(12)	0.0048(10)	0.0031(12)
C4	0.0426(15)	0.0337(16)	0.0374(15)	0.0119(12)	0.0035(12)	0.0015(12)
C5	0.0393(14)	0.0239(14)	0.0382(15)	0.0044(11)	0.0042(11)	0.0023(11)
C6	0.0287(12)	0.0258(13)	0.0290(13)	0.0044(10)	0.0043(10)	-0.0003(10)
C7	0.0305(13)	0.0273(14)	0.0299(13)	0.0000(10)	0.0057(10)	-0.0019(10)
C8	0.0345(13)	0.0247(13)	0.0265(13)	-0.0019(10)	0.0035(10)	-0.0004(10)
C9	0.0303(13)	0.0264(13)	0.0246(12)	0.0007(10)	0.0042(9)	-0.0003(10)
C10	0.0424(15)	0.0255(14)	0.0288(13)	-0.0030(10)	0.0044(11)	0.0010(11)
C11	0.0451(15)	0.0280(15)	0.0275(13)	0.0031(10)	0.0056(11)	0.0036(11)
C12	0.0472(16)	0.0294(15)	0.0282(13)	-0.0032(11)	0.0036(11)	-0.0061(12)
C13	0.0440(15)	0.0258(14)	0.0266(13)	-0.0003(10)	0.0042(11)	-0.0032(11)

Table A9. Bond Distances (Angstrom) for compound **5a**.

Cl1	C2	1.735(3)	C5	C6	1.398(4)
O1	C1	1.348(3)	C6	C7	1.457(4)
O2	C8	1.218(3)	C8	C9	1.502(4)
N1	N2	1.375(3)	C9	C10	1.394(4)
N1	C7	1.284(3)	C9	C13	1.390(4)
O1	H1	0.87(4)	C10	C11	1.378(4)
N2	C8	1.359(3)	C12	C13	1.378(4)
N3	C12	1.337(3)	C3	H3	0.9500
N3	C11	1.338(3)	C4	H4	0.9500
C1	C2	1.392(4)	C5	H5	0.9500
C1	C6	1.414(4)	C7	H7	0.9500
N2	H1BB	0.88(4)	C10	H10	0.9500
C2	C3	1.386(4)	C11	H11	0.9500
N3	H3A	1.310(2)	C12	H12	0.9500
C3	C4	1.391(4)	C13	H13	0.9500
C4	C5	1.381(4)			

Table A10. Bond Angles (Degrees) for compound **5a**.

N2	N1	C7	118.5(2)	C8	C9	C13	124.6(2)
C1	O1	H1	109.5(5)	C10	C9	C13	118.9(2)
N1	N2	C8	115.8(2)	C8	C9	C10	116.5(2)
C11	N3	C12	119.6(2)	C9	C10	C11	119.3(2)
O1	C1	C2	118.8(2)	N3	C11	C10	121.4(2)
C2	C1	C6	118.5(2)	N3	C12	C13	122.6(2)
O1	C1	C6	122.7(2)	C9	C13	C12	118.3(2)
Cl1	C2	C1	119.0(2)	C2	C3	H3	120.00
Cl1	C2	C3	119.4(2)	C4	C3	H3	120.00
N1	N2	H1BB	123(2)	C3	C4	H4	120.00
C8	N2	H1BB	121(2)	C5	C4	H4	120.00
C1	C2	C3	121.6(2)	C4	C5	H5	119.00
C2	C3	C4	119.7(3)	C6	C5	H5	119.00
C11	N3	H3A	123(3)	N1	C7	H7	121.00
C12	N3	H3A	117(3)	C6	C7	H7	121.00
C3	C4	C5	119.6(2)	C9	C10	H10	120.00
C4	C5	C6	121.3(2)	C11	C10	H10	120.00
C1	C6	C5	119.2(2)	N3	C11	H11	119.00
C1	C6	C7	121.6(2)	C10	C11	H11	119.00
C5	C6	C7	119.2(2)	N3	C12	H12	119.00
N1	C7	C6	118.8(2)	C13	C12	H12	119.00
O2	C8	C9	120.8(2)	C9	C13	H13	121.00
N2	C8	C9	116.4(2)	C12	C13	H13	121.00
O2	C8	N2	122.7(2)				

Table A11. Torsion Angles (Degrees) for compound **5a**.

C7	N1	N2	C8	177.0(2)
N2	N1	C7	C6	178.53(19)
N1	N2	C8	O2	-1.1(4)
N1	N2	C8	C9	-179.5(2)
C12	N3	C11	C10	-0.1(4)
C11	N3	C12	C13	-0.4(4)
O1	C1	C2	Cl1	-0.9(3)
O1	C1	C2	C3	178.7(3)
C6	C1	C2	Cl1	179.78(18)
C6	C1	C2	C3	-0.6(4)
O1	C1	C6	C5	-177.5(2)
O1	C1	C6	C7	3.5(3)
C2	C1	C6	C5	1.8(3)
C2	C1	C6	C7	-177.3(2)
Cl1	C2	C3	C4	178.6(2)
C1	C2	C3	C4	-1.1(4)
C2	C3	C4	C5	1.4(5)
C3	C4	C5	C6	-0.2(4)
C4	C5	C6	C1	-1.4(4)
C4	C5	C6	C7	177.6(2)
C1	C6	C7	N1	-3.7(3)
C5	C6	C7	N1	177.3(2)
O2	C8	C9	C10	4.9(4)
O2	C8	C9	C13	-173.8(3)
N2	C8	C9	C10	-176.7(3)
N2	C8	C9	C13	4.7(4)
C8	C9	C10	C11	-179.4(3)
C13	C9	C10	C11	-0.7(4)
C8	C9	C13	C12	178.9(3)
C10	C9	C13	C12	0.3(4)
C9	C10	C11	N3	0.6(4)
N3	C12	C13	C9	0.2(5)

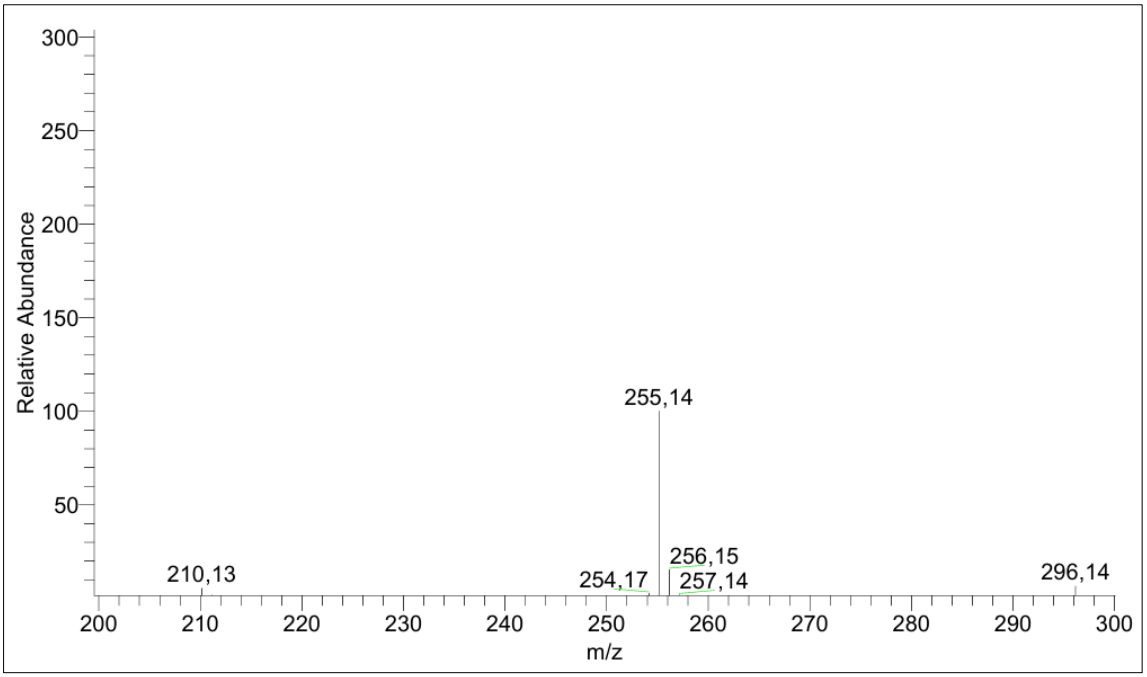

Figure A10. GC-MS chromatogram of the compound **3a**.

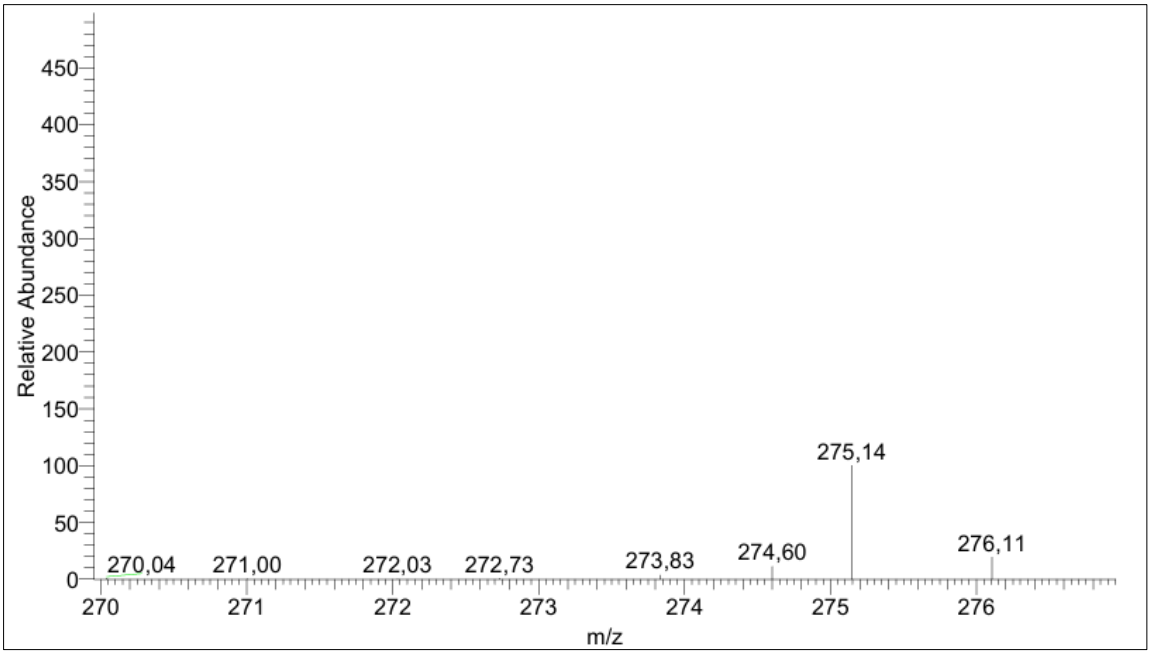

Figure A11. GC-MS chromatogram of the compound **5a**.

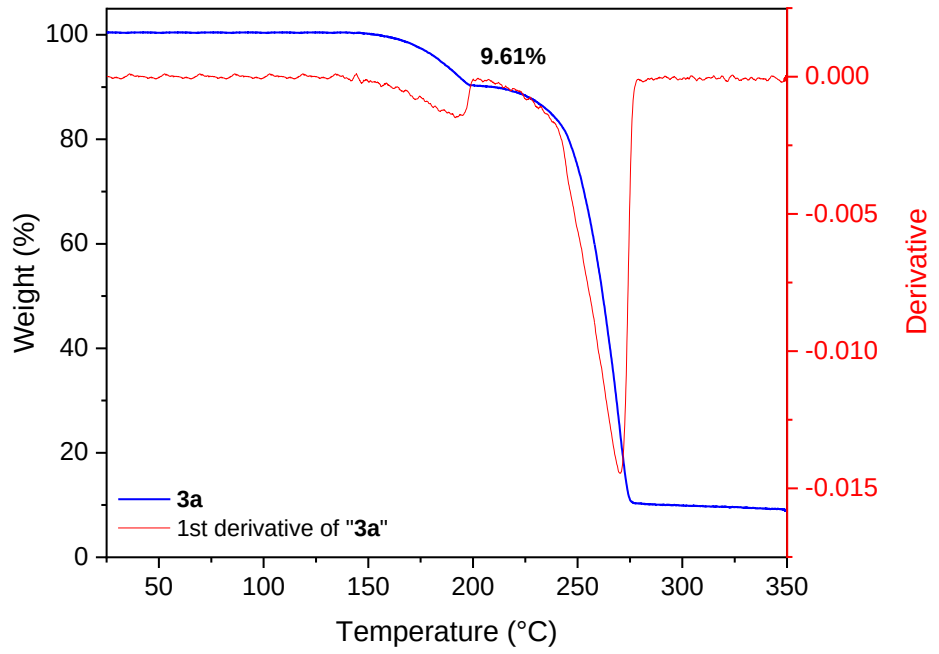

Figure A12. Thermogravimetric curve of **3a** between 25-350 ºC, under N_2 flow. Heating rate of 10 ºC min^{-1}.

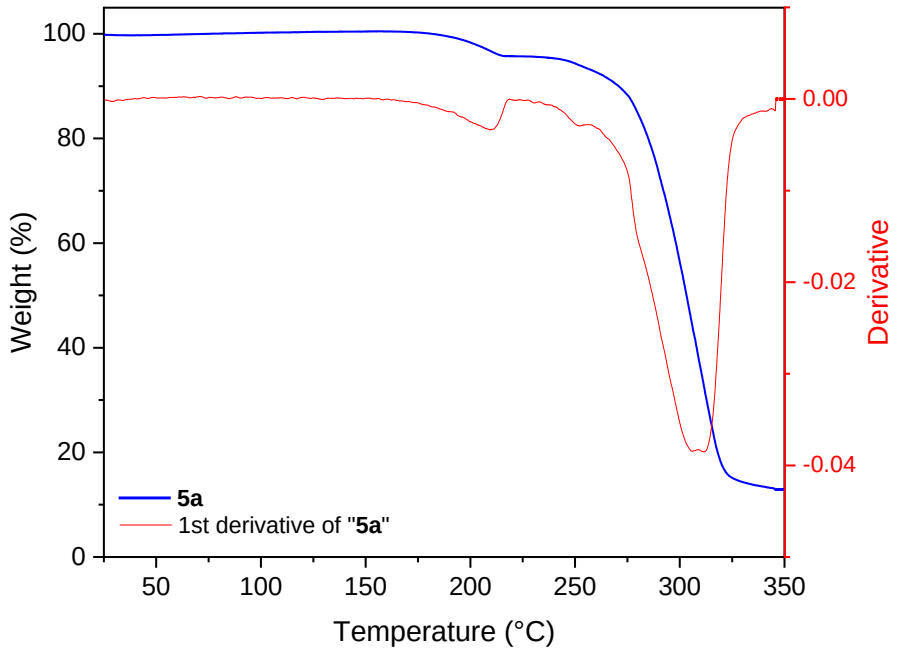

Figure A13. Thermogravimetric curve of **5a** between 25-350 ºC, under N_2 flow. Heating rate of 10 ºC min^{-1}.

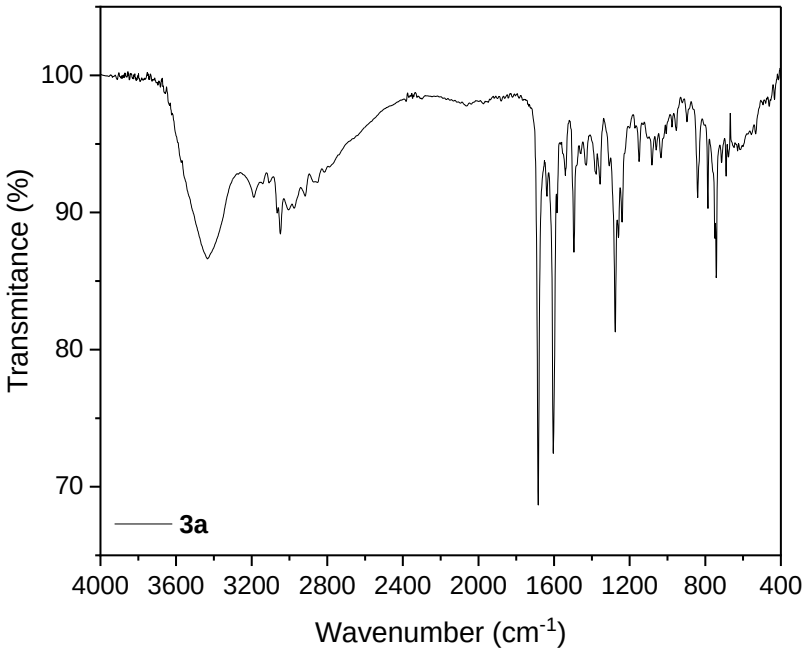

Figure A14. Mid-infrared spectra of **3a**. Experimental conditions: KBr pellets, room temperature

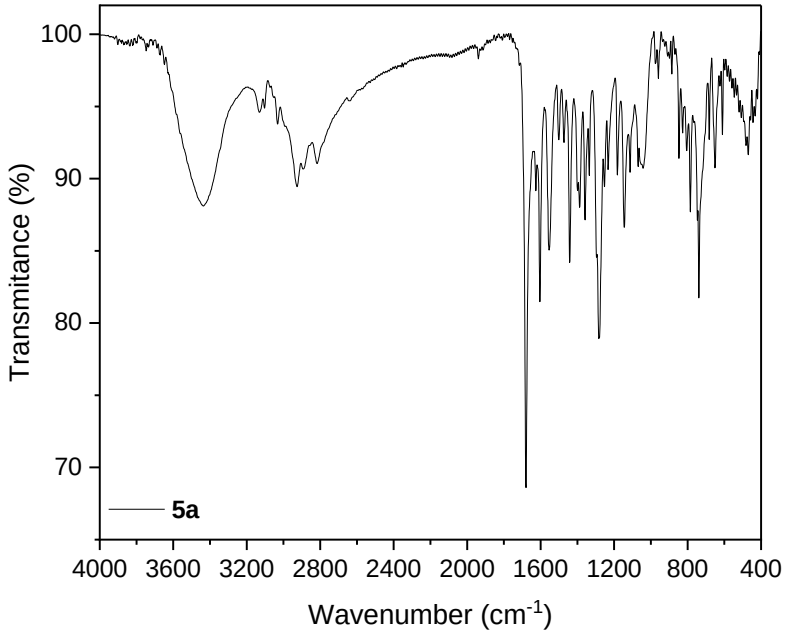

Figure A15. Mid-infrared spectra of **5a**. Experimental conditions: KBr pellets, room temperature.

Table A12. ^{1}H (400 MHz) signal assignments for compounds **3a** and **5a**, in DMSO-d_6 solution at 25 ºC.

	3a	**5a**
C/H	δ ^{1}H (ppm)	δ ^{1}H (ppm)
C1	-	-
C2	-	-
C3	-	-
C4	7.25115 (d, 1H, $^{3}J_{H4\text{-}H5}$ = 7.3012 Hz)	7.5287 (td, 2H, $^{3}J_{H6\text{-}H5}$ = 7.7159 Hz)
C5	6.8769 (t, 1H, $^{3}J_{H5\text{-}H4,6}$ = 7.5314 Hz)	6.9908 (t, 1H, $^{3}J_{H5\text{-}H4,6}$ = 7.8339 Hz)
C6	7.3235 (d, 1H, $^{3}J_{H6\text{-}H5}$ = 7.6821 Hz)	7.5287 (td, 2H, $^{3}J_{H6\text{-}H5}$ = 7.7159 Hz)
C7	8.7072 (s, 1H)	8.7058 (s, 1H)
C8	-	-
C9	-	-
C10	8.1372 (d, 2H, $^{3}J_{HH}$ = 6.2364 Hz)	8.007175 (dd, 2H, $^{3}J_{H10\text{-}H11}$ = 6.1976 Hz)
C11	8.9460 (d, 2H, $^{3}J_{HH}$ = 6.2364 Hz)	8.88865 (dd, 2H, $^{3}J_{H11\text{-}H10}$ = 6.1452 Hz)
C12	8.9460 (d, 2H, $^{3}J_{HH}$ = 6.2696 Hz)	8.88865 (dd, 2H, $^{3}J_{H12\text{-}H13}$ = 6.1452 Hz)
C13	8.1372 (d, 2H, $^{3}J_{HH}$ = 6.2696 Hz)	8.007175 (dd, 2H, $^{3}J_{H13\text{-}H12}$ = 6.1976 Hz)
C14	2.2202 (s, 3H)	-
OH	11.7283 (*broad s*, 1H)	12.1717 (s, 1H)
NH	12.8373 (s, 1H)	12.7901 (s, 1H)

Multiplicity: s: singlet, d: doublet, dd: doublet of doublets, t: triplet, dt: doublet triplet m: multiplet.

Table A13. Final coordinates and equivalent isotropic displacement parameters of the non-Hydrogen atoms for compound **3b**.

Atom	x	y	z	U(eq)	[Ang^2]
O1	0.42207(4)		0.84485(15)	0.48144(11)	0.0567(4)
O2	0.53669(5)		0.68634(15)	0.63564(11)	0.0628(5)
O3	0.60489(5)		0.05964(16)	0.83661(11)	0.0662(5)
O4	0.68071(5)		0.22531(18)	0.93676(10)	0.0626(5)
O5	0.68935(4)		0.52186(18)	0.88766(10)	0.0622(5)
N1	0.45460(5)		0.57115(17)	0.55161(11)	0.0456(5)
N2	0.49043(5)		0.47804(18)	0.60945(11)	0.0455(5)
C1	0.37663(6)		0.6091(2)	0.45360(12)	0.0437(5)
C2	0.38140(6)		0.7724(2)	0.44231(12)	0.0453(5)
C3	0.34332(7)		0.8659(2)	0.38980(14)	0.0545(6)
C4	0.30174(7)		0.7931(3)	0.34880(16)	0.0640(7)
C5	0.29642(7)		0.6320(3)	0.35729(16)	0.0662(7)
C6	0.33364(6)		0.5415(2)	0.40980(15)	0.0556(6)
O6	0.52956(7)		0.84682(19)	0.45857(13)	0.0788(6)
C7	0.41526(6)		0.5105(2)	0.51100(13)	0.0460(6)
C8	0.53151(6)		0.54788(19)	0.65184(12)	0.0435(5)
C9	0.57007(6)		0.4506(2)	0.72145(12)	0.0426(5)
C10	0.56680(6)		0.2924(2)	0.74102(13)	0.0467(5)
C11	0.60448(6)		0.2142(2)	0.81062(14)	0.0486(6)
C12	0.64489(6)		0.2952(2)	0.86038(13)	0.0489(6)
C13	0.64802(6)		0.4529(2)	0.83732(13)	0.0473(6)
C14	0.61066(6)		0.5307(2)	0.76879(13)	0.0458(5)
C15	0.34913(9)		1.0406(3)	0.38065(19)	0.0754(8)
C16	0.56570(8)		-0.0306(2)	0.78414(17)	0.0681(7)
C17	0.69173(7)		0.6871(3)	0.87834(19)	0.0744(8)
C18	0.70841(9)		0.1262(4)	0.9080(2)	0.0901(9)

Table A14. (An)isotropic Displacement Parameters for compound **3b**.

Atom	U(1,1)	U(2,2)	U(3,3)	U(2,3)	U(1,3)	U(1,2)
O1	0.0466(7)	0.0484(7)	0.0676(8)	-0.0011(6)	0.0145(6)	-0.0018(6)
O2	0.0561(8)	0.0447(7)	0.0677(9)	0.0034(6)	0.0033(7)	-0.0045(6)
O3	0.0582(9)	0.0480(8)	0.0735(9)	0.0064(6)	0.0059(7)	0.0051(6)
O4	0.0492(8)	0.0737(9)	0.0510(8)	0.0044(6)	0.0050(6)	0.0172(6)
O5	0.0371(7)	0.0756(10)	0.0619(9)	0.0001(7)	0.0069(6)	-0.0054(6)
N1	0.0384(8)	0.0477(8)	0.0455(8)	0.0017(6)	0.0111(6)	0.0058(6)
N2	0.0374(8)	0.0437(8)	0.0488(8)	0.0055(6)	0.0099(6)	0.0051(6)
C1	0.0375(9)	0.0492(9)	0.0430(9)	0.0014(7)	0.0143(7)	0.0025(7)
C2	0.0398(9)	0.0530(10)	0.0428(9)	0.0012(7)	0.0159(7)	0.0017(7)
C3	0.0499(11)	0.0611(11)	0.0524(10)	0.0097(8)	0.0200(8)	0.0130(8)
C4	0.0425(10)	0.0823(15)	0.0620(12)	0.0185(10)	0.0151(9)	0.0155(9)
C5	0.0372(10)	0.0894(16)	0.0648(12)	0.0080(11)	0.0125(9)	-0.0032(9)
C6	0.0451(10)	0.0604(11)	0.0598(11)	0.0027(8)	0.0190(9)	-0.0036(8)
O6	0.0927(12)	0.0559(9)	0.0787(11)	-0.0018(8)	0.0240(9)	-0.0219(8)
C7	0.0417(10)	0.0460(9)	0.0501(10)	0.0038(7)	0.0179(8)	0.0025(7)
C8	0.0428(9)	0.0426(9)	0.0407(9)	-0.0017(7)	0.0117(7)	0.0023(7)
C9	0.0370(9)	0.0488(9)	0.0390(8)	-0.0023(7)	0.0118(7)	0.0025(7)
C10	0.0383(9)	0.0491(10)	0.0460(9)	-0.0037(7)	0.0095(7)	0.0012(7)
C11	0.0473(10)	0.0463(9)	0.0478(10)	-0.0014(7)	0.0140(8)	0.0063(7)
C12	0.0390(9)	0.0597(11)	0.0411(9)	0.0002(7)	0.0084(7)	0.0102(7)
C13	0.0347(9)	0.0596(11)	0.0440(9)	-0.0034(7)	0.0118(7)	-0.0013(7)
C14	0.0392(9)	0.0491(9)	0.0468(9)	-0.0002(7)	0.0147(7)	-0.0017(7)
C15	0.0748(15)	0.0625(13)	0.0850(16)	0.0172(11)	0.0275(12)	0.0191(11)
C16	0.0736(14)	0.0491(11)	0.0672(12)	-0.0031(9)	0.0124(11)	-0.0048(9)
C17	0.0507(12)	0.0816(16)	0.0769(15)	0.0057(11)	0.0104(10)	-0.0215(10)
C18	0.0696(15)	0.0927(18)	0.0852(16)	-0.0118(14)	0.0063(12)	0.0372(14)

Table A15. Bond Distances (Angstrom) for compound **3b**.

O1	C2	1.350(2)	C10	C11	1.397(3)
O2	C8	1.222(2)	C11	C12	1.392(3)
O3	C11	1.362(2)	C12	C13	1.391(2)
O3	C16	1.411(3)	C13	C14	1.383(3)
O4	C12	1.372(2)	C4	H4	0.9300
O4	C18	1.400(4)	C5	H5	0.9300
O5	C13	1.368(2)	C6	H6	0.9300
O5	C17	1.413(3)	O6	H6A	0.83(2)
N1	N2	1.373(2)	O6	H6B	0.84(2)
N1	C7	1.273(3)	C7	H7	0.9300
O1	H1	0.94(2)	C10	H10	0.9300
N2	C8	1.353(3)	C14	H14	0.9300
C1	C6	1.395(3)	C15	H15B	0.9600
C1	C7	1.453(3)	C15	H15A	0.9600
C1	C2	1.410(2)	C15	H15C	0.9600
C2	C3	1.402(3)	C16	H16B	0.9600
N2	H2A	0.827(18)	C16	H16A	0.9600
C3	C4	1.376(3)	C16	H16C	0.9600
C3	C15	1.506(3)	C17	H17B	0.9600
C4	C5	1.389(4)	C17	H17C	0.9600
C5	C6	1.370(3)	C17	H17A	0.9600
C8	C9	1.496(2)	C18	H18C	0.9600
C9	C14	1.388(3)	C18	H18A	0.9600
C9	C10	1.384(2)	C18	H18B	0.9600

Table A16. Bond Angles (Degrees) for compound **3b**.

C11	O3	C16	117.77(16)	O3	C11	C10	124.43(17)
C12	O4	C18	116.97(16)	O3	C11	C12	115.37(17)
C13	O5	C17	116.86(16)	C10	C11	C12	120.19(16)
N2	N1	C7	119.26(15)	C11	C12	C13	119.53(17)
C2	O1	H1	109.4(13)	O4	C12	C11	121.03(16)
N1	N2	C8	117.18(15)	O4	C12	C13	119.28(17)
C2	C1	C7	121.55(17)	O5	C13	C12	115.58(16)
C6	C1	C7	119.42(16)	O5	C13	C14	124.13(16)
C2	C1	C6	119.02(17)	C12	C13	C14	120.28(18)
O1	C2	C1	122.06(16)	C9	C14	C13	119.94(16)
O1	C2	C3	117.54(16)	C3	C4	H4	119.00
N1	N2	H2A	116.7(17)	C5	C4	H4	119.00
C8	N2	H2A	126.0(18)	C4	C5	H5	120.00
C1	C2	C3	120.40(18)	C6	C5	H5	120.00
C2	C3	C4	118.05(18)	C1	C6	H6	120.00
C2	C3	C15	119.4(2)	C5	C6	H6	120.00
C4	C3	C15	122.5(2)	H6A	O6	H6B	106(2)
C3	C4	C5	122.5(2)	C1	C7	H7	120.00
C4	C5	C6	119.3(2)	N1	C7	H7	120.00
C1	C6	C5	120.79(18)	C11	C10	H10	120.00
N1	C7	C1	119.91(16)	C9	C10	H10	120.00
O2	C8	N2	121.17(17)	C9	C14	H14	120.00
O2	C8	C9	121.24(17)	C13	C14	H14	120.00
N2	C8	C9	117.58(15)	C3	C15	H15A	109.00
C10	C9	C14	120.50(17)	C3	C15	H15B	109.00
C8	C9	C14	115.33(15)	H15A	C15	H15B	109.00
C8	C9	C10	124.16(17)	H15A	C15	H15C	109.00
C9	C10	C11	119.49(17)	H15B	C15	H15C	109.00
C3	C15	H15C	109.00	H17A	C17	H17C	109.00
O3	C16	H16B	109.00	O5	C17	H17C	109.00
O3	C16	H16C	109.00	H17B	C17	H17C	109.00
O3	C16	H16A	109.00	O4	C18	H18B	109.00
H16A	C16	H16C	109.00	O4	C18	H18C	109.00
H16B	C16	H16C	110.00	O4	C18	H18A	109.00
H16A	C16	H16B	109.00	H18A	C18	H18C	109.00
O5	C17	H17A	109.00	H18B	C18	H18C	109.00
O5	C17	H17B	109.00	H18A	C18	H18B	109.00
H17A	C17	H17B	109.00				

Table A17. Torsion Angles (Degrees) for compound **3b**.

C16	O3	C11	C10	5.0(3)
C16	O3	C11	C12	-176.29(18)
C18	O4	C12	C11	81.8(3)
C18	O4	C12	C13	-102.7(2)
C17	O5	C13	C12	-170.22(18)
C17	O5	C13	C14	8.7(3)
C7	N1	N2	C8	-179.41(16)
N2	N1	C7	C1	177.05(15)
N1	N2	C8	O2	-3.0(3)
N1	N2	C8	C9	175.37(15)
C6	C1	C2	O1	-179.00(17)
C6	C1	C2	C3	1.5(3)
C7	C1	C2	O1	2.0(3)
C7	C1	C2	C3	-177.56(17)
C2	C1	C6	C5	-0.6(3)
C7	C1	C6	C5	178.45(18)
C2	C1	C7	N1	-0.7(3)
C6	C1	C7	N1	-179.72(18)
O1	C2	C3	C4	179.42(18)
O1	C2	C3	C15	-0.9(3)
C1	C2	C3	C4	-1.0(3)
C1	C2	C3	C15	178.69(18)
C2	C3	C4	C5	-0.3(3)
C15	C3	C4	C5	-180.0(2)
C3	C4	C5	C6	1.2(3)
C4	C5	C6	C1	-0.7(3)
O2	C8	C9	C10	-178.25(18)
O2	C8	C9	C14	3.0(3)
N2	C8	C9	C10	3.4(3)
N2	C8	C9	C14	-175.40(16)
C8	C9	C10	C11	-177.36(17)
C14	C9	C10	C11	1.4(3)
C8	C9	C14	C13	177.79(17)
C10	C9	C14	C13	-1.0(3)
C9	C10	C11	O3	179.07(18)
C9	C10	C11	C12	0.5(3)
O3	C11	C12	O4	-5.8(3)
O3	C11	C12	C13	178.70(17)
C10	C11	C12	O4	172.92(17)
C10	C11	C12	C13	-2.6(3)
O4	C12	C13	O5	6.3(3)
O4	C12	C13	C14	-172.67(17)
C11	C12	C13	O5	-178.17(17)
C11	C12	C13	C14	2.9(3)
O5	C13	C14	C9	-179.96(18)
C12	C13	C14	C9	-1.1(3)

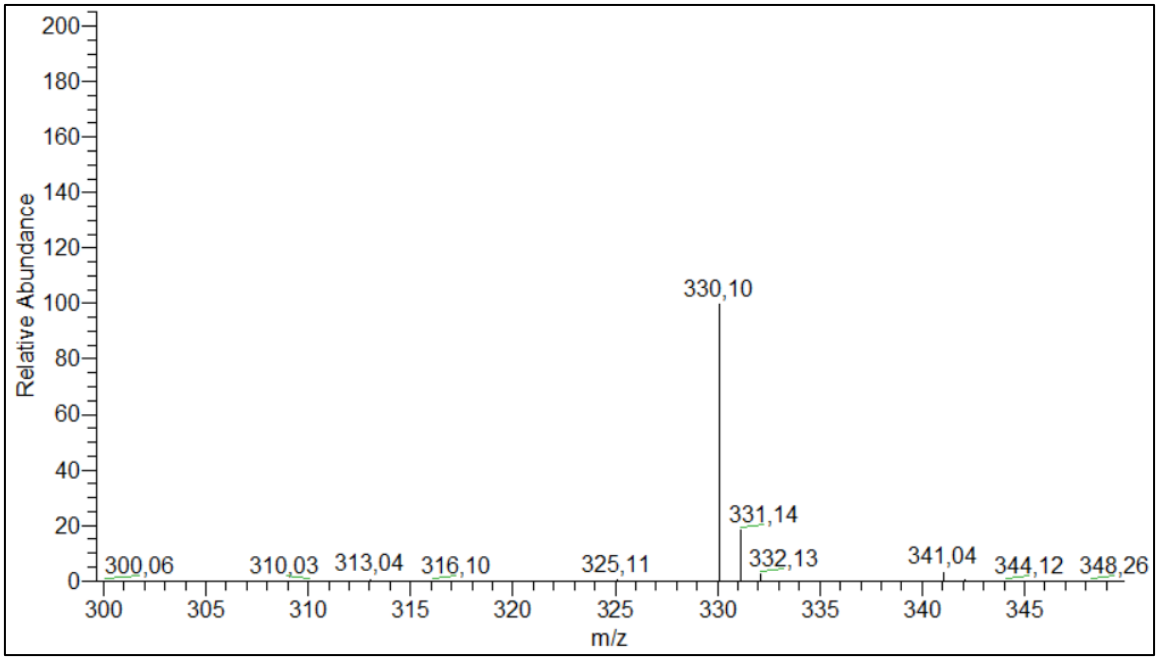

Figure A16. GC-MS chromatogram of the compound **1b**.

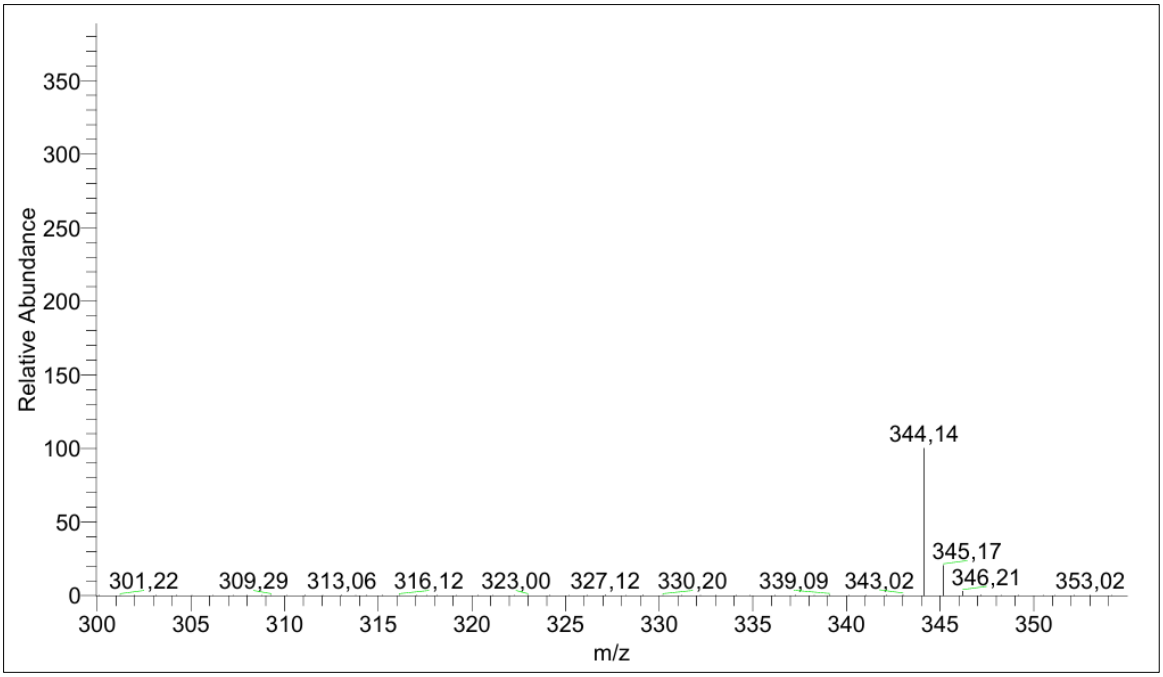

Figure A17. GC-MS chromatogram of the compound **3b**.

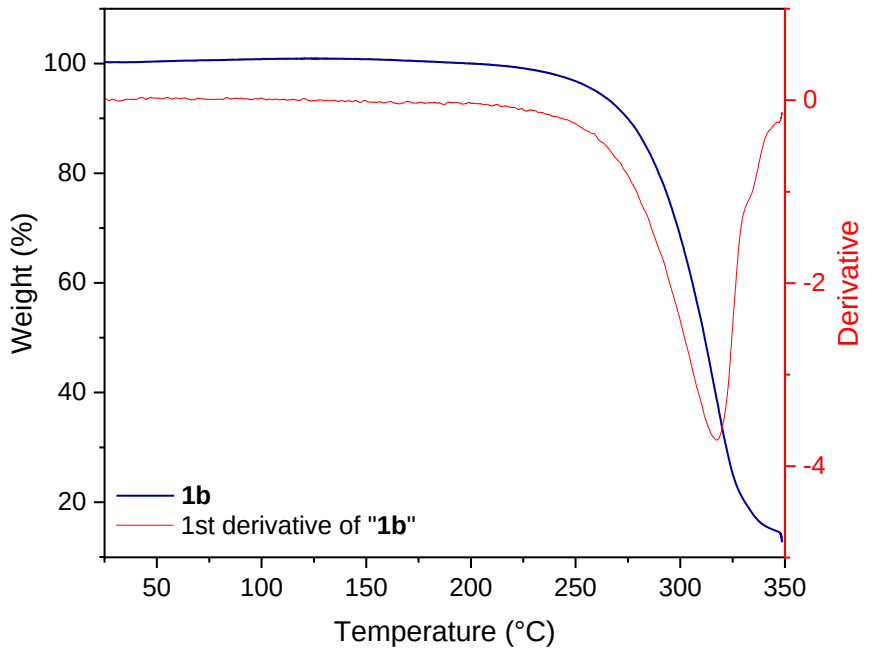

Figure A18. Thermogravimetric curve of **1b** between 25-350 ºC, under N_2 flow. Heating rate of 10 ºC min^{-1}.

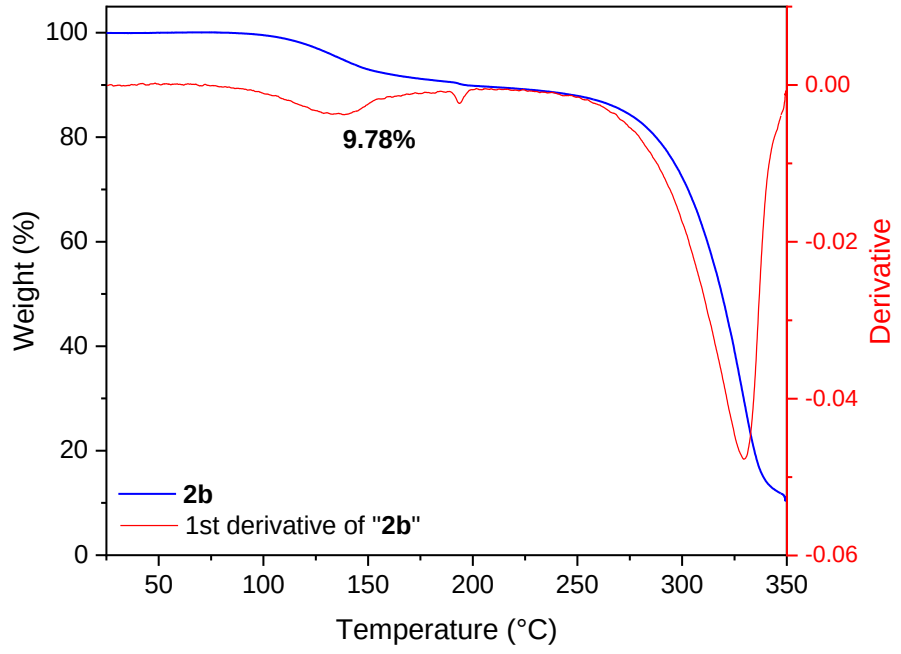

Figure A19. Thermogravimetric curve of **3b** between 25-350 ºC, under N_2 flow. Heating rate of 10 ºC min^{-1}.

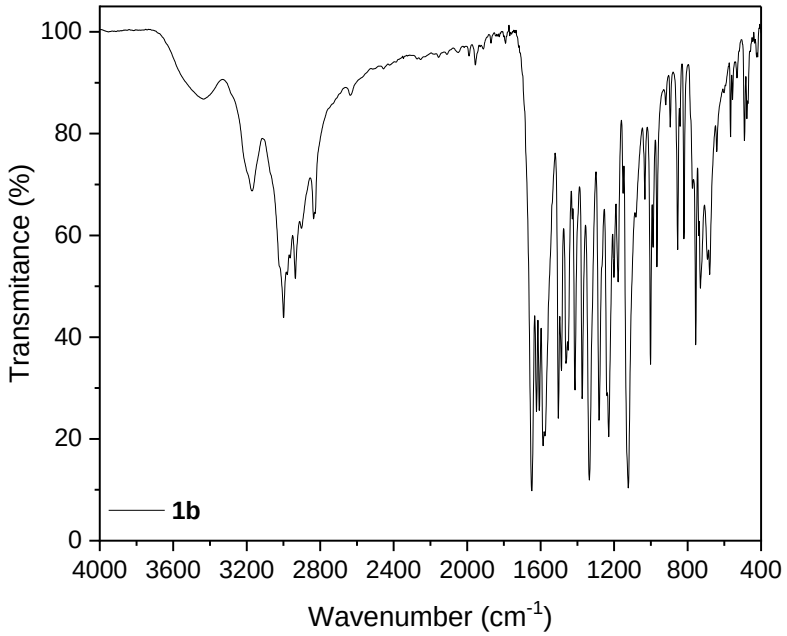

Figure A20. Mid-infrared spectra of **1b**. Experimental conditions: KBr pellets, room temperature.

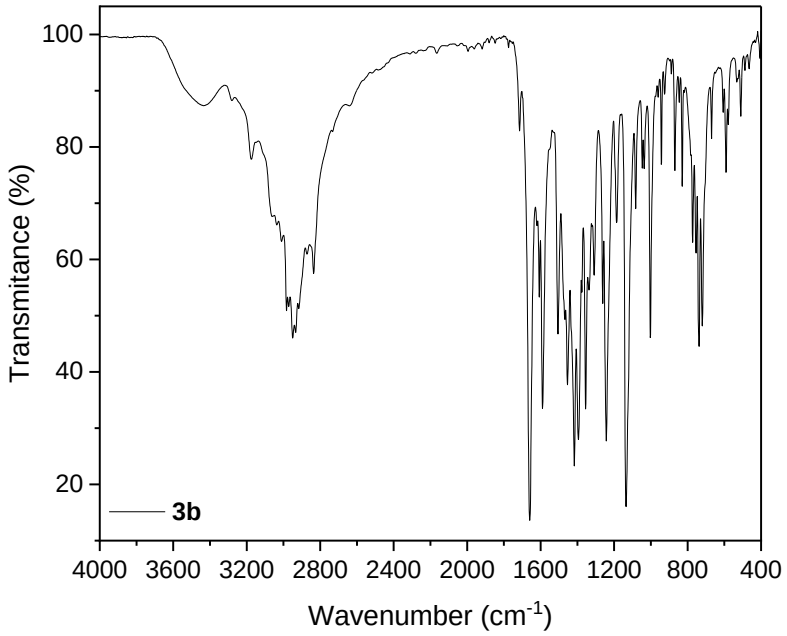

Figure A21. Mid-infrared spectra of **3b**. Experimental conditions: KBr pellets, room temperature.

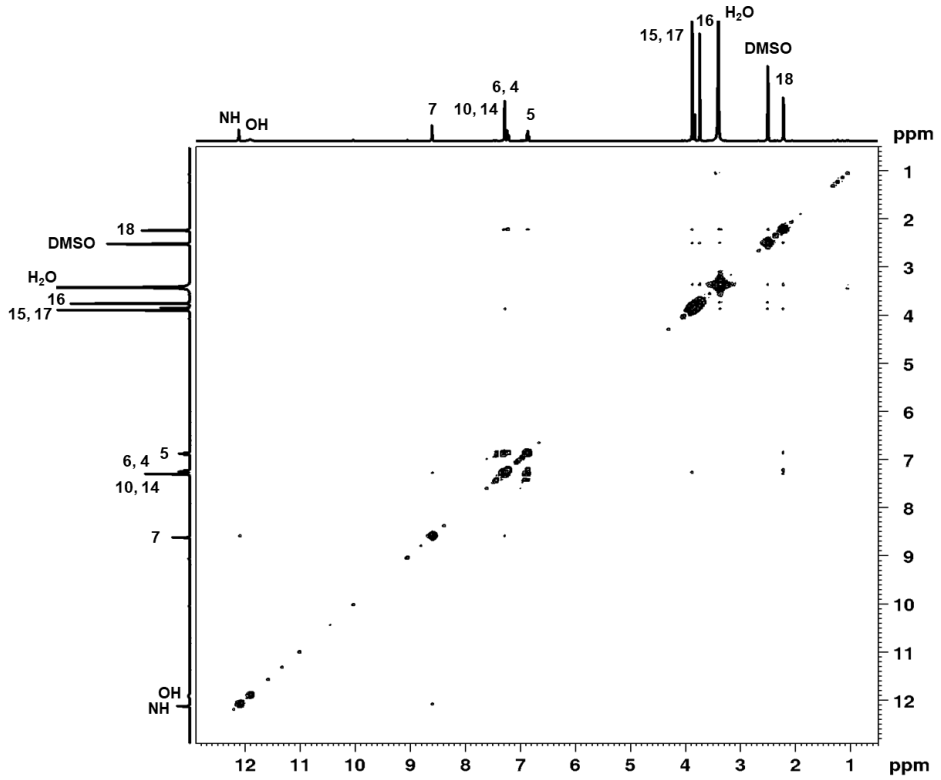

Figure A22. COSY contour map of **3b** in DMSO-d_6 at 25 ºC.

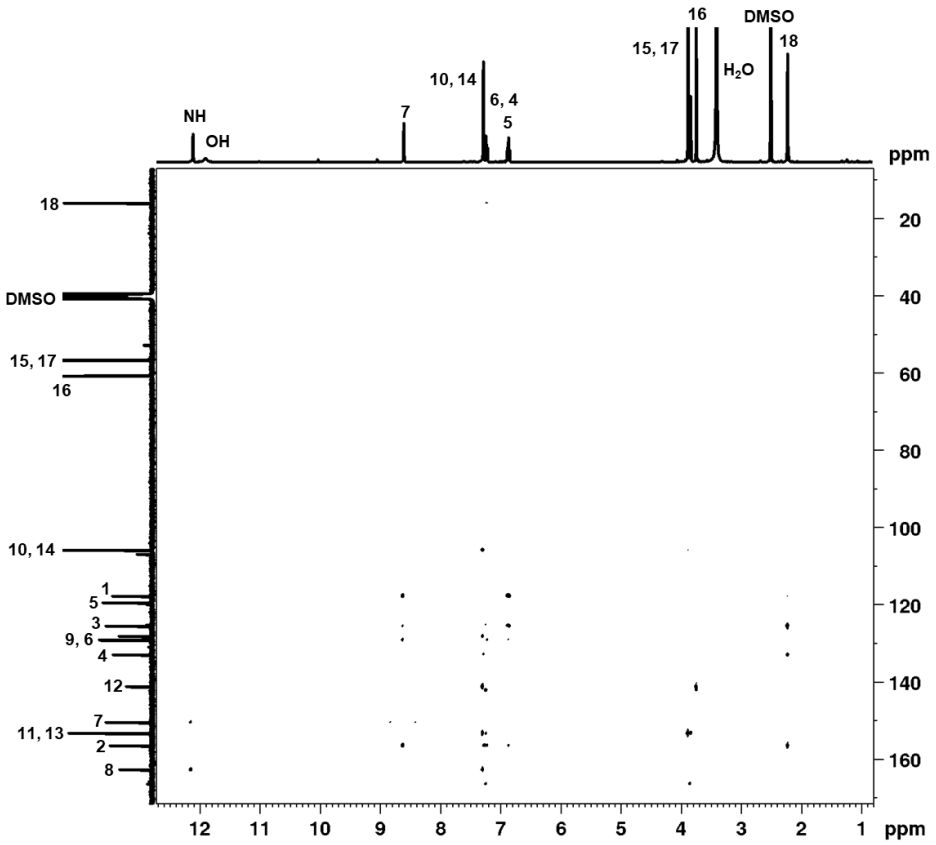

Figure A23. HMBC contour map of **3b** in DMSO-d_6 at 25 ºC.

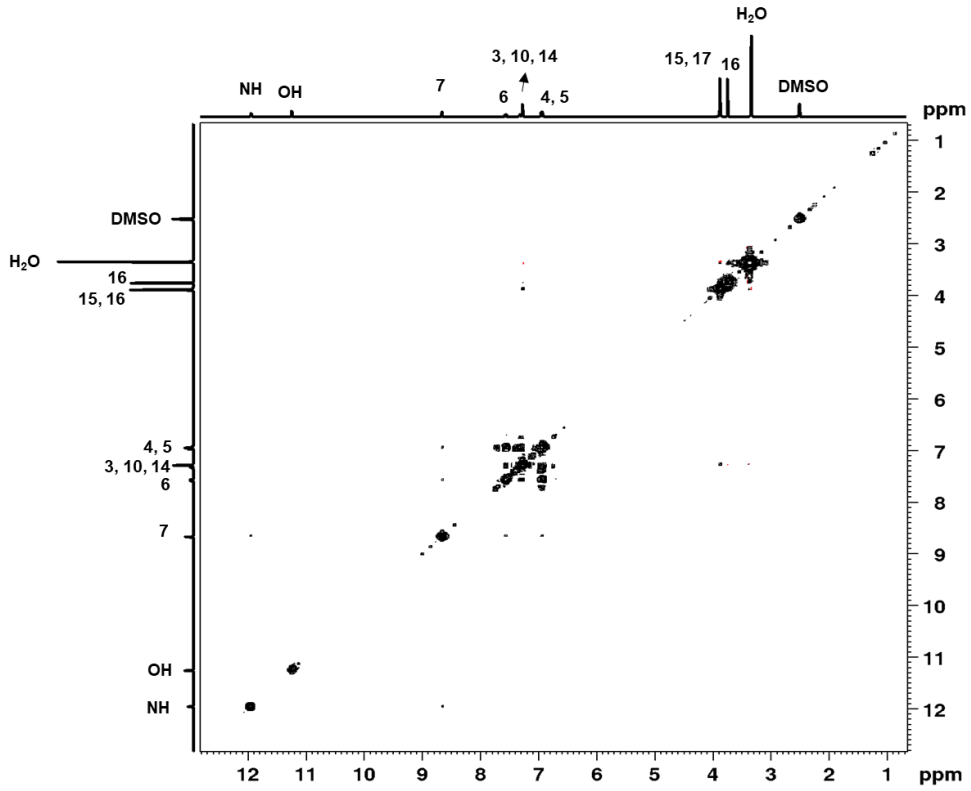

Figure A24. COSY contour map of **1b** in DMSO-d_6 at 25 ºC.

Table A18. ^{1}H (400 MHz) signal assignments for compounds **1b**; ^{1}H (400 MHz) and ^{13}C (100 MHz) signal assignments **3b**, in DMSO-d_6 solution at 25 ºC.

	1b	**3b**	
C/H	**δ ^{1}H (ppm)**	**δ ^{1}H (ppm)**	**^{13}C x ^{1}H HMBC**
C1	-	-	H5 ($^{3}J_{CH}$), H7 ($^{2}J_{CH}$), H18 ($^{4}J_{CH}$)
C2	-	-	H4 ($^{3}J_{CH}$), H5 ($^{4}J_{CH}$), H6 ($^{3}J_{CH}$), H7 ($^{3}J_{CH}$), H18 ($^{3}J_{CH}$)
C3	7.3070 (td, 1H, $^{3}J_{H3-H4}$ = 7.7671 Hz)	-	H4 ($^{2}J_{CH}$), H5 ($^{3}J_{CH}$), H7 ($^{4}J_{CH}$), H18 ($^{2}J_{CH}$)
C4	6.9306 (t, 2H, $^{3}J_{H4-H5}$ = 8.1146 Hz; $^{3}J_{H4-H3}$ = 7.7671)	7.22 (d, 1H, $^{3}J_{HH}$ = 7.5 Hz)	H5 ($^{2}J_{CH}$), H6 ($^{3}J_{CH}$), H18 ($^{3}J_{CH}$)
C5	6.9306 (t, 2H, $^{3}J_{H5-H4}$ = 8.1146 Hz; $^{3}J_{H5-H6}$ = 6.5489)	6.86 (t, 1H, $^{3}J_{HH}$ = 7.5 Hz)	-
C6	7.5562 (dd, 1H, $^{3}J_{H6-H5}$ = 6.5489 Hz)	7.28 (d, 1H, $^{3}J_{HH}$ = 7.5 Hz)	H4 ($^{3}J_{CH}$), H5 ($^{2}J_{CH}$), H7 ($^{3}J_{CH}$)
C7	8.6560 (s, 1H)	8.58 (s, 1H)	H6 ($^{3}J_{CH}$), NH ($^{3}J_{CH}$)
C8	-	-	H10/H14 ($^{3}J_{CH}$), NH ($^{2}J_{CH}$)
C9	-	-	H10/H14 ($^{2}J_{CH}$)
C10	7.2689 (s, 2H)	7.27 (s, 2H)	H10/H14 ($^{3}J_{CH}$)*, H15/H17 ($^{4}J_{CH}$)
C11	-	-	H10/H14 ($^{2}J_{CH}$ / $^{4}J_{CH}$), H15/H17 ($^{3}J_{CH}$)
C12	-	-	H10/H14 ($^{3}J_{CH}$), H16 ($^{3}J_{CH}$)

C13	-	-	H10/H14 ($^{2}J_{CH}$ / $^{4}J_{CH}$), H15/H17 ($^{3}J_{CH}$)
C14	7.2689 (s, 2H)	7.27 (s, 2H)	H10/H14 ($^{3}J_{CH}$)*, H15/H17 ($^{4}J_{CH}$)
C15	3.8712 (s, 6H)	3.88 (s, 6H)	-
C16	3.7373 (s, 3H)	3.74 (s, 3H)	-
C17	3.8712 (s, 6H)	3.88 (s, 6H)	-
C18	-	2.22 (s, 3H)	H4 ($^{3}J_{CH}$)
OH	11.2444 (s, 1H)	11.89 (*broad s*, 1H)	-
NH	11.9443 (s, 1H)	12.05 (s, 1H)	-

Multiplicity: s: singlet, d: doublet, dd: doublet of doublets, t: triplet, dt: doublet triplet.

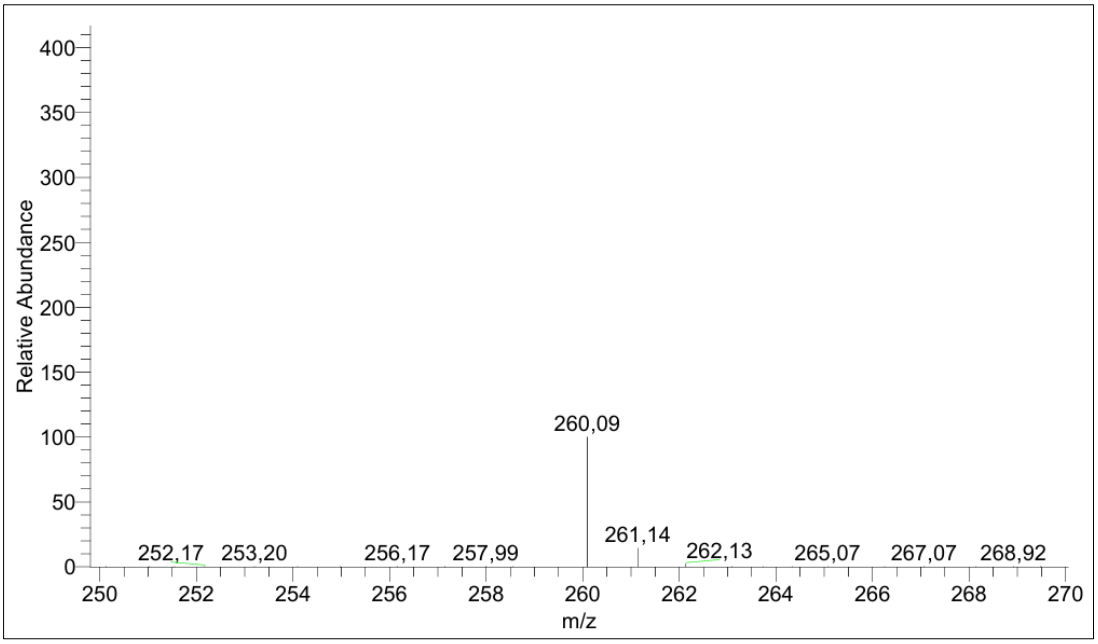

Figure A25. GC-MS chromatogram of the compound **2c**.

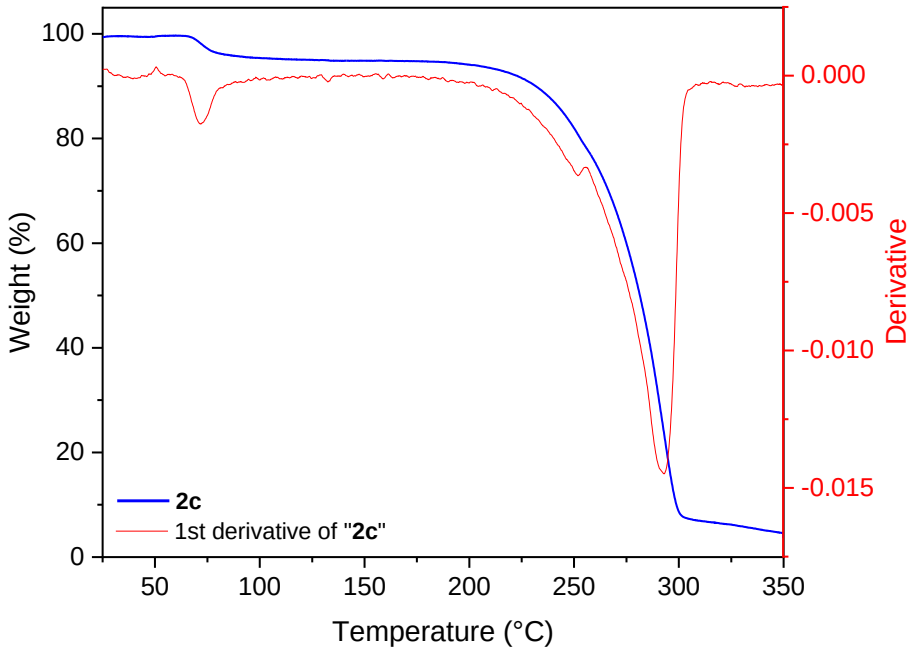

Figure A26. Thermogravimetric curve of **2c** between 25-350 ºC, under N_2 flow. Heating rate of 10 ºC min^{-1}.

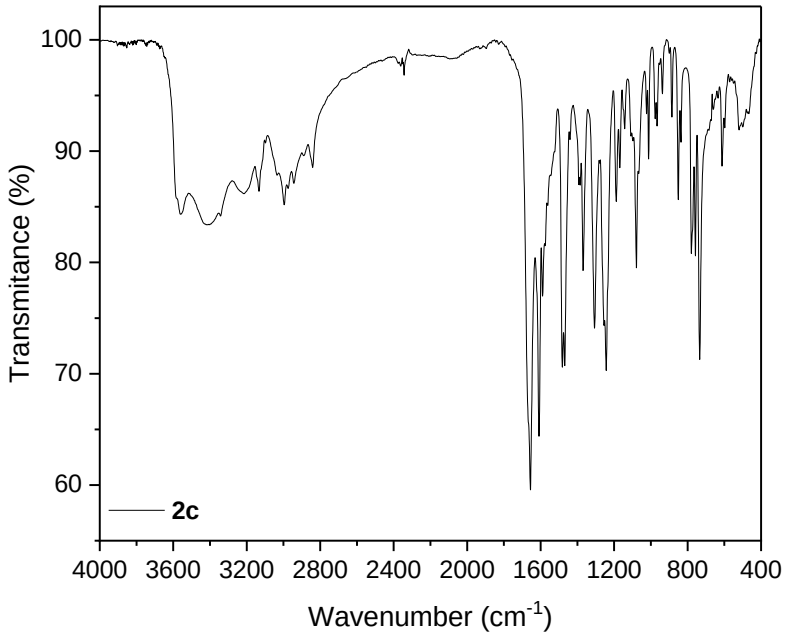

Figure A27. Mid-infrared spectra of **2c**. Experimental conditions: KBr pellets, room temperature.

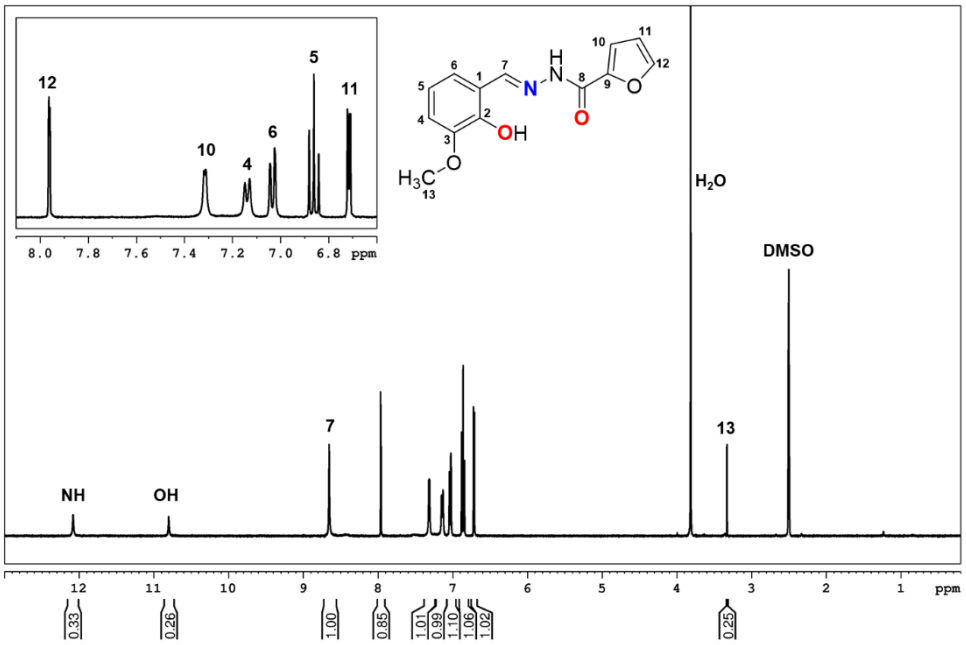

Figure A28. ^{1}H NMR (400 MHz) spectrum of **2c** in DMSO-d_6 at 25 ºC.

Table A19. ^{1}H (400 MHz) signal assignments for compounds **1c, 2c, 3c** and **5c**, in DMSO-d_6 solution at 25 ºC.

	2a
C/H	δ ^{1}H (ppm)
C1	-
C2	-
C3	-
C4	7.1369 (d, 1H, $^{3}J_{H4\text{-}H5}$ = 7.6825 Hz)
C5	6.8597 (t, 1H, $^{3}J_{H5\text{-}H4,6}$ = 7.9226 Hz)
C6	7.0321 (d, 1H, $^{3}J_{H6\text{-}H5}$ = 7.1623 Hz)
C7	8.6518 (s, 1H)
C8	-
C9	-
C10	7.3133 (d, 1H, $^{3}J_{H10\text{-}H11}$ = 2.6809 Hz)
C11	6.7140 (dd, 1H, $^{3}J_{H11\text{-}H10,12}$ = 3.5011 Hz)
C12	7.9618 (dd, 1H, $^{3}J_{H12\text{-}H11}$ = 1.6805 Hz)
OH	10.7993 (s, 1H)
NH	12.0796 (s, 1H)

Multiplicity: s: singlet, d: doublet, dd: doublet of doublets, t: triplet, m: multiplet.

Table A20. Final coordinates and equivalent isotropic displacement parameters of the non-Hydrogen atoms for compound **3c**.

Atom	x	y	z	U(eq)
O1	0.1050(4)	0.61916(8)	0.63810(12)	0.0594(6)
O2	0.7176(3)	0.76204(8)	0.61376(11)	0.0555(5)
*O3A	1.0791(7)	0.82071(15)	0.8484(2)	0.0476(9)
*O3B	1.085(9)	0.851(2)	0.673(2)	0.043(5)
N1	0.6418(3)	0.74275(7)	0.78562(13)	0.0399(5)
N2	0.4375(3)	0.69788(7)	0.75944(13)	0.0410(5)
C1	0.1109(4)	0.62511(9)	0.82788(16)	0.0424(6)
C2	0.0118(4)	0.59947(9)	0.73064(16)	0.0440(6)
C3	-0.1901(5)	0.55163(9)	0.72536(18)	0.0515(7)
C4	-0.2889(5)	0.53081(10)	0.8181(2)	0.0577(8)
O4	0.2020(4)	0.73399(10)	0.50174(12)	0.0650(6)
C5	-0.1953(5)	0.55552(10)	0.9153(2)	0.0592(8)
C6	0.0034(5)	0.60253(10)	0.91979(18)	0.0513(7)
C7	0.3246(4)	0.67367(9)	0.83871(16)	0.0436(6)
C8	0.7717(4)	0.77179(9)	0.70932(15)	0.0401(6)
*C9A	0.990(2)	0.8164(4)	0.7431(4)	0.0388(12)
*C9B	0.984(14)	0.824(3)	0.757(3)	0.0388(12)
*C10A	1.138(2)	0.8596(5)	0.6908(6)	0.052(2)
*C10B	1.085(9)	0.8416(13)	0.856(3)	0.054(6)
*C11A	1.3194(11)	0.8916(2)	0.7651(5)	0.0571(16)
*C11B	1.281(9)	0.8849(15)	0.830(2)	0.065(9)
*C12A	1.2802(11)	0.8668(2)	0.8592(4)	0.0568(13)
*C12B	1.287(7)	0.8876(17)	0.724(2)	0.050(6)
C13	-0.2948(6)	0.52503(13)	0.6198(2)	0.0749(10)

Table A21. (An)isotropic Displacement Parameters for compound **3c**.

Atom	U(1,1)	U(2,2)	U(3,3)	U(2,3)	U(1,3)	U(1,2)
O1	0.0678(11)	0.0602(10)	0.0507(9)	-0.0017(7)	0.0083(8)	-0.0076(8)
O2	0.0447(8)	0.0848(11)	0.0374(8)	-0.0033(7)	0.0054(6)	-0.0069(7)
O3A	0.0498(12)	0.049(2)	0.0439(12)	-0.0081(11)	0.0032(9)	-0.0075(13)
O3B	0.018(9)	0.050(11)	0.059(7)	0.006(7)	-0.006(7)	-0.020(6)
N1	0.0366(8)	0.0435(9)	0.0396(9)	-0.0002(7)	0.0034(7)	-0.0037(7)
N2	0.0335(8)	0.0407(8)	0.0488(9)	-0.0016(7)	0.0027(7)	-0.0003(6)
C1	0.0350(9)	0.0405(10)	0.0513(11)	0.0042(8)	0.0020(8)	0.0029(8)
C2	0.0408(10)	0.0406(10)	0.0508(11)	0.0019(8)	0.0042(8)	0.0064(8)
C3	0.0461(11)	0.0413(11)	0.0664(14)	-0.0054(10)	0.0011(10)	0.0015(9)
C4	0.0486(12)	0.0439(11)	0.0809(16)	0.0031(11)	0.0078(11)	-0.0054(9)
O4	0.0484(9)	0.1093(14)	0.0371(8)	-0.0024(8)	0.0024(6)	0.0050(9)
C5	0.0549(13)	0.0568(13)	0.0669(15)	0.0137(11)	0.0118(11)	-0.0064(10)
C6	0.0486(12)	0.0531(12)	0.0522(12)	0.0052(9)	0.0046(9)	-0.0025(9)
C7	0.0402(10)	0.0438(10)	0.0463(11)	0.0019(8)	0.0015(8)	0.0010(8)
C8	0.0323(9)	0.0471(10)	0.0416(10)	0.0016(8)	0.0068(8)	0.0046(8)
C9A	0.0343(10)	0.042(3)	0.0407(19)	-0.0021(14)	0.0070(16)	0.0034(16)
C9B	0.0343(10)	0.042(3)	0.0407(19)	-0.0021(14)	0.0070(16)	0.0034(16)
C10A	0.045(5)	0.054(3)	0.057(3)	0.007(2)	0.003(2)	-0.007(3)
C10B	0.079(14)	0.032(12)	0.051(6)	-0.021(8)	0.000(7)	-0.003(12)
C11A	0.050(2)	0.0441(18)	0.077(4)	-0.002(3)	0.004(3)	-0.0084(14)
C11B	0.081(16)	0.043(15)	0.067(14)	-0.011(11)	-0.009(11)	-0.011(11)
C12A	0.0529(18)	0.046(3)	0.070(2)	-0.0111(18)	-0.0036(17)	-0.0047(18)
C12B	0.034(9)	0.046(10)	0.066(14)	-0.012(11)	-0.010(10)	-0.011(6)
C13	0.0774(18)	0.0670(16)	0.0790(18)	-0.0170(13)	-0.0017(14)	-0.0125(13)

Table A22. Bond Distances (Angstrom) for compound **3c**.

O1	C2	1.355(3)	C9A	C10A	1.369(13)
O2	C8	1.237(2)	C9B	C10B	1.36(6)
O3A	C9A	1.369(6)	C10A	C11A	1.397(11)
O3A	C12A	1.370(6)	C10B	C11B	1.37(5)
O3B	C9B	1.34(6)	C11A	C12A	1.338(8)
O3B	C12B	1.35(5)	C11B	C12B	1.35(4)
N1	N2	1.383(2)	C4	H4	0.9300
N1	C8	1.341(2)	O4	H4B	0.85(2)
O1	H1	0.85(2)	O4	H4A	0.87(2)
N2	C7	1.285(3)	C5	H5	0.9300
C1	C2	1.398(3)	C6	H6	0.9300
C1	C7	1.448(3)	C7	H7	0.9300
N1	H1A	0.855(19)	C10A	H10A	0.9300
C1	C6	1.396(3)	C10B	H10B	0.9300
C2	C3	1.399(3)	C11A	H11A	0.9300
C3	C13	1.504(3)	C11B	H11B	0.9300
C3	C4	1.375(3)	C12A	H12A	0.9300
C4	C5	1.383(3)	C12B	H12B	0.9300
C5	C6	1.376(3)	C13	H13B	0.9600
C8	C9A	1.442(9)	C13	H13C	0.9600
C8	C9B	1.59(6)	C13	H13A	0.9600

Table A23. Bond Angles (Degrees) for compound **3c**.

C9A	O3A	C12A	107.2(5)	O3B	C9B	C8	105(3)
C9B	O3B	C12B	99(3)	C8	C9B	C10B	135(4)
N2	N1	C8	119.97(16)	O3B	C9B	C10B	120(5)
C2	O1	H1	108.0(17)	C9A	C10A	C11A	108.3(6)
N1	N2	C7	114.65(16)	C9B	C10B	C11B	99(4)
C2	C1	C7	123.26(18)	C10A	C11A	C12A	106.4(5)
C6	C1	C7	117.82(18)	C10B	C11B	C12B	110(3)
C8	N1	H1A	119.9(16)	O3A	C12A	C11A	110.5(4)
C2	C1	C6	118.91(18)	O3B	C12B	C11B	112(3)
N2	N1	H1A	120.1(15)	C3	C4	H4	119.00
O1	C2	C3	117.03(19)	C5	C4	H4	119.00
O1	C2	C1	122.29(18)	H4A	O4	H4B	106(2)
C1	C2	C3	120.68(19)	C4	C5	H5	120.00
C2	C3	C4	118.3(2)	C6	C5	H5	120.00
C2	C3	C13	119.7(2)	C5	C6	H6	120.00
C4	C3	C13	122.0(2)	C1	C6	H6	120.00
C3	C4	C5	122.2(2)	N2	C7	H7	118.00
C4	C5	C6	119.1(2)	C1	C7	H7	118.00
C1	C6	C5	120.8(2)	C11A	C10A	H10A	126.00
N2	C7	C1	123.02(18)	C9A	C10A	H10A	126.00
O2	C8	N1	124.12(18)	C9B	C10B	H10B	130.00
O2	C8	C9A	119.2(3)	C11B	C10B	H10B	131.00
N1	C8	C9B	111.3(15)	C12A	C11A	H11A	127.00
O2	C8	C9B	124.4(15)	C10A	C11A	H11A	127.00
N1	C8	C9A	116.7(3)	C10B	C11B	H11B	125.00
O3A	C9A	C10A	107.7(7)	C12B	C11B	H11B	125.00
O3A	C9A	C8	118.9(6)	C11A	C12A	H12A	125.00
C8	C9A	C10A	133.4(5)	O3A	C12A	H12A	125.00
C11B	C12B	H12B	124.00	C3	C13	H13C	109.00
O3B	C12B	H12B	124.00	H13A	C13	H13B	109.00
C3	C13	H13A	109.00	H13A	C13	H13C	109.00
C3	C13	H13B	109.00	H13B	C13	H13C	110.00

Table A24. Torsion Angles (Degrees) for compound **3c**.

C12A	O3A	C9A	C8	-178.8(6)
C12A	O3A	C9A	C10A	0.2(8)
C9A	O3A	C12A	C11A	0.3(6)
C8	N1	N2	C7	-179.18(17)
N2	N1	C8	C9A	-177.8(4)
N2	N1	C8	O2	1.4(3)
N1	N2	C7	C1	-178.76(16)
C6	C1	C2	O1	179.67(19)
C2	C1	C6	C5	0.5(3)
C7	C1	C6	C5	-178.6(2)
C2	C1	C7	N2	1.1(3)
C6	C1	C7	N2	-179.87(19)
C7	C1	C2	C3	178.49(19)
C6	C1	C2	C3	-0.5(3)
C7	C1	C2	O1	-1.3(3)
O1	C2	C3	C4	-179.87(19)
C1	C2	C3	C13	179.7(2)
O1	C2	C3	C13	-0.5(3)
C1	C2	C3	C4	0.3(3)
C2	C3	C4	C5	0.0(3)
C13	C3	C4	C5	-179.4(2)
C3	C4	C5	C6	0.0(3)
C4	C5	C6	C1	-0.2(3)
O2	C8	C9A	O3A	-170.6(5)
O2	C8	C9A	C10A	10.7(12)
N1	C8	C9A	O3A	8.6(8)
N1	C8	C9A	C10A	-170.1(9)
O3A	C9A	C10A	C11A	-0.6(10)
C8	C9A	C10A	C11A	178.2(8)
C9A	C10A	C11A	C12A	0.8(9)
C10A	C11A	C12A	O3A	-0.6(7)

Table A25. Final coordinates and equivalent isotropic displacement parameters of the non-Hydrogen atoms for compound **5c**.

Atom	x	y	z	U(eq)
Cl1	0.27418(6)	-0.2543(3)	0.38696(11)	0.0689(5)
O1	0.37444(16)	0.1511(8)	0.4215(2)	0.0574(11)
O2	0.51978(16)	0.7694(7)	0.4073(2)	0.0557(12)
O3	0.60571(18)	1.1564(9)	0.4702(3)	0.0697(14)
N1	0.45132(17)	0.4601(8)	0.5482(3)	0.0438(11)
N2	0.49668(19)	0.6554(9)	0.5775(3)	0.0443(12)
C1	0.37531(19)	0.1251(9)	0.6113(4)	0.0420(16)
C2	0.35194(19)	0.0451(10)	0.5126(4)	0.0417(16)
C3	0.3040(2)	-0.1578(10)	0.5088(4)	0.0477(16)
C4	0.2796(2)	-0.2736(10)	0.5982(4)	0.0520(16)
O4	0.4941(2)	0.2831(9)	0.2961(3)	0.0638(15)
C5	0.3028(2)	-0.1964(12)	0.6955(4)	0.0587(19)
C6	0.3496(2)	0.0024(11)	0.7031(4)	0.0507(16)
C7	0.4241(2)	0.3336(10)	0.6254(4)	0.0453(16)
C8	0.5280(2)	0.7981(10)	0.5035(4)	0.0410(16)
C9	0.57410(19)	1.0024(10)	0.5442(3)	0.0437(17)
C10	0.5921(3)	1.0763(13)	0.6410(4)	0.067(2)
C11	0.6409(3)	1.2905(13)	0.6218(6)	0.073(3)
C12	0.6450(3)	1.3259(14)	0.5236(7)	0.080(2)

Table A26. (An)isotropic Displacement Parameters for compound **5c**.

Atom	U(1,1)	U(2,2)	U(3,3)	U(2,3)	U(1,3)	U(1,2)
Cl1	0.0586(7)	0.0806(10)	0.0674(9)	-0.0165(7)	-0.0150(7)	-0.0043(7)
O1	0.058(2)	0.066(2)	0.0483(19)	0.0032(18)	0.0012(14)	-0.0116(19)
O2	0.079(2)	0.047(2)	0.041(2)	0.0000(16)	-0.0032(15)	-0.0138(19)
O3	0.070(2)	0.070(3)	0.069(2)	0.002(2)	0.009(2)	-0.011(2)
N1	0.0415(19)	0.040(2)	0.050(2)	-0.0031(18)	-0.0033(17)	-0.0018(19)
N2	0.044(2)	0.046(2)	0.043(2)	-0.0035(18)	0.0017(17)	-0.007(2)
C1	0.036(2)	0.035(3)	0.055(3)	-0.001(2)	-0.001(2)	-0.002(2)
C2	0.036(2)	0.042(3)	0.047(3)	-0.001(2)	-0.002(2)	0.004(2)
C3	0.037(2)	0.048(3)	0.058(3)	-0.010(3)	-0.004(2)	0.003(2)
C4	0.041(2)	0.047(3)	0.068(3)	0.000(3)	-0.002(2)	-0.006(3)
O4	0.093(3)	0.056(3)	0.0423(19)	0.0032(16)	-0.0073(18)	-0.019(2)
C5	0.050(3)	0.060(4)	0.066(3)	0.014(3)	0.014(3)	-0.006(3)
C6	0.051(3)	0.051(3)	0.050(2)	0.004(2)	0.006(2)	-0.002(3)
C7	0.044(3)	0.046(3)	0.046(2)	0.002(2)	-0.001(2)	-0.001(2)
C8	0.046(2)	0.036(3)	0.041(3)	0.000(2)	0.003(2)	0.001(2)
C9	0.048(3)	0.038(3)	0.045(3)	0.009(2)	0.007(2)	0.000(2)
C10	0.099(4)	0.055(4)	0.046(3)	0.002(3)	-0.009(3)	0.003(3)
C11	0.058(4)	0.057(4)	0.103(5)	-0.021(4)	-0.034(3)	0.000(3)
C12	0.058(3)	0.073(4)	0.109(5)	0.003(4)	-0.004(4)	-0.020(3)

Table A27. Bond Distances (Angstrom) for compound **5c**.

Cl1	C3	1.733(5)	C4	C5	1.379(7)
O1	C2	1.347(6)	C5	C6	1.373(7)
O2	C8	1.240(6)	C8	C9	1.470(6)
O3	C9	1.365(6)	C9	C10	1.333(7)
O3	C12	1.342(8)	C10	C11	1.471(9)
N1	N2	1.387(6)	C11	C12	1.260(12)
N1	C7	1.285(6)	C4	H4	0.9300
O1	H1	1.06(7)	O4	H4B	0.84(7)
N2	C8	1.334(6)	O4	H4A	0.84(5)
C1	C2	1.400(7)	C5	H5	0.9300
C1	C7	1.443(6)	C6	H6	0.9300
C1	C6	1.411(7)	C7	H7	0.9300
C2	C3	1.402(6)	C10	H10	0.9300
N2	H2	0.94(6)	C11	H11	0.9300
C3	C4	1.362(7)	C12	H12	0.9300

Table A28. Bond Angles (Degrees) for compound **5c**.

C9	O3	C12	106.2(5)	C8	C9	C10	133.4(5)
N2	N1	C7	114.8(4)	O3	C9	C8	115.9(4)
C2	O1	H1	108(3)	O3	C9	C10	110.6(4)
N1	N2	C8	119.7(4)	C9	C10	C11	103.4(5)
C2	C1	C7	123.5(4)	C10	C11	C12	107.7(6)
C6	C1	C7	117.2(4)	O3	C12	C11	112.2(6)
C2	C1	C6	119.3(4)	C3	C4	H4	120.00
O1	C2	C1	122.7(4)	C5	C4	H4	120.00
C1	C2	C3	118.4(4)	H4A	O4	H4B	106(6)
C8	N2	H2	121(3)	C4	C5	H5	120.00
O1	C2	C3	118.9(4)	C6	C5	H5	120.00
N1	N2	H2	120(3)	C5	C6	H6	120.00
Cl1	C3	C2	118.6(4)	C1	C6	H6	120.00
C2	C3	C4	121.6(5)	N1	C7	H7	118.00
Cl1	C3	C4	119.8(4)	C1	C7	H7	118.00
C3	C4	C5	120.1(4)	C11	C10	H10	128.00
C4	C5	C6	120.3(5)	C9	C10	H10	128.00
C1	C6	C5	120.3(5)	C10	C11	H11	126.00
N1	C7	C1	123.2(5)	C12	C11	H11	126.00
O2	C8	N2	124.5(4)	O3	C12	H12	124.00
O2	C8	C9	120.8(4)	C11	C12	H12	124.00
N2	C8	C9	114.7(4)				

Table A29. Torsion Angles (Degrees) for compound **5c**.

C12	O3	C9	C8	-179.9(4)
C12	O3	C9	C10	1.1(6)
C9	O3	C12	C11	0.3(7)
C7	N1	N2	C8	179.8(4)
N2	N1	C7	C1	179.5(4)
N1	N2	C8	O2	-0.2(7)
N1	N2	C8	C9	179.0(4)
C6	C1	C2	O1	-179.4(4)
C6	C1	C2	C3	-0.7(6)
C7	C1	C2	O1	1.9(7)
C7	C1	C2	C3	-179.4(4)
C2	C1	C6	C5	1.0(7)
C7	C1	C6	C5	179.7(4)
C2	C1	C7	N1	-1.5(7)
C6	C1	C7	N1	179.9(4)
O1	C2	C3	Cl1	-2.1(6)
O1	C2	C3	C4	179.7(4)
C1	C2	C3	Cl1	179.2(3)
C1	C2	C3	C4	0.9(7)
Cl1	C3	C4	C5	-179.6(4)
C2	C3	C4	C5	-1.3(7)
C3	C4	C5	C6	1.5(7)
C4	C5	C6	C1	-1.4(7)
O2	C8	C9	O3	0.8(6)
O2	C8	C9	C10	179.8(5)
N2	C8	C9	O3	-178.4(4)
N2	C8	C9	C10	0.6(8)
O3	C9	C10	C11	-1.9(6)
C8	C9	C10	C11	179.1(5)
C9	C10	C11	C12	2.1(7)
C10	C11	C12	O3	-1.5(8)

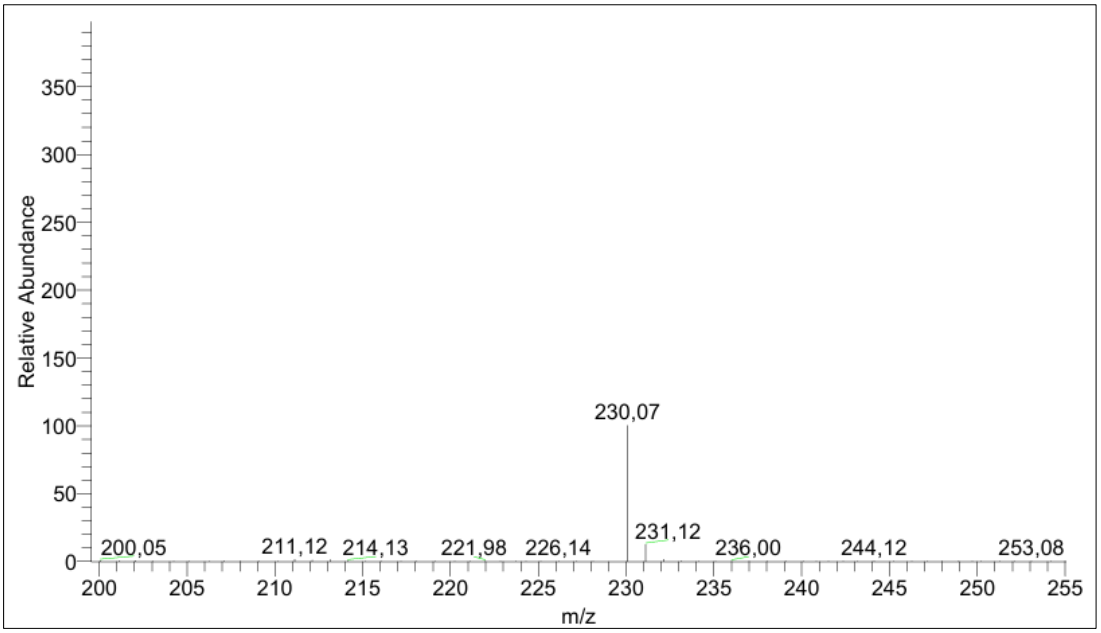

Figure A29. GC-MS chromatogram of the compound **1c**.

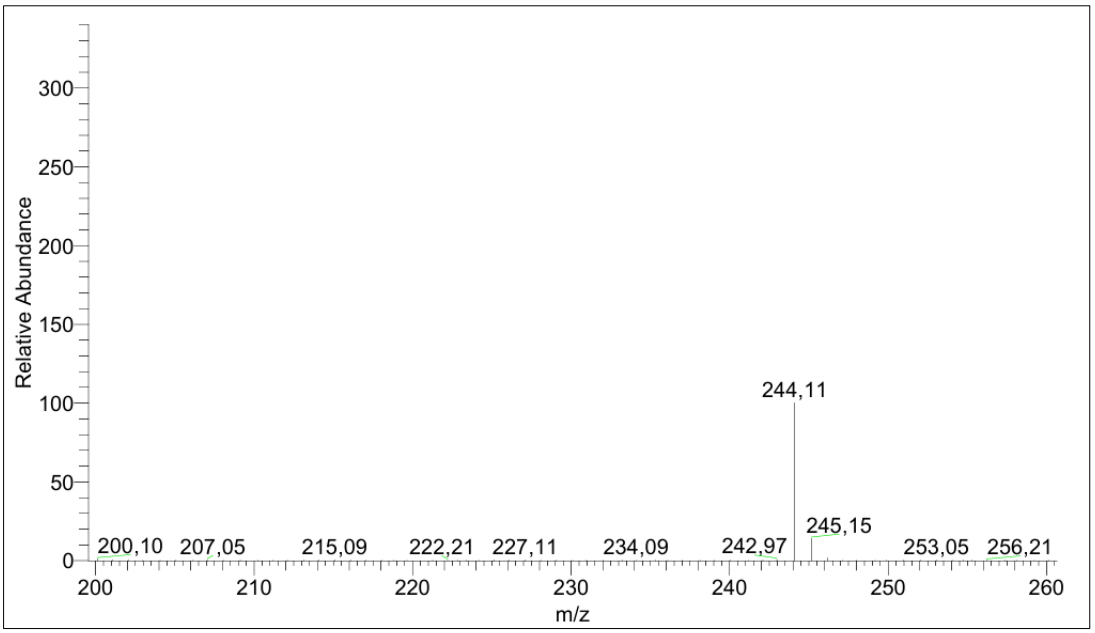

Figure A30. GC-MS chromatogram of the compound **3c**.

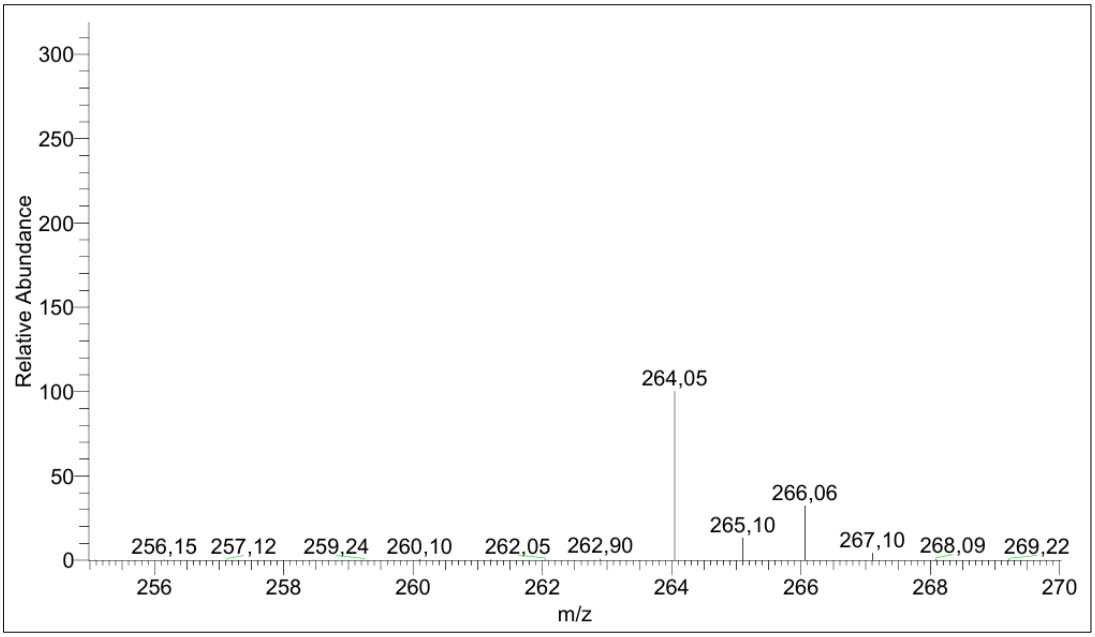

Figure A31. GC-MS chromatogram of the compound **5c**.

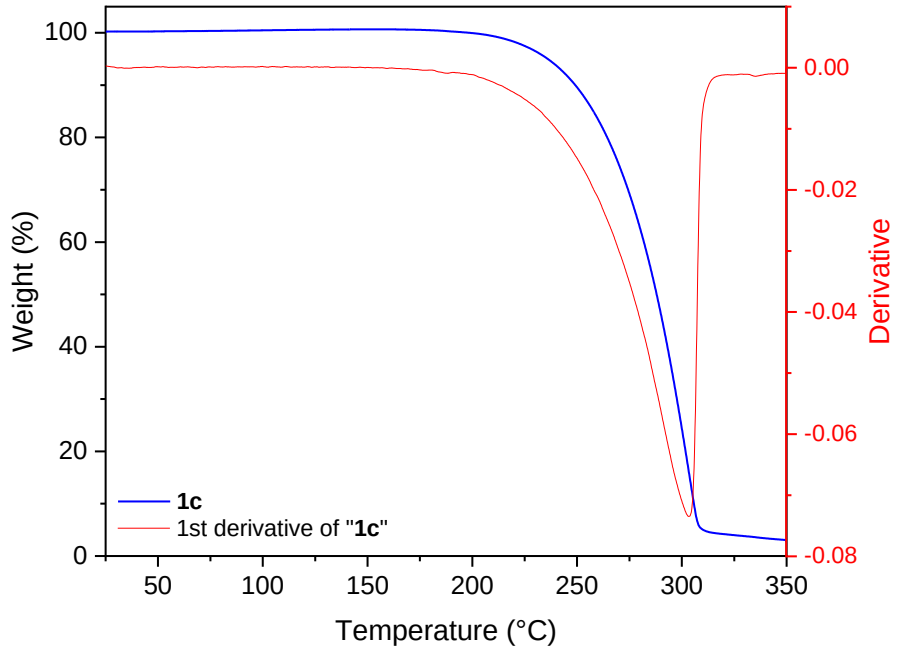

Figure A32. Thermogravimetric curve of **1c** between 25-350 ºC, under N_2 flow. Heating rate of 10 ºC min^{-1}.

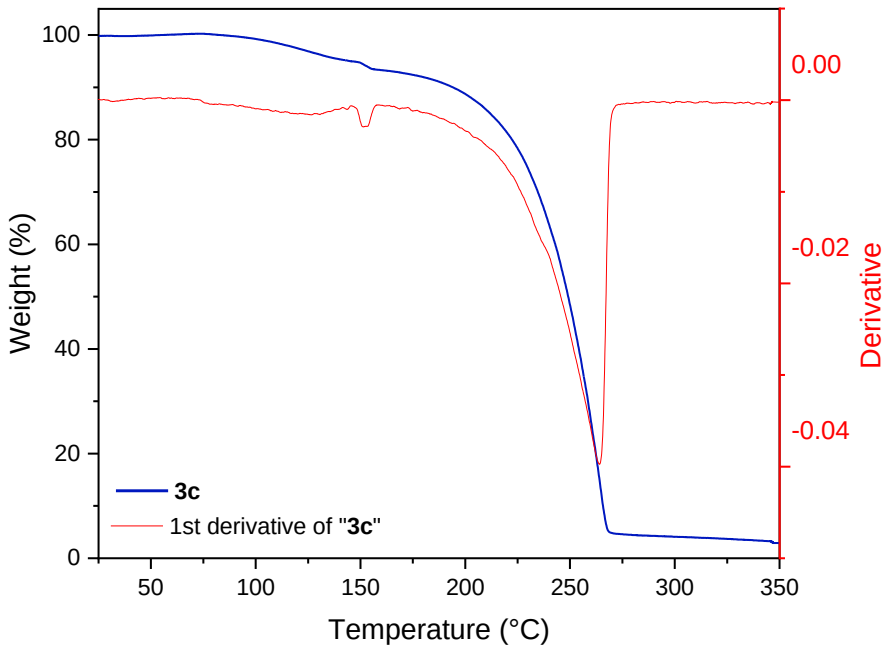

Figure A33. Thermogravimetric curve of **3c** between 25-350 ºC, under N_2 flow. Heating rate of 10 ºC min^{-1}.

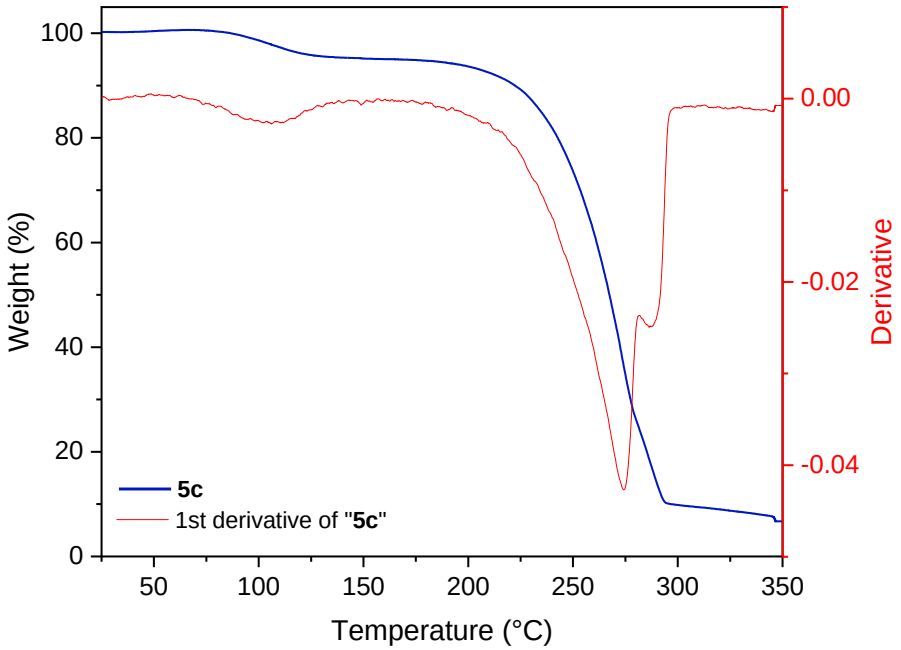

Figure A34. Thermogravimetric curve of **5c** between 25-350 ºC, under N_2 flow. Heating rate of 10 ºC min^{-1}.

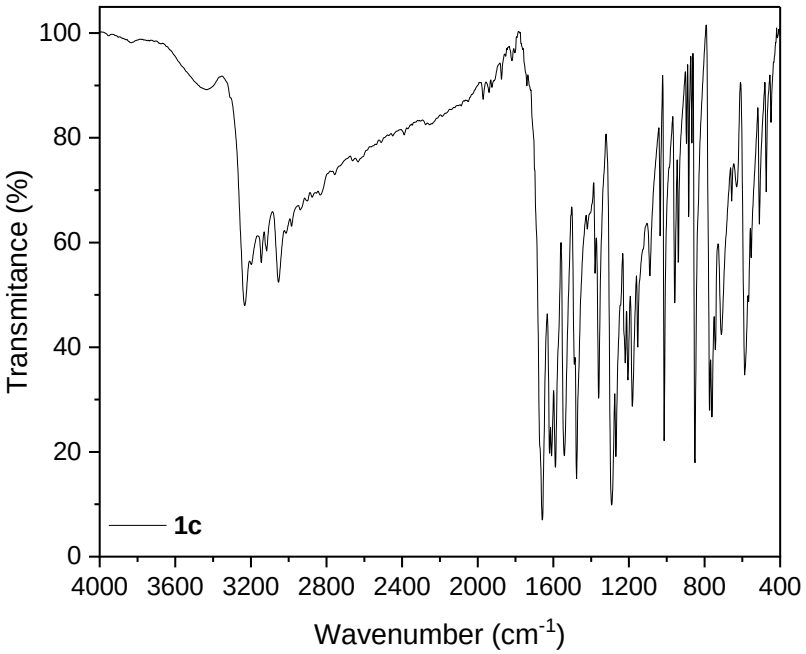

Figure A35. Mid-infrared spectra of **1c**. Experimental conditions: KBr pellets, room temperature.

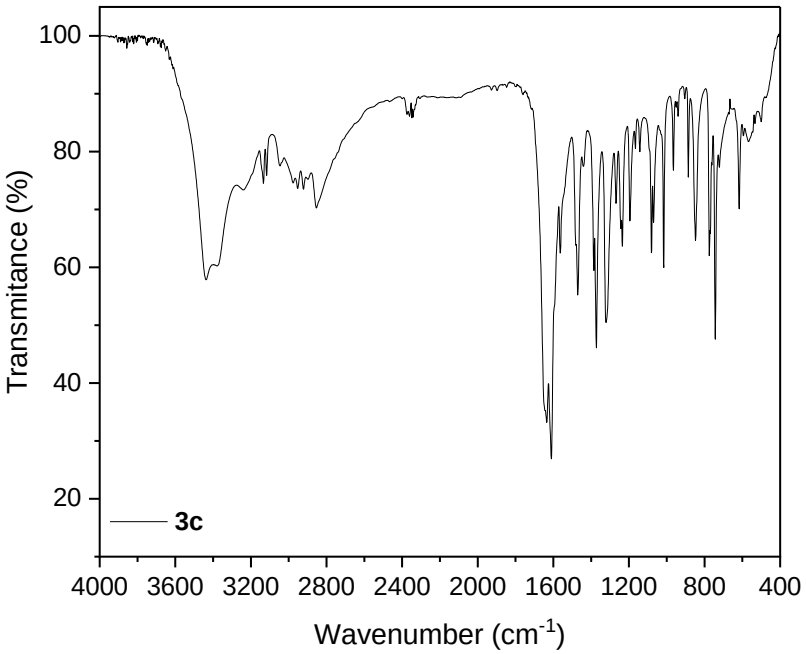

Figure A36. Mid-infrared spectra of **3c**. Experimental conditions: KBr pellets, room temperature.

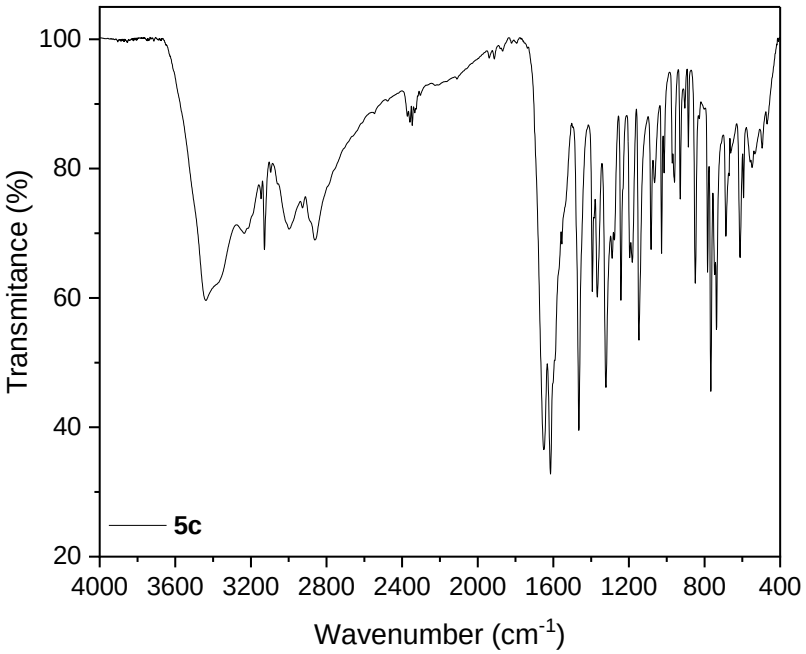

Figure A37. Mid-infrared spectra of **5c**. Experimental conditions: KBr pellets, room temperature.

Table A30. ^{1}H (400 MHz) signal assignments for compounds **1c, 3c** and **5c**, in DMSO-d_6 solution at 25 ºC.

	1a	**3a**	**5a**
C/H	δ ^{1}H (ppm)	δ ^{1}H (ppm)	δ ^{1}H (ppm)
C1	-	-	-
C2	-	-	-
C3	7.3060 (m, 2H, $^{3}J_{H3-H4}$ = 6.7578 Hz)	-	-
C4	6.9064 (t, 2H, $^{3}J_{H4-H5}$ = 7.8357 Hz)	7.2347 (dd, 2H, $^{3}J_{H4-H5}$ = 8.3227 Hz)	7.4788 (m, 2H, $^{3}J_{H4-H5}$ = 7.19375 Hz)
C5	6.9064 (t, 2H, $^{3}J_{H5-H4,6}$ = 7.8357 Hz)	6.8523 (t, 1H, $^{3}J_{H5-H4,6}$ = 7.5425 Hz)	6.9683 (t, 1H, $^{3}J_{H5-H4,6}$ = 7.8321 Hz)
C6	7.3060 (m, 2H, $^{3}J_{H6-H5}$ = 6.7578 Hz)	7.2347 (dd, 2H, $^{3}J_{H6-H5}$ = 8.3227 Hz)	7.4788 (m, 2H, $^{3}J_{H6-H5}$ = 7.19375 Hz)
C7	8.6491 (s, 1H)	8.5740 (s, 1H)	8.6134 (s, 1H)
C8	-	-	-
C9	-	-	-
C10	7.5416 (d, 1H, $^{3}J_{H10-H11}$ = 7.3460 Hz)	7.3299 (d, 1H, $^{3}J_{H10-H11}$ = 3.5001 Hz)	7.3544 (d, 1H, $^{3}J_{H10-H11}$ = 3.3847 Hz)
C11	6.7244 (dd, 1H, $^{3}J_{H11-H10,12}$ = 5.1749 Hz)	6.7305 (dd, 1H, $^{3}J_{H11-H10,12}$ = 5.2817 Hz)	6.7398 (dd, 1H, $^{3}J_{H11-H10,12}$ = 5.2657 Hz)
C12	7.9725 (d, 1H, $^{3}J_{H12-H11}$ = 0.9335 Hz)	7.9824 (dd, 1H, $^{3}J_{H12-H11}$ = 0.9603 Hz)	7.9977 (dd, 1H, $^{3}J_{H12-H11}$ = 0.9527 Hz)
OH	11.1449 (s, 1H)	11.7996 (s, 1H)	12.4039 (s, 1H)
NH	12.1189 (s, 1H)	12.2460 (s, 1H)	12.2731 (s, 1H)

Multiplicity: s: singlet, d: doublet, dd: doublet of doublets, t: triplet, m: multiplet.

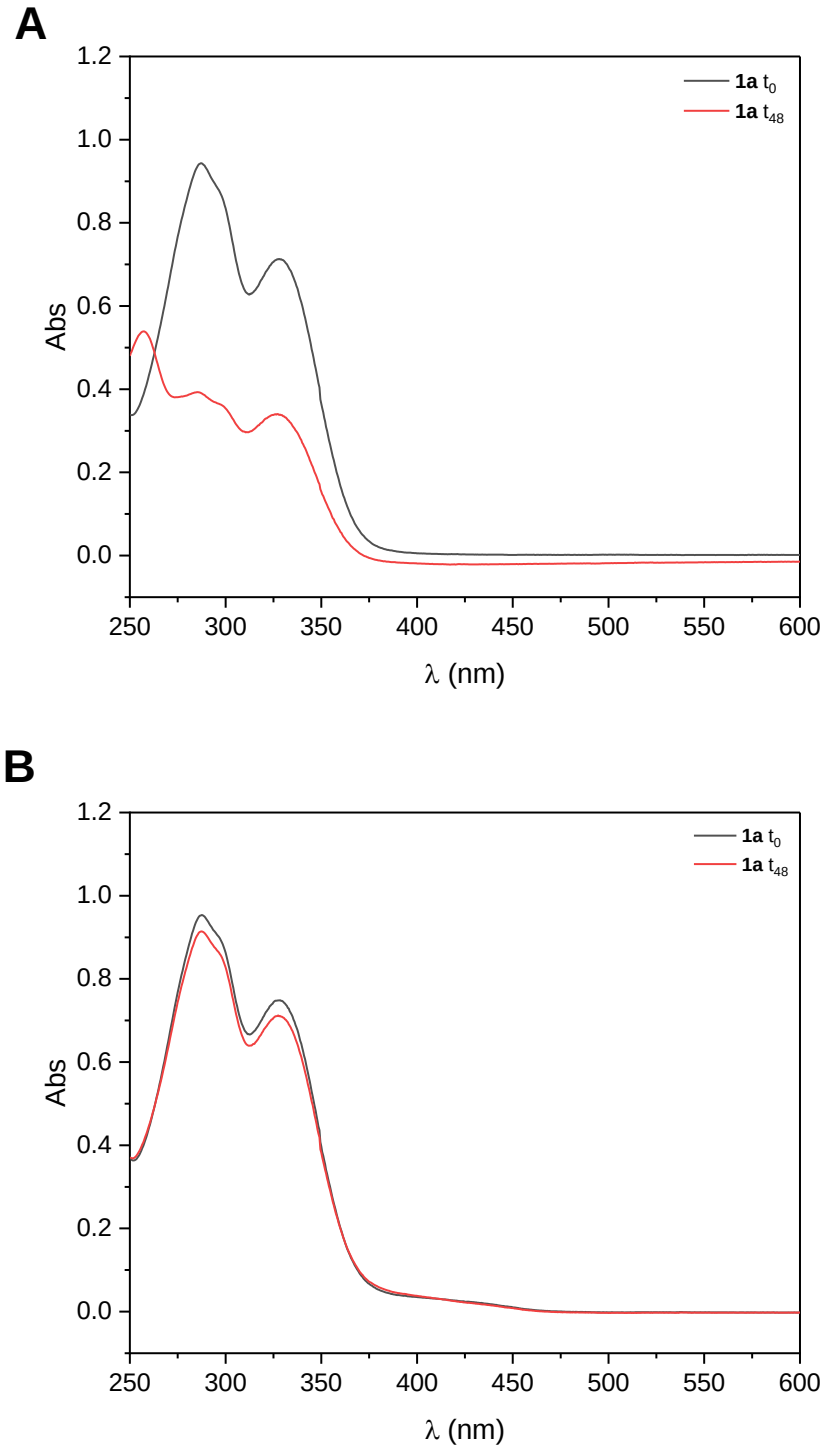

Figure A38. Electronic absorption spectra in selected wavelength regions for a 5×10^{-5} mol L^{-1} solution of **1a**. (**A**) Spectra measured at t_0 and after 48h in 1% DMSO/acetate buffer mixture, pH 4.5 (**B**) Spectra measured at t_0 and after 48h in 1% DMSO/HEPES buffer mixture, pH 7.4.

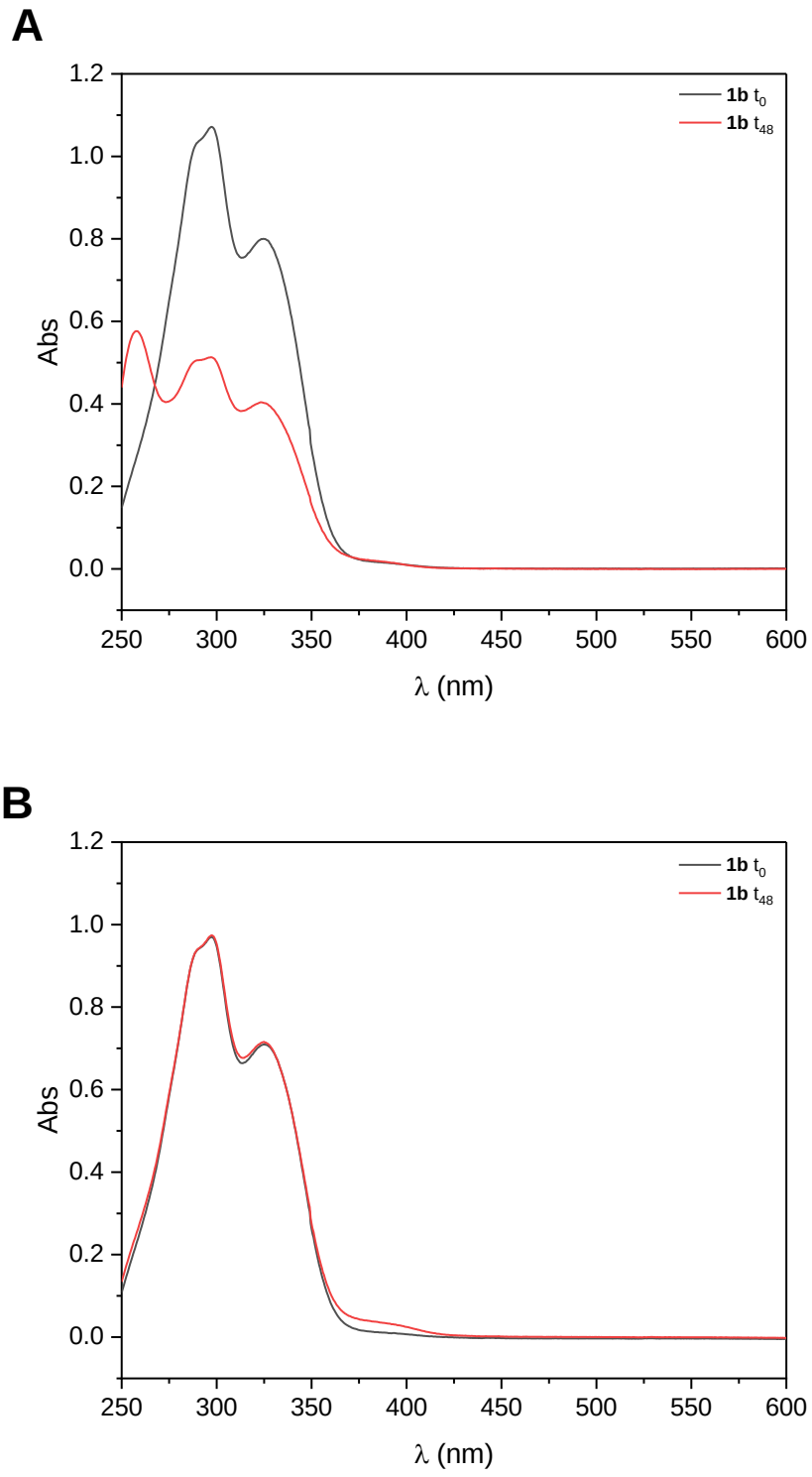

Figure A39. Electronic absorption spectra in selected wavelength regions for a 5×10^{-5} mol L^{-1} solution of **1b**. (**A**) Spectra measured at t_0 and after 48h in 1% DMSO/acetate buffer mixture, pH 4.5 (**B**) Spectra measured at t_0 and after 48h in 1% DMSO/HEPES buffer mixture, pH 7.4.

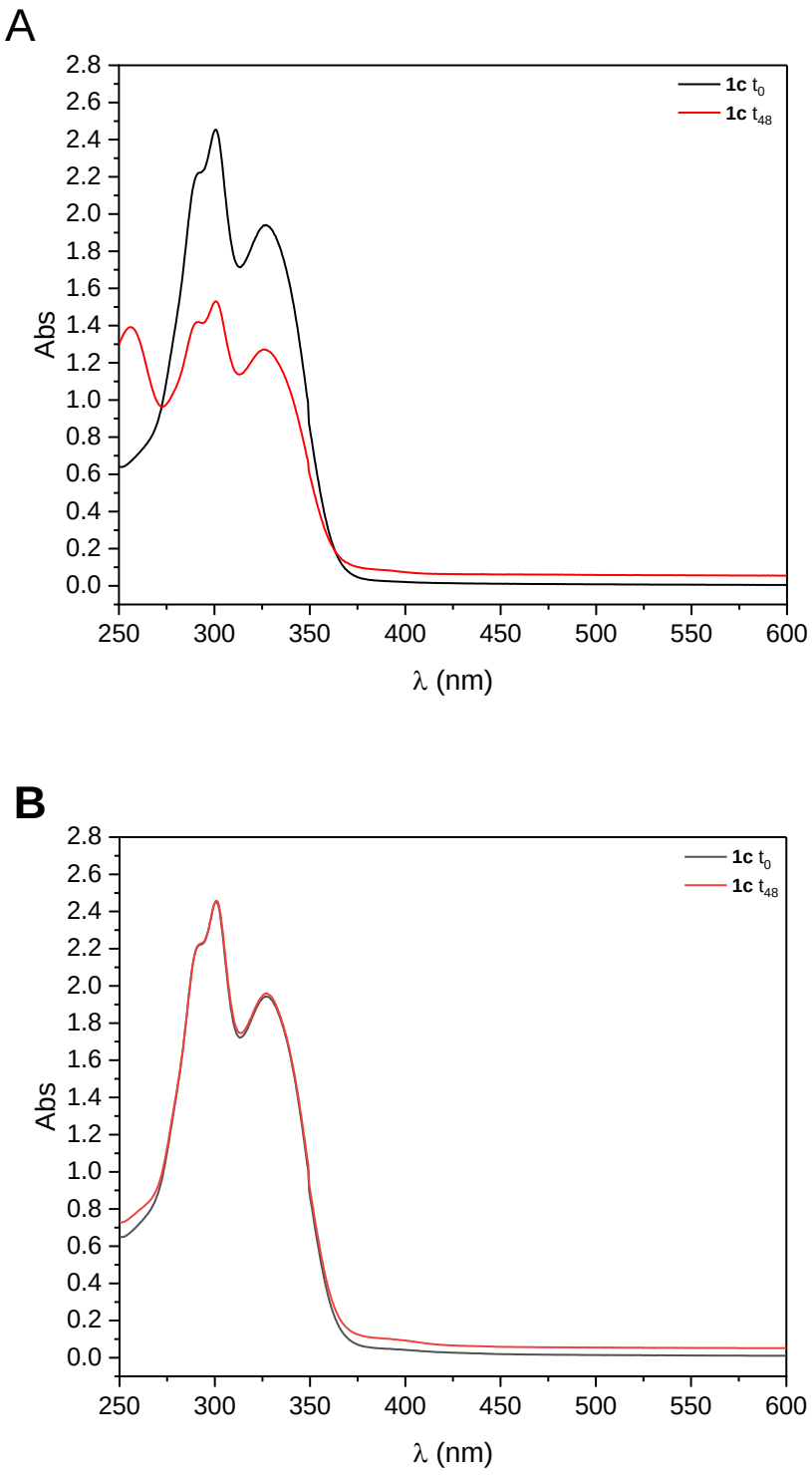

Figure A40. Electronic absorption spectra in selected wavelength regions for a 5×10^{-5} mol L^{-1} solution of **1c**. (**A**) Spectra measured at t_0 and after 48h in 1% DMSO/acetate buffer mixture, pH 4.5 (**B**) Spectra measured at t_0 and after 48h in 1% DMSO/HEPES buffer mixture, pH 7.4.

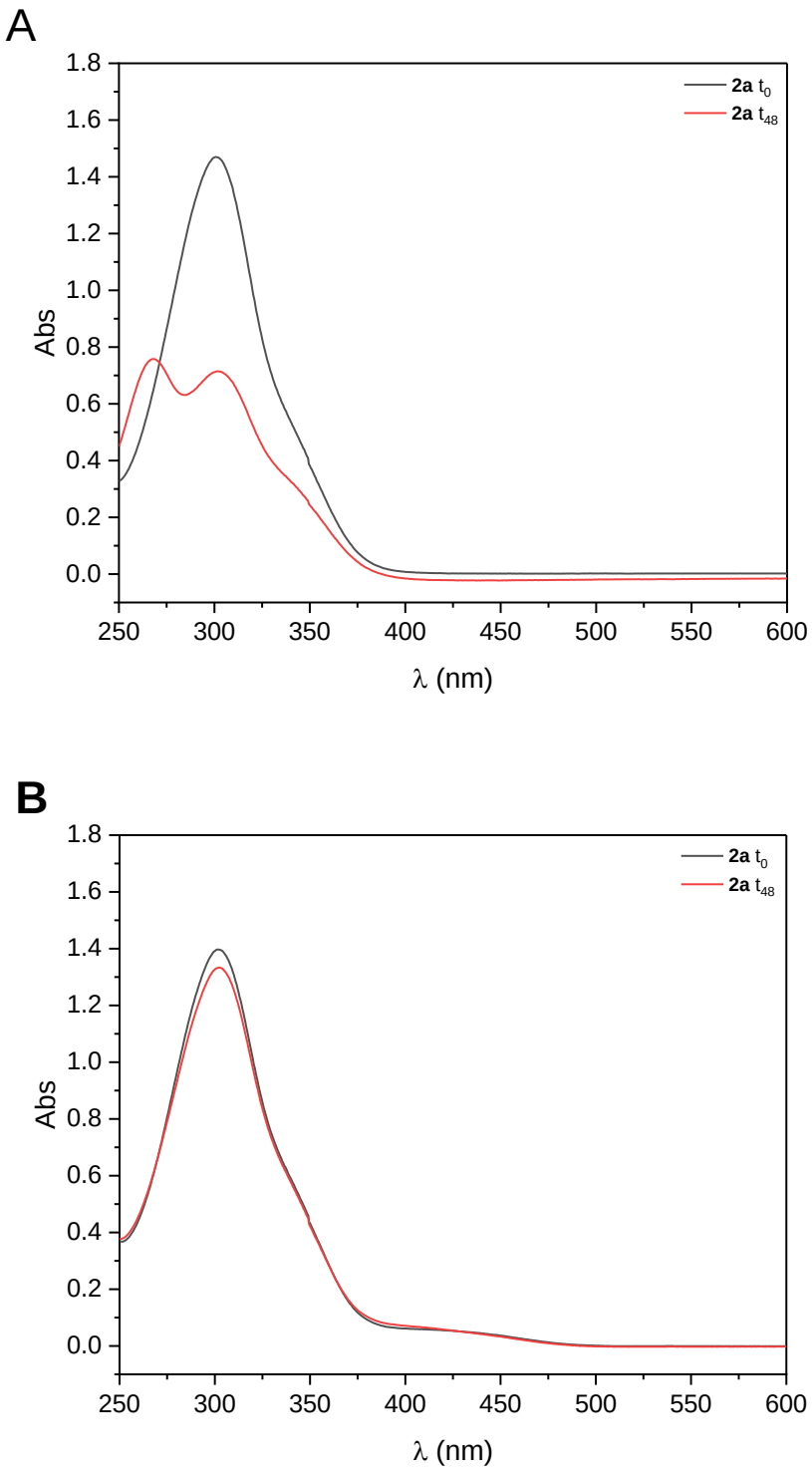

Figure A41. Electronic absorption spectra in selected wavelength regions for a 5×10^{-5} mol L^{-1} solution of **2a**. (**A**) Spectra measured at t_0 and after 48h in 1% DMSO/acetate buffer mixture, pH 4.5 (**B**) Spectra measured at t_0 and after 48h in 1% DMSO/HEPES buffer mixture, pH 7.4.

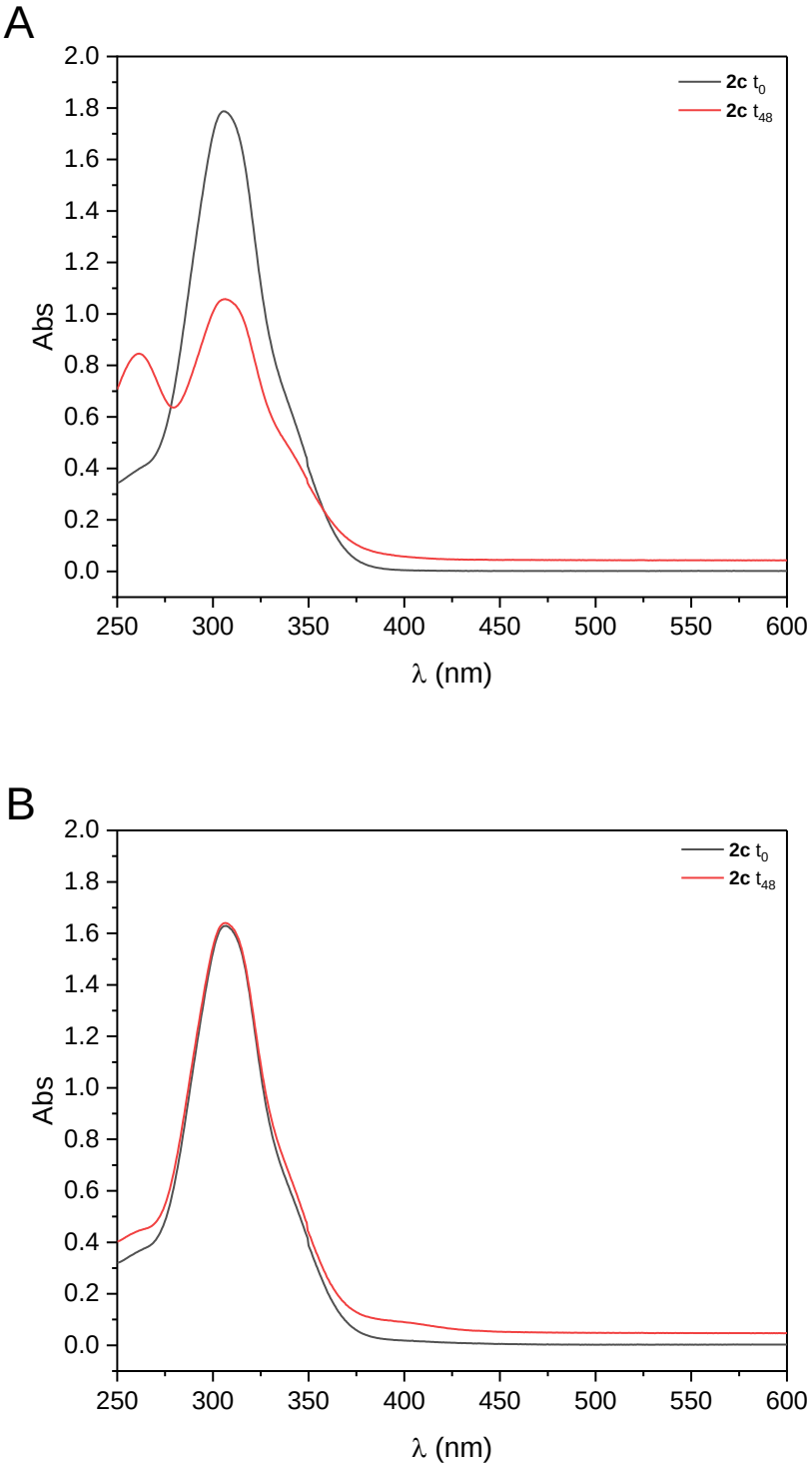

Figure A42. Electronic absorption spectra in selected wavelength regions for a 5×10^{-5} mol L^{-1} solution of **2c**. (**A**) Spectra measured at t_0 and after 48h in 1% DMSO/acetate buffer mixture, pH 4.5 (**B**) Spectra measured at t_0 and after 48h in 1% DMSO/HEPES buffer mixture, pH 7.4.

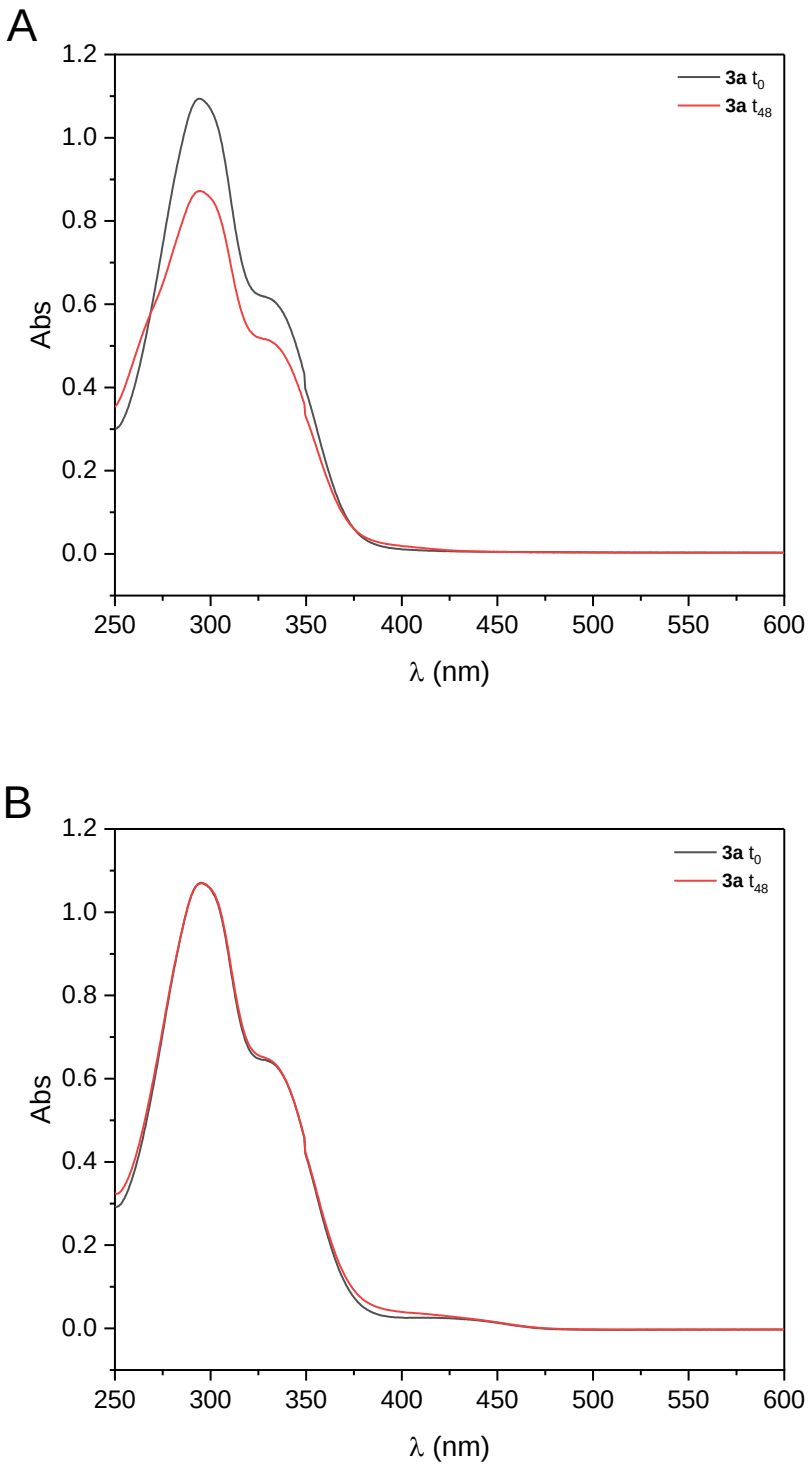

Figure A43. Electronic absorption spectra in selected wavelength regions for a 5×10^{-5} mol L^{-1} solution of **3a**. (**A**) Spectra measured at t_0 and after 48h in 1% DMSO/acetate buffer mixture, pH 4.5 (**B**) Spectra measured at t_0 and after 48h in 1% DMSO/HEPES buffer mixture, pH 7.4.

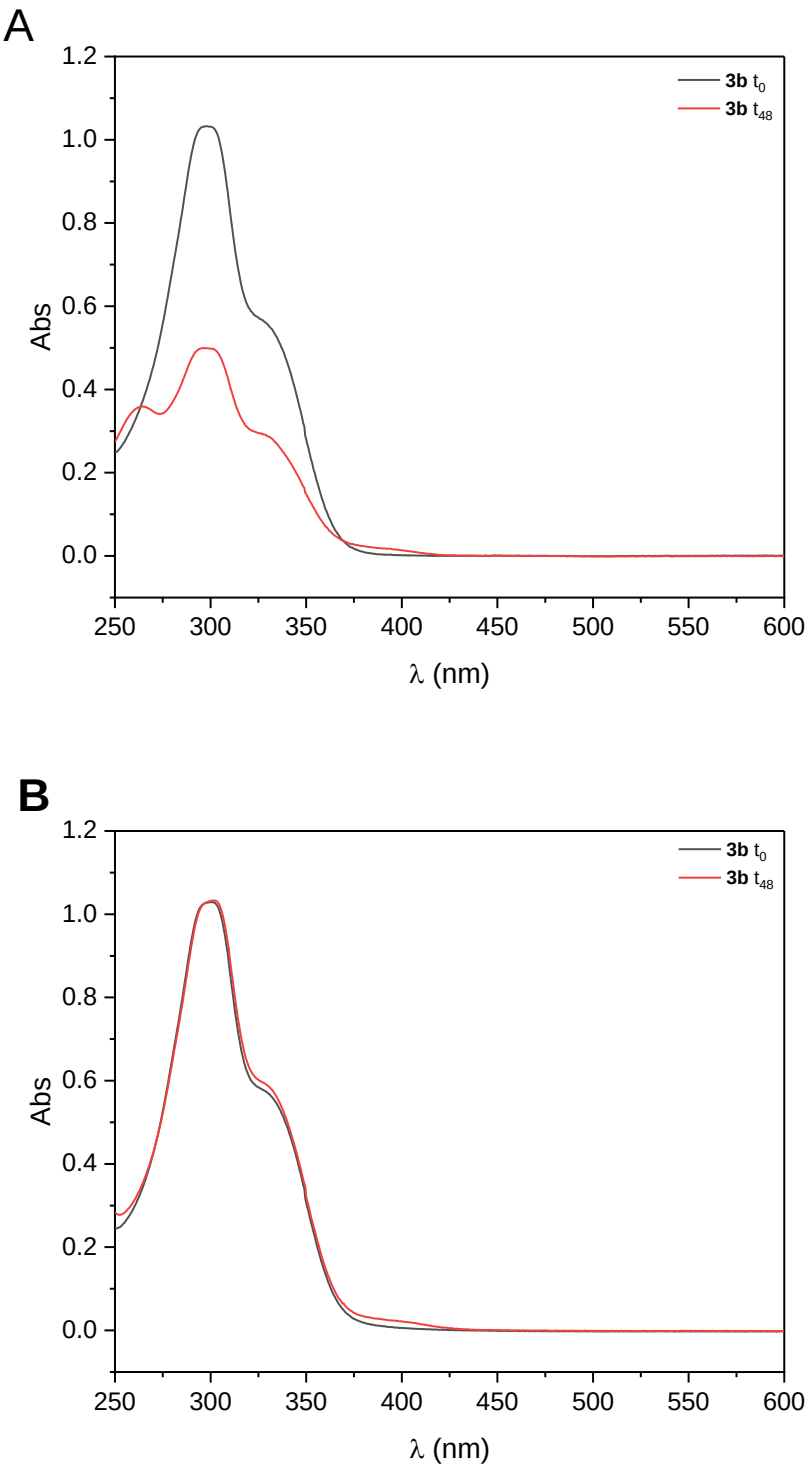

Figure A44. Electronic absorption spectra in selected wavelength regions for a 5×10^{-5} mol L^{-1} solution of **3b**. (**A**) Spectra measured at t_0 and after 48h in 10% DMSO/acetate buffer mixture, pH 4.5 (**B**) Spectra measured at t_0 and after 48h in 10% DMSO/HEPES buffer mixture, pH 7.4

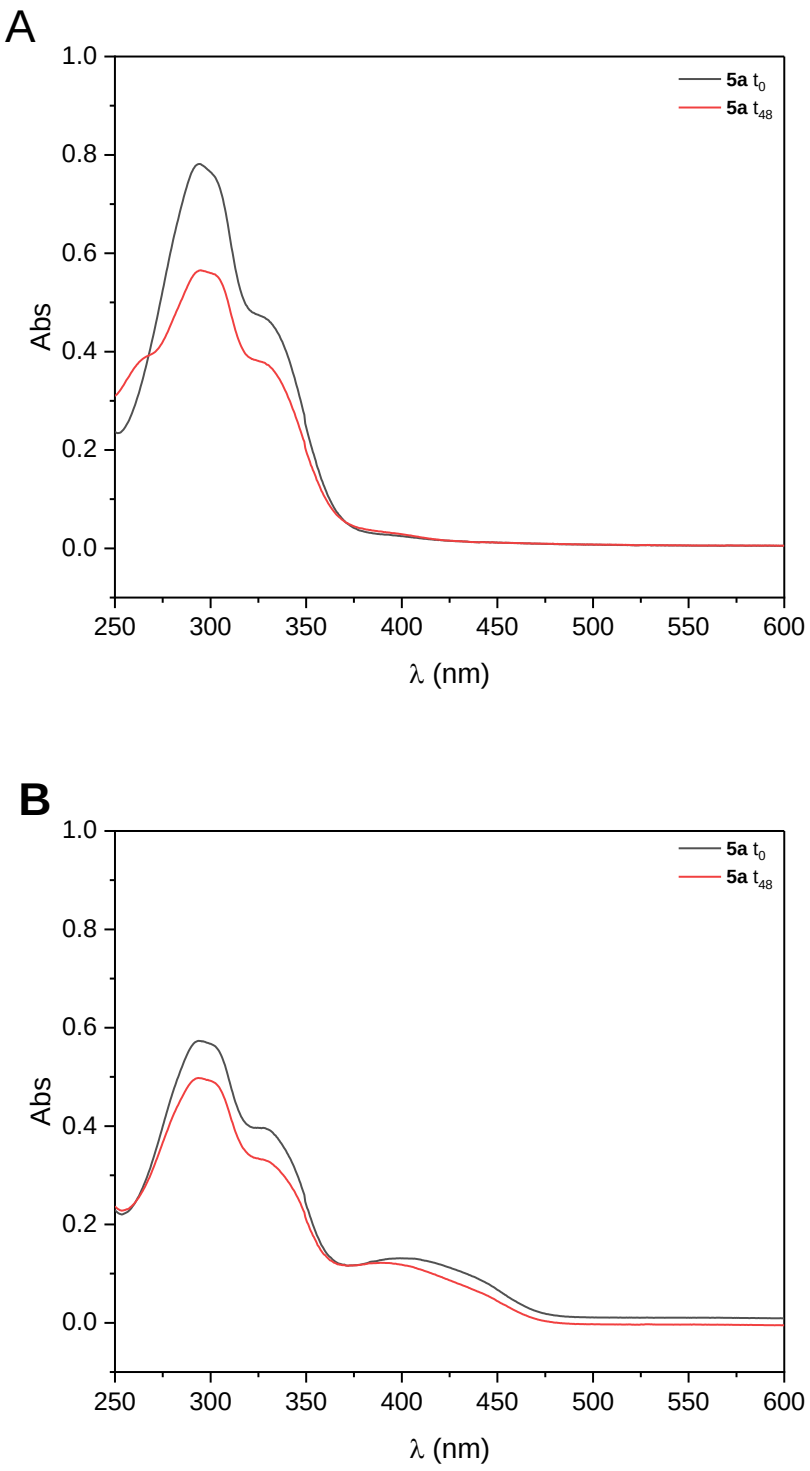

Figure A45. Electronic absorption spectra in selected wavelength regions for a 5×10^{-5} mol L^{-1} solution of **5a**. (**A**) Spectra measured at t_0 and after 48h in 10% DMSO/acetate buffer mixture, pH 4.5 (**B**) Spectra measured at t_0 and after 48h in 10% DMSO/HEPES buffer mixture, pH 7.4.

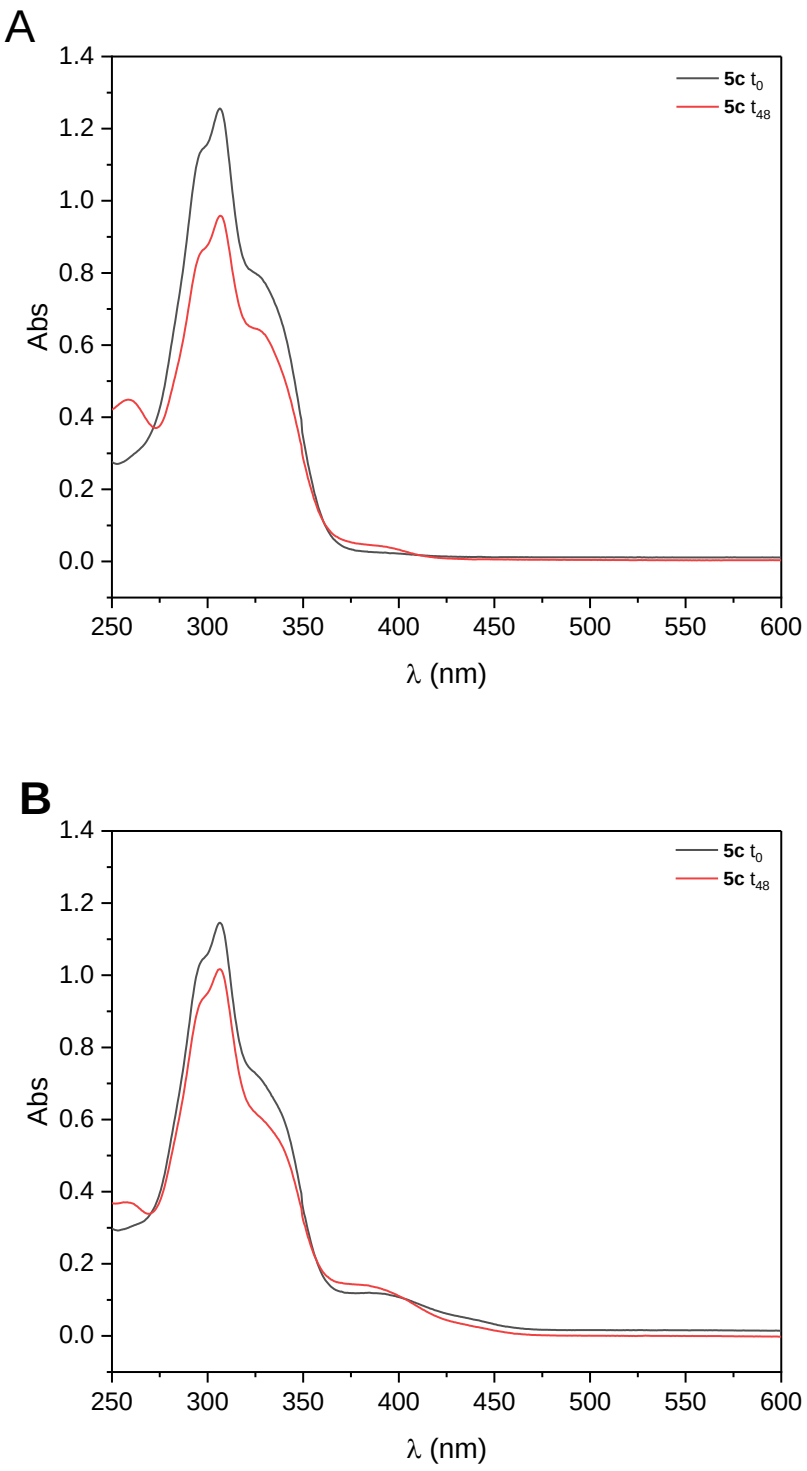

Figure A46. Electronic absorption spectra in selected wavelength regions for a 5×10^{-5} mol L^{-1} solution of **5c**. (**A**) Spectra measured at t_0 and after 48h in 10% DMSO/acetate buffer mixture, pH 4.5 (**B**) Spectra measured at t_0 and after 48h in 10% DMSO/HEPES buffer mixture, pH 7.4.

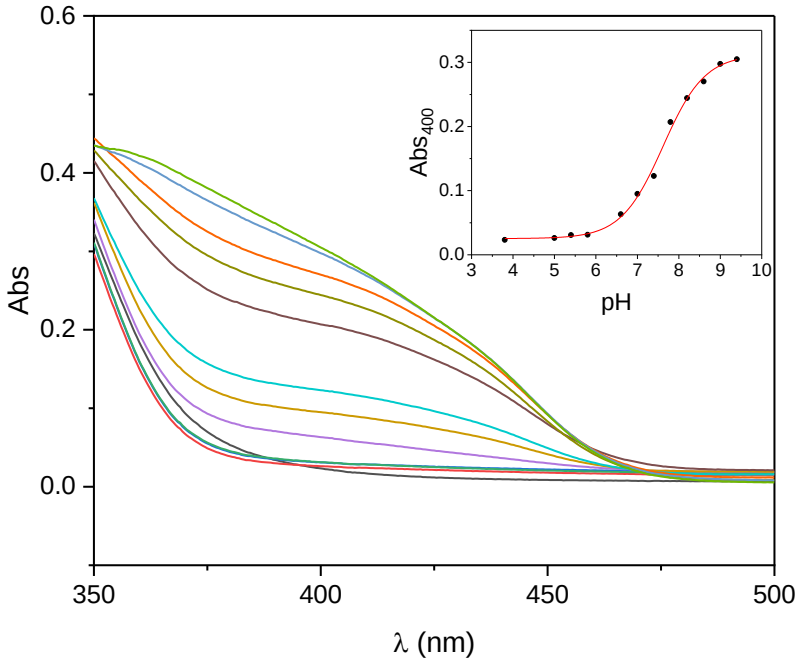

Figure A47. Electronic absorption spectra in selected wavelength regions for a 5×10^{-5} mol L^{-1} solution of **1a**. Deprotonation band centered at 400 nm, measured in different 1% DMSO/buffer mixtures (pH range from 3.8 to 9.4). *Inset*: Abs_{400} *versus* pH with sigmoidal fitting.

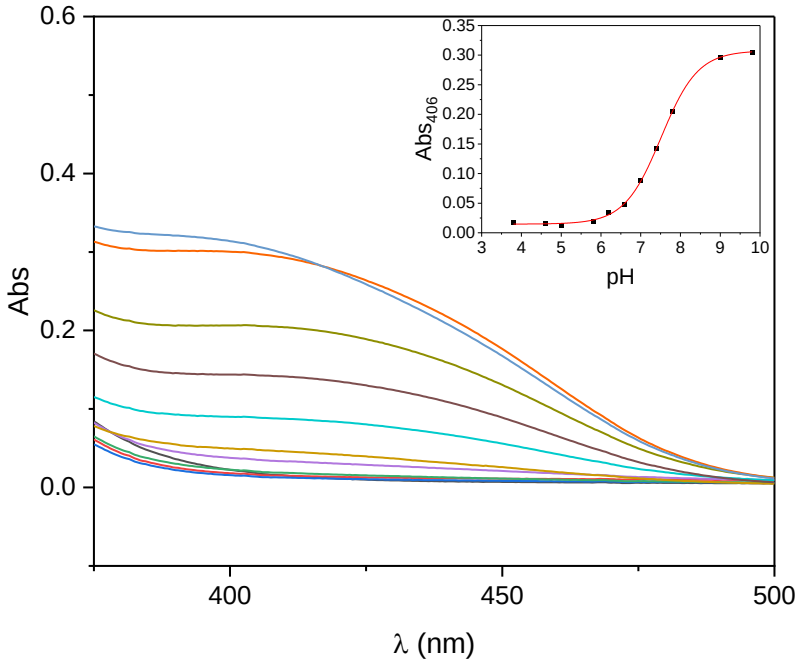

Figure A48. Electronic absorption spectra in selected wavelength regions for a 5×10^{-5} mol L^{-1} solution of **2a**. Deprotonation band centered at 406 nm, measured in different 1% DMSO/buffer mixtures (pH range from 3.8 to 9.8). Inset: Abs_{406} *versus* pH with sigmoidal fitting.

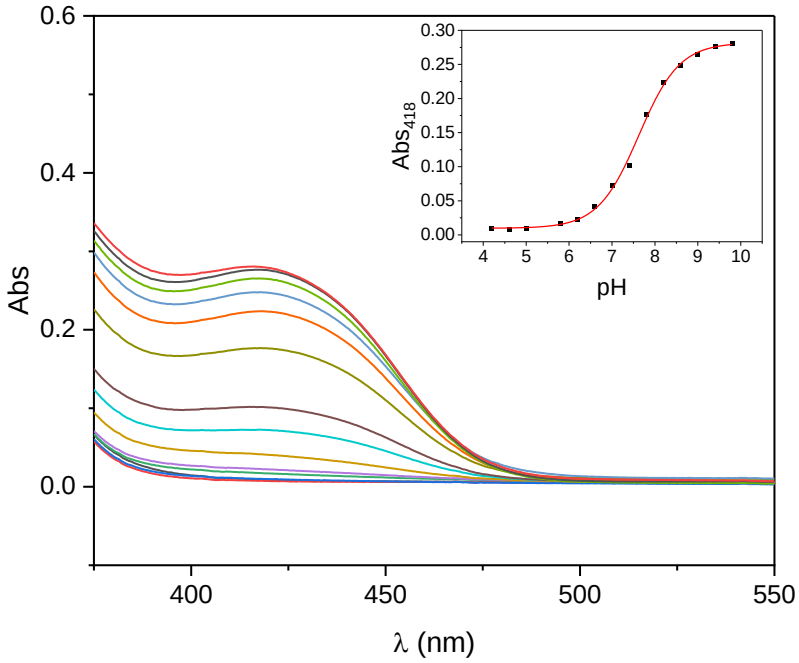

Figure A49. Electronic absorption spectra in selected wavelength regions for a 5×10^{-5} mol L^{-1} solution of **3a**. Deprotonation band centered at 418 nm, measured in different 1% DMSO/buffer mixtures (pH range from 3.8 to 9.4). Inset: Abs_{418} *versus* pH with sigmoidal fitting.

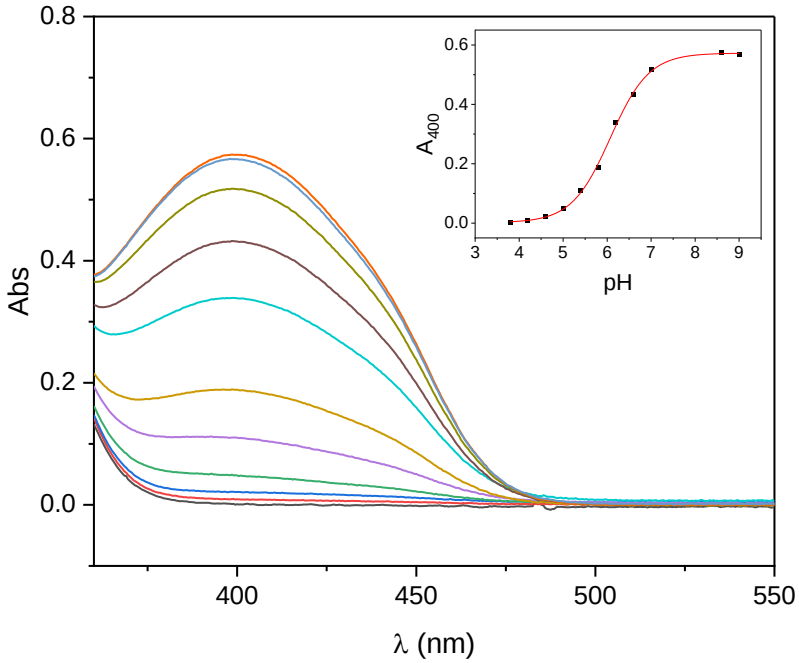

Figure A50. Electronic absorption spectra in selected wavelength regions for a 5×10^{-5} mol L^{-1} solution of **5a**. Deprotonation band centered at 400 nm, measured in different 10% DMSO/buffer mixtures (pH range from 3.8 to 9.0). Inset: Abs_{400} *versus* pH with sigmoidal fitting.

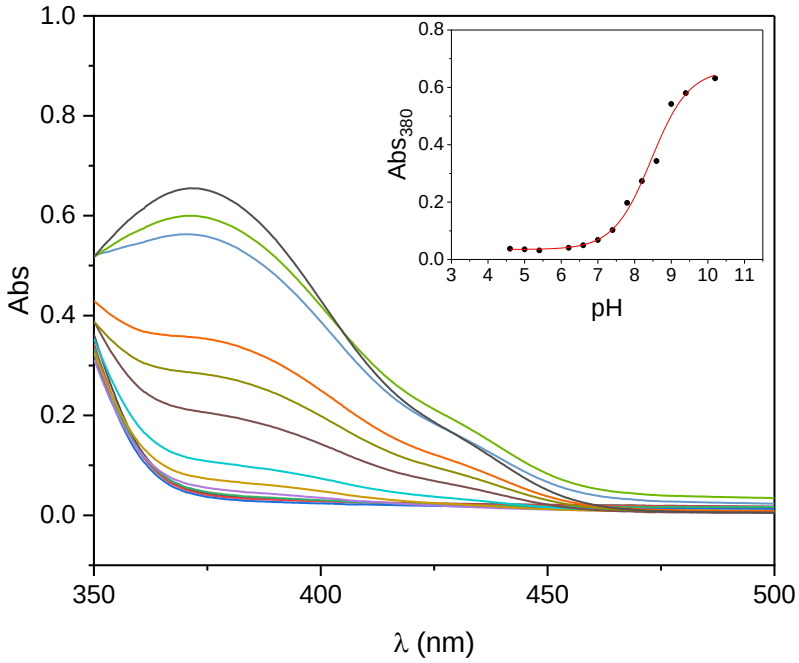

Figure A51. Electronic absorption spectra in selected wavelength regions for a 5×10^{-5} mol L^{-1} solution of **1b**. Deprotonation band centered at 380 nm, measured in different 1% DMSO/buffer mixtures (pH range from 4.6 to 10.2). Inset: Abs_{380} *versus* pH with sigmoidal fitting.

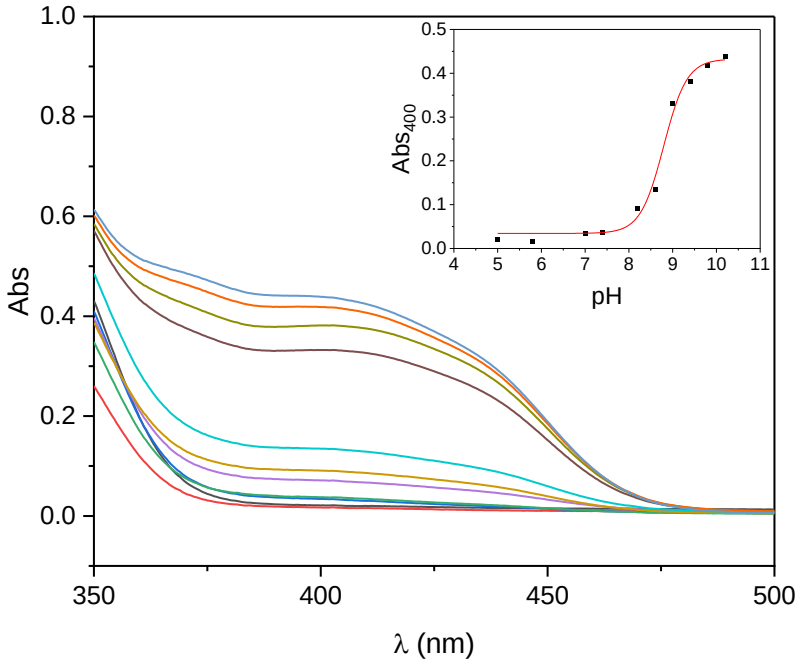

Figure A52. Electronic absorption spectra in selected wavelength regions for a 5×10^{-5} mol L^{-1} solution of **3b**. Deprotonation band centered at 400 nm, measured in different 10% DMSO/buffer mixtures (pH range from 5.0 to 10.2). Inset: Abs_{400} *versus* pH with sigmoidal fitting.

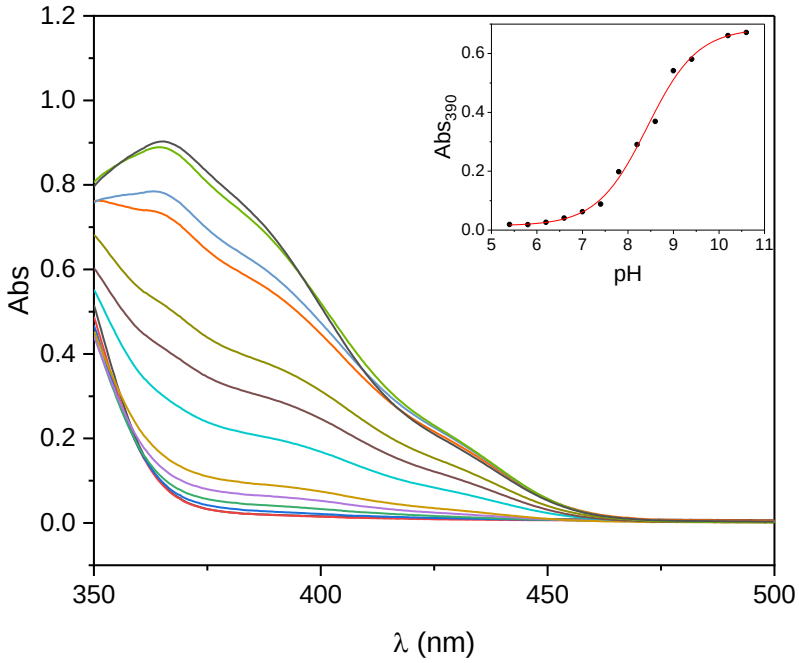

Figure A53. Electronic absorption spectra in selected wavelength regions for a 5×10^{-5} mol L^{-1} solution of **1c**. Deprotonation band centered at 390 nm, measured in different 1% DMSO/buffer mixtures (pH range from 5.4 to 10.6). Inset: Abs_{390} *versus* pH with sigmoidal fitting.

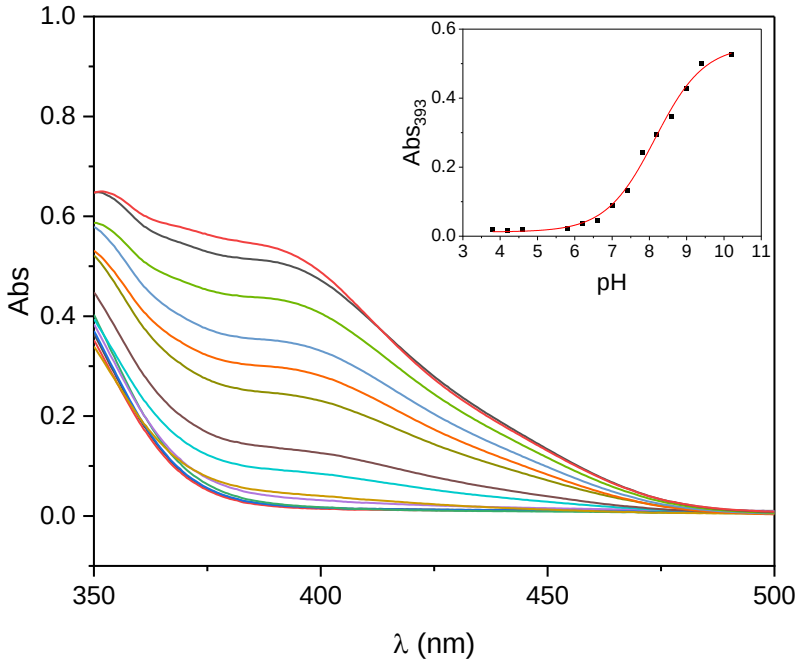

Figure A54. Electronic absorption spectra in selected wavelength regions for a 5×10^{-5} mol L^{-1} solution of **2c**. Deprotonation band centered at 393 nm, measured in different 1% DMSO/buffer mixtures (pH range from 3.8 to 10.2). Inset: Abs_{393} *versus* pH with sigmoidal fitting.

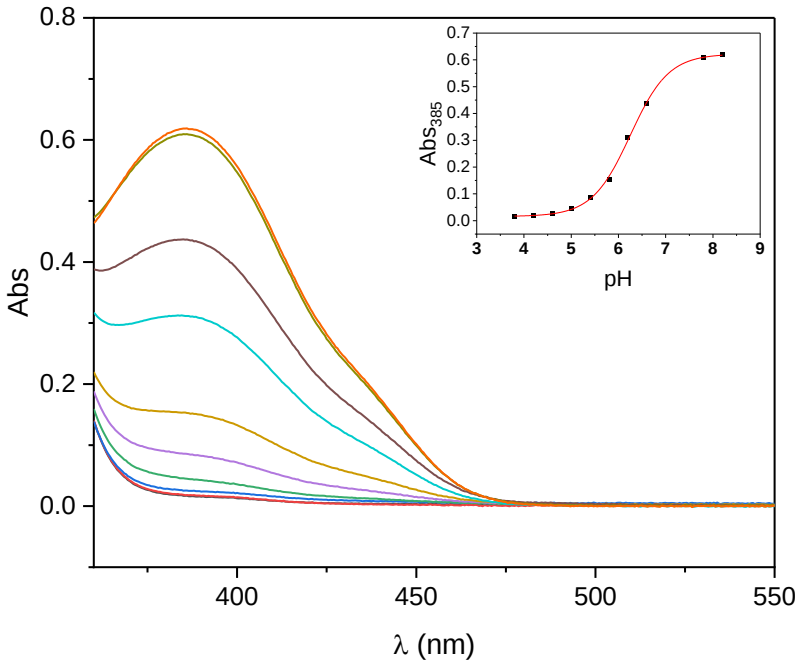

Figure A55. Electronic absorption spectra in selected wavelength regions for a 5×10^{-5} mol L^{-1} solution of **5c**. Deprotonation band centered at 385 nm, measured in different 10% DMSO/buffer mixtures (pH range from 3.8 to 9.4). Inset: Abs_{385} *versus* pH with sigmoidal fitting.

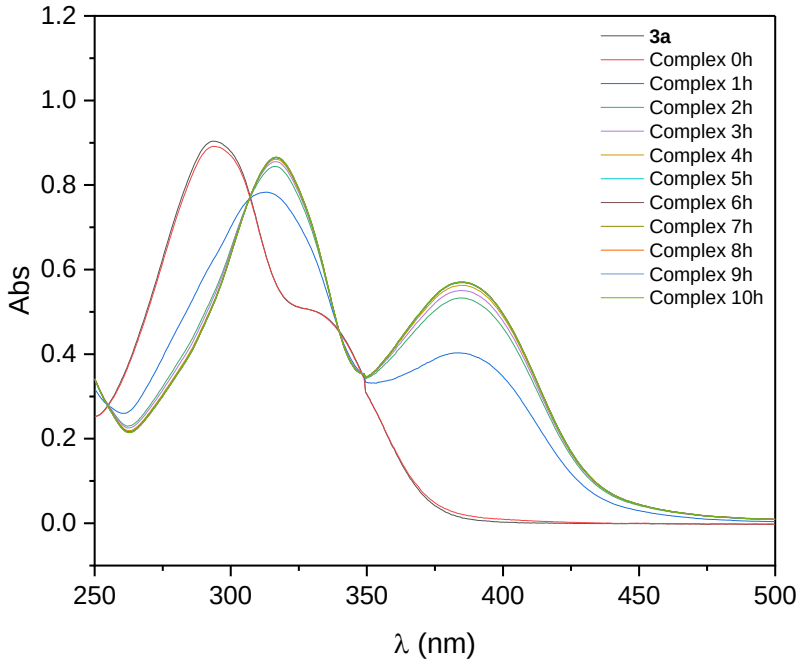

Figure A56. Electronic absorption spectra in selected wavelength regions from the complexation study of **3a**:Al^{3+} (1:2), in a 1% DMSO/acetate buffer mixture (pH = 4.5). Experimental conditions: l = 1 cm and θ = (25.0 ± 0.1) °C.

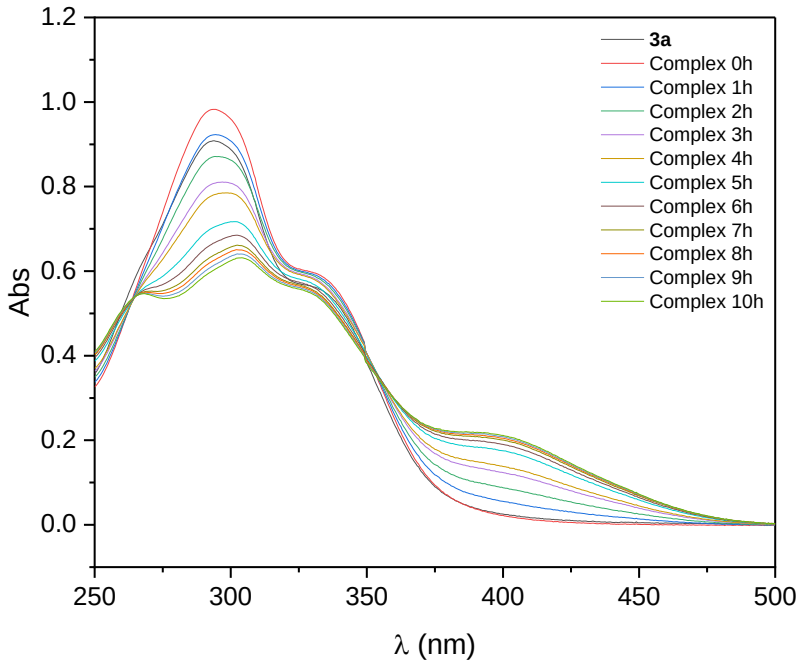

Figure A57. Electronic absorption spectra in selected wavelength regions from the complexation study of **3a**:Al^{3+} (1:1), in a 1% DMSO/acetate buffer mixture (pH = 4.5). Experimental conditions: l = 1 cm and θ = (25.0 ± 0.1) °C.

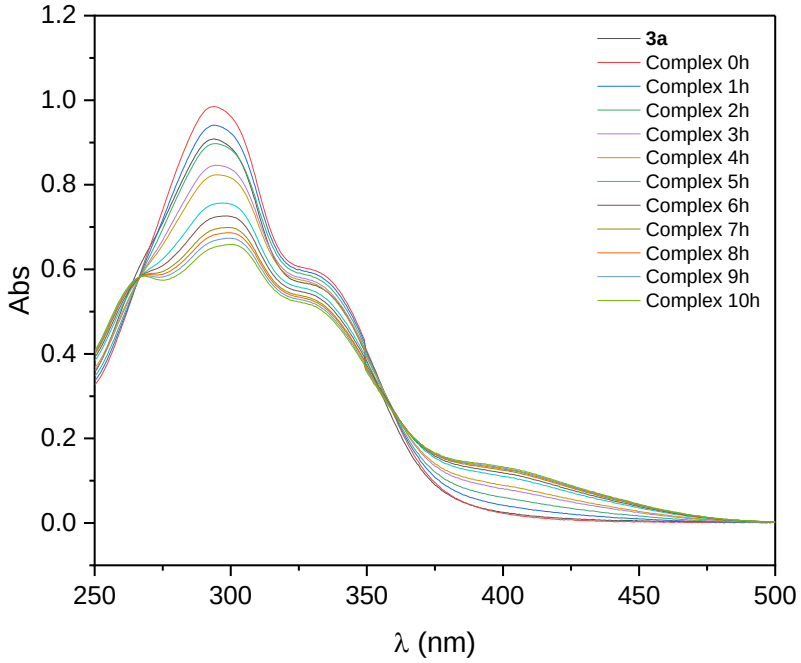

Figure A58. Electronic absorption spectra in selected wavelength regions from the complexation study of **3a**:Al^{3+} (2:1), in a 1% DMSO/acetate buffer mixture (pH = 4.5). Experimental conditions: l = 1 cm and θ = (25.0 ± 0.1) °C.

Table A31. ^{1}H (400 MHz) NMR signal assignments for **3a** and 0.5, 1 and 2 equivalents of Al^{3+}, in DMSO-d_6/D_2O (v/v) at 25 ºC.

	3a	**0.5**	**1.0**	**2.0**
C/H	**δ 1H (ppm)**	**δ 1H (ppm)**	**δ 1H (ppm)**	**δ 1H (ppm)**
1	-	-	-	-
2	-	-	-	-
3	-	-	-	-
4	7.22845 (d, 2H)	7.1539 (d, 1H)	7.1541 (d, 1H)	7.1519 (d, 1H)
5	6.8613 (t, 1H)	6.6200 (t, 1H)	6.6202 (t, 1H)	6.6189 (t, 1H)
6	7.22845 (d, 2H)	7.230275 (d, 1H)	7.225833 (d, 1H)	7.2236 (d, 1H)
7	8.4706 (s, 1H)	8.4574 (s, 1H)	8.4555 (s, 1H)	8.4464 (s, 1H)
8	-	-	-	-
9	-	-	-	-
10	8.2164 (d, 2H)	8.3937 (d, 2H)	8.38155 (d, 2H)	8.32915 (d, 2H)
11	8.82625 (d, 2H)	8.7495 (d, 2H)	8.7460 (d, 2H)	8.7284 (d, 2H)
12	8.82625 (d, 2H)	8.7495 (d, 2H)	8.7460 (d, 2H)	8.7284 (d, 2H)
13	8.2164 (d, 2H)	8.3937 (d, 2H)	8.38155 (d, 2H)	8.32915 (d, 2H)
14	2.1386 (s, 3H)	2.1004 (s, 3H)	2.1004 (s, 3H)	2.0997 (s, 3H)
OH	-	-	-	-
NH	-	-	-	-

Table A32. Final coordinates and equivalent isotropic displacement parameters of the non-Hydrogen atoms for complex **1**.

Atom	x	y	z	U(eq)
Al	0.66364(19)	0.31236(8)	0.52225(6)	0.0375(4)
O1	0.6010(5)	0.26313(18)	0.44130(14)	0.0462(10)
O2	0.7421(4)	0.38105(17)	0.59839(14)	0.0402(9)
O3	0.3903(5)	0.34535(19)	0.53059(16)	0.0424(10)
O4	0.9342(5)	0.2808(2)	0.52326(16)	0.0440(11)
O5	0.6169(5)	0.21609(19)	0.57319(16)	0.0433(10)
N1	0.7040(5)	0.4237(2)	0.47797(17)	0.0355(11)
N2	0.7480(5)	0.4928(2)	0.52253(17)	0.0382(11)
N3	0.8816(6)	0.6287(3)	0.7481(2)	0.0503(14)
C1	0.6535(6)	0.3764(3)	0.3629(2)	0.0390(12)
C2	0.6172(6)	0.2898(3)	0.3785(2)	0.0403(14)
C3	0.5911(7)	0.2295(3)	0.3255(2)	0.0493(17)
C4	0.5979(8)	0.2582(4)	0.2601(2)	0.0598(19)
C5	0.6249(8)	0.3440(4)	0.2445(2)	0.0592(19)
C6	0.6538(7)	0.4022(3)	0.2957(2)	0.0477(16)
O6	0.0913(5)	0.8989(2)	0.4051(2)	0.0633(13)
C7	0.6948(6)	0.4404(3)	0.4144(2)	0.0387(12)
O7	0.3033(6)	0.9856(3)	0.4551(3)	0.0924(18)
O8	0.0141(6)	1.0305(2)	0.4176(2)	0.0810(18)
C8	0.7667(6)	0.4611(2)	0.5839(2)	0.0354(12)
C9	0.8120(6)	0.5213(3)	0.6412(2)	0.0349(12)
C10	0.8187(7)	0.4897(3)	0.7065(2)	0.0461(16)
C11	0.8543(8)	0.5453(3)	0.7599(2)	0.0535(17)
C12	0.8801(7)	0.6604(3)	0.6862(2)	0.0491(16)
C13	0.8461(7)	0.6075(3)	0.6314(2)	0.0437(14)
C14	0.5584(9)	0.1371(3)	0.3417(3)	0.0647(19)

N4	0.1395(7)	0.9726(3)	0.4264(2)	0.0575(16)
O9	0.7482(7)	0.6227(2)	0.3485(2)	0.0803(18)
O10	0.8775(7)	0.6667(2)	0.26168(18)	0.0721(14)
O11	0.8803(6)	0.7473(2)	0.34991(17)	0.0650(14)
N5	0.8360(6)	0.6794(2)	0.3212(2)	0.0475(14)
O12	0.8707(7)	0.7976(3)	0.5666(2)	0.0666(16)
O13	0.6771(7)	0.8885(3)	0.4296(3)	0.095(2)

Table A33. Bond Distances (Angstrom) for complex **1**.

Al	O1	1.803(3)	C5	C6	1.367(7)
Al	O2	1.894(3)	O6	N4	1.259(6)
Al	O3	1.955(4)	O7	N4	1.222(7)
Al	O4	1.907(4)	O8	N4	1.245(6)
Al	O5	1.858(3)	C8	C9	1.489(6)
Al	N1	1.980(3)	C9	C10	1.389(6)
O1	C2	1.334(5)	C9	C13	1.382(7)
O2	C8	1.297(4)	C10	C11	1.377(6)
N1	N2	1.412(5)	C12	C13	1.372(6)
N1	C7	1.290(5)	C4	H4	0.93
N2	C8	1.315(5)	C5	H5	0.93
N3	C11	1.339(7)	C6	H6	0.93
N3	C12	1.329(6)	C7	H7	0.93
O3	H3C	0.82(4)	C10	H10	0.93
O3	H3B	0.82(4)	C11	H11	0.93
O4	H4B	0.82(4)	C12	H12	0.93
O4	H4A	0.81(5)	C13	H13	0.93
O5	H5A	0.82(4)	C14	H14A	0.96
O5	H5B	0.82(3)	C14	H14B	0.96
C1	C2	1.414(7)	C14	H14C	0.96
C1	C7	1.441(6)	O9	N5	1.224(5)
C1	C6	1.400(6)	O10	N5	1.262(5)
C2	C3	1.414(6)	O11	N5	1.229(5)

C3	C14	1.499(7)	O12	H12A	0.87(8)
C3	C4	1.384(6)	O12	H12B	0.84(7)
N3	H3A	0.86(6)	O13	H13A	0.82(5)
C4	C5	1.391(9)	O13	H13B	0.82(7)

Table A34. Bond Angles (Degrees) for complex **1**.

O1	Al	O2	169.86(14)	H5A	O5	H5B	117(5)
O1	Al	O3	92.38(15)	Al	O5	H5A	114(3)
O1	Al	O4	92.66(15)	Al	O5	H5B	122(4)
O1	Al	O5	96.13(14)	C6	C1	C7	117.7(4)
O1	Al	N1	90.33(14)	C2	C1	C6	120.1(4)
O2	Al	O3	88.96(13)	C2	C1	C7	122.2(4)
O2	Al	O4	86.46(14)	O1	C2	C3	118.6(4)
O2	Al	O5	93.97(14)	O1	C2	C1	122.4(4)
O2	Al	N1	79.65(14)	C1	C2	C3	119.0(4)
O3	Al	O4	174.53(15)	C2	C3	C14	119.3(4)
O3	Al	O5	87.28(15)	C2	C3	C4	118.4(4)
O3	Al	N1	88.88(14)	C11	N3	H3A	122(4)
O4	Al	O5	90.05(15)	C12	N3	H3A	115(4)
O4	Al	N1	93.24(15)	C4	C3	C14	122.2(5)
O5	Al	N1	172.62(15)	C3	C4	C5	122.6(4)
Al	O1	C2	132.4(3)	C4	C5	C6	119.0(4)
Al	O2	C8	113.5(2)	C1	C6	C5	120.7(4)
Al	N1	N2	114.8(2)	N1	C7	C1	123.3(4)
Al	N1	C7	128.3(3)	O2	C8	N2	124.5(3)
N2	N1	C7	116.9(3)	O2	C8	C9	117.3(3)
N1	N2	C8	107.1(3)	N2	C8	C9	118.2(3)
C11	N3	C12	122.4(4)	C10	C9	C13	119.1(4)
H3B	O3	H3C	109(5)	C8	C9	C10	118.8(4)

Al	O3	H3B	120(4)	C8	C9	C13	122.1(4)
Al	O3	H3C	117(4)	C9	C10	C11	119.3(4)
H4A	O4	H4B	101(5)	N3	C11	C10	119.6(4)
Al	O4	H4A	132(3)	N3	C12	C13	120.1(4)
Al	O4	H4B	122(3)	C9	C13	C12	119.4(4)
C3	C4	H4	119	N3	C12	H12	120
C5	C4	H4	119	C13	C12	H12	120
O7	N4	O8	122.0(5)	C9	C13	H13	120
O6	N4	O7	120.5(5)	C12	C13	H13	120
O6	N4	O8	117.5(4)	C3	C14	H14C	110
C6	C5	H5	120	H14A	C14	H14C	110
C4	C5	H5	120	H14B	C14	H14C	109
C1	C6	H6	120	H14A	C14	H14B	109
C5	C6	H6	120	C3	C14	H14A	110
N1	C7	H7	118	C3	C14	H14B	109
C1	C7	H7	118	O9	N5	O10	117.9(4)
C11	C10	H10	120	O9	N5	O11	121.7(4)
C9	C10	H10	120	O10	N5	O11	120.5(4)
C10	C11	H11	120	H12A	O12	H12B	104(7)
N3	C11	H11	120	H13A	O13	H13B	117(9)

Table A35. ^{1}H (400 MHz) NMR signal assignments for **3a** and complex **1**, in DMSO-d_6/D_2O (v/v) at 25 ºC.

	3a	Complex **1**
C/H	**δ 1H (ppm)**	**δ 1H (ppm)**
1	-	-
2	-	-
3	-	-
4	7.22 (d, 2H, $^{3}J_{HH}$ = 5.3021 Hz)	7.14 (d, 1H, $^{3}J_{HH}$ = 7.7393 Hz)
5	6.86 (t, 1H, $^{3}J_{HH}$ = 7.5038 Hz)	6.62 (t, 1H, $^{3}J_{HH}$ = 7.3238 Hz)
6	7.22 (d, 2H, $^{3}J_{HH}$ = 5.3021 Hz)	7.21 (d, 1H, $^{3}J_{HH}$ = 7.0995 Hz)
7	8.47 (s, 1H)	8.40 (s, 1H)
8	-	-
9	-	-
10	8.21 (d, 2H, $^{3}J_{HH}$ = 6.3217 Hz)	8.04 (d, 2H, $^{3}J_{HH}$ = 4.4723 Hz)
11	8.82 (d, 2H, $^{3}J_{HH}$ = 6.4193 Hz)	8.63 (d, 2H, $^{3}J_{HH}$ = 4.7179 Hz)
12	8.82 (d, 2H, $^{3}J_{HH}$ = 6.4193 Hz)	8.63 (d, 2H, $^{3}J_{HH}$ = 4.7179 Hz)
13	8.21 (d, 2H, $^{3}J_{HH}$ = 6.3217 Hz)	8.04 (d, 2H, $^{3}J_{HH}$ = 4.4723 Hz)
14	2.13 (s, 3H)	2.11 (s, 3H)
OH	-	-
NH	-	-

Multiplicity: s = singlet; d = doublet; dd = double of doublets; t = triplet; td = triplet of doublets. (*), (**) and (***) stands for equivalences.

Table A36. Weight of rats per group from the first to the tenth day of the experiment.

		Dia 1	Dia 2	Dia 3	Dia 4	Dia 5	Dia 6	Dia 7	Dia 8	Dia 9	Dia 10
Control Group	R1GC	279,5	281,0	285,0	288,0	290,5	289,0	288,0	295,0	299,0	304,0
	R2GC	251,0	251,0	251,5	256,0	263,0	256,0	258,0	259,5	265,0	271,0
	R3GC	265,0	260,5	263,0	268,0	266,0	263,0	273,0	281,5	279,0	268,5
	R4GC	250,0	244,0	252,0	249,5		250,0	254,0	263,0	262,5	253,5
	R5GC	249,0	260,0	254,0	258,0	265,5	261,0	268,0	274,0	278,5	263,0
	R6GC	235,0	237,0	238,5	240,0	241,0	245,0	247,5	256,0	257,0	244,0
	R7GC	273,5	271,0	275,0	278,5	279,0	282,5	286,5	291,0	289,0	280,5
	R8GC	297,5	292,0	294,5	295,0	295,0	295,5	294,0	303,0	302,5	296,5
	R9GC	250,5	251,0	247,0	255,0	253,0	270,0	271,0	261,0	272,0	282,0
	R10GC	240,0	239,5	239,0	243,0	243,5	252,0	262,0	252,0	257,0	261,0
Vehicle Group	R1GV	230,0	223,5	228,5	231,5	233,5	235,5	231,5	234,5	236,0	242,0
	R2GV	286,0	287,0	283,0	286,0	285,5	288,0	289,0	285,0	289,0	294,0
	R3GV	262,0	260,5	263,0	268,5	262,0	266,0	270,5	271,0	272,0	266,0
	R4GV	268,0	264,5	263,0	273,0	270,0	275,5	273,5	282,0	278,0	271,5
	R5GV	226,5	229,0	230,0	231,0	233,5	238,0	234,0	239,0	243,0	233,5
	R6GV	241,0	241,5	242,0	240,5	247,0	245,0	249,0	253,0	258,0	246,5
	R7GV	248,0	251,0	246,5	252,0	255,5	260,0	259,5	262,5	268,0	255,0
	R8GV	300,0	300,0	299,0	300,5	306,0	307,0	310,0	316,5	318,0	315,0
	R9GV	280,0	280,5	278,0	281,0	280,0	292,0	292,0	284,0	299,0	297,5
	R10GV	245,5	244,0	243,0	246,0	246,5	251,0	255,5	251,0	256,0	256,0
Group 1: 5 mg/Kg of compound 3a	R1G1	232,0	231,0	235,0	236,0	240,5	246,0	248,0	247,5	252,0	255,0
	R2G1	253,0	246,5	251,0	254,0	257,0	266,5	265,0	268,0	272,0	275,0
	R3G1	301,0	300,0	303,5	309,5	310,5	311,0	313,0	322,0	324,0	310,0
	R4G1	266,0	263,0	268,0	270,0	273,0	269,0	273,0	274,0	279,0	270,5
	R5G1	296,0	297,0	299,0	306,0	309,5	310,0	310,0	320,0	325,0	323,0
	R6G1	255,0	260,0	260,0	262,0	266,0	267,0	269,0	276,0	276,5	265,0
	R7G1	254,0	256,0	257,5	259,5	263,0	262,0	262,0	268,0	272,0	261,5
	R8G1	236,0	239,0	239,0	241,0	242,0	240,5	245,5	248,0	252,0	242,5
	R9G1	263,0	262,0	260,0	265,0	268,0	274,5	277,0	253,5	277,5	279,0
	R10G1	260,5	260,5	258,0	262,0	264,0	258,0	263,5	243,0	257,0	262,5
	R11G1	242,5	246,0	246,0	243,0	245,0	279,5	279,0	278,0	278,0	281,5
Group 2: 25 mg/Kg of compound 3a	R1G2	231,0	237,5	233,0	239,5	245,0	249,5	248,5	253,0	258,5	260,0
	R2G2	265,0	268,0	269,0	267,0	274,0	279,5	276,5	277,0	283,0	284,0
	R3G2	256,0	250,0	252,5	253,0	255,0	256,0	260,0	261,0	266,0	256,6
	R4G2	223,0	223,0	229,5	225,0	226,5	227,0	225,5	234,0	230,0	227,1
	R5G2	247,0	242,0	245,5	246,5	244,0	246,5	247,0	254,0	254,0	247,4
	R6G2	276,0	274,0	278,0	281,0	279,0	276,0	281,5	282,0	288,0	279,5
	R7G2	249,0	245,0	250,0	249,5	252,0	249,5	251,0	250,0	262,0	250,0
	R8G2	283,0	282,0	285,0	290,0	291,5	291,0	290,0	300,0	301,0	290,0
	R9G2	248,0	246,0	247,0	247,5	249,0	267,0	270,0	259,0	268,0	275,0
	R10G2	263,0	265,0	256,0	262,0	265,0	278,0	276,0	248,0	281,5	280,0
	R11G2	249,0	249,5	250,0	250,0	251,0	265,0	263,5	269,5	260,0	263,0
	R1G3	278,0	278,5	283,0	276,0	276,0	284,0	286,0	286,0	287,0	288,0

Group 3: 50 mg/Kg of compound 3a	R2G3	273,0	267,5	271,0	265,0	267,5	270,5	270,5	272,0	281,0	279,0
	R3G3	264,0	264,5	266,0	267,0	268,5	266,0	266,0	267,0	272,0	279,0
	R4G3	279,0	277,0	281,0	285,0	289,0	293,0	293,0	298,0	305,0	288,0
	R5G3	233,0	237,0	235,0	236,0	238,5	242,0	241,0	245,0	249,0	239,5
	R6G3	250,0	251,0	250,0	248,5	249,0	249,0	248,0	259,0	262,0	251,0
	R7G3	276,0	278,0	279,0	282,0	282,0	281,0	279,0	288,0	294,0	282,0
	R8G3	246,0	248,0	246,0	254,0	252,0	251,0	256,0	257,0	265,0	252,0
	R9G3	242,5	243,0	242,0	243,0	244,0	258,0	256,0	248,0	257,0	260,5
	R10G3	269,5	271,5	269,0	270,0	269,0	277,5	276,0	271,0	278,0	276,5
	R11G3	224,0	225,5	223,0	226,0	256,0	254,0	269,5	255,5	266,5	270,5

13. Scientific Production

This work was developed over the 48 months of the Ph.D. Program of the Department of Chemistry at the Pontifical Catholic University of Rio de Janeiro (PUC-Rio). The research was conducted mainly at LABSO-Bio (Laboratory of Organic Synthesis and Coordination Chemistry Applied to Biological Systems, PUC-Rio), under the supervision of Prof. Dr. Nicolás A. Rey, co-supervision of Prof. Dr. Daphne S. Cukierman, and in collaboration with research partners, in addition to a 6-month research stay at the Max Planck Laboratory for Structural Biology, Chemistry and Molecular Biophysics of Rosario (MPLbioR, UNR-MPINAT), a Partner Laboratory of the Max Planck Institute for Multidisciplinary Sciences (MPINAT, MPG), at the Centro de Estudios Interdisciplinarios, Universidad Nacional de Rosario, in Rosario, Argentina.

This work also played a significant role in final course projects, with co-supervision and/or co-authorship of papers. The results of this work were also presented at several regional and international conferences, both orally and in poster presentations. These works are referenced below.

1. **MARTINS, D.**; GONCALVES, P. C.; HITA, F.; CUKIERMAN, D. S.; REY, N. A.; FERNANDEZ, C. O. Exploring the aluminum(iii)-aSyn-hydrazone interplay in the context of parkinson's treatment. 2024.
2. **MARTINS, D.**; RODRIGUES, H. C. I.; LAMOSA, ROBERTA; LIGIERO, CAROLINA B P.; CUKIERMAN, D. S.; REY, N. A. Aluminum(III) Interactions with alpha-Synuclein and a Hydrazonic Metallophore: Potential Implications for the Treatment of Parkinsonism Syndrome.. In: XXI Brazilian Meeting on Inorganic Chemistry / X Brazilian Meeting on Rare Earths, 2024, Belo Horizonte. Proceedings of the XXI Brazilian Meeting on Inorganic Chemistry / X Brazilian Meeting on Rare Earths, 2024. p. BIC-089.
3. **MARTINS, D.**; GONCALVES, P. C.; HITA, F.; CUKIERMAN, D. S.; REY, N. A.; FERNANDEZ, C. O. Interactions between Aluminum(III) Ions, aSyn and a New *N*-Acylhydrazonic Metallophore: Implications for the Treatment of Aluminum Associated Parkinsonism. In: XXXVIII Congreso Anual de la Sociedad Argentina de Investigación en Neurociencias, 2023,

San Luis. Acta del XXXVIII Congreso Anual de la Sociedad Argentina de Investigación en Neurociencias, 2023.

4. **MARTINS, D.**; LAMOSA, R.; CUKIERMAN, D. S.; REY, N. A. Synthesis, Characterization and Solution Studies of the Interaction of a New *N*-Acylhydrazone Containing the 3,4,5 Trimethoxybenzoyl Group with Aluminium. In: XLVI Reunião Anual da Sociedade Brasileira de Química, 2023, Águas de Lindóia. Livro de Resumos da XLVI Reunião Anual da Sociedade Brasileira de Química, 2023. p. INO070.
5. LAMOSA, R.; **MARTINS, D.**; REY, N. A. Studies of the Interaction between an Acetyl-Derived *N*-Acylhydrazone and Aluminium in the Context of Parkinson´s Disease. In: XLVI Reunião Anual da Sociedade Brasileira de Química, 2023, Águas de Lindóia. Livro de Resumos da XLVI Reunião Anual da Sociedade Brasileira de Química, 2023. p. INO046.
6. **SILVA, D. M.**; GUERRA, R. L.; CUKIERMAN, D. S.; REY, N. A. An isoniazid-derived *N*-acylhydrazone coordinates Al^{3+} at an unexpected M_2L stoichiometry: relevance to metal overload. In: XX Brazilian Meeting on Inorganic Chemistry, 2022, Bento Gonçalves - RS. XX Brazilian Meeting on Inorganic Chemistry, 2022.
7. Roberta Lamosa Guerra. Desenvolvimento e avaliação de ligantes *N*-acilhidrazônicos como quelantes de Aluminio(III) para tratamento de efluentes industriais. 2023. Trabalho de Conclusão de Curso. (Graduação em Engenharia Química) Pontifícia Universidade Católica do Rio de Janeiro. Orientador: Nicolás A. Rey. **coorientador: Dayanne Martins da Silva.**

The present thesis work resulted in one full publication in an indexed scientific journal and two additional manuscripts currently in progress, with the Ph.D. student listed as the first author on all of them. The complete published article is presented below. Parts of this work have also been submitted to various regional and international conferences, including oral and poster presentations.

BEILSTEIN JOURNAL OF ORGANIC CHEMISTRY

Effects of the aldehyde-derived ring substituent on the properties of two new bioinspired trimethoxybenzoyl-hydrazones: methyl vs nitro groups

Dayanne Martins[1], Roberta Lamosa[1], Talis Uelisson da Silva[2], Carolina B. P. Ligiero[3], Sérgio de Paula Machado[4], Daphne S. Cukierman[*1,5] and Nicolás A. Rey[*1,§]

Full Research Paper

Open Access

Address:
[1]Departmento de Química, Pontifícia Universidade Católica do Rio de Janeiro (PUC-Rio), Rio de Janeiro, 22451-900, Brazil, [2]Instituto de Química, Universidade Federal Rural do Rio de Janeiro (UFRRJ), Seropédica 23890-000, Brazil, [3]Departamento de Química Inorgânica, Universidade Federal Fluminense (UFF), Niterói, 24020-141, Brazil, [4]Instituto de Química, Universidade Federal do Rio de Janeiro (UFRJ), Rio de Janeiro 21945-970, Brazil and [5]Departamento de Química Geral e Inorgânica, Universidade do Estado do Rio de Janeiro (UERJ), Rio de Janeiro, 20950-000, Brazil

Email:
Daphne S. Cukierman[*] - dcukierman.uerj@gmail.com;
Nicolás A. Rey[*] - nicoarey@puc-rio.br

* Corresponding author
§ phone +55 21 3527-1813

Keywords:
DFT calculations; *N*-acylhydrazones; phenol acidity; ring substituents; XRD

Beilstein J. Org. Chem. **2023,** *19,* 1713–1727.
https://doi.org/10.3762/bjoc.19.125

Received: 02 August 2023
Accepted: 01 November 2023
Published: 10 November 2023

Associate Editor: P. Schreiner

Abstract

N-Acylhydrazones are a versatile class of organic compounds with a diversity of potential applications. In this study, two new structure-related 3,4,5-trimethoxybenzoyl-containing *N*-acylhydrazones were synthesized and fully characterized, both in solution and in the solid state. The compounds differ with respect to the carbonyl precursors, i.e., 3-substituted salicylaldehydes with either a methyl or a nitro group. Single crystals of both compounds were isolated from the respective mother liquors and, in both cases, XRD confirmed the obtention of the (*E*)-isomer, in an *anti*-conformation. Computational calculations (gas and water phases) were performed in order to confirm some of the structural and vibrational aspects of the compounds. An important intramolecular H bond involving the phenolic hydroxy group and the azomethine nitrogen was identified in the solid state and seems to be maintained in solution. Moreover, the presence of the electron-withdrawing nitro substituent makes this interaction stronger. However, the contact should probably not subsist for the nitro compound under physiological conditions since the presence of this substituent significantly affects the pK_a of the phenol: an apparent value of 5.68 ± 0.02 was obtained. This also impacts the basicity of the azomethine nitrogen and, as a consequence, increases the hydrazone's susceptibility to hydrolysis. Nevertheless, both compounds are

stable at physiological-like conditions, especially the methyl-derived one, which qualifies them for further toxicological and activity studies, such as those involving trivalent metal ions sequestering in the context of neurodegenerative diseases.

Introduction

N-Acylhydrazones are a class of compounds that contain the hydrazonic functional group (–NH–N=C–) attached to an acyl group, which can be modified to generate a range of different structures with varying properties [1]. The versatility of this class of compounds is also related to the ability of *N*-acylhydrazones to exist as different isomers and/or tautomers. They can exist as geometric isomers (*E*/*Z*), which differ in the orientation of the groups around the carbon–nitrogen double bond [2,3], as well as amido and iminol tautomers [4]. The ability to undergo *E*/*Z* isomerization in a stimuli-responsive imine bond is what makes this class useful for applications in the field of molecular electronics, as switchers [5,6]. In addition, these compounds can also adopt *syn*- or *antiperiplanar* conformations, due to the constriction of the rotation around the conjugated amide single bond (N–C=O).

N-Acylhydrazones have also gained attention in literature due to other applications, ranging from medicine to supramolecular chemistry [7,8]. Among their applicability is the area of optoelectronic devices, in which they are used for the manufacture of organic light-emitting diodes (OLEDs) [9-11]. Moreover, studies involving *N*-acylhydrazonic derivatives have highlighted their suitability for the treatment of pathologies associated with infection and/or inflammation [12-17]. Antimicrobial activity is one of the most frequently studied and reported biological properties of this class [2,18-20]. Angelova and co-workers, for example, reported the ability of sulfonyl hydrazones and 4-methyl-1,2,3-thiadiazole-based hydrazone derivatives to inhibit the growth of several bacterial strains by interfering with their metabolism or cell membrane integrity [21].

In the context of cancer therapy development, metal complexes of *N*-acylhydrazones stand out. For example, Firmino et al. demonstrated that gallium(III) complexes of isoniazid-derived hydrazones exhibit strong cytotoxicity against HL-60 and HCT-116 cancer cell lines [22]. The study also found that those coordination compounds were selective towards abnormal cells, exhibiting lower toxicity for healthy human hepatocytes. On the other hand, an important development in cancer research is the use of physiological metal ion complexes, which afford more biocompatibility and thus less side-effects in therapy [23]. In this sense, we have reported dicopper(II) complexes from different *N*-acylhydrazonic binucleating ligands with potent antiproliferative activity against a panel of cancer cell lines [24-26].

On the field of neurodegeneration, our research group was the first to establish the suitability of *N*-acylhydrazones as novel metallophores able to affect protein aggregation and/or oxidation enhanced by physiological metal–protein anomalous interactions related to Alzheimer's (AD) and Parkinson's (PD), as well as to prion diseases [27-36]. Our lead compound INHHQ (or 8-hydroxyquinoline-2-carboxaldehyde isonicotinoyl hydrazone) has been successfully tested in the prevention of short- and long-term memory deficits in a mice model of sporadic AD [33]. Additionally, INHHQ decreases copper-mediated production of reactive oxygen species (ROS) in vitro, which may be another mechanism through which the compound exerts its protective effects in the brain.

From a drug development perspective, however, INHHQ has some pharmacological limitations, such as low solubility and certain susceptibility to hydrolysis in a water-rich medium. The protective character and high metallophoric potential of INHHQ, nevertheless, prompted us to design and synthesize new optimized derivatives. In this context, we recently described a family of pharmocologically improved *N*-acylhydrazones containing the 1-methylimidazole moiety [37]. In 2020, we proved the promising anti-PD and metallophoric effect, especially towards intracellularly relevant copper(I) ions, of X1INH (1-methyl-1*H*-imidazole-2-carboxaldehyde isonicotinoyl hydrazone) [32].

This year, we evaluated the effects of the presence of three methoxy substituents in an *N*-acylhydrazone derived from 3,4,5-trimethoxybenzoic acid hydrazide, a modification inspired by mescaline, the active principle of the hallucinogenic cactus peyote, which could result in a greater BBB penetration [36]. In this study, however, the structural modifications in the compound did not seem to significantly affect its pharmacological properties and metallophoric potential against copper(II) when compared to the unsubstituted counterpart. Nevertheless, the bioinspired compound was still able to reduce oxidative stress and affect the aggregation of the amyloid-β peptide, related to pathophysiological events in AD.

As a continuation of our long-term effort on the development of potentially bioactive *N*-acylhydrazones, the present work comprises a structural and spectroscopic comparison, from both experimental and theoretical viewpoints, of two structure-related hydrazones. Both compounds are new, and derived from the same 3,4,5-trimethoxybenzoic acid hydrazide, but differ

with respect to the carbonyl precursors: herein, 3-substituted salicylaldehydes (Scheme 1) are used, which assure for a harder donor-atoms set in order to target trivalent metal ions such as aluminum(III), which has been proposed to display a role in neurodegeneration [38].

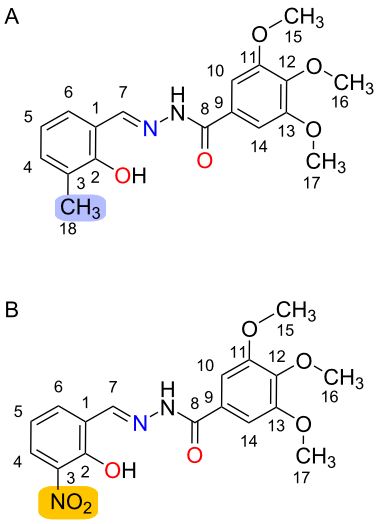

Scheme 1: Structure of (A) 3-methylsalicylaldehyde 3,4,5-trimethoxybenzoyl hydrazone (**hdz-CH$_3$**) and (B) 3-nitrosalicylaldehyde 3,4,5-trimethoxybenzoyl hydrazone (**hdz-NO$_2$**).

A comparative study between these two *N*-acylhydrazones is interesting, especially considering that they possess different substituents at the same position in the phenol ring: the electron-donating methyl group (**hdz-CH$_3$**) and the electron-withdrawing nitro group (**hdz-NO$_2$**). It is expected that those substituents impact the chemical (e.g., acidity and hydrolysis susceptibility) as well as the structural and spectroscopic properties of the compounds.

Results and Discussion

The methyl-substituted **hdz-CH$_3$** and its nitro-containing analogue **hdz-NO$_2$** were isolated as beige and light-yellow solids with 78% and 44% yield, respectively. Thermal analyses between 25 and 350 °C were performed in order to verify the hydration status of the bulk. Regarding **hdz-CH$_3$**, a weight loss of 9.78% from around 80 to 190 °C was observed, suggesting the presence of two crystallization water molecules in the network (calcd.: 9.47% for $C_{18}H_{20}O_5N_2{\cdot}2H_2O$, MW = 380.39 g mol^{-1}). On the other hand, **hdz-NO$_2$** did not show any mass loss below 250 °C, indicating the absence of solvation molecules in the sample ($C_{17}H_{17}O_7N_3$, MW = 375.34 g mol^{-1}).

Single crystals of both compounds, as monohydrates, were isolated from the respective mother liquors. The structures of **hdz-CH$_3$** and **hdz-NO$_2$** are displayed in Figure 1 and an overview of the crystallographic data can be found in Table 1.

Both molecules are near planar and correspond to the (*E*)-isomer, in an *antiperiplanar* conformation. Superposition of the structures (Figure 2A) shows that spatial arrangements are nearly the same and even the crystallization water molecules were allocated in nearby sites, interacting as H-acceptors in a hydrogen bond with the respective N2H groups. In spite of these similarities, the compounds were indexed in different space groups. The methyl-containing **hdz-CH$_3$** crystallized in the monoclinic system, *C*2/*c* space group, while the nitro derivative **hdz-NO$_2$** belongs to the $P\bar{1}$ group, from the triclinic system. In both cases, a moderate to strong intramolecular H-bond involving the phenol oxygen O1 as H-donor and the azomethine nitrogen N1 as H-acceptor is observed, which originates six-membered cyclic motifs with a graph-set $R_1^1(6)$ [39]. The hydrogen atom is closer to O1 than to N1, indicating that the preferred protonation site is the former, as can be observed at the Fourier difference maps (Figure S1A and S1B in Support-

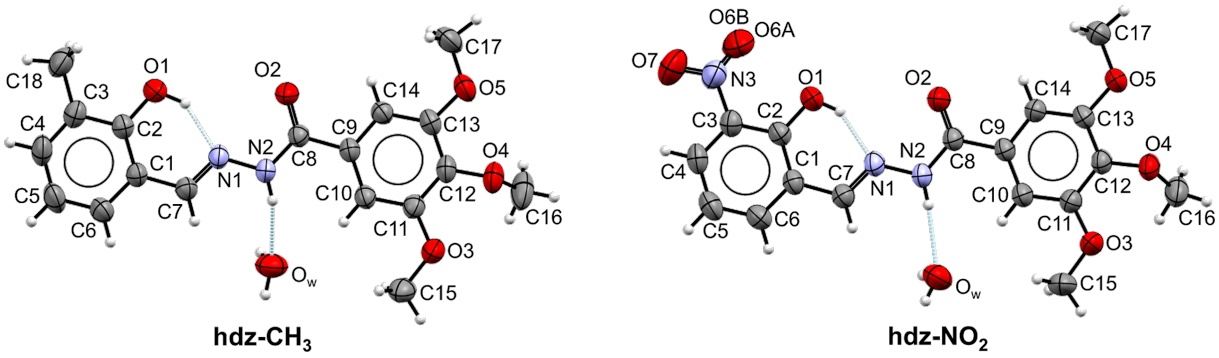

Figure 1: ORTEP representation of the new *N*-acylhydrazones synthesized in the present work, drawn with thermal ellipsoids at 30% probability. Left: **hdz-CH$_3$** and right: **hdz-NO$_2$**.

Table 1: Crystal, data collection and refinement parameters for **hdz-CH_3** and **hdz-NO_2**.[a]

Data	**hdz-CH_3**	**hdz-NO_2**
crystal size (mm)	0.99 × 0.14 × 0.14	0.57 × 0.32 × 0.12
empirical formula	$C_{18}H_{22}N_2O_6$	$C_{17}H_{19}N_3O_8$
formula weight (g mol^{-1})	362.37	393.35
F(000)	1536	412
temperature (K)	293	293
absorption coefficient μ (mm^{-1})	0.101	0.117
calculated density (g·cm^{-3})	1.337	1.452
crystal system	monoclinic	triclinic
space group	C_2/c (n° 15)	$P\bar{1}$ (n° 2)
a, *b*, *c* (Å)	32.1401(15) 8.4828(4) 14.3708(6)	8.3230(9) 8.5243(9) 13.3392(14)
α, β, γ (°)	90.000 113.2650(10) 90.000	88.593(4) 87.468(4) 72.105(3)
cell volume ($Å^3$)	3599.4(3)	899.66(17)
Z, *Z'*	8, 1	2, 1
reflections collected, R_{int}	48639, 0.0363	35549, 0.1407
independent reflections	3651	3238
index ranges	−40 < *h* < 40 −10 < *k* < 10 −17 < *l* < 17	−10 < *h* < 10 −10 < *k* < 10 −16 < *l* < 16
data/restrains/parameters	3651/3/250	3238/9/277
final residual factor [$I > 2\sigma(I)$]	R_1: 0.0486 wR_2: 0.1450	R_1: 0.0746 wR_2: 0.1929
goodness-of-fit on F^2	1.11	0.99
T_{min}, T_{max}	0.906, 0.986	0.936, 0.986
theta range for data collection (°)	2.789 to 26.372	2.573 to 25.345
largest diff. peak and hole (e·$Å^{-3}$)	0.17, −0.19	0.290, −0.291

[a]*a*, *b*, *c*, α, β, γ: unit cell parameters; *Z*: formula unit per unit cell; *Z'*: number of formula units in the crystallographic unit cell divided by the number of independent general positions; F(000): structure factor in the zeroth-order case; F: structure factor; F^2: squared structure factor; T: transmission factor.

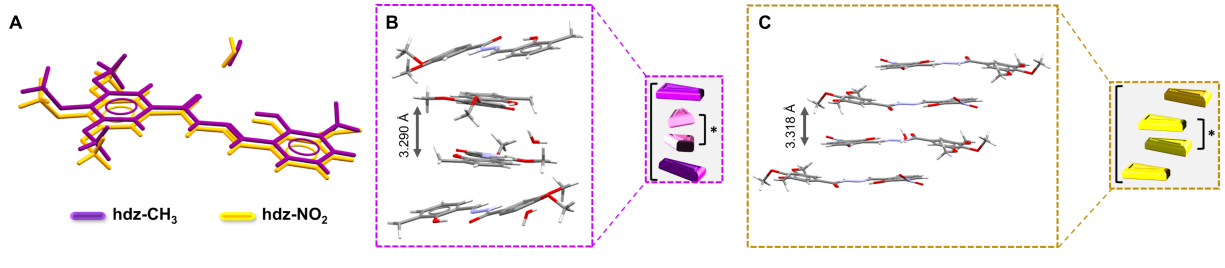

Figure 2: (A) Superposition of molecular structures and stacked motifs of (B) **hdz-CH_3** and (**C**) **hdz-NO_2**.

ing Information File 1), but the presence of the hydrogen bond influences the contiguous aromatic system, as can be inferred by the characteristic elongation of the C1–C2 bond, which is 1.405(2) Å in **hdz-CH_3** and 1.411(3) Å in **hdz-NO_2** [40-42]. The effect is also noticed through the HOMA (harmonic oscillator model of aromaticity) indexes [43] of the rings: while the trimethoxy-substituted, hydrazide-derived one presents values of 0.995 (**hdz-CH_3**) and 0.990 (**hdz-NO_2**), indicating high aromaticity, the aldehyde-derived ring shows HOMA indexes of 0.964 (**hdz-CH_3**) and 0.961 (**hdz-NO_2**), suggesting that, for both compounds, this H-bond decreases the aromaticity of the phenol-containing ring. Finally, O1···N1 distances are 2.581(2)

and 2.539(3) Å for **hdz-CH$_3$** and **hdz-NO$_2$**, respectively (Table 2). Thus, all the structural evidence discussed above converges to the conclusion that the presence of the electron-withdrawing nitro substituent in **hdz-NO$_2$** makes the intramolecular H-bond stronger.

Regarding lattice organization, both structures exhibit stacked motifs. In **hdz-CH$_3$**, the $(30\bar{2})$ planes were organized by C–H···O non-conventional H-bonds comprising the methoxy groups (Figure 2B). In the columns, there are antiparallel dimers (marked as *) sandwiched between two non-parallel molecules. The planes in **hdz-NO$_2$** present similar intermolecular interactions, but they grow as (101) planes. The columns also present the antiparallel dimers, but they are intercalated by antiparallel slipped molecules (Figure 2C).

The supramolecular organization of the *N*-acylhydrazones was also studied through their Hirshfeld surfaces, in which π–π interactions play an important role. When the normalized distance between a molecule and the closest neighbors are plotted (Figures S2A and S2C, and S3A and S3C in Supporting Information File 1), it becomes possible to calculate the contribution of each type of intermolecular interaction to the whole profile [44]. In our case, results show that the sum of π···π and C–H···π contacts comprises almost 20% of the Hirshfeld surface for both compounds. The curvedness maps were also plotted over the Hirshfeld surfaces and evidence the strong flatness of the structures (Figures S2B and S3B in Supporting Information File 1). Important contributions of hydrogen bonds (O···H/H···O) can also be found, especially for **hdz-NO$_2$**. Besides the interaction maps, crystal structures themselves may be used to calculate the electrostatic potential over an electronic density map as well. For **hdz-NO$_2$**, results show the alternated slipped stack motif involves the assembly of portions with opposite electrostatic potentials.

Computational calculations were performed in order to confirm some of the structural and vibrational aspects of the compounds. The optimized structures obtained with B3LYP/6-311G(d,p) (both in gas and water phases) were compared to the respective experimental XRD structures (Figure 3). The RMSD values for **hdz-NO$_2$** in gas (0.431 Å) and water (0.405 Å) phases were lower than the respective values for **hdz-CH$_3$** (0.648 Å in the gas phase and 0.623 Å in water). However, the small RMSD values in all cases showed that the calculated structures correlated pretty well with the respective experimental ones [45,46]. The biggest differences between the theoretical structures and the experimental data corresponded to the aldehyde-derived ring, containing the –CH$_3$ (or –NO$_2$) substituents, an effect which is more explicit in **hdz-NO$_2$**, probably due to the intrinsic disorder observed in its structure.

The comparison between theoretical and experimental selected geometric parameters can be seen in Tables S1 and S2 (Sup-

Table 2: H-bonding parameters for **hdz-CH$_3$** and **hdz-NO$_2$**.

D–H···A	Symmetry operation	D–H (Å)	H···A (Å)	D···A (Å)	D–H···A (°)	% Σ*vdWr*
hdz-CH$_3$						
O1–H1···N1	intra	0.93(2)	1.772(18)	2.581(2)	144(2)	64.4
Ow–Hw1···O2	–	0.84(3)	2.00(3)	2.816(2)	166(3)	73.5
N2–H2a···Ow	1–x,1–y,1–z	0.840(17)	2.164(18)	2.910(2)	148(2)	79.6
C14–H14···O2	intra	0.9300	2.400	2.734(2)	101.00	87.3
hdz-NO$_2$[a]						
O1–H1···N1	intra	0.86(4)	1.79(3)	2.539(3)	146(3)	65.1
Ow–Hw2···O4	–	0.83(5)	2.03(5)	2.839(4)	169(5)	74.6
Ow–Hw1···O2A	1–*x* , –*y*, 1–*z*	0.82(4)	2.48(5)	3.143(13)	138(4)	91.2
Ow–Hw1···O1	1–*x* , –*y* , 1–*z*	0.82(4)	2.34(4)	3.061(3)	147(4)	86.0
N2–H2a···Ow	1–*x* , 1–*y* , 1–*z*	0.83(2)	2.09(2)	2.898(4)	163(3)	76.8
C5–H5···O2	–1+*x* , *y* , 1+*z*	0.9300	2.5800	3.175(4)	162.00	94.8
C10–H10···Ow	1–*x* , 1–*y* , 1–*z*	0.9300	2.4600	3.360(4)	162.00	91.2
C14–H14···O4	intra	0.9300	2.4400	7.758(4)	100.00	89.7
C16–H16c···O5	intra	0.9600	2.4100	2.975(5)	117.00	88.6
C17–H17b···O3	1–*x* , –*y* , 1–*z*	0.9600	2.5900	3.536(5)	168.00	95.2

[a]Data shown only for the major component of disorder.

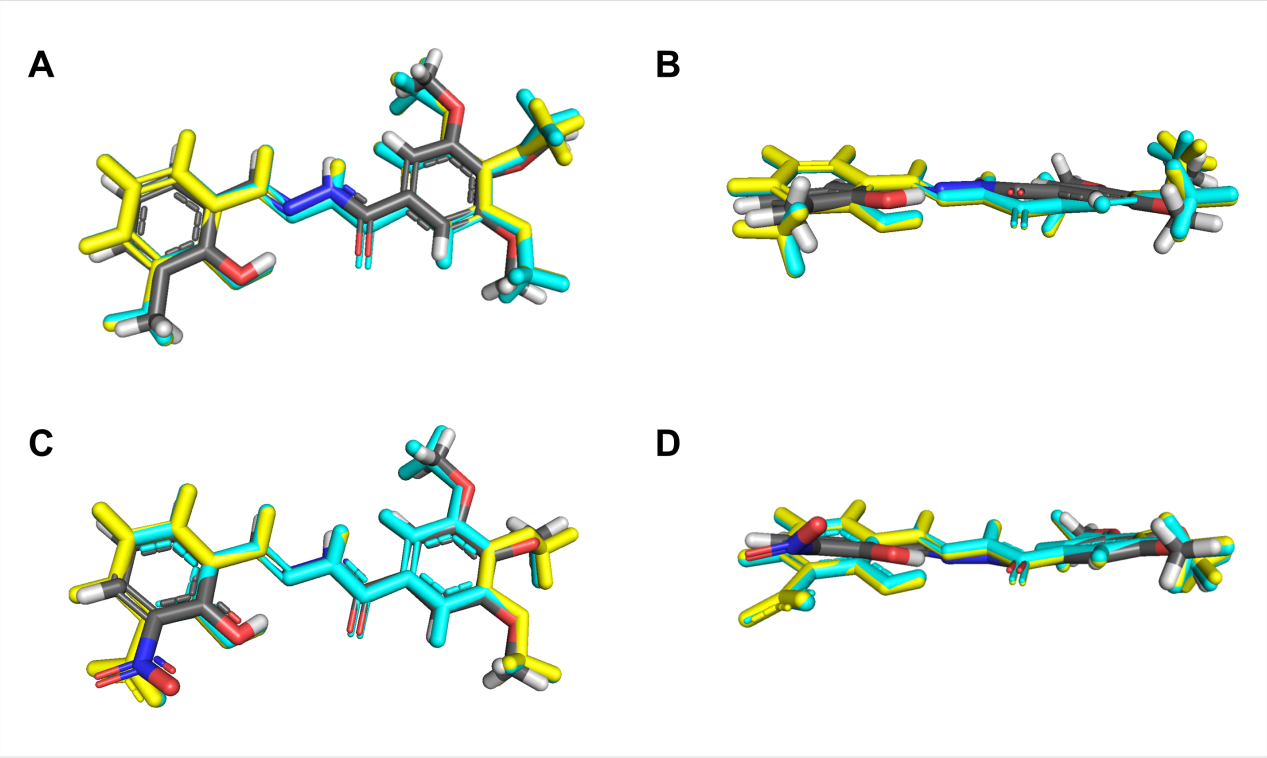

Figure 3: Overlap of the experimental (carbon atoms colored in gray) and theoretical structures (calculated with B3LYP/6-311G(d,p) in gas and water phases colored in yellow and cyan, respectively): **hdz-CH$_3$** seen from (A) above and (B) from the side; **hdz-NO$_2$** seen from (C) above and (D) from the side. The optimized structures of **hdz-CH$_3$** and **hdz-NO$_2$** can be seen in Figure S4 in Supporting Information File 1.

porting Information File 1) and confirms they are in good accordance. For **hdz-CH$_3$**, a maximum percentage error of 3% for bonds and 2% for angles was observed, while **hdz-NO$_2$** presented values of 2% and 3% for these parameters, respectively. In turn, the intramolecular interaction OH···N1 showed maximum errors of 2% (**hdz-CH$_3$**) and 0% (**hdz-NO$_2$**). In general, the structures calculated involving the IEFPCM formalism (water phase) displayed the best agreement with the experimental data.

Regarding the vibrational characterization, infrared spectra were also calculated with both B3LYP/6-311G(d,p) – gas phase – and B3LYP/6-311G(d,p)/IEFPCM – water – for **hdz-CH$_3$** and **hdz-NO$_2$** and fitted very well with the respective experimental data, especially in the lower-frequencies region, i.e., below 2000 cm^{-1} (Figure 4 and Tables S3 and S4 in Supporting Information File 1). It is worth noting that the assignments of experimental absorptions were performed not only with the aid of DFT calculations, but also checked by comparing them to the vibrations of the respective carbonyl and hydrazide precursors.

Although the phenol-related ν(O–H) bands could not be accurately identified due to overlapping with the water stretching modes, theoretical results indicate that the frequency in **hdz-CH$_3$** (3407 cm^{-1}) is higher than that in **hdz-NO$_2$** (3326 cm^{-1}), suggesting a lower bond force constant in the latter. Differences were observed in the hydroxy bending vibrations as well, and those were perfectly observable in the spectra: δ_{ip}(C–O–H) and δ_{oop}(O–H) modes were assigned, respectively, at 1376 and 720 cm^{-1} for **hdz-CH$_3$**, and at 1359 and 747 cm^{-1} for **hdz-NO$_2$**. Interestingly, DFT showed that, while these vibrations are "clean" in **hdz-CH$_3$**, they were coupled with NBA ring movements in **hdz-NO$_2$**. Therefore, the IR results confirm the stronger character of the intramolecular H-bond in the nitro-substituted *N*-acylhydrazone. As previously observed for other compounds of this class, the azomethine ν(C=N) modes are barely susceptible to interactions involving the nitrogen atom, being located at 1620 cm^{-1} in **hdz-CH$_3$** and at 1622 cm^{-1} in compound **hdz-NO$_2$**.

Other typical bands of *N*-acylhydrazones were also attributed, such as ν(C=O) at 1658 (**hdz-CH$_3$**) and 1648 cm^{-1} (**hdz-NO$_2$**), as well as ν(N–N) at 1003 (**hdz-CH$_3$**) and 997 cm^{-1} (**hdz-NO$_2$**). The $\nu_{as}(NO_2)$ and $\nu_{sym}(NO_2)$ vibrations of the nitro group in **hdz-NO$_2$** were identified as medium and strong intensity bands, respectively, at 1519 and 1336 cm^{-1}. These modes were calculated at 1608 and 1379 cm^{-1} in the gas phase.

Although *N*-acylhydrazones are usually prone to undergo speciation in DMSO-d_6 solution [47], ^{1}H NMR measurements

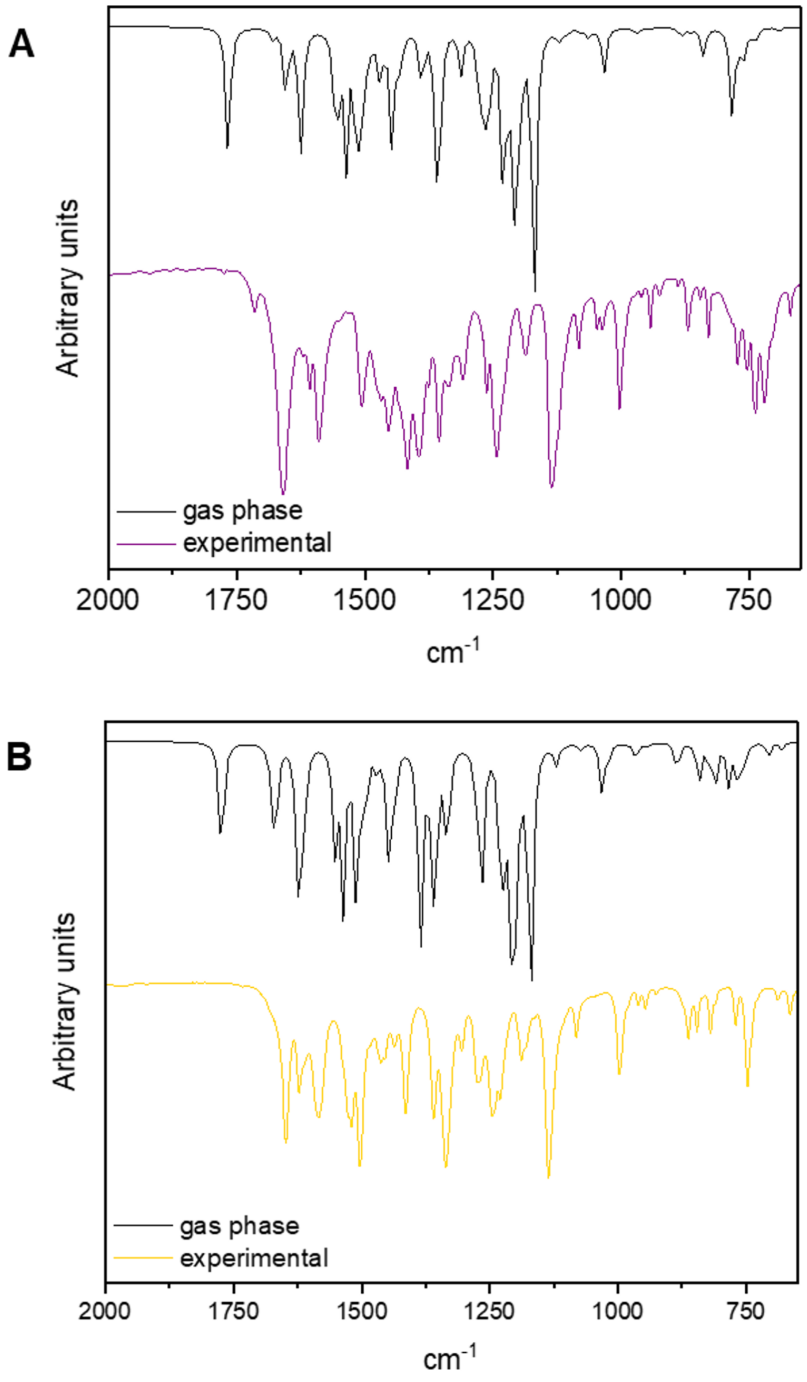

Figure 4: Mid-infrared spectra of the compounds. Experimental conditions: KBr pellets, room temperature. Calculated conditions: gas phase, level of theory B3LYP/6-311G(d,p). (A) Overlapping of the theoretical (black) and experimental (purple) spectra of **hdz-CH_3**. (B) Overlapping of the theoretical (black) and experimental (yellow) spectra of **hdz-NO_2**.

showed the existence of only one set of signals in the spectra of **hdz-CH_3** and **hdz-NO_2** (Figure 5A and 5B, respectively). ^{13}C NMR and 2D homonuclear (COSY) and heteronuclear (^{13}C,^{1}H-HSQC and HMBC) experiments were employed for the full characterization of these hydrazones, and the spectra can be seen in Supporting Information File 1, Figures S5–S12. Both compounds exhibit only one NH signal around 12 ppm, indicating the presence exclusively of the (*E*)-isomer in solution. Furthermore, steric hindrance in these cases allow only for the formation of the *antiperiplanar* conformation around the conjugated amide single bond. Full assignments, with the chemical shifts and coupling constants, can be found in Table S5 of

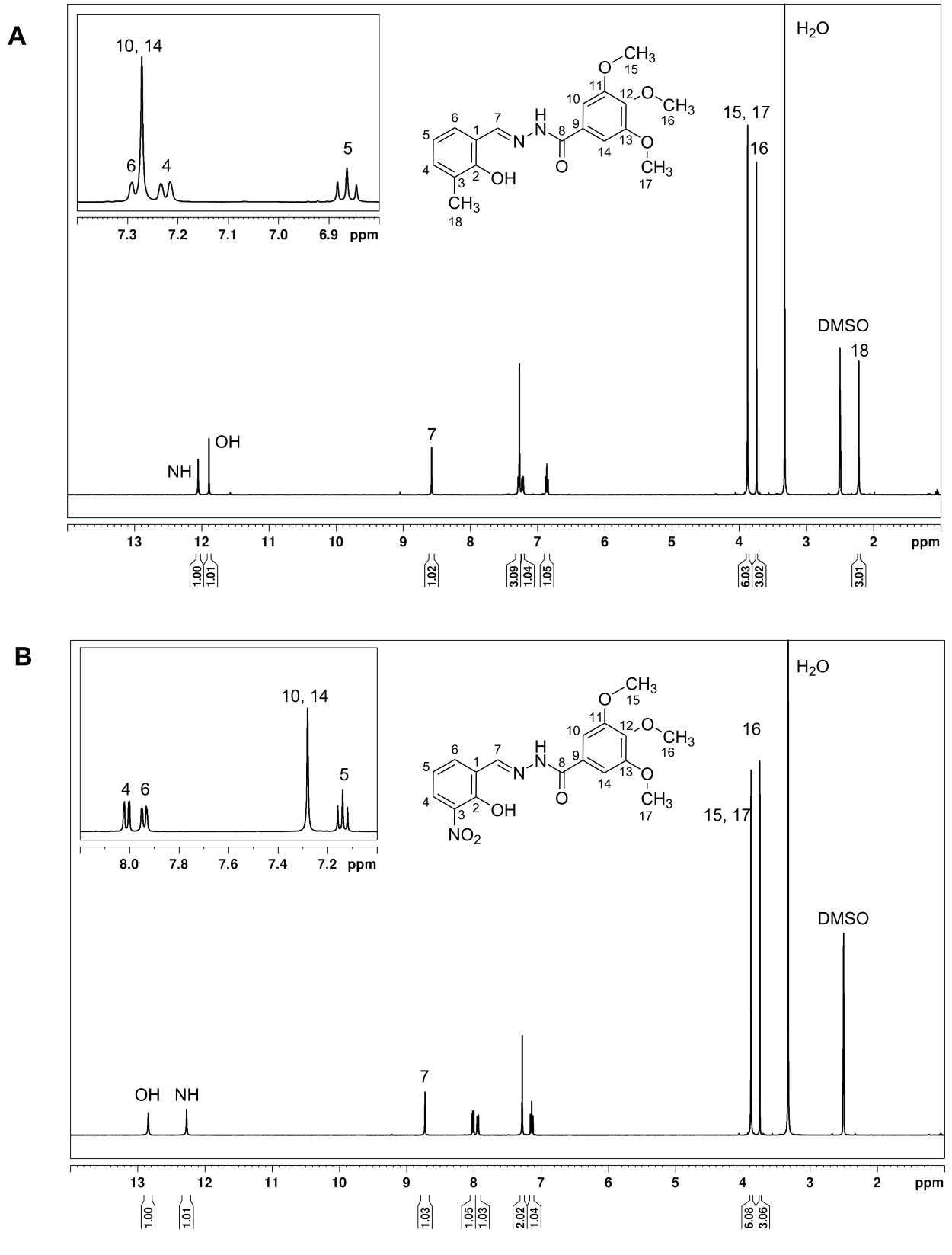

Figure 5: ^{1}H NMR (400 MHz) spectra of (A) **hdz-CH$_3$** and (B) **hdz-NO$_2$** in DMSO-d_6 at 25 °C.

Supporting Information File 1. The azomethine hydrogen H7 appears as a singlet at 8.58 ppm for **hdz-CH$_3$** and is slightly deshielded in the nitro-derivative, resonating at 8.74 ppm, since the electron density-withdrawing substituent in **hdz-NO$_2$** increases the electrophilic character of C7.

In both **hdz-CH$_3$** and **hdz-NO$_2$**, methoxy hydrogens occur as a pair of singlets: H15 and H17 at 3.88 ppm, and H16 at 3.74 ppm. Methyl H18 in **hdz-CH$_3$** appears as a more shielded singlet at 2.22 ppm. Regarding the aromatic region of this compound, the doublet related to H6 (7.28 ppm) is partially overlapped with the singlet appointed to H10 and H14 (7.27 ppm). These signals were unequivocally assigned using the 2D COSY and HMBC experiments. The most shielded doublet at 7.22 ppm corresponds to H4, and H5 occurs as a triplet at 6.86 ppm. With respect to the aromatic hydrogen atoms of **hdz-NO$_2$**, the singlet at 7.28 ppm was assigned to the equivalent H10 and H14. In this case, not only there was no overlapping of signals but also H4 appears more deshielded (8.01 ppm) when compared to **hdz-CH$_3$**. H5, in turn, appears as a triplet at 7.14 ppm.

The presence of the electron-withdrawing NO_2-substituent in the aldehyde-derived portion of **hdz-NO$_2$** caused a strong deshielding of the hydroxy group (assigned at 12.84 ppm) due to the removal of electron density on the carbon adjacent to –OH. On the other hand, in **hdz-CH$_3$**, the presence of the methyl substituent moderately shields this proton (11.89 ppm). A comparison of the H7 and –OH chemical shifts of the related hydrazones **hdz-CH$_3$** and **hdz-NO$_2$** indicates that, also in solution, the intramolecular H-bond is stronger in the latter.

Since *N*-acylhydrazones may be susceptible to hydrolysis, especially those containing a hydroxy group in *ortho*-position relative to the azomethine group as the intramolecular H-bond between the phenolic hydrogen and double-bonded nitrogen activates the azomethine carbon for a nucleophilic attack by a solvent molecule, an important step in the development of a new bioactive hydrazonic derivative is the assessment of its stability in aqueous medium. Thus, the electronic absorption spectra of **hdz-CH$_3$** and **hdz-NO$_2$** were recorded in a 10% DMSO/buffer solution (pH 7.4) immediately after preparation and at regular time intervals.

The UV–vis spectrum of **hdz-CH$_3$** between 250 and 450 nm (Figure 6A) shows two multicomponent absorptions centered at 298 (ε_{app} = 20,700 ± 40 L mol^{-1} cm^{-1}) and 338 nm (10,000 ± 25 L mol^{-1} cm^{-1}), which could be fitted to the sum of five gaussian bands. Of these, the one at 276 nm and that of very low intensity at 307 nm were tentatively assigned by comparison with the spectra of the precursors to transitions mainly localized in the TMP ring. Nevertheless, a contribution of the phenol-containing MBA ring to the component at 276 nm cannot be ruled out. On the other hand, the constituent at 333 nm was attributed to transitions from MBA. Finally, the component at 298 nm possesses no correlates in the precursors' absorption profiles, being consequently assigned to the hydrazone moiety, meaning that it probably involves a transition delocalized throughout the molecule (i.e., electronic density moving from one ring to the other).

No significant changes were observed in the **hdz-CH$_3$** spectra during the 48 hours of follow-up study in solution (Figure 6B),

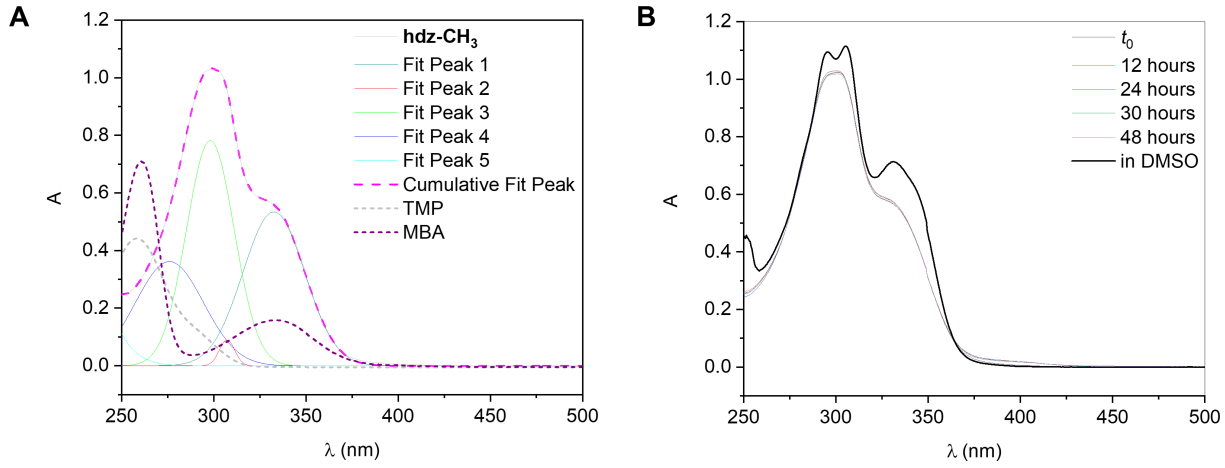

Figure 6: Electronic absorption spectra in a selected wavelength region for a solution of **hdz-CH$_3$** in 10% DMSO/HEPES mixture (pH 7.4). Experimental conditions: l = 1.0 cm and T = (25.0 ± 0.1) °C. (A) Gaussian fitting of the bands in the spectrum at t_0, along with the spectra of precursors TMP (dotted gray curve) and MBA (dotted purple). Deconvolution performed with Origin software. (B) Spectra measured at t_0 and after 12, 24, 30, and 48 h. Absorption in pure DMSO (black curve) was added for the sake of comparison.

indicating that the compound is stable in a water-rich medium. The spectrum of **hdz-CH$_3$** in DMSO, a solvent in which *N*-acylhydrazones are usually considered long-lived species, is included in the figure for the sake of comparison. Thus, the presence of the methyl electron-donating group decreases the compound's hydrolysis rate and therefore improves its suitability for uses demanding physiological-like conditions.

On the other hand, the presence of the –NO$_2$ group has a very pronounced effect on the pK_a of the phenol moiety and, to a lesser extent, on the stability of the resulting hydrazone: a considerable amount of **hdz-NO$_2$** deprotonates immediately upon dilution in the aqueous-rich medium at pH 7.4, affording a deep yellow solution due to phenolate-based absorptions centered at around 440 nm. For this reason, we decided to investigate this deprotonation by registering the UV–vis spectra of a series of **hdz-NO$_2$** 10% DMSO/buffer (acetate, phosphate or Tris-HCl) solutions with different pH values, ranging from 3.8 to 8.2 (Figure 7A). By plotting the absorbance at λ_{max} as a function of pH and then fitting the curve with a sigmoidal function (Figure 7A, inset), an apparent pK_a of 5.68 ± 0.02 was obtained. This is quite lower than the pK_a of 2-nitrophenol (around 7.2), but a similar experiment by us demonstrated that it is higher than the one of the precursor 2-hydroxy-3-nitrobenzaldehyde (4.80 ± 0.04), since the aldehyde group has a stronger electron-withdrawing power than the hydrazone moiety.

Because of this particularity, we analyzed individually the absorption patterns of fully protonated and phenol-deprotonated **hdz-NO$_2$** at the pH values of 3.8 and 8.2, respectively. When the phenol group is protonated, the spectrum of this hydrazone is very similar to that observed for **hdz-CH$_3$**, with a multicomponent band and a shoulder centered, correspondingly, at 300 and 343 nm (Figure 7B). We propose that the latter is exclusively related to a broad gaussian component calculated at 331 nm, which was assigned to a protonated NBA transition through comparison with the spectrum of this precursor at pH 3.8 (dotted dark yellow curve). On the other hand, under similar arguments, the constituent at 284 nm is probably related to a TMP-based transition. In contrast, the intense component at 307 nm has no parallel in the spectra of precursors and was consequently attributed to a hydrazone-involving process, meaning, once again, that it probably involves a transition delocalized throughout the molecule. At pH 8.2, the scenario is very different: due to phenol deprotonation, the spectrum now displays three well-defined bands centered at 281, 331 and 440 nm that can be fitted by the sum of the same number of gaussian components at 282, 332 and 439 nm, which perfectly match the individual absorptions observed (Figure 7C). Comparing the contributing constituents at pH 3.8 and pH 8.2, we can conclude that the two less energetic ones are

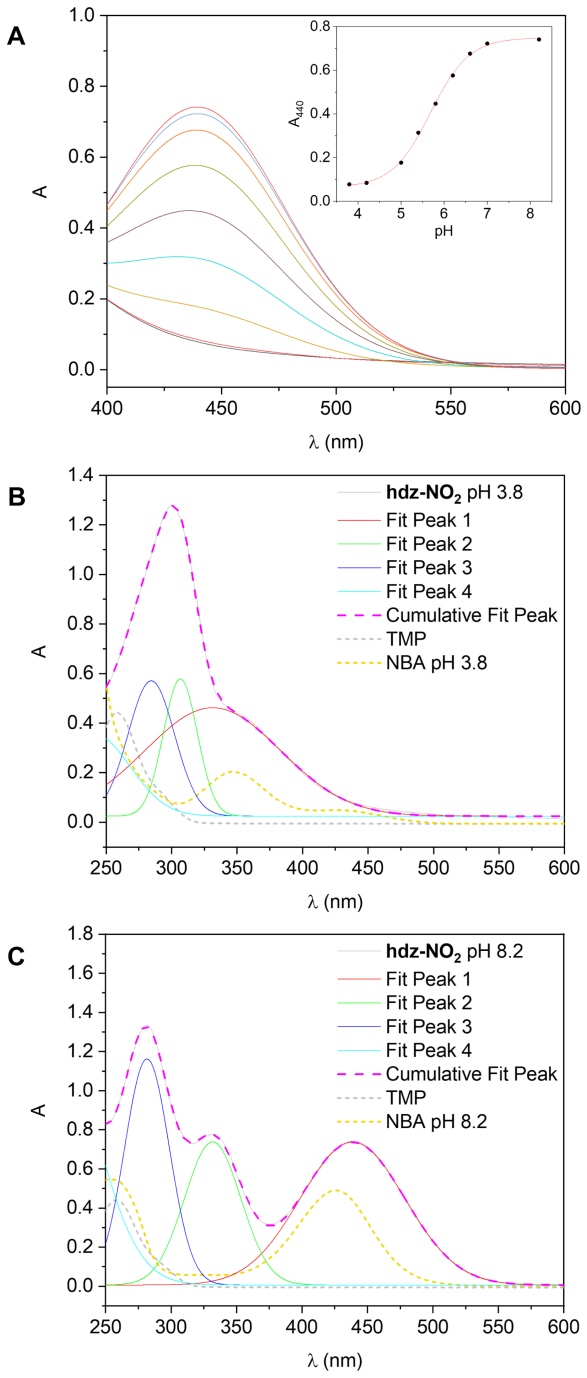

Figure 7: Electronic absorption spectra of **hdz-NO$_2$** in selected wavelength regions. Experimental conditions: l = 1.0 cm and T = (25.0 ± 0.1) °C. (A) Deprotonation band centered at 440 nm, measured in different 10% DMSO/buffer mixtures (pH ranging from 3.8 to 8.2). Inset: A_{440} versus pH with sigmoidal fitting. Gaussian fitting of the bands in a solution of the hydrazone in (B) 10% DMSO/acetate buffer (pH 3.8) and (C) 10% DMSO/Tris-HCl buffer (pH 8.2). Deconvolution performed with Origin software. Spectra of precursors TMP (dotted gray curve) and NBA (dotted dark yellow) were included to aid in band attribution.

bathochromically shifted by 25 (moving from 307 to 332) and 108 (from 331 to 439) nm in the phenolate form of **hdz-NO$_2$**, being the higher energy component quite unsusceptible to deprotonation and therefore confirming our assignment as a TMP-involving transition.

From the pK_a determined for the phenol group of the nitro-substituted hydrazone, it is evident that deprotonation is almost complete at pH 7.4. For this reason, the intramolecular H-bond identified both in the solid state (XRD, IR) and in solution (^{1}H NMR) is probably absent under physiological or pseudo-physiological conditions.

Although still stable at pH 7.4, the **hdz-NO$_2$** absorptions lose intensity by around 10% along the first 48 hours after dilution in buffer (Figure S13 in Supporting Information File 1). The mechanism associated with the hydrolysis of *N*-acylhydrazones involves the protonation of the azomethine nitrogen (in this case, N1), followed by the nucleophilic attack of a water molecule on the carbon bound to it (C7), culminating in the generation of a carbinolamine intermediate. Decomposition of this species gives the respective carbonyl compound and *N*-acylhydrazide [48,49]. In the phenol-deprotonated form of **hdz-NO$_2$**, both electron-withdrawing groups (namely, nitro and azomethine) compete for the delocalized negative charge coming from the *ortho* phenolate oxygen. Even though the azomethine group has a weaker deactivating effect on the ring than the nitro group, the electron density obtained by it through this mechanism increases the basicity of the N1 atom. In fact, the proton affinity (PA) of each hydrazone was calculated and the values suggest that **hdz-NO$_2$** has a higher tendency to be protonated in N1 than **hdz-CH$_3$** at about 2.40 kcal mol^{-1} (PA equal to −169.711 kcal mol^{-1} for the former and −167.316 kcal mol^{-1} for the latter), favoring the hydrolysis of the nitro-containing compound.

Conclusion

Two new structure-related 3,4,5-trimethoxybenzoyl-containing *N*-acylhydrazones, bioinspired by the hallucinogenic natural compound mescaline, were synthesized and fully characterized, both in solution and in the solid state. The compounds are derived from *meta*-substituted salicylaldehydes comprising either a methyl or a nitro group. In both cases, XRD confirmed the obtention of the (*E*)-isomer, in an *anti*-conformation.

An intramolecular H-bond involving the phenolic hydroxy group and the azomethine nitrogen N1 was identified in the solid state, and seems to be maintained in DMSO-d_6 solution. It is worth noting that the presence of the electron-withdrawing nitro substituent in **hdz-NO$_2$** makes the interaction stronger. An IR spectroscopy study, which was supported by computational calculations, as well as a complete NMR characterization of both compounds, align with the crystallographic observations surrounding the stronger character of this bond in the nitro-substituted hydrazone. Nevertheless, this interaction should not subsist for **hdz-NO$_2$** in a more physiological environment, since the presence of an *ortho*-nitro group affects in a significant way the pK_a of the phenol: an apparent value of 5.68 ± 0.02 was obtained.

In spite of this difference in acidity, both hydrazones are stable at physiological-like conditions, especially **hdz-CH$_3$**, as deprotonation of the phenol group also impacts the basicity of N1, increasing it and thus turning **hdz-NO$_2$** more susceptible to hydrolysis. This is also in conformity with the calculated proton affinity values for each compound, which indicate higher propensity towards hydrolysis for the nitro-derivative (−169.711 kcal mol^{-1}) over the methyl-containing one (−167.316 kcal mol^{-1}) when comparing their tendency to be protonated at N1, which constitutes the first step in the mechanism.

Overall, the *N*-acylhydrazones presented in this work are pure, well-characterized from structural and spectroscopic points of view, stable at physiological pH, and contain an ONO set of donor atoms potentially able to target trivalent metal ions. For this reason, we feel quite comfortable to state that these compounds are promising, and deserve deeper studies regarding their interactions with, for example, aluminum(III) and cell toxicity assessments.

Experimental

All solvents and reagents were purchased from commercial suppliers Sigma-Aldrich and Vetec in the highest purity available and used without further purification.

Syntheses of the compounds

Compounds were synthesized by modifying the existing methodology in the literature [50]. The compounds were prepared by condensation between 3,4,5-trimethoxybenzoic acid hydrazide (TMP, 1.0 mmol, 0.226 g) and 2-hydroxy-3-methylbenzaldehyde (MBA, 1.0 mmol, 0.136 g), for **hdz-CH$_3$**, or 2-hydroxy-3-nitrobenzaldehyde (NBA, 1.0 mmol, 0.167 g), for **hdz-NO$_2$**, in 20 mL ethanol (Scheme 2). One drop of concentrated HCl was added to the mixture as a catalyst. After stirring at 50 °C for 4 h, the mixture was cooled to room temperature and set for slow evaporation of the solvent.

3-Methylsalicylaldehyde 3,4,5-trimethoxybenzoyl hydrazone, **hdz-CH$_3$**. Yield 78%; mp 180 ± 1 °C; ^{1}H NMR (400 MHz, DMSO-d_6) δ (ppm) 2.22 (s, 3H), 3.74 (s, 3H), 3.88 (s, 6H), 6.86 (t, $^3J_{HH}$ = 7.52 Hz, 1H), 7.22 (d, $^3J_{HH}$ = 7.52 Hz, 1H), 7.27 (s,

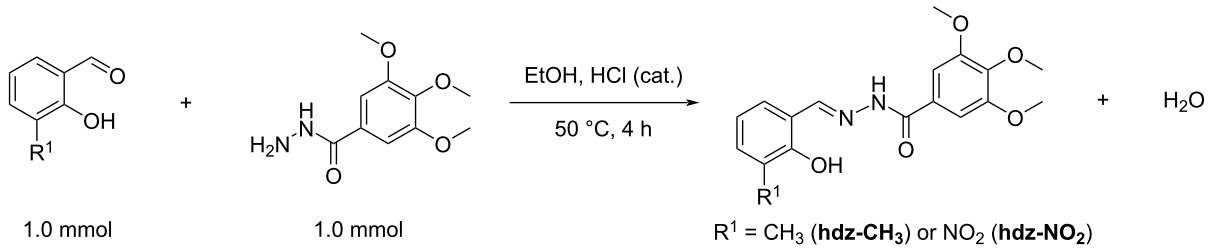

Scheme 2: General scheme for the synthesis of the studied hydrazones.

2H), 7.28 (d, $^3J_{HH}$ = 7.52 Hz, 1H), 8.58 (s, 1H), 11.89 (s, 1H), 12.05 (s, 1H); MS (*m*/*z*) 344.18 (calcd. 344.36).

3-Nitrosalicylaldehyde 3,4,5-trimethoxybenzoyl hydrazone, **hdz-NO$_2$**. Yield 44%; mp 205 ± 1 °C; ^{1}H NMR (400 MHz, DMSO-d_6) δ (ppm) 3.74 (s, 3H), 3.88 (s, 6H), 7.14 (t, $^3J_{HH}$ = 7.92 Hz, 1H), 7.28 (s, 2H), 7.94 (dd, $^3J_{HH}$ = 7.92 Hz, $^4J_{HH}$ = 1.49 Hz, 1H), 8.01 (dd, $^3J_{HH}$ = 7.92 Hz, $^4J_{HH}$ = 1.49 Hz, 1H), 8.74 (s, 1H), 12.27 (s, 1H) 12.84 (s, 1H); MS (*m*/*z*): 375.44 (calcd. 375.33).

Chemical characterization

A Perkin-Elmer 100 FT-IR spectrometer was used to record the mid-infrared spectra of the solid samples in spectroscopic grade potassium bromide (KBr). Thermogravimetric analyses were performed using a Pyris 1 TGA thermoanalyzer (Perkin-Elmer), at 10 °C min^{-1} heating rate, under nitrogen flow (20 mL min^{-1}), from 25 to 350 °C. Melting points were determined in triplicate using a Fisatom Model 431 apparatus. Hydrogen and carbon nuclear magnetic resonance spectra (NMR), homonuclear ^{1}H,^{1}H (COSY and NOESY) and heteronuclear ^{1}H,^{13}C (HSQC, HMBC) experiments were recorded on a 400 MHz Avance III (Bruker, Billerica, MA) spectrometer. Samples were dissolved in 0.5 mL DMSO-d_6 and spectra were referenced based on the residual solvent signal (quintet at 2.50 ppm for ^{1}H and septet at 39.52 for ^{13}C). Mass spectra were obtained on a Trace 1300 gas chromatograph connected to ISQ QD single quadrupole mass spectrometer (Thermo Fisher Scientific Inc., Waltham, MA, USA). Samples were prepared in dichloromethane at 1 mg mL^{-1} concentration.

Molecular absorption spectroscopy

Molecular absorption spectra were recorded on Agilent Cary 100 conc UV–visible spectrophotometer between the range of 200 and 800 nm in quartz cuvettes. Stock solutions of the compounds were prepared in spectroscopic grade DMSO at 5×10^{-3} mol L^{-1}. Dilutions (5×10^{-5} mol L^{-1}) were prepared in DMSO/buffer (50×10^{-3} mol L^{-1}) in a 10:90 (v/v) ratio and kept at 25 °C during the whole experiment. Spectra were recorded immediately after preparation of the solutions and at defined time intervals. The changes in absorbance intensity were used to calculate the percentage decrease in concentration of the compound with respect to the first reading and data were processed using the OriginPro 21 software.

X-ray diffraction

Single crystals of **hdz-CH$_3$** and **hdz-NO$_2$** suitable for X-ray diffraction were obtained from the slow evaporation of the syntheses' mother liquors. They were analyzed in a D8-Venture Bruker diffractometer equipped with Mo Kα X-ray source at 293 K. Diffraction images were collected with a Photon III area detector and the frames were integrated with the Bruker SAINT software using a narrow-frame algorithm [51]. Absorption correction was conducted with the multi-scan method in SADABAS software (APEX3 system) [52]. The structures were solved with directed methods in ShelxS [53] and refined with full-matrix least-square in ShelxL [53], implemented in WinGX [54] and ShelxLE [55] platforms. Non-hydrogen atoms were located from the electron density maps and anisotropically refined. C–H hydrogens were ride over the parent carbon with H(Uiso) = 1.2 or 1.5 C (Ueq). N–H and O–H hydrogens were located from the difference maps and isotropically refined using adequate restrains. Disordered nitro group oxygen in **hdz-NO$_2$** was treated as a two-position model (O6A, O6B), being O6A the major position with 72% of occupancy. Figures were prepared with Mercury [56], Fourier maps, data and tables were prepared with Platon [57], and the Hirshfeld surfaces and fingerprint plots were calculated from the CIF files using Crystal Explorer [58]. Potential electrostatic maps and electron density surfaces were calculated with DFT method from the CIF files using TONTO, also implemented in Crystal Explorer [58].

Computational methods

All calculations were done with the Gaussian 16 package [59] using the B3LYP exchange and correlation functional [60,61]. The 6-311G(d,p) basis set, which included polarization functions, was employed for all atoms [62,63]. The calculations

were performed in the gas and water phases. This last was used the implicit solvation effect with the IEFPCM formalism [64]. The absence of imaginary frequencies showed that the obtained structures corresponded to energy minimums. The proton affinity (PA = $E_{HL}^{+} - E_L$) was calculated from the energy difference between each protonated molecule and the respective neutral molecule [65]. The Root Medium Square Difference (RMSD) between each experimental and theoretical structure was calculated with the Pymol tool [66].

Supporting Information

Supporting Information contains Fourier difference maps (Figure S1), Hirshfeld surface analyses (Figures S2 and S3), optimized calculated structures (Figure S4), experimental and calculated geometric parameters (Tables S1 and S2) and vibrational assignments (Tables S3 and S4), ^{13}C, COSY, HMBC and HSQC spectra (Figures S5–S12) and the full NMR characterization (Table S5) for both hydrazones reported herein. Hydrolytic stability of **hdz-NO_2** at pH 7.4 is also shown (Figure S13). Accession codes CCDC 2254324 and 2255022 contain the supplementary crystallographic data for the new hydrazones **hdz-CH_3** and **hdz-NO_2**, respectively. These data can be obtained free of charge via https://www.ccdc.cam.ac.uk/data_request/cif, or by emailing data_request@ccdc.cam.ac.uk, or by contacting Cambridge Crystallographic Data Centre, 12 Union Road, Cambridge CB2 1EZ, UK; fax: +44 1223 336033.

Supporting Information File 1

Additional information.
[https://www.beilstein-journals.org/bjoc/content/supplementary/1860-5397-19-125-S1.pdf]

Acknowledgements

We thank the Centro Nacional de Biologia Estrutural e Bioimagem (CENABIO) and Laboratório de Raios-X from the Federal Fluminense University (LDRX-UFF: http://ldrx.sites.uff.br/) for the X-ray diffraction facilities.

Funding

SPM, DSC and NAR thank the scientific Brazilian funding agency CNPq (Conselho Nacional de Desenvolvimento Científico e Tecnológico) - 304105/2021-0, 150898/2022-3 and 306866/2021-8, respectively. CBPL, SPM and NAR are grateful to FAPERJ (Fundação Carlos Chagas Filho de Amparo à Pesquisa do Estado do Rio de Janeiro) - SEI-260003/006613/2022, E-26/010.210.513/2019 and E-26/201.174/2021, respectively. We would like to acknowledge Ministério da Ciência e Tecnologia (MCT) and Financiadora de Estudos e Projetos (FINEP) – Convênio 01.11.0100.00. This study was financed in part by the Brazilian *Coordenação de Aperfeiçoamento de Pessoal de Nível Superior* (CAPES) – Finance Code 001.

Conflict of Interest

The authors declare no competing interest.

ORCID® iDs

Dayanne Martins - https://orcid.org/0000-0003-2868-7433
Roberta Lamosa - https://orcid.org/0009-0003-2851-5946
Talis Uelisson da Silva - https://orcid.org/0000-0002-0745-0042
Carolina B. P. Ligiero - https://orcid.org/0000-0002-1944-9030
Sérgio de Paula Machado - https://orcid.org/0000-0002-5506-9174
Daphne S. Cukierman - https://orcid.org/0000-0002-8606-2194
Nicolás A. Rey - https://orcid.org/0000-0002-0624-7560

References

1. Kostova, I.; Saso, L. *Curr. Med. Chem.* **2013,** *20,* 4609–4632. doi:10.2174/09298673113209990149
2. Morjan, R. Y.; Mkadmh, A. M.; Beadham, I.; Elmanama, A. A.; Mattar, M. R.; Raftery, J.; Pritchard, R. G.; Awadallah, A. M.; Gardiner, J. M. *Bioorg. Med. Chem. Lett.* **2014,** *24,* 5796–5800. doi:10.1016/j.bmcl.2014.10.029
3. Țînțaș, M. L.; Diac, A. P.; Soran, A.; Terec, A.; Grosu, I.; Bogdan, E. *J. Mol. Struct.* **2014,** *1058,* 106–113. doi:10.1016/j.molstruc.2013.11.005
4. Wegermann, C. A.; Monzani, E.; Casella, L.; Ribeiro, M. A.; Bruzeguini, C. E. T.; Vilcachagua, J. D.; Costa, L. A. S.; Ferreira, A. M. D. C. *J. Mol. Struct.* **2022,** *1250,* 131633. doi:10.1016/j.molstruc.2021.131633
5. Su, X.; Aprahamian, I. *Chem. Soc. Rev.* **2014,** *43,* 1963–1981. doi:10.1039/c3cs60385g
6. Tatum, L. A.; Su, X.; Aprahamian, I. *Acc. Chem. Res.* **2014,** *47,* 2141–2149. doi:10.1021/ar500111f
7. Abumelha, H. M. A. *J. Heterocycl. Chem.* **2018,** *55,* 1738–1745. doi:10.1002/jhet.3211
8. Abulkhair, H. S.; Turky, A.; Ghiaty, A.; Ahmed, H. E. A.; Bayoumi, A. H. *Bioorg. Chem.* **2020,** *100,* 103899. doi:10.1016/j.bioorg.2020.103899
9. Bieliauskas, A.; Getautis, V.; Martynaitis, V.; Jankauskas, V.; Kamarauskas, E.; Krikštolaitytė, S.; Šačkus, A. *Synth. Met.* **2013,** *179,* 27–33. doi:10.1016/j.synthmet.2013.07.003
10. Moraes, R. S.; Aderne, R. E.; Cremona, M.; Rey, N. A. *Opt. Mater. (Amsterdam, Neth.)* **2016,** *52,* 186–191. doi:10.1016/j.optmat.2015.12.039
11. Chai, Q.; Wei, J.; Bai, B.; Wang, H.; Li, M. *Dyes Pigm.* **2018,** *152,* 93–99. doi:10.1016/j.dyepig.2018.01.051
12. Dascalu, A.-E.; Ghinet, A.; Lipka, E.; Furman, C.; Rigo, B.; Fayeulle, A.; Billamboz, M. *Bioorg. Med. Chem. Lett.* **2020,** *30,* 127220. doi:10.1016/j.bmcl.2020.127220
13. Thota, S.; Rodrigues, D. A.; Pinheiro, P. d. S. M.; Lima, L. M.; Fraga, C. A. M.; Barreiro, E. J. *Bioorg. Med. Chem. Lett.* **2018,** *28,* 2797–2806. doi:10.1016/j.bmcl.2018.07.015
14. Li, M.; Cheng, L. P.; Pang, W.; Zhong, Z. J.; Guo, L. L. *ACS Med. Chem. Lett.* **2020,** *11,* 1745–1750. doi:10.1021/acsmedchemlett.0c00313

15. Singh, U. P.; Bhat, H. R.; Verma, A.; Kumawat, M. K.; Kaur, R.; Gupta, S. K.; Singh, R. K. *RSC Adv.* **2013,** *3,* 17335–17348. doi:10.1039/c3ra41604f
16. de Queiroz, A. C.; Barbosa, G.; de Oliveira, V. R. T.; de Mattos Alves, H.; Alves, M. A.; Carregaro, V.; Santana da Silva, J.; Barreiro, E. J.; Alexandre-Moreira, M. S.; Lima, L. M. *PLoS One* **2022,** *17,* e0269447. doi:10.1371/journal.pone.0269447
17. da Costa Salomé, D.; de Freitas, R. H. C. N.; Fraga, C. A. M.; Fernandes, P. D. *Int. J. Mol. Sci.* **2022,** *23,* 13562. doi:10.3390/ijms232113562
18. Rezki, N.; Al-Sodies, S. A.; Ahmed, H. E. A.; Ihmaid, S.; Messali, M.; Ahmed, S.; Aouad, M. R. *J. Mol. Liq.* **2019,** *284,* 431–444. doi:10.1016/j.molliq.2019.04.010
19. Rohane, S. H.; Chauhan, A. J.; Fuloria, N. K.; Fuloria, S. *Arabian J. Chem.* **2020,** *13,* 4495–4504. doi:10.1016/j.arabjc.2019.09.004
20. Xia, L.; Xia, Y.-F.; Huang, L.-R.; Xiao, X.; Lou, H.-Y.; Liu, T.-J.; Pan, W.-D.; Luo, H. *Eur. J. Med. Chem.* **2015,** *97,* 83–93. doi:10.1016/j.ejmech.2015.04.042
21. Angelova, V. T.; Pencheva, T.; Vassilev, N.; K-Yovkova, E.; Mihaylova, R.; Petrov, B.; Valcheva, V. *Antibiotics (Basel, Switz.)* **2022,** *11,* 562. doi:10.3390/antibiotics11050562
22. Firmino, G. d. S. S.; André, S. C.; Hastenreiter, Z.; Campos, V. K.; Abdel-Salam, M. A. L.; de Souza-Fagundes, E. M.; Lessa, J. A. *Inorg. Chim. Acta* **2019,** *497,* 119079. doi:10.1016/j.ica.2019.119079
23. Wehbe, M.; Leung, A. W. Y.; Abrams, M. J.; Orvig, C.; Bally, M. B. *Dalton Trans.* **2017,** *46,* 10758–10773. doi:10.1039/c7dt01955f
24. Rada, J. P.; Bastos, B. S. M.; Anselmino, L.; Franco, C. H. J.; Lanznaster, M.; Diniz, R.; Fernández, C. O.; Menacho-Márquez, M.; Percebom, A. M.; Rey, N. A. *Inorg. Chem.* **2019,** *58,* 8800–8819. doi:10.1021/acs.inorgchem.9b01195
25. Rada, J. P.; Forté, J.; Gontard, G.; Corcé, V.; Salmain, M.; Rey, N. A. *ChemBioChem* **2020,** *21,* 2474–2486. doi:10.1002/cbic.202000122
26. Rada, J. P.; Forté, J.; Gontard, G.; Bachelet, C.-M.; Rey, N. A.; Salmain, M.; Corcé, V. *J. Biol. Inorg. Chem.* **2021,** *26,* 675–688. doi:10.1007/s00775-021-01885-5
27. de Freitas, L. V.; da Silva, C. C. P.; Ellena, J.; Costa, L. A. S.; Rey, N. A. *Spectrochim. Acta, Part A* **2013,** *116,* 41–48. doi:10.1016/j.saa.2013.06.105
28. Hauser-Davis, R. A.; de Freitas, L. V.; Cukierman, D. S.; Cruz, W. S.; Miotto, M. C.; Landeira-Fernandez, J.; Valiente-Gabioud, A. A.; Fernández, C. O.; Rey, N. A. *Metallomics* **2015,** *7,* 743–747. doi:10.1039/c5mt00003c
29. Cukierman, D. S.; Pinheiro, A. B.; Castiñeiras-Filho, S. L. P.; da Silva, A. S. P.; Miotto, M. C.; De Falco, A.; de P. Ribeiro, T.; Maisonette, S.; da Cunha, A. L. M. C.; Hauser-Davis, R. A.; Landeira-Fernandez, J.; Aucélio, R. Q.; Outeiro, T. F.; Pereira, M. D.; Fernández, C. O.; Rey, N. A. *J. Inorg. Biochem.* **2017,** *170,* 160–168. doi:10.1016/j.jinorgbio.2017.02.020
30. Cukierman, D. S.; Accardo, E.; Gomes, R. G.; De Falco, A.; Miotto, M. C.; Freitas, M. C. R.; Lanznaster, M.; Fernández, C. O.; Rey, N. A. *J. Biol. Inorg. Chem.* **2018,** *23,* 1227–1241. doi:10.1007/s00775-018-1606-0
31. Cukierman, D. S.; Bodnár, N.; Evangelista, B. N.; Nagy, L.; Kállay, C.; Rey, N. A. *J. Biol. Inorg. Chem.* **2019,** *24,* 1231–1244. doi:10.1007/s00775-019-01700-2
32. Cukierman, D. S.; Lázaro, D. F.; Sacco, P.; Ferreira, P. R.; Diniz, R.; Fernández, C. O.; Outeiro, T. F.; Rey, N. A. *Dalton Trans.* **2020,** *49,* 16252–16267. doi:10.1039/d0dt01138j
33. De Falco, A.; Kincheski, G. C.; Atrián-Blasco, E.; Hureau, C.; Ferreira, S. T.; Rey, N. A. *Behav. Pharmacol.* **2020,** *31,* 738–747. doi:10.1097/fbp.0000000000000578
34. Cukierman, D. S.; Bodnár, N.; Diniz, R.; Nagy, L.; Kállay, C.; Rey, N. A. *Inorg. Chem.* **2022,** *61,* 723–737. doi:10.1021/acs.inorgchem.1c03598
35. Cukierman, D. S.; Rey, N. A. *Front. Neurol.* **2022,** *13,* 828654. doi:10.3389/fneur.2022.828654
36. Carvalho, A.; Barbosa, B. M.; Flores, J. S.; do Carmo Gonçalves, P.; Diniz, R.; Cordeiro, Y.; Fernández, C. O.; Cukierman, D. S.; Rey, N. A. *J. Inorg. Biochem.* **2023,** *238,* 112033. doi:10.1016/j.jinorgbio.2022.112033
37. Cukierman, D. S. Physico-chemical optimization and Structure–Activity Relationship studies of aldehyde-derived *N*-acylhydrazones: towards the improvement of moderate metal chelators as a strategy against metal-enhanced aggregopathies. Ph.D. Thesis, Pontifical Catholic University of Rio de Janeiro, Rio de Janeiro, Brazil, 2021.
38. Exley, C.; Mold, M. J. *J. Biol. Inorg. Chem.* **2019,** *24,* 1279–1282. doi:10.1007/s00775-019-01710-0
39. Etter, M. C.; MacDonald, J. C.; Bernstein, J. *Acta Crystallogr., Sect. B: Struct. Sci.* **1990,** *46,* 256–262. doi:10.1107/s0108768189012929
40. Palusiak, M.; Simon, S.; Solà, M. *J. Org. Chem.* **2006,** *71,* 5241–5248. doi:10.1021/jo060591x
41. Guevara-Vela, J. M.; Gallegos, M.; Valentín-Rodríguez, M. A.; Costales, A.; Rocha-Rinza, T.; Pendás, Á. M. *Molecules* **2021,** *26,* 4196. doi:10.3390/molecules26144196
42. Pareras, G.; Palusiak, M.; Duran, M.; Solà, M.; Simon, S. *J. Phys. Chem. A* **2018,** *122,* 2279–2287. doi:10.1021/acs.jpca.7b12066
43. Kruszewski, J.; Krygowski, T. M. *Tetrahedron Lett.* **1972,** *13,* 3839–3842. doi:10.1016/s0040-4039(01)94175-9
44. Spackman, M. A.; Jayatilaka, D. *CrystEngComm* **2009,** *11,* 19–32. doi:10.1039/b818330a
45. Albuquerque, S. O.; Barros, T. G.; Dias, L. R. S.; Lima, C. H. d. S.; Azevedo, P. H. R. d. A.; Flores-Junior, L. A. P.; dos Santos, E. G.; Loponte, H. F.; Pinheiro, S.; Dias, W. B.; Muri, E. M. F.; Todeschini, A. R. *Eur. J. Pharm. Sci.* **2020,** *154,* 105510. doi:10.1016/j.ejps.2020.105510
46. dos Santos, E. S.; de Souza, L. C. V.; de Assis, P. N.; Almeida, P. F.; Ramos-de-Souza, E. *J. Biomol. Struct. Dyn.* **2014,** *32,* 1780–1792. doi:10.1080/07391102.2013.834850
47. Munir, R.; Javid, N.; Zia-ur-Rehman, M.; Zaheer, M.; Huma, R.; Roohi, A.; Athar, M. M. *Molecules* **2021,** *26,* 4908. doi:10.3390/molecules26164908
48. Ji, K.; Lee, C.; Janesko, B. G.; Simanek, E. E. *Mol. Pharmaceutics* **2015,** *12,* 2924–2927. doi:10.1021/acs.molpharmaceut.5b00205
49. Kalia, J.; Raines, R. T. *Angew. Chem., Int. Ed.* **2008,** *47,* 7523–7526. doi:10.1002/anie.200802651
50. González-Baró, A. C.; Pis-Diez, R.; Parajón-Costa, B. S.; Rey, N. A. *J. Mol. Struct.* **2012,** *1007,* 95–101. doi:10.1016/j.molstruc.2011.10.026
51. *APEX3;* Bruker: Madison, Wisconsin, USA, 2012.
52. Krause, L.; Herbst-Irmer, R.; Sheldrick, G. M.; Stalke, D. *J. Appl. Crystallogr.* **2015,** *48,* 3–10. doi:10.1107/s1600576714022985
53. Sheldrick, G. M. *Acta Crystallogr., Sect. A: Found. Adv.* **2015,** *71,* 3–8. doi:10.1107/s2053273314026370
54. Farrugia, L. J. *J. Appl. Crystallogr.* **2012,** *45,* 849–854. doi:10.1107/s0021889812029111
55. Hübschle, C. B.; Sheldrick, G. M.; Dittrich, B. *J. Appl. Crystallogr.* **2011,** *44,* 1281–1284. doi:10.1107/s0021889811043202

56. Macrae, C. F.; Edgington, P. R.; McCabe, P.; Pidcock, E.; Shields, G. P.; Taylor, R.; Towler, M.; van de Streek, J. *J. Appl. Crystallogr.* **2006,** *39,* 453–457. doi:10.1107/s002188980600731x
57. Spek, A. L. *Acta Crystallogr., Sect. D: Biol. Crystallogr.* **2009,** *65,* 148–155. doi:10.1107/s090744490804362x
58. Spackman, P. R.; Turner, M. J.; McKinnon, J. J.; Wolff, S. K.; Grimwood, D. J.; Jayatilaka, D.; Spackman, M. A. *J. Appl. Crystallogr.* **2021,** *54,* 1006–1011. doi:10.1107/s1600576721002910
59. *Gaussian 16,* Rev. C.01; Gaussian Inc.: Wallingford, CT, 2016.
60. Becke, A. D. *J. Chem. Phys.* **1993,** *98,* 5648–5652. doi:10.1063/1.464913
61. Lee, C.; Yang, W.; Parr, R. G. *Phys. Rev. B* **1988,** *37,* 785–789. doi:10.1103/physrevb.37.785
62. Petersson, G. A.; Bennett, A.; Tensfeldt, T. G.; Al-Laham, M. A.; Shirley, W. A.; Mantzaris, J. *J. Chem. Phys.* **1988,** *89,* 2193–2218. doi:10.1063/1.455064
63. Petersson, G. A.; Al-Laham, M. A. *J. Chem. Phys.* **1991,** *94,* 6081–6090. doi:10.1063/1.460447
64. Scalmani, G.; Frisch, M. J. *J. Chem. Phys.* **2010,** *132,* 114110. doi:10.1063/1.3359469
65. Mary, C. P. V.; Vijayakumar, S.; Shankar, R. *J. Mol. Graphics Modell.* **2018,** *79,* 1–14. doi:10.1016/j.jmgm.2017.10.022
66. Yuan, S.; Chan, H. C. S.; Hu, Z. *Wiley Interdiscip. Rev.: Comput. Mol. Sci.* **2017,** *7,* e1298. doi:10.1002/wcms.1298

License and Terms